



**Numerical Simulation of Natural Convection in an  
Enclosure Partly Filled with a Porous Medium  
Saturated with a Nanofluid**

*Thesis submitted for the degree of*

*Doctor of Philosophy*

*at the University of Leicester*

by

**Basil Mahdi Hadi Srayyih**

The school of Engineering

University of Leicester

United Kingdom

**September 2019**

# **Numerical Simulation of Natural Convection in an Enclosure Partly Filled with a Porous Medium Saturated with a Nanofluid**

**Basil Mahdi Hadi**

## **Abstract**

Natural convection inside an enclosure partly filled with a porous slab saturated with a nanofluid has been investigated numerically using various thermal boundary conditions. The Galerkin finite element method was used to solve the governing equations. Four different scenarios were modelled. Firstly, two-dimensional laminar natural convection in a vertical or a horizontal alignment to the porous-nanofluid layers was investigated with a linearly heated left-hand side enclosure wall. At low values of the thermal conductivity ratio and Darcy number, the heat transfer rate was higher for the horizontal alignment compared to the vertical alignment and vice versa at a high value of the Darcy number. Secondly, the same geometry was studied with a sinusoidally heated left-hand side enclosure wall. It was found that the temperature amplitude and wave number of the sinusoidally heated wall significantly affected the heat transfer rate. At the thermal conductivity ratio  $< 1$  and the Darcy number  $\geq 10^{-3}$ , the heat transfer rate increased in the vertical alignment of the porous-nanofluid layers compared to the horizontal alignment. In both of these scenarios, the porous slab direction inside the enclosure played a significant role on the heat transfer. Thirdly, two-dimensional laminar natural convection of a hybrid nanofluid inside the porous-nanofluid layers using a thermal non-equilibrium model has been simulated. It was found that increasing the modified thermal conductivity ratio and interphase heat transfer coefficient values strongly enhanced the heat transfer rate and satisfy the thermal equilibrium case. Finally, the amplitude and the wave number of the corrugated wall have a significant role on the turbulent natural convection in a three-dimensional enclosure partly filled with porous slab saturated with a hybrid nanofluid. For all scenarios, the lower thickness of the porous slab using the nanofluid predicted a new trend of the fluid flow and heat transfer compared to the porous enclosure.

## **Acknowledgment**

First, I would like to express my special gratitude towards ‘Allah’, for giving me the ability to complete my PhD study. After, I would first like to thank my supervisor Dr. Shian Gao for his supervision and encouragement throughout my study. Then I would like to thank my co-supervisors Dr. Andrew McMullan and Dr. Salam Hadi Hussain and my examiners for their advice during my PhD progress.

My appreciation goes to my colleagues in the School of Engineering (Thermal Engineering Group) and to Dr. Peter Polak for their support during my study. Additionally, I would like to thank the Ministry of Higher Education and Scientific Research of Iraq for the financial support of the project.

Finally, I would like to thank my father and mother, my wife, my children and my brothers, my siblings and all my friends for their support during my PhD progress.

*Basil Mahdi Hadi*

*09/2019*

# Table of contents

<b>Abstract.....</b>	<b>i</b>
<b>Acknowledgment.....</b>	<b>ii</b>
<b>Table of contents .....</b>	<b>iii</b>
<b>Abbreviation.....</b>	<b>ix</b>
<b>Chapter 1: Introduction .....</b>	<b>1</b>
1.1 Context.....	1
1.2 Flow and heat transfer control techniques .....	2
1.2.1 Porous medium technique .....	2
1.2.2 Nanofluid technique .....	4
1.2.3 Corrugated wall technique.....	6
1.3 Aims and objectives .....	8
1.4 Thesis structure .....	11
<b>Chapter 2: Literature review.....</b>	<b>14</b>
2.1 Introduction.....	14
2.2 Laminar flow .....	14
2.2.1 Porous medium in an enclosure saturated with a single-phase fluid.....	14
2.2.2 Porous medium in an enclosure saturated with a nanofluid.....	20
2.2.3 Porous medium in a corrugated enclosure.....	24
2.3 Turbulent flow.....	26

2.3.1 Enclosure entirely filled with a porous medium saturated with a single-phase fluid.....	27
2.3.2 Enclosure entirely filled with a porous medium saturated with a nanofluid ..	27
2.3.3 Porous medium in a corrugated enclosure.....	28
2.4 Conclusions .....	28
<b>Chapter 3: Methodology .....</b>	<b>31</b>
3.1 Introduction .....	31
3.2 The domain and governing equations discretization.....	32
3.2.1 Discretize domain .....	33
3.2.2 The governing equations discretization.....	33
3.3 Numerical solver .....	34
3.4 The governing equations of the laminar and turbulent heat transfer .....	35
3.4.1 Laminar heat transfer case study .....	36
3.4.2 Turbulent heat transfer case study .....	36
3.5 Thermo-physical properties .....	37
3.6 Code validations.....	37
3.6.1 Laminar heat transfer validations .....	37
3.6.2 Turbulent heat transfer validations .....	44
3.7 Conclusions .....	46
<b>Chapter 4: Natural Convection within an Enclosure Filled with Composite Nanofluid-Porous Layers with a Linearly Heated Left Wall .....</b>	<b>47</b>
4.1 Motivation and introduction.....	47

4.2 A model problem.....	48
4.2.1 Physical model.....	48
4.2.2 Boundary conditions.....	49
4.2.3 Grid independence test .....	49
4.3 Results and discussion.....	50
4.3.1 Streamlines and isotherms .....	50
4.3.2 Velocity distribution .....	61
4.3.3 Normalized temperature distribution, $\theta$ .....	64
4.3.4 Heat transfer rate: Local Nusselt number .....	67
4.3.1 The average Nusselt number, $Nu_{av}$ .....	70
4.4 Conclusions .....	73
<b>Chapter 5: Effects of a Sinusoidally Heated Left Wall on Natural Convection within an Enclosure Filled with Composite Nanofluid-Porous Layers .....</b>	<b>75</b>
5.1 Motivation and introduction.....	75
5.2 A model problem.....	76
5.2.1 Physical model.....	76
5.2.2 Boundary conditions.....	77
5.2.3 Grid independence test .....	77
5.3 Results and discussion.....	78
5.3.1 Streamlines and isotherms .....	78
5.3.2 Velocity magnitude, $R$ .....	95

5.3.3 Normalized temperature distribution, $\theta$ .....	96
5.3.4 Heat transfer rate: Local Nusselt Number .....	98
5.3.5 The average Nusselt number, $Nu_{av}$ .....	100
5.4 Conclusions .....	103
<b>Chapter 6: Natural Convection of a Hybrid Nanofluid in a Square Enclosure Partially Filled with a Porous Medium Using a Thermal Non-Equilibrium Model.....</b>	<b>105</b>
6.1 Motivation and introduction.....	105
6.2 A model problem.....	105
6.2.1 Physical model.....	105
6.2.2 Boundary conditions.....	106
6.2.3 Grid independence test .....	107
6.3 Results and discussion.....	108
6.3.1 Streamlines and isotherms .....	108
6.3.2 Velocity magnitude, $R$ .....	116
6.3.3 Normalized temperature distribution, $\theta$ .....	117
6.3.4 Heat transfer rate: Local Nusselt number .....	119
6.3.5 The average Nusselt number, $Nu_{av}$ .....	121
6.4 Conclusions .....	125
<b>Chapter 7: Turbulent Natural Convection inside a 3-D Corrugated Sidewall Enclosure Partially Filled with a Porous Medium Saturated by a Hybrid Nanofluid Using <math>\kappa - \epsilon</math> Model.....</b>	<b>127</b>

7.1 Motivation and introduction.....	127
7.2 A model problem.....	127
7.2.1 Physical model.....	127
7.2.2 Boundary conditions.....	128
7.2.3 Grid independent test.....	129
7.3 Results and discussion.....	130
7.3.1 Streamlines and isotherms .....	130
7.3.2 Average normalized turbulent kinetic energy, $\mathbf{K}$ .....	136
7.3.3 Average normalized temperature distribution, $\theta$ .....	137
7.3.4 The average Nusselt number, $Nu_{av}$ .....	138
7.4 Conclusions.....	142
<b>Chapter 8: Conclusions and Recommendations .....</b>	<b>144</b>
8.1 Conclusions.....	144
8.1.1 Natural Convection within an Enclosure Filled with Composite Nanofluid-Porous Layers with a Linearly Heated Left Wall .....	144
8.1.2 Effects of a Sinusoidally Heated Left Wall on Natural Convection within an Enclosure Filled with Composite Nanofluid-Porous Layers.....	145
8.1.3 Natural Convection of a Hybrid Nanofluid in a Square Enclosure Partially Filled with a Porous Medium Using a Thermal Non-Equilibrium Model .....	145
8.1.4 Turbulent Natural Convection inside a 3-D Corrugated Sidewall Enclosure Partially Filled with a Porous Medium Saturated by a Hybrid Nanofluid Using $\kappa - \epsilon$ Model.....	146
8.2 Recommended future work.....	146

<b>References.....</b>	<b>148</b>
<b>Appendix A: Equations discretization and shape function.....</b>	<b>162</b>
<b>A1: Non-linear discretization equations .....</b>	<b>162</b>
<b>A1.1 Equations discretization of the nanofluid layer .....</b>	<b>162</b>
<b>A.1.2 Equations discretization of the porous medium layer .....</b>	<b>163</b>
<b>A2: Shape function: .....</b>	<b>164</b>
<b>Appendix B: Laminar flow governing equations.....</b>	<b>169</b>
<b>B1: Two-dimensional laminar flow governing dimensionless equations using a local thermal equilibrium model (LTE).....</b>	<b>169</b>
<b>B2: Two-dimensional laminar flow governing dimensionless equations using a local thermal non-equilibrium model (LTNE).....</b>	<b>171</b>
<b>Appendix C: Three-dimensional turbulent flow governing equations .....</b>	<b>175</b>
<b>Appendix D: List of publications.....</b>	<b>179</b>

## Abbreviation

<i>A</i>	amplitude
<i>b</i>	heat source length, (m)
<i>B</i>	dimensionless heat source length, ( $B = b \cdot L^{-1}$ )
<i>Cp</i>	specific heat capacity (J. kg. K <sup>-1</sup> )
<i>CF</i>	Forchhemier coefficient, ( $CF = (1.75/\sqrt{175}) \cdot \varepsilon^{-1.5}$ )
<i>d</i>	heat source position, (m)
<i>D</i>	dimensionless heat source position, ( $D = d \cdot L^{-1}$ )
<i>Da</i>	Darcy Number, ( $Da = \lambda \cdot L^{-2}$ )
<i>F<sub>o</sub></i>	Non-dimensional form drag coefficient, ( $F_o = CF/\sqrt{Da}$ )
<i>g</i>	gravitational field, (m.s <sup>-2</sup> )
<i>Gr</i>	Grashof number, ( $Gr = \beta \cdot g \cdot \Delta T \cdot L^3/v^2$ )
<i>h</i>	heat transfer coefficient, (W.m <sup>-2</sup> . K <sup>-1</sup> )
<i>H</i>	interphase heat transfer coefficient, ( $H = (h \cdot L^2)/(k)_{hnf}$ )
<i>k</i>	thermal conductivity, (W.m <sup>-1</sup> . K <sup>-1</sup> )
<i>K</i>	dimensionless thermal conductivity, ( $K = (k)_p/(k)_{nf}$ )
<i>L</i>	length of the cavity
<i>N</i>	frequency
<i>Nu</i>	Nusselt number, ( $Nu = (h \cdot L/k)$ )
<i>p</i>	pressure (N.m <sup>-2</sup> )
<i>P</i>	dimensionless pressure, ( $P = p \cdot L/((\rho)_{bf} \cdot (\alpha)_{bf}^2)$ )
<i>Pr</i>	Prandtl number, ( $Pr = \mu \cdot Cp/k$ )
<i>Ra</i>	Rayleigh number, ( $Ra = Gr \cdot Pr$ )
<i>Res</i>	residual error
<i>s</i>	porous layer thickness (m)
<i>S</i>	dimensionless porous layer thickness, ( $S = s/L^{-1}$ )
<i>sn</i>	selected node of the element
<i>SN</i>	total selected node of the element
<i>T</i>	temperature (K)

$u, v, w$	dimensional velocity components in the $x$ , $y$ and $z$ -directions respectively. ( $\text{m}\cdot\text{s}^{-1}$ )
$U, V, W$	dimensionless velocity components for $(u/L)$ , $(v/L)$ , and $(w/L)$ in the $X$ , $Y$ and $Z$ -directions respectively
$V$	volume, ( $\text{m}^3$ )
$x, y, z$	cartesian coordinates (m)
$X, Y, Z$	dimensionless cartesian coordinates at $(x/L)$ , $(y/L)$ and $(z/L)$ respectively
<i>Greek symbols</i>	
$\alpha$	thermal diffusivity, ( $\text{m}^2\cdot\text{s}^{-1}$ )
$\beta$	thermal expansion coefficient ( $\text{K}^{-1}$ )
$\gamma$	modified hybrid nanofluid/porous thermal conductivity ratio
$\varepsilon$	porosity, ( $\frac{V_f}{V}$ )
$\epsilon$	dimensional dissipation rate of specific turbulent kinetic energy ( $\text{m}^2\cdot\text{s}^{-3}$ )
$E$	dimensionless dissipation rate of specific turbulent kinetic energy, ( $E = \epsilon / ((\alpha_{bf})^2 / L^4)$ )
$\theta$	dimensionless temperature, ( $\theta = (T - T_c) / (T_h - T_c)$ )
$\vartheta$	kinematic viscosity, ( $\text{m}^2\cdot\text{s}^{-1}$ )
$\kappa$	dimensional turbulent kinetic energy, ( $\text{m}^2\cdot\text{s}^{-2}$ )
$K$	dimensionless average turbulent kinetic energy, ( $K = \kappa / (\alpha_{bf}^2 / L^2)$ )
$\lambda$	permeability of porous medium, ( $\text{m}^2$ )
$\mu$	dynamic viscosity, (Pa.s)
$\rho$	density, ( $\text{kg}\cdot\text{m}^{-3}$ )
$\Phi$	unknown variable
$\Phi$	test function
$\phi$	volume fraction of nanoparticles

$\psi$	stream function, ( $\text{m}^2.\text{s}^{-1}$ )
$\Psi$	dimensionless stream function, ( $\psi/\alpha$ )

*Subscript*

*av* average

$\text{Al}_2\text{O}_3$  alumina nanoparticles

*bf* base fluid (single-phase fluid)

*c* cold

*cr* corrugated

*Cu* copper nanoparticles

*f* fluid

*hnf* hybrid nanofluid

*nf* nanofluid

*o* initial

*p* porous

*r* ratio

*sn* selected node of the element

*SN* total selected node of the element

*td* dimensionless turbulent flow

*th* thermal

*w* wall

# Chapter 1: Introduction

## 1.1 Context

The modern world has witnessed remarkable development in the technology of components and devices. For example, in some applications, these components or devices may increase their temperature due to their electrical resistance, which can sometimes lead to an increased risk of the device generating a fault. This initiated the requirement to dissipate the heat from these components. The purpose of thermal management is to ensure that the temperature of the system components remains within the design limits, as well as to ensure the control of convective heat transfer using a single-phase fluid such as air, water, mineral oils, or ethylene glycol as the working fluid. In other applications, a system receives heat from a source, for instance, a solar collector. Accordingly, researchers and scientists aim to find appropriate means of controlling the heat transfer rate and enhance the performance of these systems and make them more efficient. In these applications, modelling the convective heat transfer within enclosures under different boundary conditions, typically using numerical methods, is also important to design efficient thermal exchange systems. These models allow for extensive simulation and analysis prior to manufacture in order to reduce the costs associated with physical tests. Interesting details in this regard can be found in the reference books (Cheng, 1978, Nield and Bejan, 2006, Kumar, 2011, Bagchi and Kulacki, 2014).

Several studies investigated the different types of the laminar and turbulent flow heat transfer, including free (natural), forced and mixed convection in enclosures or cavities with simple cross-sections, such as square, rectangle, trapezoidal, triangle and circle. Heat transfer by forced convection requires a driven flow. This is typically in cooling situations. This leads to an extra cost for generating the flow. Alternatively, natural convection depends on the density gradient of the upper and lower parts of the free flow, which move the fluid at a lower cost. Most studies considered the steady and unsteady natural convection of fluid and heat transfer by using different boundary conditions of heat sources, such as differentially heated walls distributions (fully uniform or non-uniform heated walls, partly heated walls and heat flux) and internal heat generation. The velocity value of the fluid flow in natural convection is lower as compared with its value in forced convection. Therefore, researchers found that the convective heat transfer can

be enhanced by changing the geometry design or the position of the selected boundary conditions, or by improving the thermal conductivity of the base fluid (Mebrouk *et al.*, 2016). Accordingly, researchers developed techniques to control the fluid flow and heat transfer rate for natural convection, for instance, using a porous medium, nanofluid, and corrugated cavity walls techniques.

In the next sections, this thesis will illustrate the related information in the literature about the convective heat transfer controlling techniques to provide an overview of the topic.

## **1.2 Flow and heat transfer control techniques**

### **1.2.1 Porous medium technique**

The first technique is the convective heat transfer inside enclosures or cavities containing a porous medium. Faghiri (2014) defined a porous medium as a substance with a solid matrix where there exist many voids and the induced fluid flows among those pores. The specifications of the porous medium have attracted the attention of scientists to use it as a way for controlling the heat transfer in specific applications. One of these specifications is the ability to dissipate heat over a large area in the porous medium, which is greater than by conventional means, such as by using fins that improve the heat transfer rate by convection. Another specification is the random movement of the fluid flow through the porous medium, which leads to the fluid being more effective in drawing heat from the components (Mahdi *et al.*, 2013). Despite these features, the porous medium is generally regarded as an insulation medium, due to the flow resistance offered by the porous material, which leads to reducing the heat transfer from the heated components. The ability of the fluid to penetrate through the porous medium depends on the size and shape of the porous medium (Bagchi and Kulacki, 2011, Bagchi and Kulacki, 2010).

Figure 1.1(a) shows the sketch of an ideal porous medium that consists of regularly spaced particles with spherical shape saturated by a fluid. In reality, the porous medium particles in nature have irregular shapes; as sketched in Figure 1.1(b). The most significant characteristic of the porous medium is its porosity. Porosity ( $\varepsilon$ ) can be defined as the free space that is inside the porous medium where fluid can flow compared to the total volume of the porous medium. In other words, it is the size occupied by the saturated fluid in the void space over the volume of the system (Nield and Bejan, 2006).

$$\varepsilon = \frac{V_f}{V} \quad (1.1)$$

where,  $V_f$  represents the volume of fluid in the void space and,  $V$  is the total volume of the porous medium.

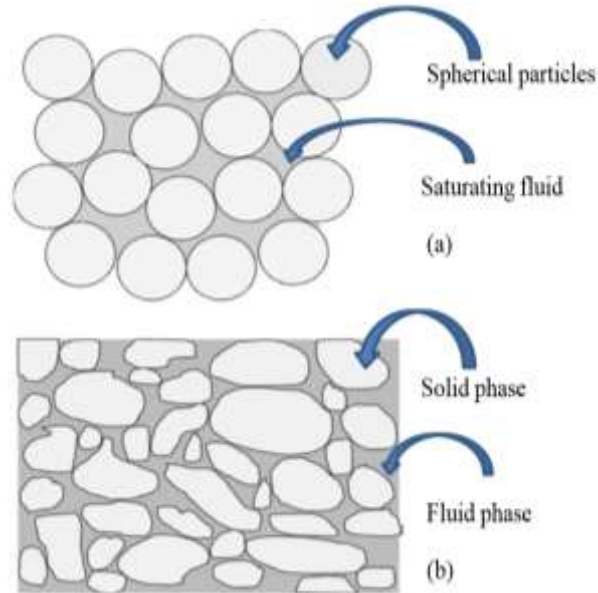


Figure 1.1: (a) An idealized saturated porous medium; (b) A naturally occurring porous medium (Bagchi and Kulacki, 2011).

Another important parameter of a porous medium is its permeability ( $\lambda$ ). The permeability expresses the ratio of the area through which fluid flows in a porous medium to the full cross-section area [ $\text{m}^2$ ] (Mahdi *et al.*, 2013).  $\lambda$  is estimated as:

$$\lambda = \frac{D_p^2 \varepsilon^3}{C (1-\varepsilon)^2} \quad (1.2)$$

where  $D_p$  is the effective pore diameter and  $C$  is a dimensionless constant that is related to the configuration of the flow-paths. Mahdi *et al.* (2013) defined the Darcy velocity as “the velocity of the fluid inside the porous region and is related to the physical velocity, or the actual velocity outside the porous region, by the porosity”. Permeability is one factor of the proportionality constant in Darcy’s law that relates the flow rate and physical properties of the fluid flow to the pressure gradient across the porous media.

$$u_{p,m} = \frac{\lambda}{\mu} \frac{dP}{dx} \quad (1.3)$$

The commonly used equations to describe the motion of a fluid are the Navier-Stokes equations. However, these equations do not provide a microscopic description of the flow in a porous medium. In fact, different models have been suggested to describe the fluid flowing through a porous medium. First, the Darcy model is assumed, and it is used to express the relationship between the superficial velocities with the pressure drop. This model is simple, and it allows to investigate a wide range of fluid flow cases with low velocity. The Brinkman (viscous effects) and the Forchheimer (inertia effects) are used with the Darcy model to investigate the more complex configuration of a flow with a no slip condition between the fluid and the porous region at a high Rayleigh number (buoyancy driven effect).

### **1.2.2 Nanofluid technique**

The type of the selected fluid is an important issue in heat transfer technology. The fluid is used to exchange the heat that generates from components that perform work. The convective heat transfer by a traditional fluid has attracted considerable attention from many researchers in recent years because modern technology requires heat transfer by fluid transport. In some cases, the traditional fluids such as air, water, oil, and ethylene glycols cannot meet the heat transfer rate. For example, the use of a single-phase fluid such as air, water, mineral oils, and ethylene glycol as a working fluid inside a clear enclosure (not porous) may not satisfy the temperature design limits of some components. In addition, researchers Muthamilselvan (2011) found that in a porous enclosure with a low permeability value of the porous media layers, the heat transfer rate tends to decline. As a result, researchers and scientists are attempting to find alternative fluids to enhance the heat transfer rate. This motivated researchers to develop the idea of natural convection inside enclosures using a new technique, which is called nanotechnology. The suspension of nanoparticles in a single-phase fluid is known as a nanofluid. This is obtained with nanometer-sized particles of less than 100nm. These particles can be manufactured from different types of powder, such as polymer, metallic and non-metallic particles (Choi, 1995). The nanoparticles may be an oxide ceramic ( $\text{Al}_2\text{O}_3$ ), oxide copper (CuO), a metal carbide (SiC), nitride (AlN, SiN) or a metal (Al, Cu) (Chand and Rana, 2012). The addition of nanoparticles to the single-phase fluid changes in the heat transfer rate depending on the type, volume fraction, and size of the added nanoparticles to the single-phase fluid. One of the significant points of using nanoparticles is that the nanoparticles

have a thermal conductivity that is higher than the one of the single-phase fluid which produces changes in the physical properties of the single-phase fluid such as density, viscosity and the thermal conductivity (Kakaç and Pramuanjaroenkij, 2009, Bashirnezhad *et al.*, 2015). The thermal conductivity of the working fluid has been improved by using a new type of nanofluid, which is called hybrid nanofluid. This type of nanofluid is prepared by suspending dissimilar nanoparticles either in a mixture or composite form in the single-phase fluid (Sarkar *et al.*, 2015). Some metallic nanoparticles such as copper, aluminium, and zinc provide high thermal conductivity, but these metallic nanoparticles are limited in nanofluid applications because of their high reactivity and low stability. In addition, non-metallic nanoparticles such as alumina ( $\text{Al}_2\text{O}_3$ ) have lower thermal conductivities than metallic nanoparticles, but these types of nanoparticle have preferable properties, such as high stability and chemical inertness (Sarkar *et al.*, 2015).

Figure 1.2 shows a sample of  $\text{Al}_2\text{O}_3$  and  $\text{CuO}$  nanoparticles that is imaged by TEM

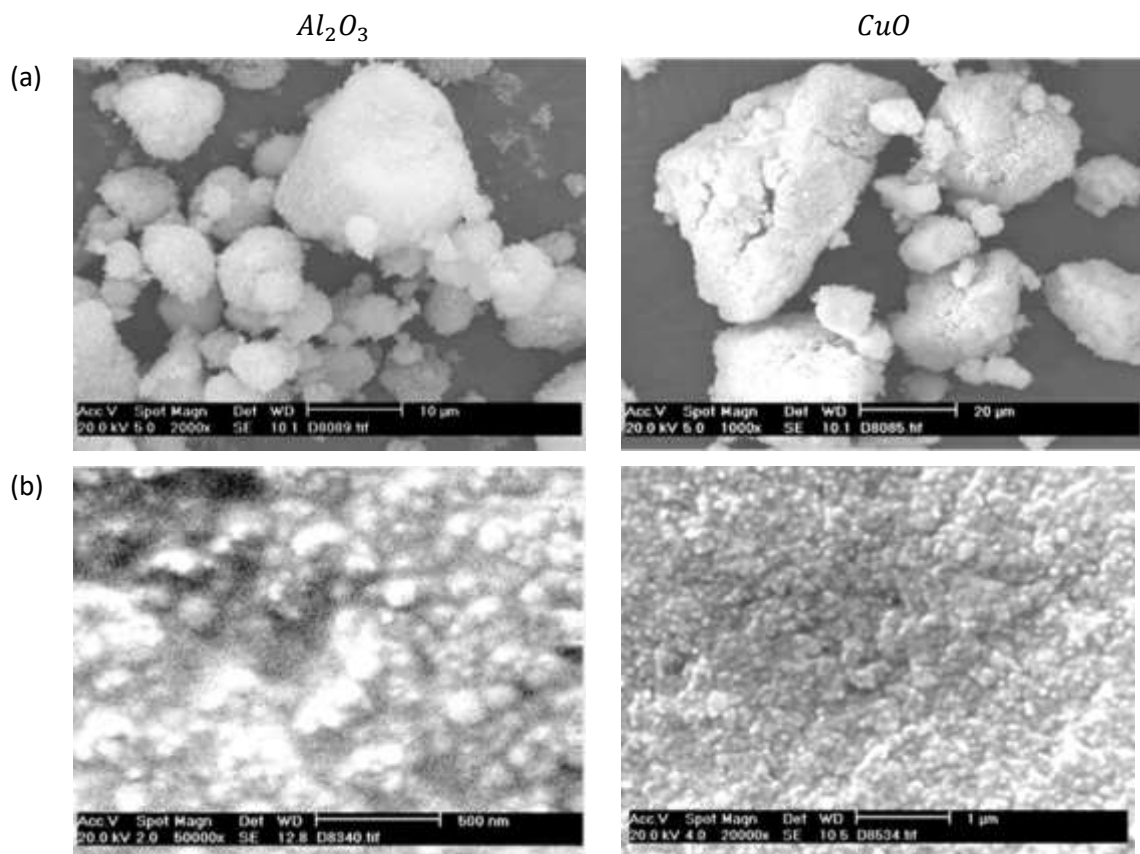


Figure 1.2: (a) TEM of nanoparticle agglomerates; (b) TEM of dispersed nanoparticles (Putra *et al.*, 2003).

(Transmission Electron Microscope) (a) loose agglomerates in the micro meters order (b) dispersed particles. This sample can be found in the reference (Putra *et al.*, 2003). Putra *et al.* (2003) observed that the agglomerated particles which dispersed in the fluid seem much smaller than those of the powder case. These particles behave the same as the fluid molecules in the homogeneous mixture. Therefore, nanofluid can flow smoothly through different types of channels or porous media without clogging the passage.

### 1.2.3 Corrugated wall technique

Another approach for enhancing natural convection inside enclosures or cavities is the use of wavy and V shape corrugated walls. The parameters that are typically used to control the flow and heat transfer inside the wavy geometries are the amplitude and the wave number of the wavy surface. (Khanafar *et al.*, 2009, Mushate, 2011, Sojoudi *et al.*, 2014, Hussain, 2016) found that the convective heat transfer could be controlled using the corrugated walls by changing the amplitude and the wave number of the corrugated wall. Figure 1.3 shows an application of using convective heat transfer in terms of wavy solar energy cavity and in the meantime, this figure displays the convective fluid that can be used as a convection medium to perform a thermal exchange between the working fluid in the enclosure and the inlet and outlet fluid through the tube. Figure 1.4 shows examples of natural convection applications using a porous medium as a heat sink to cool the electronic devices that have a low output heat flux. The design of porous medium may have a wavy surface area that contributes to increasing the surface area subjected to

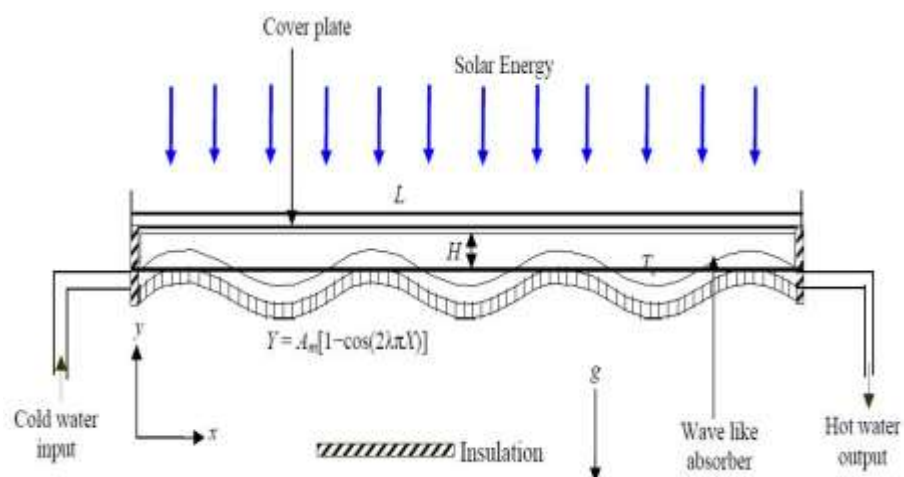


Figure 1.3: Performance of nanofluids on heat transfer in a wavy solar collector (Nasrin and Alim, 2013).



Figure 1.4: Examples of industrial applications for various electronica devices (Amecthermasol, 2017).

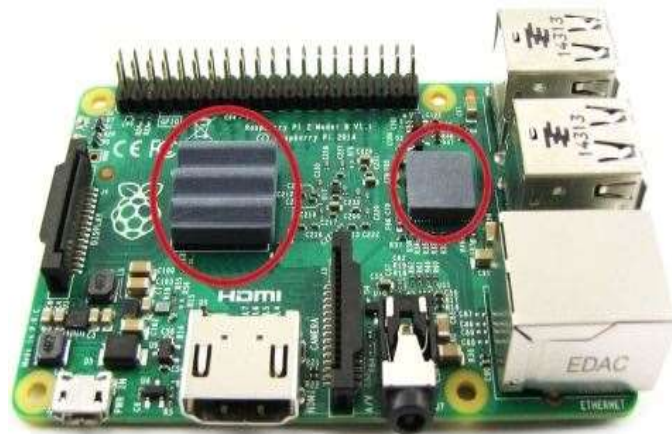


Figure 1.5: Porous medium with various shape designs for cooling electrical device(xxxx).

the convection as well as disturbs the flow. Therefore, it can dissipate more heat input per unit time compared to the flat surface area. A porous medium directly attached to the heat source component is shown in Figure 1.5. The use of the opened porous enclosure saturated with air as a working fluid as shown in Figure 1.5 produces a better heat transfer for cooling the electronically devices; however, in this study, the use of the confined square enclosure partly filled with a porous medium saturated with a nanofluid is suggested for the academic purposes using the liquid as a working fluid and it may be interesting in the next modern industry technology.

In general, these techniques are used to control and enhance the convective heat transfer either individually (porous medium, nanofluid or corrugated surface wall) or by in combination (porous medium-nanofluid, porous medium–corrugated surface wall, porous medium-nanofluid and corrugated surface wall) inside enclosures or cavities, depending on the application.

### **1.3 Aims and objectives**

Despite the fact that natural convection heat transfer inside enclosures using various types of controlling flow techniques to enhance the heat transfer has been widely investigated over the last few years, it represents a broad range of different convective heat transfer cases within the different flow types (laminar and turbulent) and thermal boundary conditions. Heat transfer enhancement using various types of convective heat transfer controlling techniques has attracted a growing interest in terms of increasing the heat received or removed from the heat source. Thus, many interesting investigations to study the convective heat transfer inside clear and porous enclosures have been considered

In the case of laminar flow, several aspects have been considered in the literature such as the laminar natural convection inside an enclosure entirely filled with a single-phase fluid or nanofluid with uniform and non-uniform thermal boundary conditions. In addition, other studies discussed the natural convection inside an enclosure entirely filled with a porous medium saturated with a single-phase fluid or nanofluid with uniform and non-uniform thermal boundary conditions as well as the enclosure that filled partly with a porous medium saturated with a single-phase fluid or nanofluid under the effect of the uniform heating. In the case of turbulent flow, several important studies have been investigated the turbulent natural convection in a two or three-dimensional clear enclosure (no porous) filled with a single-phase fluid or nanofluid as well as the two-dimensional enclosure that was entirely filled with a porous medium saturated with a single-phase fluid.

Nonetheless, the mentioned investigations have helped to motivate the present research to carry out further study on the laminar and turbulent heat transfer inside an enclosure partly filled with porous medium saturated with nanofluid under various thermal boundary conditions. In this study, the porous medium is used as a heat exchanger to receive or dissipate the heat from the heat source. A new simulation results are presented

to develop the convective heat transfer inside an enclosure partly filled by a porous slab rather than that of using a porous enclosure under different thermal boundary conditions by a combination with other types of the heat transfer controlling techniques (the nanofluid or the corrugated wall of the enclosure).

The thermal boundary condition such as linear, sinusoidal and heat flux temperature distribution and the geometrical design such as the corrugated wall in an enclosure partly filled with a porous medium saturated with a nanofluid could have a significant effect on the convective heat transfer. The use of these boundary conditions makes the complex nature of the system and it may be important in the sense of many engineering applications in the next modern technology. In this enclosure with the suggested boundary condition, the heat transfer prediction gives different simulation results compared to the enclosures that were used in the previous literature.

Accordingly, this study have been addressed in four parts to investigate a new simulation results in natural convection within enclosure partly filled with a porous medium saturated with a nanofluid, of which three parts are focused on the two-dimensional laminar heat transfer using the effect of the non-uniform or the heat flux thermal boundary condition, while the fourth part is devoted to investigate the turbulent heat transfer inside a three-dimensional corrugated enclosure using a uniform thermal boundary condition and these parts have not been filled yet. In addition, both of the single-phase fluid and different types of the nanofluid, under different parameters are investigated. This thesis seeks to obtain data that will help to address these research gaps. The author of this thesis believes that this work will be highly applicable and that it can be used in many engineering applications, for instance, solar collectors and electrical cooling systems.

Therefore, the aim of the present study can be summarized as follows:

- The first aim will study the effect of the linearly heated left-hand sidewall on laminar natural convection inside an enclosure partly filled with a porous medium saturated with a nanofluid with various physical parameters values like the Rayleigh number, the Darcy number, the porous layer thickness and the ratio of porous to nanofluid thermal conductivity. A comparison between two cases where

the porous medium is in the form of either a vertical or a horizontal slab is presented.

- The second aim will address the effect of a sinusoidally heated left-hand sidewall on laminar natural convection inside an enclosure partly filled with a porous medium saturated with a nanofluid with various physical parameters like the Rayleigh number, the Darcy number, the porous layer thickness, the amplitude and wave number of the heating and the ratio of porous to nanofluid thermal conductivity. A comparison between two cases where the porous medium is in the form of either a vertical or a horizontal slab is investigated.
- The third aim will investigate the case study of the laminar natural convection performance inside an enclosure partially filled with porous medium saturated with hybrid nanofluid using a local thermal non-equilibrium (LTNE) model with various physical parameters like the Rayleigh number, the Darcy number, the porous layer thickness, the modified conductivity ratio, the interphase heat transfer coefficient, the heat source length, and the nanoparticles volume fraction.
- The fourth aim will be accomplished for the performance of turbulent natural convection in a three-dimensional corrugated enclosure filled by hybrid nanofluid-porous layers using the  $(\kappa - \epsilon)$  turbulence model, enclosure under various physical and geometrical parameters effects like the Rayleigh number, the Darcy number, the porous layer thickness, the nanoparticles volume fraction, and the amplitude and wave number of the corrugated wall.

This study is concerned with the numerical investigation of natural convection inside an enclosure partly filled with a porous medium saturated with a nanofluid. The objectives below have guided the conduct of this research and have framed the content of this study. The objectives of this research are as follows:

- To investigate the effect of using the nanofluid on the laminar and turbulent heat transfer with different parameters
- To study the effect of the porous slab thickness on the laminar and turbulent heat transfer enhancement.
- To study the influence of the porous-nanofluid alignment in a vertical and a horizontal direction on the laminar heat transfer inside an enclosure.

- To understand the effect of the non-uniform heating on the laminar natural convection.
- To investigate the laminar natural convection and the temperature difference between the porous medium and the nanofluid phases inside an enclosure under the effect of the isoflux heating and different thermo-physical parameters.
- To analyse the turbulent natural convection by combining the selected heat transfer controlling techniques under the effect of the uniform heating.

#### **1.4 Thesis structure**

The overall structure of this thesis consists of eight chapters. Subsequent to the introduction in Chapter one, which introduces the context and the main aims and objective of this research. Chapter two presents the related literature for the enclosures with various convective heat transfer controlling techniques.

Chapter three includes the laminar and turbulent governing equations and the discretization of these equations as well as the domain using the Galerkin finite element method. In addition, various validations have been done to have the confidence in the obtained results from the present solver with the previous results in the literature.

The fourth chapter reveals the effects of the linearly heated left-hand sidewall on laminar natural convection within an enclosure filled with composite nanofluid-porous layers with various physical parameters are described in detail. This chapter contains the first aim of this investigation. It includes new findings of the convective heat transfer in a comparing of the alignment of the porous slab in a vertical or horizontal direction inside the enclosure and focusses on the influences of the thermophysical parameters such as the Rayleigh number, the Darcy number, the porous medium thickness, the nanoparticles volume fraction, and the thermal conductivity ratio between the porous medium and the nanofluid. A comparison between the vertical and horizontal alignments of the porous medium and the nanofluid layers in term of the streamlines and isotherms contours, the nondimensional velocity and temperature distribution at the interface line between the porous and nanofluid layers, the local and average Nusselt number with different parameters is included.

Chapter five includes the effects of the sinusoidal heated left-hand sidewall on laminar natural convection within an enclosure filled with composite nanofluid-porous layers are discussed. This chapter contains the second aim of this investigation. It includes new findings of the convective heat transfer in a comparing of the alignment of the porous slab in a vertical or horizontal direction inside the enclosure and focusses on the influences of the thermophysical parameters on the laminar heat transfer such as the Rayleigh number, the Darcy number, the porous medium thickness, the nanoparticles volume fraction, the thermal conductivity ratio between the porous medium and the nanofluid, the thermal wave number, and the thermal amplitude. A comparison between the vertical and horizontal alignments of the porous medium and the nanofluid layers in term of the streamlines and isotherms contours, the nondimensional velocity and temperature distribution at the interface line between the porous and nanofluid layers, the local and average Nusselt number with different parameters is investigated.

Chapter six focuses on the study of laminar natural convection flow of a hybrid nanofluid in a square enclosure partially filled with a porous medium under the effect of the isoflux bottom- heated wall of the enclosure using a thermal non-equilibrium model, where the temperature of the porous medium phase is different from that of the fluid phase. This chapter contains the third aim of this investigation. It includes the influences of the thermophysical parameters on the laminar heat transfer such as the Rayleigh number, the Darcy number, the porous medium thickness, the nanoparticles volume fraction, the modified conductivity ratio, the interphase heat transfer coefficient, and the heat source length.

In Chapter seven, the investigation of the turbulent natural convection in a three-dimensional enclosure partly filled with hybrid nanofluid-superposed porous layers with corrugated right-hand vertical sidewall under the effect of the uniform heating on the left-hand vertical sidewall using the  $(\kappa - \varepsilon)$  turbulence model is completed. This chapter contains the fourth aim of this investigation. It includes the influences of the thermophysical parameters on the turbulent heat transfer such as the Rayleigh number, the Darcy number, the porous medium thickness, the nanoparticles volume fraction, the corrugated wall amplitude, the corrugated wall wave number.

Finally, Chapter eight will use the research and findings of the previous chapters to address the thesis questions and goals regarding the use of the heat transfer controlling techniques and provides some recommendations for future study.

## **Chapter 2: Literature review**

### **2.1 Introduction**

In the past decades, researchers have sought to investigate the convective heat transfer inside enclosures or cavities. These studies provided fundamental and important information regarding the thermo-physical and geometrical parameters affecting the convective heat transfer inside enclosures. In order to meet the objectives stated in Chapter 1, it is necessary to understand the effects of the thermo-physical and geometrical parameters in heat transfer controlling techniques like a porous medium, nanofluid and, complex wall geometries. The topic of this thesis is the laminar and turbulent flow inside enclosures using different types of convective heat transfer controlling techniques and thermal boundary conditions. There are many investigations on laminar flow natural convection, while limited studies have been conducted on turbulent flow natural convection. Considerable research into using a porous medium with other techniques has addressed the control of the convective heat transfer inside enclosures. Therefore, the next subsections will deal with the porous medium with other techniques that include the single-phase fluid or the nanofluid as well as the complex geometry of enclosure walls. The background of convective heat transfer inside enclosures using different heat transfer controlling techniques for laminar and turbulent flows are reviewed in the next sections.

### **2.2 Laminar flow**

#### **2.2.1 Porous medium in an enclosure saturated with a single-phase fluid**

The study of convective heat transfer within an enclosure using porous media is an important issue in many industrial engineering applications such as heat exchangers, ground-coupled heat pumps, solar collectors, cooling of computers systems, and other electronic equipment (Basak *et al.*, 2010). A porous medium has been used to improve heat transfer rates in recent years (Al-Nimr and Khadrawi, 2003, Arpino *et al.*, 2011, Chamkha and Ismael, 2014, Ismael and Chamkha, 2015).

There is a growing body of literature that recognizes the importance of using the porous medium as a controlling technique in the convective heat transfer inside enclosures. Convective heat transfer has been studied by many researchers inside enclosures entirely or partially filled with a porous medium saturated with a single-phase fluid or nanofluid.

Many works in this topic are related to the convective heat transfer, with the enclosure either entirely filled with a porous medium or partly filled in vertical or horizontal slabs.

### **2.2.1.1 Enclosure entirely filled with a porous medium saturated with a single-phase fluid**

Several numerical studies focused on the steady-state convective heat transfer inside two-dimensional enclosures filled entirely with porous media and saturated by a single-phase fluid with uniform heating on the vertical walls (Walker and Homsy, 1978, de Medeiros *et al.*, 1999, Ismaeel, 2011, Tiwari *et al.*, 2012, Fard *et al.*, 2012, Muthtamilselvan, 2011) or uniform heating over the horizontal walls (Kim *et al.*, 2003, Balla and Naikoti, 2015). Muthtamilselvan (2011) examined the onset of the convective instability inside a porous enclosure saturated by water and with the boundary conditions of a cold temperature at the sidewalls and a hot temperature at the bottom wall while the upper wall remained adiabatic. The results showed that the porous medium, especially at low permeability values, caused the heat transfer to decline. Basak *et al.* (2007) have used the Darcy-Brinkman model to simulate the momentum equations for natural convection in a square porous enclosure saturated with a single-phase fluid under various thermal boundary conditions at the left and bottom walls of the enclosure (uniform and non-uniform temperature distribution). The Galerkin finite element method was used to solve the non-linear partial differential equations of the governing flow and heat fields. The main conclusion was that at the centre of the non-uniformly heated bottom wall, the heat was more than in the case of a uniformly heated bottom wall for all Rayleigh numbers. Basak *et al.* (2009) studied the natural convection flows in porous trapezoidal enclosures with various inclination angles. The Brinkman extension of the Darcy model was used to simulate the fluid flow in the porous medium. Using the Galerkin finite element method, the authors found that the heat transfer rate at the inclination angle of  $0^\circ$  increased more than at  $30^\circ$  and at  $45^\circ$ .

### **2.2.1.2 Enclosure partly filled with a porous medium saturated with a single-phase fluid (multi-layers)**

Several studies investigated the flow inside enclosures with a porous slab. Slabs aligned were considered in either the horizontal or the vertical directions. In addition, slab surfaces may be permeable or impermeable.

For horizontally aligned slabs, Beavers and Joseph (1967) studied experimentally the natural convection inside an enclosure partially filled by a porous slab, where the no-slip condition due to the tangential velocity was not selected. The case of a multilayer enclosure with the permeable interface has received more attention in the literature over recent years. The horizontal orientation of the porous medium was considered in the published literature that deal with the fluid flow over the porous medium in an experimental study like (Wu and Mirbod, 2018) or in numerical studies for the mixed convection like (Dixon, 2013) or the free convection as (Poulikakos *et al.*, 1986, Tatsuo *et al.*, 1986, Singh *et al.*, 1999, Bagchi and Kulacki, 2011). A numerical study of natural convection in a rectangular enclosure horizontally divided into the fluid (silicone oil) and the porous (glass beads) regions was performed by Tatsuo *et al.* (1986). The authors concluded that the flow and the heat transfer are influenced by the Rayleigh number and the Darcy number values. In addition, the flow rate penetration from the fluid region into the porous region significantly changed with the Darcy number. Vasseur *et al.* (1989) examined the effects of natural convection on the instability of the homogeneous fluid overlying the porous layer. The vertical walls were insulated, while the bottom and upper walls were heated and cooled, respectively, by a uniform heat flux. The results of this study showed that, the flow circulation was stable in the presence of the porous layer as well as when increasing the solid (porous medium) to fluid thermal conductivity ratio. Increasing the Darcy number led to increasing the permeability inside the porous medium and thus a reduction in the fluid stability due to the reduction of the flow resistance through the porous medium. Two dimensional steady natural convection in an enclosure with a bottom porous slab which is heated locally from below has been studied numerically by Bagchi and Kulacki (2010) as shown in Figure 2.1. The results of this study concluded that there was an inverse relationship between the average Nusselt number and the local heating source size. The heating source size did not affect the porous layer thickness and the Darcy number, which the Nusselt number depends on. This was due to the confining of the circulation centre of the main vortex inside the fluid layer. The average Nusselt number increased with the Darcy number. An experimental study by Bagchi and Kulacki (2011) examined the findings by Bagchi and Kulacki (2010). The enclosure in Figure 2.1 was fabricated as a rectangular chamber with 3mm diameter glass beads as the porous medium and the voids saturated with distilled water.

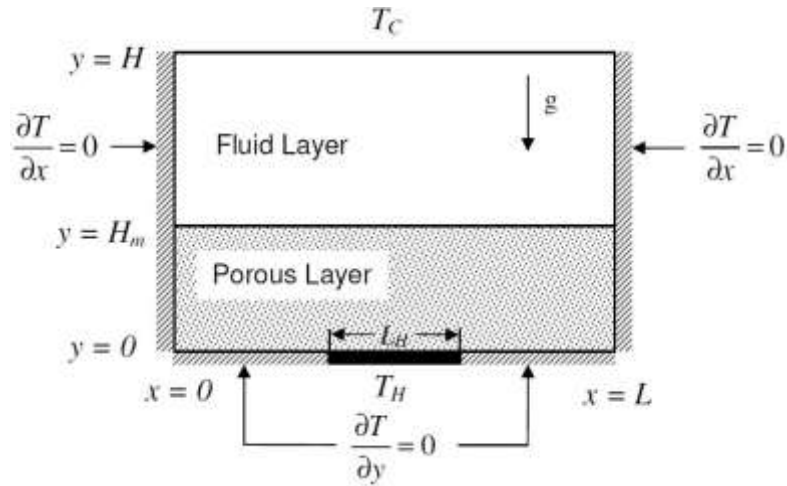


Figure 2.1: Enclosure partially filled with a horizontal layer of a porous medium adapted from (Bagchi and Kulacki, 2010).

A match was observed in the effect of the porous layer thickness with the prediction by Bagchi and Kulacki (2010), but no strong effect of the local heater size under was observed. In a numerical investigation of free convection inside a three-dimensional enclosure partly filled by a porous medium saturated with a single-phase fluid by Arpino *et al.* (2011) have found that modest flow penetration in the porous medium occurs when the Darcy number is decreased. In addition, the authors concluded that the difference between the two and three-dimensional model predictions of around 4%.

A considerable number of studies have been published on the two-dimensional natural convection that occurs in enclosures with differentially heated vertical walls and adiabatically insulated horizontal walls where the porous layer is disposed vertically and this can be found in the references (Tong and Subramanian, 1986, Beckermann *et al.*, 1987, Sathe *et al.*, 1988, Song and Viskanta, 1994, Goyeau and Gobin, 1999, Gobin *et al.*, 2005). Tong and Subramanian (1986) studied the convective heat transfer in a vertical enclosure separated into two layers as shown in Figure 2.2. The enclosure was partly filled with a single-phase fluid layer and the rest filled with a porous layer saturated by the same fluid. This study concluded that the heat transfer could be controlled or minimized when the porous layer thickness increased from zero to the enclosure width. The study presented by Tong and Subramanian (1986) motivated both scientists and engineers to perform for these investigations into the potential application of this finding to industrial cases. Most of these investigations focused on the insulating property of the porous partition and on the impact of the flow penetration through the porous layer.

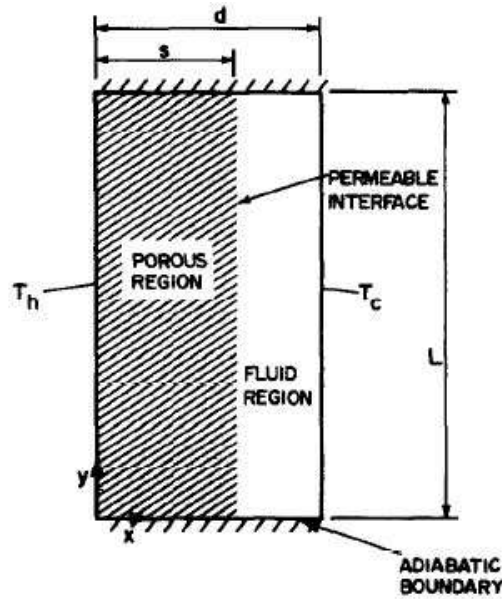


Figure 2.2: Enclosure partially filled with a vertical layer of a porous medium saturated with a single-phase fluid (Tong and Subramanian, 1986).

Beckermann *et al.* (1987) studied numerically and experimentally the free convection in the fluid and in the porous layer. These researchers found that the amount of the fluid penetrating into the porous layer depended strongly on the product of the Rayleigh and Darcy numbers, where these values should be greater than about 50 in order to have fluid penetration. Sathe *et al.* (1988) showed that increasing the porous layer thickness and the aspect ratio could minimize the heat transfer in the enclosure if the fluid/solid (porous) thermal conductivity ratio is less than one. However, the effect of increasing the porous layer thickness on convective heat transfer could be also minimized by increasing the Darcy number.

Several studies focused on heat transfer inside enclosures with three composed layers. Chen *et al.* (2009) studied horizontally the convective heat transfer inside the enclosure with three layers of single-phase fluid and porous medium saturated with the same type of the single-phase fluid, or vertically like (Du and Bilgen, 1990, Mharzi *et al.*, 2000, Al-Nimr and Khadrawi, 2003, Bennacer *et al.*, 2003). They concluded that the convective heat transfer strongly depended on the dimensionless parameters such as Rayleigh and the Darcy numbers, fluid/porous layer thickness, the solid phase properties (especially the porous medium thermal conductivity) and the aspect ratio. In general, the previous studies have shown that, with the presence of the porous medium, the convective heat transfer is increased and thus enhanced the effective thermal conductivity.

In addition to conventional uniform heating boundary conditions in natural convection enclosures, several studies focused on non-uniformly heated wall thermal boundary conditions. This idea attracted researchers due to the fact that a heated wall may be subject to non-uniform thermal boundary conditions in a significant number of engineering applications, such as in solar collector systems and in the cooling of electronic components (Sivasankaran and Bhuvaneshwari, 2013). This is because non-uniform heating is likely to affect the heat transfer inside enclosures. Therefore, it is important to study the effect of non-uniformly heated walls on the convective heat transfer inside enclosures. The influence of various thermal boundary conditions on the convective heat transfer in an enclosure filled with a porous medium saturated with single-phase fluid is reported in (Basak *et al.*, 2010, Basak *et al.*, 2011, Sathiyamoorthy *et al.*, 2007a). Sathiyamoorthy *et al.* (2007a) studied the influence of linear thermal boundary conditions on the natural convection inside a porous enclosure saturated with a single-phase fluid. They observed that the rate of heat transfer oscillated at high Rayleigh and Darcy numbers due to the formation of secondary circulation.

The majority of the previous work used of local thermal equilibrium model (LTE) where the temperature of the solid (porous) phase is equal to the temperature of the fluid phase. However, it is important to note that the temperature of the solid phase is actually different from that of the fluid phase, which is referred to as the local thermal non-equilibrium (LTNE) model. This may be found in various engineering applications, such as in solar energy collectors and in the cooling of electronic components (Wu *et al.*, 2015). Several important studies (Baytas and Pop, 2002, Baytas, 2003, Khashan *et al.*, 2006, Badruddin *et al.*, 2007, Wu *et al.*, 2016, Alsabery *et al.*, 2017a) presented natural convection within enclosures entirely filled with porous media saturated with single-phase fluid under different boundary conditions using the LTNE model. Wu *et al.* (2016) studied the effects of sinusoidally and partially heated vertical sidewalls on the natural convection in a porous enclosure saturated with a single-phase fluid using a numerical LTNE model. They concluded that the rate of heat transfer in a porous enclosure can be enhanced by using sinusoidal heating. In addition, they observed that the temperature convergence of the solid and of the fluid phases was satisfied by increasing the interphase heat transfer coefficient ( $H$ ) and the fluid/solid thermal conductivity ratio ( $\gamma$ ).

### **2.2.2 Porous medium in an enclosure saturated with a nanofluid**

In addition to using the porous medium as a heat transfer controlling technique, the use of nanoparticles with the base fluid can significantly enhance the physical properties of the base fluid and, therefore, improve the heat transfer characteristics (Gorla *et al.*, 2011, Saleh *et al.*, 2011, Basak and Chamkha, 2012, Selimefendigil *et al.*, 2016). The control that this method offers over heat transfer stems from the fact that nanoparticles have greater thermal conductivity than that of the same volume of conventional single-phase fluid. In clear enclosures (no porous medium), Chol (1995) was the first that described the term of nanofluid, and the researcher showed that the thermal conductivity of the base fluid could be improved by to two times by adding less than 1% of nanoparticles. Corcione (2010) performed a steady numerical investigation of heat transfer in buoyancy-driven flow with different types of nanofluids inside a rectangular enclosure differentially heated at the vertical sidewalls. One of the results was that the rate of heat transfer by the nanofluid is significantly higher than that transferred by the single-phase fluid. A considerable number of other studies, such as (Putra *et al.*, 2003, Saleh *et al.*, 2011, Basak and Chamkha, 2012, Selimefendigil *et al.*, 2016, Corcione, 2010, Corcione *et al.*, 2015, Roslan *et al.*, 2012, Rao and Srivastava, 2016, Goodarzi *et al.*, 2014, Garoosi *et al.*, 2015, Afrand *et al.*, 2016, Safaei *et al.*, 2016, Akbari *et al.*, 2016) have been published on the effects of using the nanofluid as working fluid or using the hybrid nanofluid, like (Sarkar *et al.*, 2015, Afrand, 2017, Karimi and Afrand, 2018).

Natural convection with non-uniformly heated walls in enclosures filled with nanofluid has received attention in recent years. The effect of a magnetic field on laminar flow and heat transfer in a nanofluid-filled enclosure with walls having a sinusoidal temperature distribution was studied by (Sivasankaran *et al.*, 2011, Kefayati, 2013, Elshehabey and Ahmed, 2015, Pordanjani *et al.*, 2018), while a linearly heated left hand vertical wall was examined in reference (Mahmoudi *et al.*, 2014).

In the next section, the literature that deals with combining porous media and a nanofluid inside an enclosure is reviewed.

### **2.2.2.1 Enclosure entirely filled with a porous medium saturated with a nanofluid**

Several studies have paid attention to the two-dimensional steady mixed convection in a porous enclosure with a nanofluid, like (Hashemi Amrei and Dehkordi, 2014, Aaiza *et al.*, 2015). A further extension to the above-mentioned field is the natural convection heat transfer in a porous enclosure saturated with a nanofluid. This problem has been investigated numerically by numerous authors, such as (Chand and Rana, 2012, Hassan and Ismael, 2015, Bourantas *et al.*, 2014, Dastmalchi *et al.*, 2015, Groşan *et al.*, 2015, Nguyen *et al.*, 2015). Bourantas *et al.* (2014) have concluded that at high Rayleigh numbers and also as the Darcy number increases, the permeability of the porous medium matrix and the solid volume fraction strengthen the natural convection, which results in the reduction of the heat source temperature. The study of natural convection heat transfer in a square enclosure filled with a porous medium saturated by a nanofluid with internal heat generation was presented by Groşan *et al.* (2015). Sheremet and co-workers published a series of papers on numerical studies of laminar natural convection in a two-dimensional porous enclosure saturated with a nanofluid (Sheremet *et al.*, 2015a) and in a two-dimensional conjugated enclosure with solid walls of finite thickness, like (Sheremet and Pop, 2014), or also in a three-dimensional enclosure, like (Sheremet *et al.*, 2015b). Natural convection inside an enclosure entirely filled with a porous medium saturated with a nanofluid has been investigated using the LTNE model in (Sheremet *et al.*, 2015a, Alsabery *et al.*, 2016, Sabour and Ghalambaz, 2016, Alsabery *et al.*, 2017a, Izadi *et al.*, 2018, Sheremet and Pop, 2018).

### **2.2.2.2 Enclosure partly filled with a porous medium saturated with a nanofluid**

Laminar natural convection in a two-dimensional enclosure partly filled in a vertical layer with a porous medium saturated by Cu-water nanofluid was studied by Chamkha and Ismael (2014), as shown in Figure 2.3. The authors have concluded that the laminar convective heat transfer is enhanced by using the nanofluid even with a low permeable porous medium, while it decreases rapidly with increases in the porous layer thickness. Ismael and Chamkha (2015) numerically examined the laminar conjugate free convection inside a square composite vertically layered enclosure by using a finite differences method. The enclosure consisted of a porous layer between a left hot solid layer and a

cold right nanofluid layer. The results of this study concluded that natural convection increases when the value of the Darcy number is very low at a thickness of the porous medium greater than 0.5; this results in a Rayleigh number less than or equal to  $10^4$ . Alsabery *et al.* (2015) investigated the heat-line visualization of natural convection in a trapezoidal enclosure partly filled with a porous layer saturated by nanofluid and partly with a non-newtonian fluid layer using a uniform thermal boundary condition. The Brinkman extended Darcy model was used to describe the fluid flow and heat transfer in the porous layer. Ag, Cu, Al<sub>2</sub>O<sub>3</sub> or TiO<sub>2</sub> nanoparticles were used with water as a base fluid to obtain the nanofluid that filled the porous medium. Some conclusions of this study are that the increase of the nanofluid thermal conductivity led to an increase in the circulation strength. It was also found that a higher value of the Nusselt number occurred at a nanoparticles volume fraction  $\phi = 0.2$ , however, the Nusselt number dropped lower than other values at  $\phi = 0, 0.05$  and  $0.1$  when the values of the Darcy number was limited between  $10^{-4}$ - $10^{-3}$ . Alsabery *et al.* (2017b) examined the effect of the inclination angle on the buoyancy-driven force inside an enclosure filled partly with a porous medium

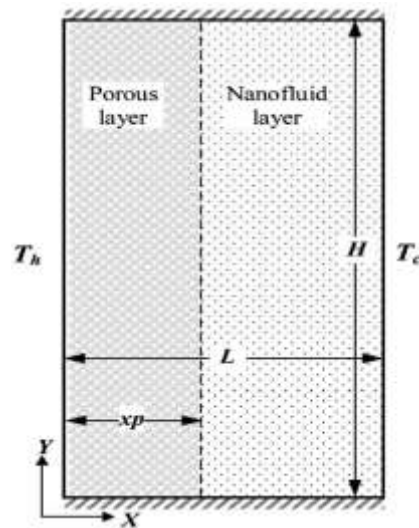


Figure 2.3: Enclosure partially filled with a vertical layer of a porous medium saturated with a nanofluid (Chamkha and Ismael, 2014).

saturated by a nanofluid and employing sinusoidal heating on the vertical walls using a finite difference methodology, as shown in Figure 2.4. The results showed that a higher heat transfer enhancement was gained with a thin porous layer using Ag nanoparticles, whereas the use of Al<sub>2</sub>O<sub>3</sub> enhanced heat transfer with increasing thickness of the porous layer. Mohebbi *et al.* (2019) examined the natural convection flow of a hybrid nanofluid inside an inverse (T) porous enclosure with various porous media in a solar energy

investigation, as shown in Figure 2.5. They concluded that increasing the Rayleigh number, the porosity, the Darcy number ratios of two porous media and decreasing the thermal conductivity ratio of two porous media led to a greater heat transfer rate. Recently, Chamkha *et al.* (2019) investigated the natural convection in composite layers of solid, porous medium and nanofluid layers using the thermal non-equilibrium model. They concluded that increasing the thickness of the nanofluid layer led to more heat transfer due to obtaining better nanofluid circulations.

In spite of the noted previous studies, a careful review of this literature reveals that there is a lack of information on the characteristics of laminar natural convection in a square enclosure partly filled by vertical or horizontal porous slabs saturated with nanofluids under linear or sinusoidal thermal boundary conditions on the left-hand sidewall of the enclosure. In addition, to the best of the author's knowledge, no such an investigation has yet been reported in the literature on the laminar flow and heat transfer rates in a composite enclosure under the effects of a bottom-heated wall using the hybrid nanofluid and the LTNE model. Therefore, in the author's opinion, this study should make an original contribution to this significant scientific field and this will form three of the objectives that will deal with in this research.

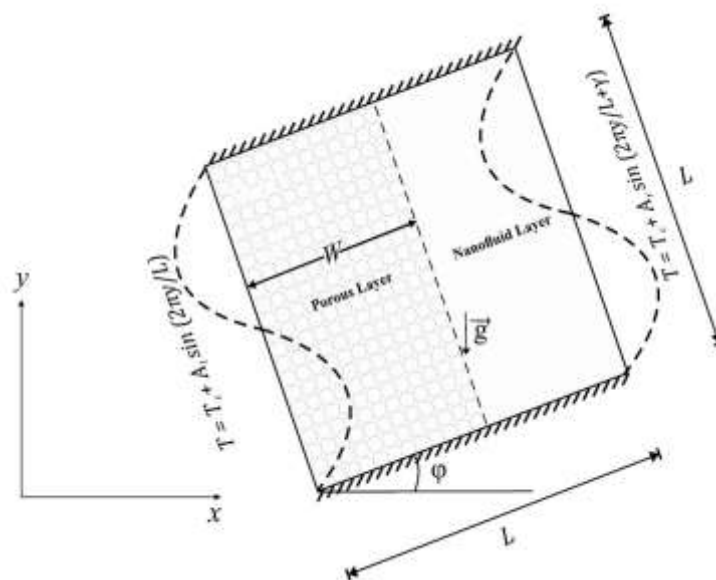


Figure 2.4: Enclosure partially filled with a vertical layer of a porous medium saturated with a nanofluid with non-uniform vertical side-walls heating adapted from (Alsabery *et al.*, 2017b).

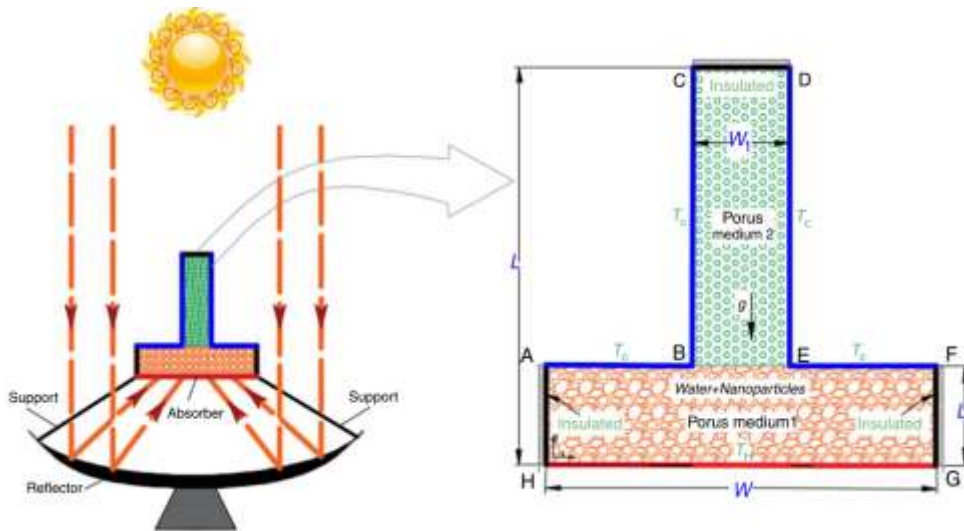


Figure 2.5: Composite porous enclosure saturated with a hybrid nanofluid (Mohebbi *et al.*, 2019).

### 2.2.3 Porous medium in a corrugated enclosure

Another technique of controlling the heat transfer by corrugating the walls of an enclosure. Convective heat transfer inside irregular enclosure surfaces is often encountered in many engineering applications to control heat transfer, such as in micro-electronic devices, flat-plate solar collectors and flat-plate condensers in refrigerators, and in geophysical applications, for instance, flows over the earth's crust, underground cable systems, electric machinery, cooling system of micro-electronic devices, and roughened surfaces (Al-Amiri *et al.*, 2007). In clear enclosures (no porous medium), (Al-Amiri *et al.*, 2007, Sabeur-Bendehina *et al.*, 2011, Hussain *et al.*, 2011, Hasan *et al.*, 2012, Hussain *et al.*, 2013, Singh and Bhargava, 2014) studied the laminar natural convective heat transfer within different complex geometries of enclosures using a single-phase fluid. These studies focused on the effects of the Rayleigh number, the corrugation amplitude and the corrugation wave number on the fluid flow and heat transfer in a corrugated enclosure.

#### 2.2.3.1 A corrugated enclosure entirely filled with a porous medium saturated with a single-phase fluid

Laminar natural convection in wavy two-dimensional porous enclosures saturated with a single-phase fluid has been extensively studied such as (Khanafar *et al.*, 2009, Mushate, 2011, Sojoudi *et al.*, 2014, Hussain, 2016). Khanafar *et al.* (2009) found that the number of wave number and amplitude of the wavy surface affect the flow and heat transfer inside

the porous enclosure that is illustrated in Figure 2.6. The intensity of convection increased when the Rayleigh number values rose. Mushate (2011) concluded that the convective heat transfer increases as the Rayleigh number increases, while it decreases as the amplitude increases. The optimum heat transfer occurred when the corrugated wave number was limited to two wave numbers. The authors concluded also that two wavy walls were better located on the vertical sides than on the horizontal sides. Sojoudi *et al.* (2014) numerically investigated the effect of sinusoidally corrugated vertical side-walls in a porous enclosure on the unsteady natural convection. Sinusoidal hot left and cold right walls were assumed to generate the temperature differences inside the enclosure, while the adiabatic condition was assumed at the upper and bottom walls. Air was the working fluid that saturated the porous medium. The results of this study concluded that the unsteady natural heat convection was influenced by the variation of the Rayleigh number with the corrugated wall amplitude and wave number. It was also found that increasing the Rayleigh number led to an increase in the average Nusselt number and the latter is higher for higher corrugation amplitude than corrugation wave number.

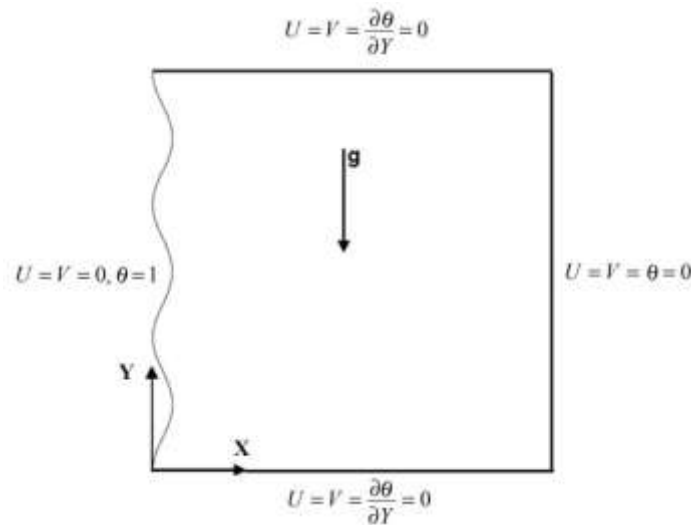


Figure 2.6: A corrugated side-wall enclosure entirely filled with a porous medium saturated with a single-phase fluid, adapted from (Khanfer *et al.*, 2009).

### 2.2.3.2 A corrugated enclosure entirely filled with a porous medium saturated with a nanofluid

In clear enclosures (no porous medium), several studies (Abu-Nada and Oztop, 2011, Nasrin and Alim, 2013, Takabi and Salehi, 2014, Hussein and Hussain, 2016, Shirvan *et al.*, 2017, Alsabery *et al.*, 2018, Dogonchi *et al.*, 2018) investigated the laminar convection heat transfer in a two-dimensional complex geometry enclosure filled with a

nanofluid. Takabi and Salehi (2014) numerically examined and compared water,  $\text{Al}_2\text{O}_3$ -water nanofluid, and hybrid nanofluid ( $\text{Al}_2\text{O}_3/\text{Cu}$ -water) to investigate the augmentation of the laminar heat transfer performance of an enclosure with sinusoidally corrugated walls. Shirvan *et al.* (2017) found that the heat transfer rate increased by increasing the amplitude and wavelength of the corrugated walls to 0.15 and 1 respectively. Sheremet *et al.* (2015c) numerically studied the unsteady laminar natural convection in a two-dimensional porous open wavy cavity saturated with a nanofluid using Buongiorno's mathematical model. The results show that the Nusselt and Sherwood numbers decreased with increasing the amplitude number.

### **2.3 Turbulent flow**

Few studies concerned turbulent convection in enclosures, which more accurately models the typical flow regime in many engineering equipment. Many numerical studies were restricted to two-dimensional enclosure models, due to the limitations of computer power up until the last decades. In addition, a fewer authors studied the three-dimensional convective heat transfer inside enclosures compared to the two-dimensional simulations. The development in the central processor unit technology and in computer memory motivated researchers to perform three-dimensional numerical simulations, using larger computational meshes. These turbulent convection models can benefit the design and analysis of industrial engineering equipment. (Farouk and Guceri, 1982, Markatos and Pericleous, 1984, Hiroyuki *et al.*, 1985, Ince and Launder, 1989, Barakos *et al.*, 1994, Sharif and Liu, 2003, Salat *et al.*, 2004, Abramov and Smirnov, 2006, Dixit and Babu, 2006, Kocutar *et al.*, 2015, Zhang *et al.*, 2014, Miroshnichenko *et al.*, 2016, Miroshnichenko and Sheremet, 2018) studied the turbulent natural convection in a two-dimensional enclosure entirely filled with a single-phase fluid, while a three-dimensional turbulent flow was studied by (Ozoe *et al.*, 1986, Fusegi *et al.*, 1991, Dol and Hanjalić, 2001, Altaç and Uğurlubilek, 2016). Markatos and Pericleous (1984) proposed the first steady two-dimensional turbulence model simulation for the buoyant flow at a Rayleigh number up to  $10^{16}$ . Using the standard  $\kappa - \epsilon$  turbulence model, Ozoe *et al.* (1986) numerically investigated the three-dimensional natural convection in a cubical enclosure at  $Ra = 10^6$  and  $Ra = 10^7$  and  $Pr = 0.7$ . The enclosure was heated from below, one vertical side partially was cooled, and the rest of the walls were thermally insulated. A top view of the velocity vectors revealed a downward spiral flow near the sidewalls along

the cooled vertical wall. A weak vortex was also found along the sidewalls near the wall opposing the partially cooled one. In addition, they also found that the isotherm lines and velocity vectors for vertical cross sections normal to the cooled wall indicated three-dimensional effects near the sidewalls. Altaç and Uğurlubilek (2016) compared the effect of using different turbulence models on the natural convection in two and three-dimensional rectangular enclosure. The results revealed that three-dimensional laminar and RANS (Reynolds Averaged Navier-Stokes equations) models yield almost identical mean Nusselt number predictions up to  $Ra = 10^{10}$ , and these predictions were compatible with those from two-dimensional simulations. They also observed that at higher Rayleigh numbers, the flow became three-dimensional and the two-dimensional RANS models did not yielded accurate predictions. In addition, the three-dimensional models yield more accurate mean Nusselt numbers than that from the two-dimensional models.

### **2.3.1 Enclosure entirely filled with a porous medium saturated with a single-phase fluid**

The turbulent natural convection in a two-dimensional porous enclosure saturated with a single-phase fluid was investigated by (de Lemos and Pedras, 2001, de Lemos and Braga, 2003, Braga and de Lemos, 2004, Braga and de Lemos, 2009, De Lemos, 2012, Carvalho and de Lemos, 2013, Carvalho and de Lemos, 2014). Braga and de Lemos (2004) modelled two-dimensional natural convection in a differentially heated porous square enclosure saturated with a single-phase fluid using the  $\kappa - \epsilon$  turbulent model. They concluded that when the parameters like the porosity, the Prandtl number, the thermal conductivity ratio (fluid/porous), and  $(Ra_f \times Da)$  value were kept fixed, a lower Darcy number caused to higher heat transfer rates.

### **2.3.2 Enclosure entirely filled with a porous medium saturated with a nanofluid**

For clear enclosures (no porous medium), a study of turbulent natural convection in a square enclosure filled by a Copper/water nanofluid was presented by Sajjadi *et al.* (2013). Their results observed that the rate of heat transfer improved by increasing the nanoparticles volume fraction. This relation became more irregular at higher values of Rayleigh numbers. Mebrouk *et al.* (2016) numerically studied the turbulent natural

convection of nanofluids in a tall enclosure heated from below and cooled from the other walls. All values of the Rayleigh number, the heat transfer rates increased with increasing the nanoparticles volume fraction and it decreased according to the ordering of nanoparticles types Cu, CuO and Al<sub>2</sub>O<sub>3</sub>. However, there is no investigation related with the turbulent natural convection inside an enclosure entirely or partly filled with a porous medium saturated with a nanofluid. Accordingly, the present study will fill this knowledge gap.

### **2.3.3 Porous medium in a corrugated enclosure**

For clear enclosures (no porous medium), a numerical investigation of turbulent natural convection in an inclined square enclosure with a hot wavy wall using a single-phase fluid was presented by (Aounallah *et al.*, 2007). The turbulent flow in wavy channels using a single-phase fluid was investigated by (Assato and de Lemos, 2009). The study of turbulent forced convection in a three-dimensional wavy channel using a single-phase fluid was presented by (Promthaisong *et al.*, 2016), and using a nanofluid in (Yang *et al.*, 2015). However, there is no study on the turbulent natural convection inside a wavy enclosure entirely or partly filled with a porous medium saturated with a single-phase fluid or nanofluid.

Therefore, according to the above review of previous studies, to the best of the author's knowledge, no investigation has yet been reported in the literature about turbulent heat transfer in a composite enclosure that combines the heat transfer controlling techniques of (a porous medium, a nanofluid and corrugated enclosure walls). Furthermore, a careful review of this literature reveals that there is a lack of information regarding the characteristics of the turbulent natural convection in a three-dimensional corrugated square enclosure partly filled with a porous medium saturated with a hybrid nanofluid.

## **2.4 Conclusions**

According to the above review of previous studies using different combinations of the heat transfer controlling techniques (the porous medium, the nanofluid and the corrugated wall of the enclosure), the convective heat transfer enhanced with increasing the Rayleigh number, the nanoparticles volume fraction, the thermal conductivity ratio of the porous medium and fluid as well as the increasing of the amplitude of the corrugated wall of the

enclosure more than the wave number of the corrugated wall. In addition, the heat transfer reduced with increasing the Darcy number and the thickness of the porous slab and it enhanced using the nanofluid with increasing the nanoparticles volume fraction compared to the single-phase fluid. Some results of literature presented that the porous slab can be enhance the heat transfer at a lower thickness.

Based on the literature review survey, and to the best of the author's knowledge, it can be summarized that the research of the laminar and turbulent convective heat transfer using various heat transfer controlling techniques has been actively pursued. Several studies that related to the present study used the non-uniform (linear and sinusoidal) thermal boundary condition. This was tested on one or two side walls of a clear or a porous enclosure filled by a single-phase fluid or nanofluid, or of an enclosure partly filled by a porous medium saturated with a nanofluid. No work has yet been done to study laminar natural convection inside an enclosure partly filled by either a horizontal or a vertical porous slab saturated with a nanofluid under the effect of the linear or sinusoidal heating on the left sidewall of the enclosure. In addition, no work has yet been done to investigate the laminar natural heat transfer inside an enclosure partly filled by a vertical porous layer saturated with a hybrid nanofluid using a local thermal non-equilibrium (LTNE) model and a discrete isoflux heat source size.

Many studies were carried out to investigate the turbulent heat transfer inside a two-dimensional conventional or complex enclosure filled by a porous medium saturated with a single-phase fluid and without porous medium saturated with a single-phase fluid or with a nanofluid. However, little attention has been paid to the study of turbulent natural convection inside an enclosure partly filled by a porous layer saturated with a nanofluid. No work has yet been done to study the turbulent natural convection inside a corrugated right-hand side wall of an enclosure partly filled by a porous layer saturated with a hybrid nanofluid. Thus, filling these knowledge gaps will form the main objectives of this thesis.

## Chapter 3: Methodology

### 3.1 Introduction

Computational Fluid Dynamics (CFD) tools are used in both the analysis and the design of flows, for example, in aerospace applications, turbo-machinery, weather forecasting, electronics cooling arrangements, and heat exchangers (2004). The development of computers technology has motivated researchers to use CFD to decrease the costs of experiment and optimize the design. Fluid dynamics in heat transport has a key role in many industrial applications, where it controls the heat transfer performance. The CFD simulations carried out in this study use on the finite element method (FEM) implemented in COMSOL Multiphasic 5.1a and 5.3a.

The finite element method governing the heat transport in discretizes the partial differential equations complex geometries. This is due to the ability of this method to solve problems in a relatively easy manner (2015). Using the finite element techniques, the physical domain is discretized. Concernedly, the partial differential equations governing the physical domain are discretized. The state of the discretised domain is solved, and the solution analysed. This process is shown in Figure 3.1. In this thesis, based on the above features of the CFD finite element method technique, the COMSOL Multi-physics solver is used to solve the governing equations of the cases of laminar and turbulent natural convection heat transfer. The selected enclosure partly filled by a porous medium saturated with a nanofluid is tested under various of thermal boundary conditions, and dimensionless parameters, such as the Rayleigh number, the Darcy number, the porous layer thickness, the thermal conductivity (porous/nanofluid) ratio, the nanoparticles volume fraction, the wave number and amplitude of a sinusoidal thermal boundary condition and the wave number and amplitude of a corrugated wall. In the present study, the case studies of laminar heat transfer with various thermal boundary conditions are applied in a two-dimensional square enclosure, while the case study of the turbulent heat transfer is presented in a three-dimensional enclosure.

This chapter includes a brief characterization of the domain and governing equations discretization, the numerical solver, the thermo-physical properties of the working fluid,

the governing equations and the code validation for both the laminar and turbulent heat transfer.

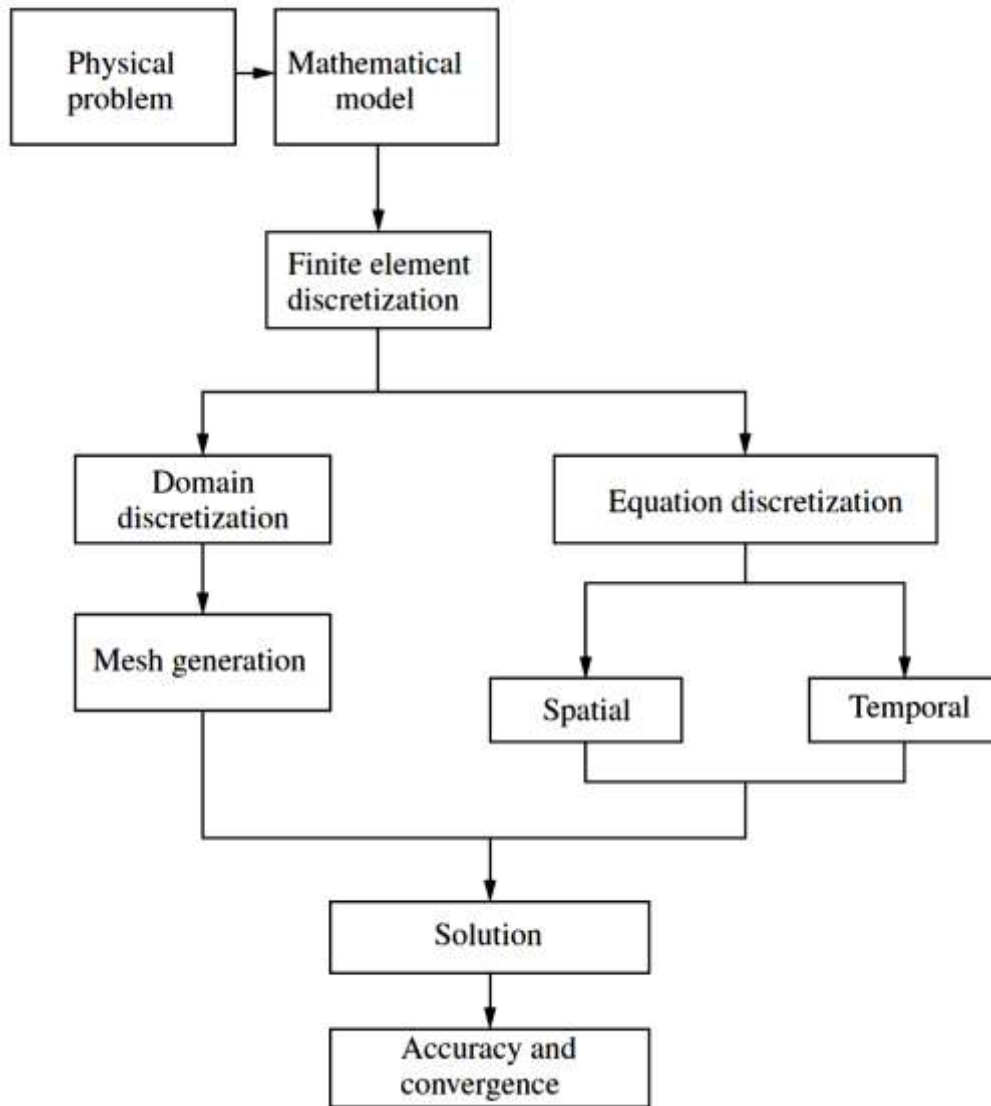


Figure 3.1: Numerical model flow chart for heat transfer calculations adapted from (Roland *et al.*, 2004).

### 3.2 The domain and governing equations discretization

As shown in Figure 3.1, the finite element method requires the discretization of both the governing equations and of the domain of the system. In this method, the variables are represented by piece-wise distributions over the domain. The discretization of the finite element techniques will be discussed in the next sections.

### 3.2.1 Discretize domain

The main idea of the domain discretization is to define a piece-wise approximation ( $\Phi$ ) of the flow state. This is carried out by discretizing the solution domain by small regions called elements. These elements are bounded by points, which are termed ‘nodal points’ and consequently, the assembly results are a grid or mesh. The type of element (interpolation function) defines the number of nodes that are employed, for example, the square and tetrahedron elements shown in Figure 3.2 use four nodes each. The square element in laminar flow and the tetrahedron element in turbulent flow are used in the present study to discretize the solution domains. The square and tetrahedron elements have four nodes, which are located at the vertices of the element. Each node stores one record of the local flow state ( $\Phi$ ) over the domain. The numerical accuracy of the results of the unknown variables depends strongly on the spacing among the nodes. In general, the approximate solution nears the exact solution of the flow governing equations as the mesh size approaches zero (Fletcher, 1988, Roland *et al.*, 2004).

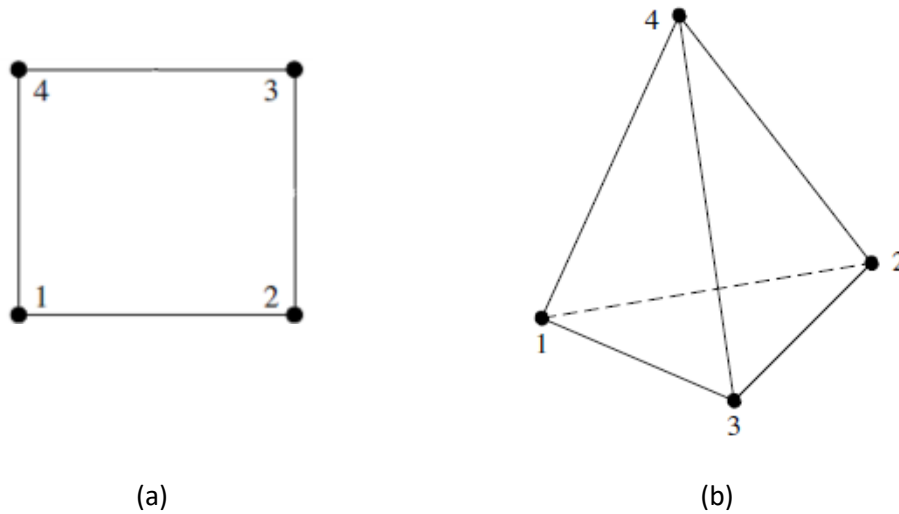


Figure 3.2: Element shapes: (a) a square element, (b) a tetrahedron element, adapted from (Roland *et al.*, 2004).

### 3.2.2 The governing equations discretization

The second step of the finite element procedure is the governing equation discretization, as mentioned in Figure 3.1. For a steady state, the variation of time is neglected, so the discretization is limited to the spatial terms of the governing equations. The Galerkin Finite Element Method (GFEM) is used to discretise the governing equations depending on the interpolating or shape function ( $F_{sn}$ ) for the unknown variable. By dividing the

domain into several elements, the solution can be approximated over these elements by a suitable known function that is employed to represent the solution within the elements. These functions are called ‘shape functions’, ‘interpolating functions’, or ‘basis functions’ ( $N$ )(Roland *et al.*, 2004). The interpolating functions is named so because it determines the values of the unknown variables by piecewise interpolating to connect the local solution to the nodal values. These functions also known as ‘basis functions’ because it is regarded as forming or shaping the basis of the discretization method (Roland *et al.*, 2004). The polynomial type function has been widely used as the low-order piecewise polynomials interpolating functions over the elements of the solution region. This feature relatively reduces the non-zero terms which can be located to the main diagonal matrix of the solution equations. This is important because the matrix solution will be more economical (Fletcher, 1988). The unknown variable values  $\Phi$  at any locations  $(X, Y, Z)$  can be calculated using basis set  $\{F_{sn}\}_{sn=1}^{SN}$  evaluated at the location  $(X, Y, Z)$ . In order to obtain a discretized form of the numerical governing equations, the weak formulation is used. The governing equation is multiplied by a test function ( $\Phi$ ) that represents the unknown variables such as the velocity components ( $U, V, W$ ), temperature  $\theta$  in the domain as follows:

$$\begin{aligned} U &\approx \sum_{sn=1}^{SN} U_{sn} F_{sn}(X, Y, Z); \quad V \approx \sum_{sn=1}^{SN} V_{sn} F_{sn}(X, Y, Z), \\ W &\approx \sum_{sn=1}^{SN} W_{sn} F_{sn}(X, Y, Z); \quad \theta \approx \sum_{sn=1}^{SN} \theta_{sn} F_{sn}(X, Y, Z) \end{aligned} \quad (3.1)$$

where  $U_{sn}, V_{sn}, W_{sn}$  and  $\theta_{sn}$  are the nodal values of  $U, V, W$  and  $\theta$  at the  $sn^{th}$  node.

By substituting these expressions for  $U, V, W$  and  $\theta$  into the governing equations of the nanofluid in the fluid layer and through the porous slab and integrating these equations and equating to zero. The approximate flow state ( $U_{sn}, V_{sn}, W_{sn}$  and  $\theta_{sn}$ ) is determined across the domain. The governing equations discretization and the shape function estimation are detailed in Appendix A.

### 3.3 Numerical solver

An iterative approach was used to solve the dimensional and dimensionless governing equations with the boundary conditions in equation via the Galerkin finite element methodology, using the solver available in the Multiphysics COMSOL 5.1a and 5.3a software suite. The nonlinear residual equations were solved where the velocity

components, and temperature are subjected to the basis set as illustrated in (Basak *et al.*, 2007).

The iteration is terminated when the dependent variables reach steady state and satisfy the criterion:

$$\frac{\sum_{i=1}^m \sum_{j=1}^n \sum_{k=1}^o |\Phi_{i,j,k}^{r+1} - \Phi_{i,j,k}^r|}{\sum_{i=1}^m \sum_{j=1}^n \sum_{k=1}^o |\Phi_{i,j,k}^{r+1}|} \leq 10^{-6} \quad (3.2)$$

where  $\Phi$  represents the velocity components ( $U$ ,  $V$ ,  $W$ ), temperature  $\theta$ , or the pressure ( $P$ ) in the domain. The subscripts  $i, j$  and  $k$  indicate the  $i^{th}$ ,  $j^{th}$  and  $k^{th}$  grid in the  $x$ ,  $y$  and  $z$  directions, respectively. The superscript  $r$  refers to the  $r^{th}$  iteration.  $m$ ,  $n$  and  $o$  represent the total number of nodes.

### 3.4 The governing equations of the laminar and turbulent heat transfer

The convective heat transfer was simulated using a Navier-Stokes model for the nanofluid layer while the Darcy–Brinkmann model is used to solve the governing equations in the porous slab. SIMPLE (Semi-Implicit Method for Pressure Linked Equations) algorithm (Patankar, 1980) was used to couple the continuity and momentum equations. The base fluid (water) and nanoparticles are taken to form a homogeneous mixture in thermal equilibrium with no slip velocity between the nanoparticles and the base fluid. The flow is considered as steady and incompressible with constant physical properties except for the density, where the latter is assumed to vary with temperature according to the Boussinesq approximation. The buoyancy-driven flow induced by temperature differences is modelled by using the Boussinesq approximation. The Boussinesq approximation states that the density variation in a liquid is small and it can be neglected except when it is considered with the gravitational acceleration ( $g$ ). The Boussinesq approximation can be expressed (Bagchi and Kulacki, 2010):

$$\rho_f = \rho_o [1 - B_{th}(T_f - T_o)] \quad (3.3)$$

In the present study, the porosity value ( $\varepsilon$ ) of the porous medium was proposed to be equal to one (Basak *et al.*, 2007) and the effects of the permeability value ( $\lambda$ ) in the Darcy number were adopted. In addition, the interface of the nanofluid-porous medium layers

is assumed permeable with matching values of tangential and normal velocities, shear and normal stresses and temperature in the case of (LTE) across the interface which can be written as:

$$\mu_p = \mu_{nf}, \quad \theta_p = \theta_{nf}, \quad \psi_p = \psi_{nf} \text{ and } \frac{\partial \theta_{nf}}{\partial X} = K_r \frac{\partial \theta_p}{\partial X} \quad (3.4)$$

where  $K_r$  is the ratio of the effective thermal conductivity of the porous medium to the thermal conductivity of the nanofluid.

### **3.4.1 Laminar heat transfer case study**

In this study, the local thermal equilibrium (LTE) and local thermal non-equilibrium (LTNE) models between the solid matrix of the porous medium and the nanofluid were investigated. According to the above assumptions, and depending on the two dimensional laminar flow governing equations given by (Hussain and Rahomey, 2018) and by using the local thermal equilibrium, the mass, momentum, and energy equations of the nanofluid-porous layers are given in Appendix B1( equations B1.1-B1.8) . In addition, the governing equations of the case study using the hybrid nanofluid-porous layers with non-equilibrium model relations, and the dimensionless parameters are illustrated in Appendix B2 (equations B2.1-B2.9).

### **3.4.2 Turbulent heat transfer case study**

There are slightly differing equations in terms of variables relevant to the present study that have been analysed in some interesting published papers and the final forms of the turbulent flow equations considered here are given in detail in (Ozoe *et al.*, 1986, de Lemos and Braga, 2003, Mebrouk *et al.*, 2016, Fraikin *et al.*, 1982, Altaç and Uğurlubilek, 2016). For the convective heat transfer calculations, several studies adopted on the standard  $\kappa - \epsilon$  model in many engineering investigations. due to its robustness, economy and reasonable accuracy (Altaç and Uğurlubilek, 2016). Furthermore, the mathematical model of turbulent natural convection equations in a corrugated enclosure partly filled by a porous medium saturated with a hybrid nanofluid is presented for the first time. The considered turbulent flow is described mathematically by the Reynolds Averaged Navier-Stokes (RANS) equations in the hybrid nanofluid layer and Darcy-Brinkmann model in the porous layer. Based on the mentioned published papers, the

dimensionless parameters and the dimensionless turbulent macroscopic governing equations are given in Appendix C.

### 3.5 Thermo-physical properties

The thermo-physical properties of the pure and nanoparticles that are used to generate the nanofluid and hybrid nanofluid cases are given in Table 3.1.

Table 3.1: Thermo-physical properties of water, copper, and alumina (Gorla *et al.*, 2017).

Property	Water	Copper (Cu)	Alumina (Al <sub>2</sub> O <sub>3</sub> )
$\rho$ (kg/m <sup>3</sup> )	997.1	8933	3970
$Cp$ (J/kg.K)	4179	385	765
$k$ (W/m.K)	0.613	401	40
$\beta$ (1/K)	$21 \times 10^{-5}$	$1.67 \times 10^{-5}$	$0.85 \times 10^{-5}$

The governing equations are combined with the adopted relations that prescribe the physical properties of the nanofluid, which depend on the nanoparticles' volume fraction,  $\phi$ , (Nasrin and Parvin, 2012) as shown in Appendix B1 ( equations B1.11-B1.16). The equations of the hybrid nanofluid thermo-physical properties are illustrated in Appendix B2 (equations B2.12-B2.16).

### 3.6 Code validations

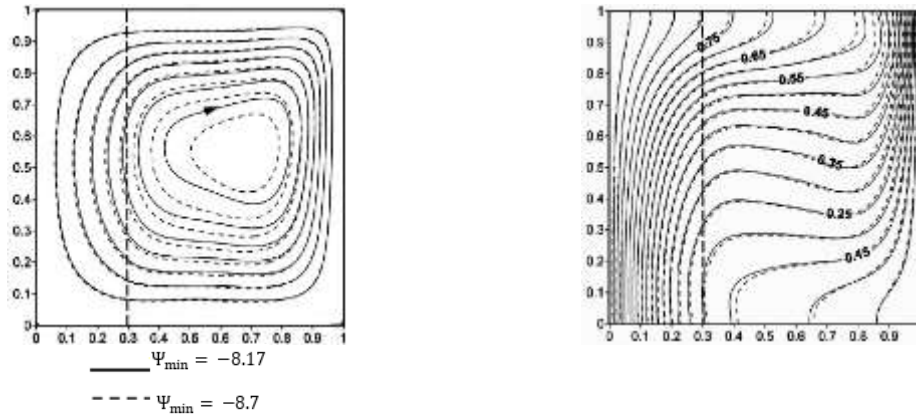
To build the confidence in the results from the present solver, validation tests were performed with previously published studies for different cases. The results from the present solver were compared with published results of laminar and turbulent heat transfer.

#### 3.6.1 Laminar heat transfer validations

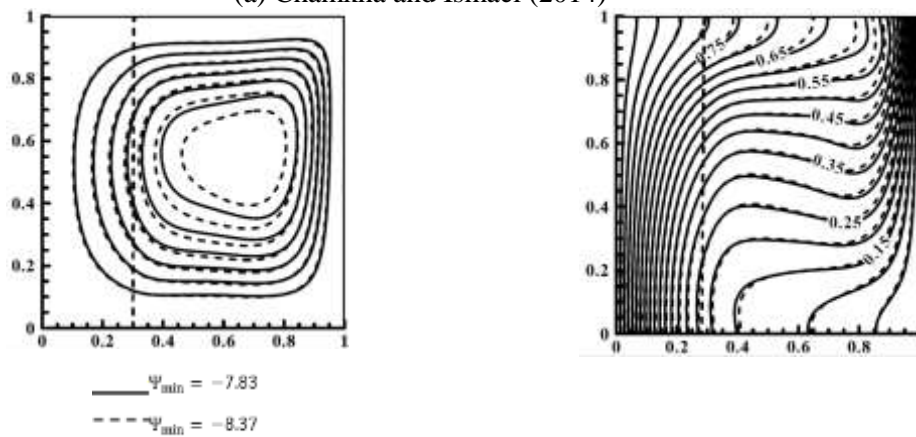
In this section, the validation of the numerical results for the laminar heat transfer is presented for seven cases.

Firstly, the present study is validated by comparing its predictions with the results by Chamkha and Ismael (2014). The validation test case domain is that of a two-dimensional laminar flow for steady natural convection inside an enclosure filled partly with nanofluid and partly with a vertical porous medium slab saturated with the same nanofluid, as

shown in Figure 3.3. The vertical walls of the enclosure were isothermal while the horizontal walls were adiabatic. The results of the comparison of the stream function and isotherms are investigated for  $Ra = 10^5$ ,  $Da = 10^{-5}$ , aspect ratio = 1 and a porous layer thickness equal to 0.3. The nanofluid is composed of water as a base fluid and copper nanoparticles at a volume fraction  $\phi$  of 0.05.



(a) Chamkha and Ismael (2014)



(b) Present study

Figure 3.3: Streamlines (a) and isotherms (b) of the present study are in agreement with those of the benchmark problem of Chamkha and Ismael (2014).

Secondly, Figure 3.4 shows a comparison between the results of this study and corresponding ones Sathiyamoorthy *et al.* (2007b). The enclosure was entirely filled with a porous medium saturated by air with linearly and uniformly heated left and bottom walls, respectively, whilst the right wall was uniformly cold, and the upper wall was adiabatic. The selected parameters of the comparison were  $Ra = 10^6$ ,  $Da = 10^{-3}$  and  $Pr = 0.7$ . The Brinkman-extended Darcy model was used to solve the equations governing the fluid flow in the porous medium for each of the selected comparisons. The results can be

seen to be in good agreement with the published reference data and give further confidence as to the accuracy of the currently selected FEM solver.

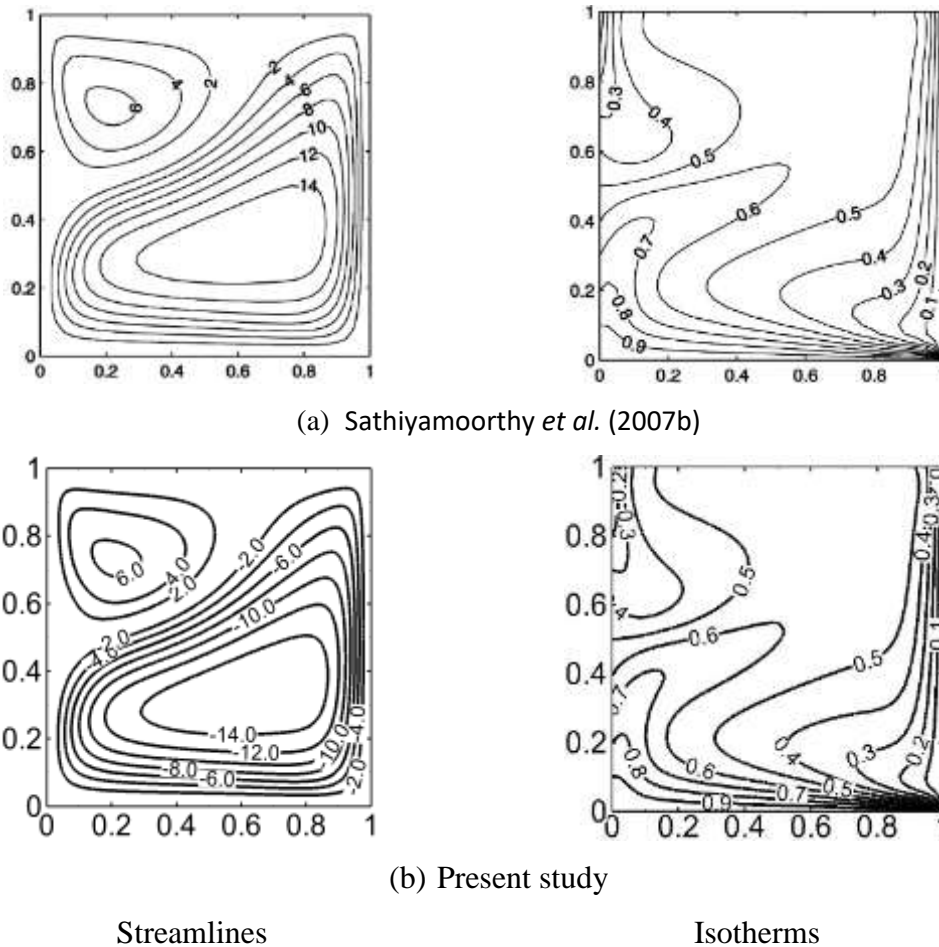


Figure 3.4: Streamlines and isotherms of the present study are in agreement with those of the benchmark problem of Sathiyamoorthy *et al.* (2007b).

Thirdly, to increase confidence in the results produced by this solver, Figure 3.5 shows a further validation with the numerical and experimental results that were presented by Beckermann *et al.* (1987) for the natural convection inside an enclosure partly filled with a porous slab saturated with a single-phase fluid. The validation is performed with the Brinkman-Forchheimer with Darcy extended model for experiment 2 by using the water as the working fluid. The difference between the numerical and the experimental results is 7% and this is attributed to the inaccuracies in determining of the exact position of the thermocouple probe and to the non-uniformities of the porosity at the walls.

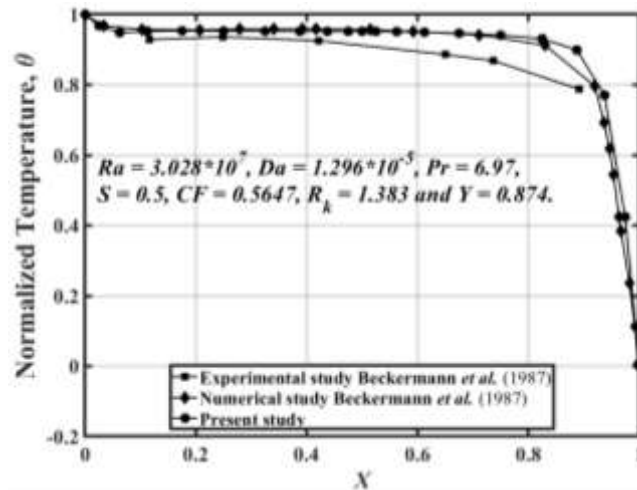


Figure 3.5: Validation of numerical and experimental results presented by Beckermann *et al.* (1987) with the present result.

In the fourth validation study, the domain is that of a two-dimensional laminar flow for steady natural convection inside an enclosure filled entirely with a porous medium saturated with a single-phase fluid ( $Pr = 0.71$ ). Sinusoidal heating was applied to the left and bottom walls of the enclosure and a uniformly cold temperature was imposed on the

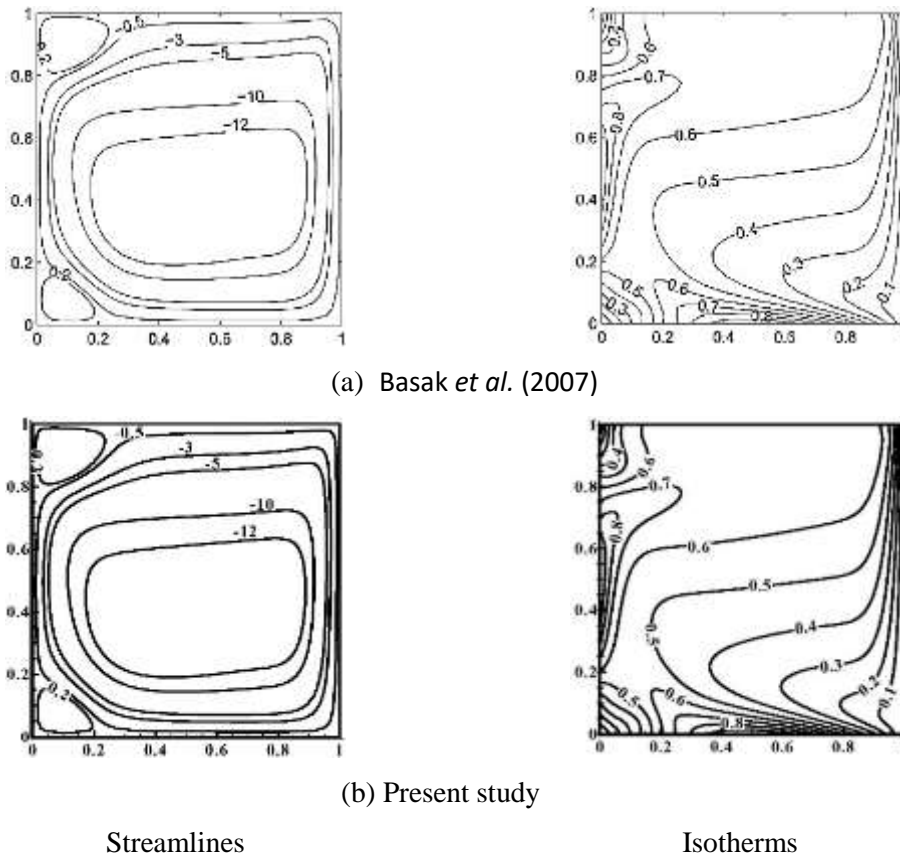


Figure 3.6: Streamlines and isotherms of the present study are in agreement with those of the benchmark problem of Basak *et al.* (2007).

vertical right wall, whereas the upper wall was modelled as adiabatic. The simulation is run at  $Ra = 10^6$  and  $Da = 10^{-3}$ . Figure 3.6 compares the predictions by Basak *et al.* (2007) and this study.

Fifthly, the configuration of a bottom heat source causing laminar natural convection inside an enclosure filled with a copper nanofluid is validated against benchmark data by Aminossadati and Ghasemi (2009) at  $Ra = 10^5$ ,  $B = 0.4$ ,  $D = 0.5$  and  $\phi = 0.1$ , in Figure 3.7. The streamlines and isotherms of the present study are in agreement with those of the benchmark problem of Aminossadati and Ghasemi (2009). Table 3.2 compares the average Nusselt number on the heat source wall for different Rayleigh numbers using at  $B = 0.4$ ,  $D = 0.5$  and  $\phi = 0.1$ . An acceptably small difference was found between the reference and the present, where the difference reduced with increasing  $Ra$ .

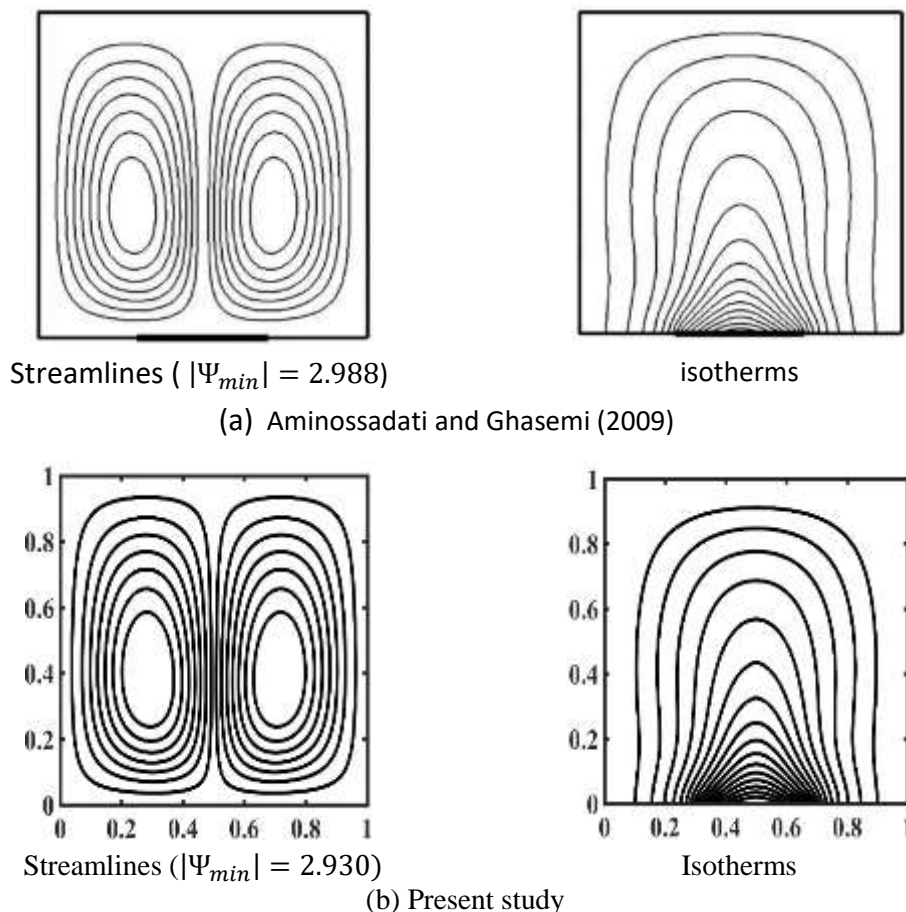


Figure 3.7: Streamlines and isotherms of the present study are in agreement with those of the benchmark problem of Aminossadati and Ghasemi (2009).

Table 3.2: Comparison of the average Nusselt number values on the bottom heat source wall of the enclosure between the present model and the results by (Aminossadati and Ghasemi, 2009).

$Ra$	Aminossadati and Ghasemi (2009)	Present study	Deviation %
$10^3$	5.451	5.566	2.11
$10^4$	5.474	5.588	2.08
$10^5$	7.121	7.218	1.36
$10^6$	13.864	14.018	1.11

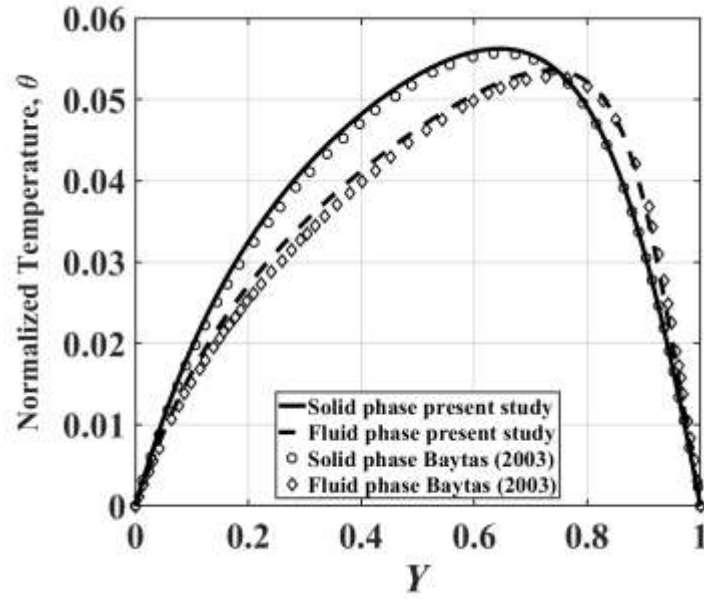


Figure 3.8: Temperature profile at vertical mid-plane ( $X = 0.5$ ). Comparison with Baytas (2003). The symbols correspond to results by Baytas (2003) and the lines correspond to the present study.

A sixth configuration was considered for validating the present model. This is the configuration reported by Baytas (2003). It is a model of the natural convection inside a porous enclosure with heat generated using the thermal non-equilibrium model. The temperature profile was predicted by the Brinkman-Darcy-Forchheimer model at  $Ra = 10^7$ ,  $Da = 10^{-2}$ ,  $\varepsilon = 0.4$ ,  $Pr = 7$ ,  $F_o = 5.648$ ,  $\gamma = 0.1$ ,  $H = 1000$  and  $X = 0.5$ . Figure 3.8 shows the midplane temperature predicted by the present model versus the reference prediction by Baytas (2003). This Figure shows the temperature difference between the porous medium phase and the fluid phase due to the thermal non-equilibrium between them. The results of the present study are in agreement with those of the benchmark problem of Baytas (2003).

To validate the hybrid nanofluid model, Figure 3.9 compares the present model predictions against results by Gorla *et al.* (2017) for a porous enclosure saturated with a hybrid nanofluid that was differentially heated and cooled using two heat sources and sinks, respectively. The streamlines and isotherms are compared at  $Ra = 10^4$ ,  $Da = 10^{-3}$ , Hartman number = 0,  $D = B = 0.5$  and  $\phi = 0.05$ . The comparison of the results showed good agreement between our results and those reported in (Gorla *et al.*, 2017), giving confidence as to the accuracy of the finite element model.

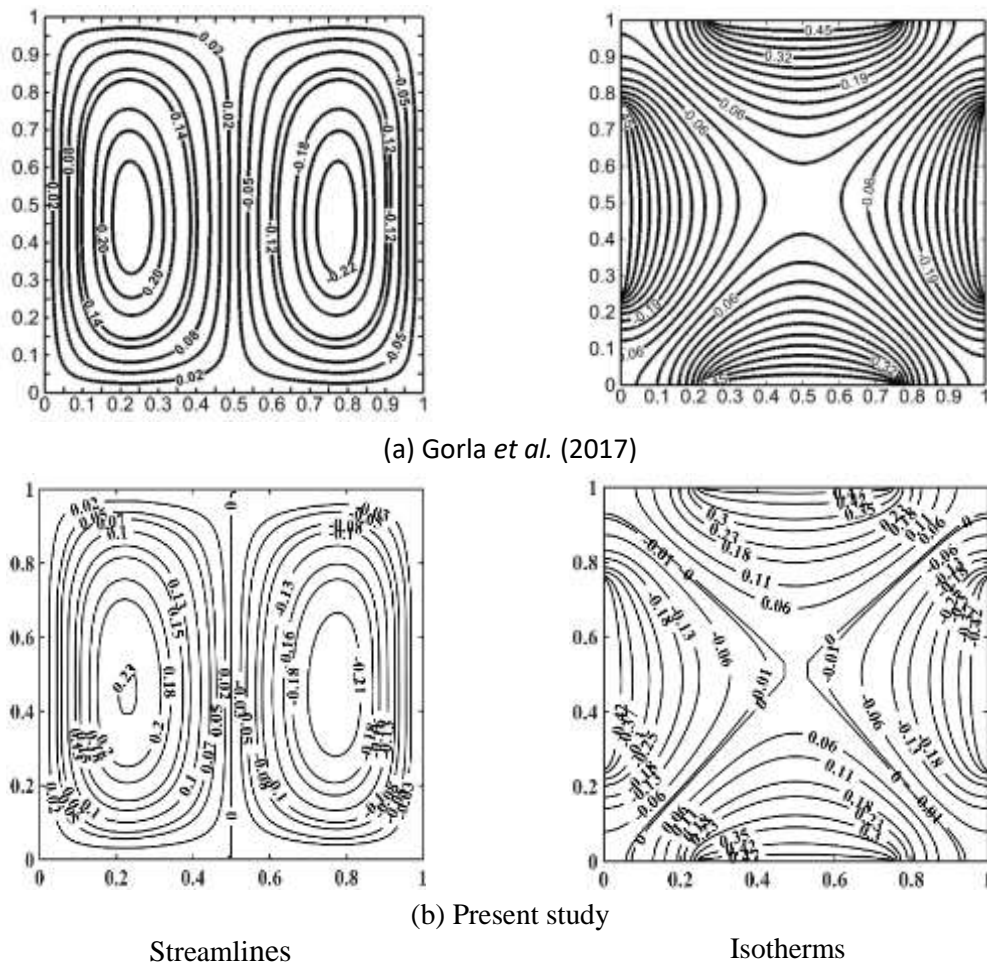


Figure 3.9: Streamlines and isotherms of the present study are in agreement with those from Gorla *et al.* (2017)

### 3.6.2 Turbulent heat transfer validations

The validation of the numerical model for turbulent heat transfer predictions is presented in four test cases. In the first test case, the turbulent natural convection is modelled inside an enclosure entirely filled with a single-phase fluid ( $Pr = 0.71$ ) and differentially heated at the vertical side walls at  $Ra = 10^9$ . The predictions from the present model are compared to predictions by Kuznetsov and Sheremet (2010) in Figure 3.10. The streamline and isotherm contours of the present study are in good agreement with those from (Kuznetsov and Sheremet, 2010). In the second test case, turbulent natural convection is modelled inside a differentially heated enclosure saturated with a single-phase fluid ( $Pr = 0.71$ ) for different values of the Rayleigh number as, shown in Table 3.3. This table shows that the spread among the predicted values of Nusselt number increases with increasing  $Ra$ . This might be attributed to the insufficient number of the selected grid element during the last decades.

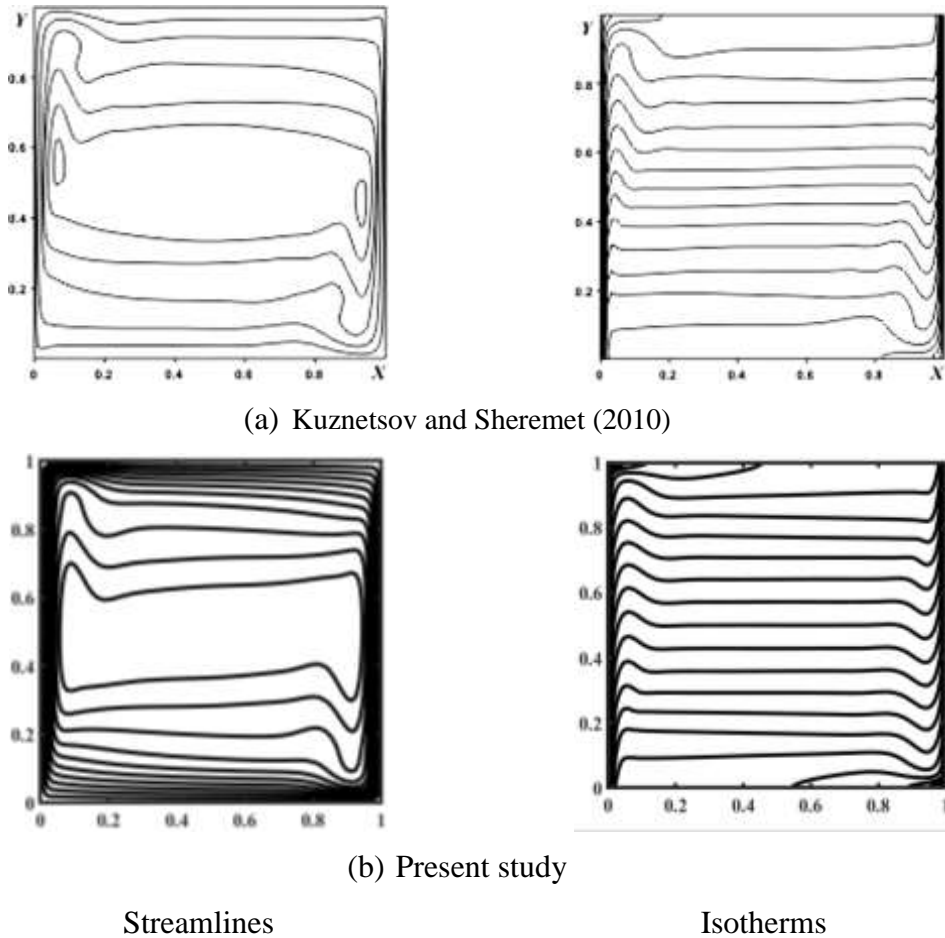


Figure 3.10 : Streamlines and isotherms of the present study are in agreement with those of the benchmark problem of Kuznetsov and Sheremet (2010).

Table 3.3: Comparison of Nusselt numbers predicted in a two-dimensional square enclosure with the literature turbulent numerical convection.

$Ra$	$10^8$	$10^9$	$10^{10}$	$10^{11}$
(Kuznetsov and Sheremet, 2010)	33.41	54.49	-	-
(Sharma <i>et al.</i> , 2007)	30.97	58.33	130.77	325.9
(Dixit and Babu, 2006)	30.506	57.350	103.66	189
(Henkes <i>et al.</i> , 1991)	32.5	47	101.25	218.1
(ElSherbiny <i>et al.</i> , 1982)	28.78	62	133.57	218.1
(Altaç and Uğurlubilek, 2016)	31.34	54.95	103.9	199.9
Present results	30.65	53.43	101.45	197.86
Standard deviation	1.47	4.623	14.378	49.126
Difference	0.601	2.197	13.18	32.34

The third validation, as shown in Table 3.4 was completed for the turbulent natural convection inside a differentially heated porous enclosure saturated with a single-phase fluid (air) for different values of Rayleigh number, at , at  $Da = 10^{-3}$ ,  $\varepsilon = 0.8$  and  $K_r = 1$ .

Table 3.4: Comparison of Nusselt numbers predicted in a two-dimensional square porous enclosure with the literature turbulent numerical convection.

$Ra$	$10^8$	$10^9$	$10^{10}$	$10^{11}$
(Carvalho and de Lemos, 2013)	1.089	3.106	13.271	41.792
(Braga and de Lemos, 2004)	1.089	3.102	13.032	40.614
(Carvalho and de Lemos, 2014)	1.089	3.106	13.315	41.717
Present results	1.097	3.11	13.319	40.81
Standard deviation	0	$1.885 \times 10^{-3}$	0.124	0.538
Difference	$8 \times 10^{-3}$	$5.333 \times 10^{-3}$	0.113	0.564

Finally, the validation of turbulent natural convection inside a three-dimensional enclosure entirely filled with a single-phase fluid ( $Pr = 0.71$ ) was compared with the results of Altaç and Uğurlubilek (2016) in Table 3.5. The results in Table 3.4 and Table 3.5 show an acceptably small difference and a good agreement between the references and the present. This indicates the confidence of using the currently selected FEM solver.

Table 3.5: Comparison of Nusselt numbers predicted in a three-dimensional square enclosure with [132] turbulent numerical convection.

$Ra$	$10^8$	$10^9$	$10^{10}$	$10^{11}$
(Altaç and Uğurlubilek, 2016)	30.23	54.53	103.31	196.86
Present results	29.47	53.21	100.86	194.94
Difference (%)	2.51	2.42	2.37	0.97

### 3.7 Conclusions

The simulation of the convective heat transfer inside a physical domain can be analysis and design using the Computational Fluid Dynamics (CFD). CFD is used to decrease the costs of experiment and optimize the design in many industrial applications. In this study, the CFD simulations carried out using the Galerkin finite element method (GFEM) implemented in COMSOL Multiphasic 5.1a and 5.3a.

This chapter observed how the solution of the flow and heat transfer inside an enclosure is simulated using GFEM, where the physical domain was discretized. Concernedly, the partial differential equations governing the physical domain for the nanofluid and porous layers were discretized. The state of the discretised domain was solved, and the solution analysed. The laminar and turbulent governing equations for the nanofluid and porous layers were presented. The mathematical model of turbulent natural convection equations is presented for the first time. The thermo-physical properties of the working fluid that is used in the present study were addressed. In addition, various validations have been done to have the confidence in the obtained results from the present solver with the previous results in the literature. The validation results agreed with those of the benchmark problems for different literature in the laminar and the turbulent heat transfers.

## **Chapter 4: Natural Convection within an Enclosure Filled with Composite Nanofluid-Porous Layers with a Linearly Heated Left Wall**

### **4.1 Motivation and introduction**

There is a knowledge gap concerning the effect of a linear thermal boundary condition on the laminar natural convection inside an enclosure partly filled with a porous medium saturated with a nanofluid. In other words, most of the previous literature focused on the effect of uniform heating on the laminar convection inside a two-dimensional enclosure entirely or partly filled with a porous medium saturated with a single-phase fluid or a nanofluid. The linear thermal boundary condition may cause a problem in the thermal management in the system. The governing equations are coupled together linked to the buoyancy force effect. In addition, the alignment of the porous slab in a vertical or horizontal direction with the selected boundary condition may play an important role on the convective heat transfer. Therefore, it is necessary to investigate the effects of the linear thermal boundary condition and the porous medium alignment to predict the thermal control inside the enclosure. The linear thermal boundary condition produces a different trend of the flow and heat transfer inside an enclosure partly filled by a porous slab compared to the enclosures that were used in the previous literature. A new simulation results are presented to develop the convective heat transfer inside an enclosure partly filled by a porous slab rather than that of using a porous enclosure under the linear thermal boundary condition. This investigation of the present study may be interested to the designer to predict the convective heat transfer in the next modern industry technology.

Therefore, this chapter investigates the effects of linear heating on the laminar convective heat transfer inside a two-dimensional enclosure partly filled by a vertical or a horizontal porous slab saturated by nanofluid. Two cases, which use the vertical and horizontal directions for the porous slab are considered. In both cases, the left vertical sidewall is linearly heated, whereas the right vertical sidewall is isothermally cooled. The horizontal walls are assumed to be thermally insulated. A local thermal equilibrium (LTE) model between the solid matrix of the porous medium and the nanofluid is assumed. The ranges of the simulation parameters in the present study are: the Rayleigh number ( $Ra$ ),  $10^3 \leq$

$Ra \leq 10^7$ , the Darcy number ( $Da$ ),  $10^{-7} \leq Da \leq 1$ , the porous layer thickness ( $S$ ),  $0.1 \leq S \leq 0.9$ , the thermal conductivity ratio of porous/nanofluid layers ( $K_r$ ),  $0.1 \leq K_r \leq 100$ , and the nanoparticle volume fraction ( $\phi$ ),  $0 \leq \phi \leq 0.2$ . This chapter includes three parts, namely the numerical model, which includes the domain physical model, the boundary conditions, the numerical procedure, and the grid independence test, the numerical results and discussions extracted from this model, and the conclusions.

## 4.2 A model problem

### 4.2.1 Physical model

Laminar natural convection is modelled in a two-dimensional square enclosure with length  $L$ , partially filled by a porous slab saturated by nanofluid. Two slab orientations are considered (vertical and horizontal) in two cases, as shown schematically in Figure 4.1. This figure illustrates case 1, in which the slab is vertical and on the left side of the enclosure, while in case 2, the porous slab horizontal and at the bottom of the enclosure. The porous slab is saturated with a nanofluid and the remainder of the enclosure is filled by the same nanofluid. The porous and nanofluid layers are simulated as having thicknesses  $S$  and  $L - S$ , respectively. In both cases, the left vertical wall is linearly heated, while the right vertical wall is isothermally cooled; the top and bottom walls are thermally insulated. The differentially heated on the vertical walls causes to develop the

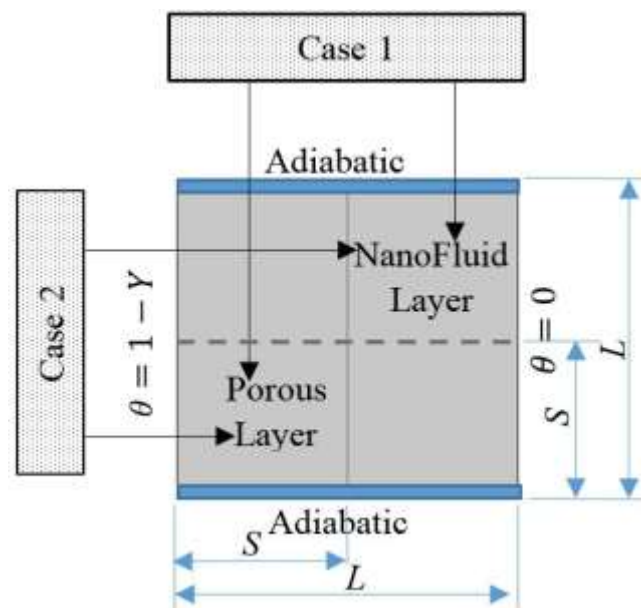


Figure 4.1: Vertical (case 1) and horizontal (case 2) porous slabs inside a nanofluid-filled two-dimensional enclosure.

to occur that the density gradient (due to temperature gradient) is horizontal and the gravity vector acts perpendicularly, where the circulation behaviour inside the enclosure depends on these vectors orientation. The interface between the nanofluid layer and porous layer is permeable with no-slip condition, while all outer boundaries are impermeable and with no-slip condition. The equations governing this set up are listed in Appendix B1 (equations B1.1-B1.8). The nanofluid is a water-based fluid containing Cu nanoparticles, with the thermal properties given in Table 3.1.

### 4.2.2 Boundary conditions

The boundary conditions for each case (vertical and horizontal orientation of the porous medium –nanofluid layers) are:

$$\text{At the left hot wall } U = 0, V = 0, \theta = 1 - Y \quad (4.1)$$

$$\text{At the right cold wall } U = 0, V = 0, \theta = 0 \quad (4.2)$$

$$\text{At the top and bottom insulated walls (adiabatic) } U = 0, V = 0, \frac{\partial \theta}{\partial Y} = 0 \quad (4.3)$$

where

$$X = \frac{x}{L}, Y = \frac{y}{L}, U = \frac{uL}{(\alpha)_{bf}}, V = \frac{vL}{(\alpha)_{bf}}, \theta = \frac{T-T_c}{T_h-T_c} \quad (4.4)$$

### 4.2.3 Grid independence test

In this model, the physical domain was discretised by quadrilateral element. The computational mesh was bilinearly stretched in  $X$  and  $Y$ . Mesh points close to the enclosure perimeter and to the interface between the porous and fluid layers were s

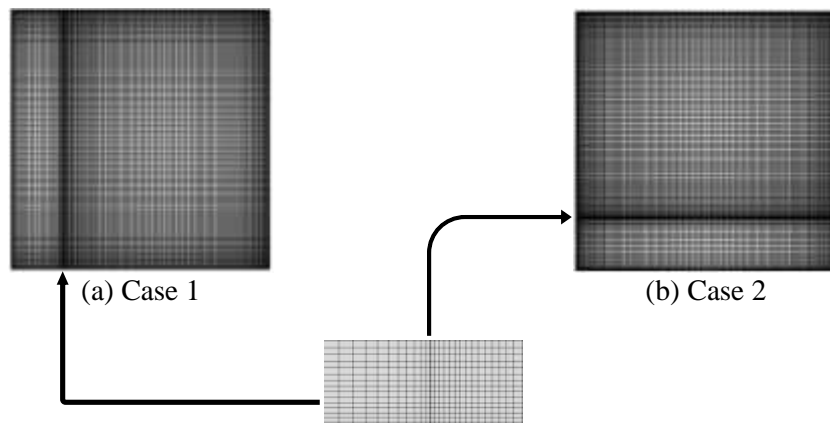


Figure 4.2: Computational mesh of the physical domain for (a) Case 1, (b) Case 2, and (c) Refined mesh detail.

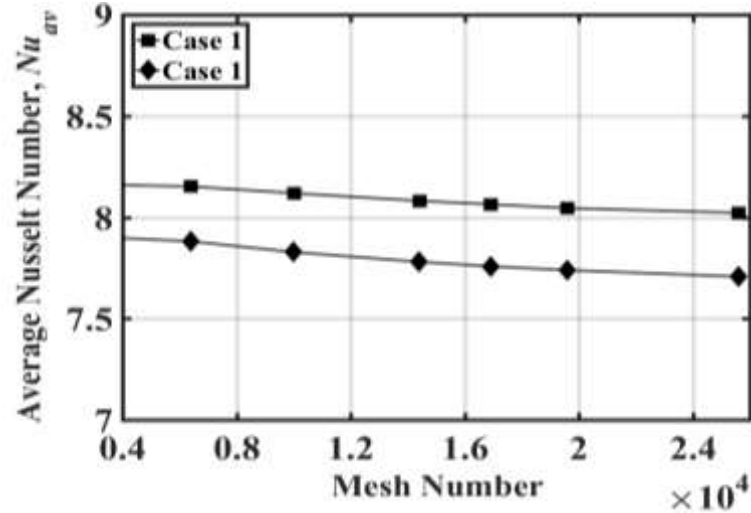


Figure 4.3: Computational mesh dependence of the average Nusselt number.

partially refined, as shown in Figure 4.2. Grid independent tests were performed with the grid sizes of 6400, 10,000, 14,400, 16,900, 19,600 and 25,600 to determine the mesh sensitivity of the predictions.

Figure 4.3 shows the calculated average Nusselt number for different computational grid sizes for an enclosure partly filled with nanofluid and partly filled with a porous layer saturated with the same nanofluid for cases 1 and 2, where  $Ra = 10^7$ ,  $Da = 10^{-3}$ ,  $K_r = 1$ ,  $\phi = 0.1$  and  $S = 0.3$ . A grid size of 16,900 was used in this chapter as this represented the best compromise in terms of both the accuracy and computational time.

## 4.3 Results and discussion

### 4.3.1 Streamlines and isotherms

#### 4.3.1.1 Vertical porous-nanofluid layers (case 1)

Figure 4.4 shows the streamlines (upper row) and isotherms (lower row) for different values of the dimensionless parameters  $S$ ,  $Ra$ ,  $Da$ , and  $K_r$  when the porous and nanofluid layers lie in a vertical direction (case 1). Figure 4.4(a)-(c) show the effect of the porous layer thickness ( $S$ ) on the flow behaviour and temperature distribution inside the enclosure for  $Ra = 10^6$ ,  $Da = 10^{-3}$ , and  $K_r = 1$ . Due to the application of linear heating to the left wall and uniform cooling on the right wall, the nanofluid inside the porous layer rises along the left sidewall and flows down along the cooled right wall in the nanofluid layer, forming two circulations. One of these, the main vortex, covers most of the enclosure by a clockwise direction while a secondary smaller circulation appears at

the top left corner of the enclosure and moves in an anticlockwise direction. For all values of  $S$ , the addition of 10% of copper nanoparticles to the single-phase fluid (water) causes the streamlines' strength for the main cell to be stronger than of the single-phase fluid. This is because the nanofluid has the ability to absorb more thermal energy than the single-phase fluid. This gives an indication that the addition of nanoparticles to the single-phase fluid increases in the heat convection by changing the mixture properties such as the density, viscosity, and thermal conductivity of the nanofluid, as shown in equations (B.11, B.12.) and (B.16). It is interesting to note that, as the value of  $S$  increases, the centre of the main cell moves from a location close to the interface line towards the right cold wall. Another interesting point that may be noted in Figure 4.4(a)-(c) is that the stream through for the porous layer with low thicknesses is stronger than through a thicker porous layer. Adding the nanoparticles changes more the streaming in the thinner porous slab. This can be clearly seen from the stream function values,  $|\Psi_{min}|$ , where for  $S = 0.1, 0.3$  and  $0.5$ , the percentage gain of  $|\Psi_{min}|$  values are 13%, 7.9% and 6.7%, respectively. The effects of increasing the porous layer thickness on the reduction of circulation strength are attributed to the hydrodynamic resistance provided by the porous layer.

The isotherm lines are parallel to the cold right-hand wall, whereas they turn away from the left-hand heated wall. The temperature contour with  $\theta = 0.31$  is pushed towards the upper left corner of the enclosure, and the isotherms gradually became denser near the left wall at  $S = 0.1$ , and more so at  $S$  values of 0.3 and 0.5. The vertical pattern of the isotherm lines within the porous layer indicates the dominance of conduction as the mechanism of heat transfer, whereas the horizontal isotherm pattern indicates convective heat transfer within the nanofluid layer. It is interesting to note that, the spot produced by the isotherm contours when  $\theta \geq 0.31$  in the upper part of the enclosure decreased with increasing porous layer thickness. Therefore, this gives an indication that increasing the porous layer thickness led to a decrease in the rate of heat transfer.

The effects of the flow parameter  $Ra$  on the streamlines and on the isotherms at  $Da = 10^{-3}$ ,  $S = 0.3$  and  $K_r = 1$  are shown in Figure 4.4(d)-(f). The streamlines appeared denser at higher values of  $Ra$ , indicating a stronger circulation of the main cell. At  $Ra = 10^4$ , as shown in Figure 4.4, the streamlines indicate that the porous layer has a resistive

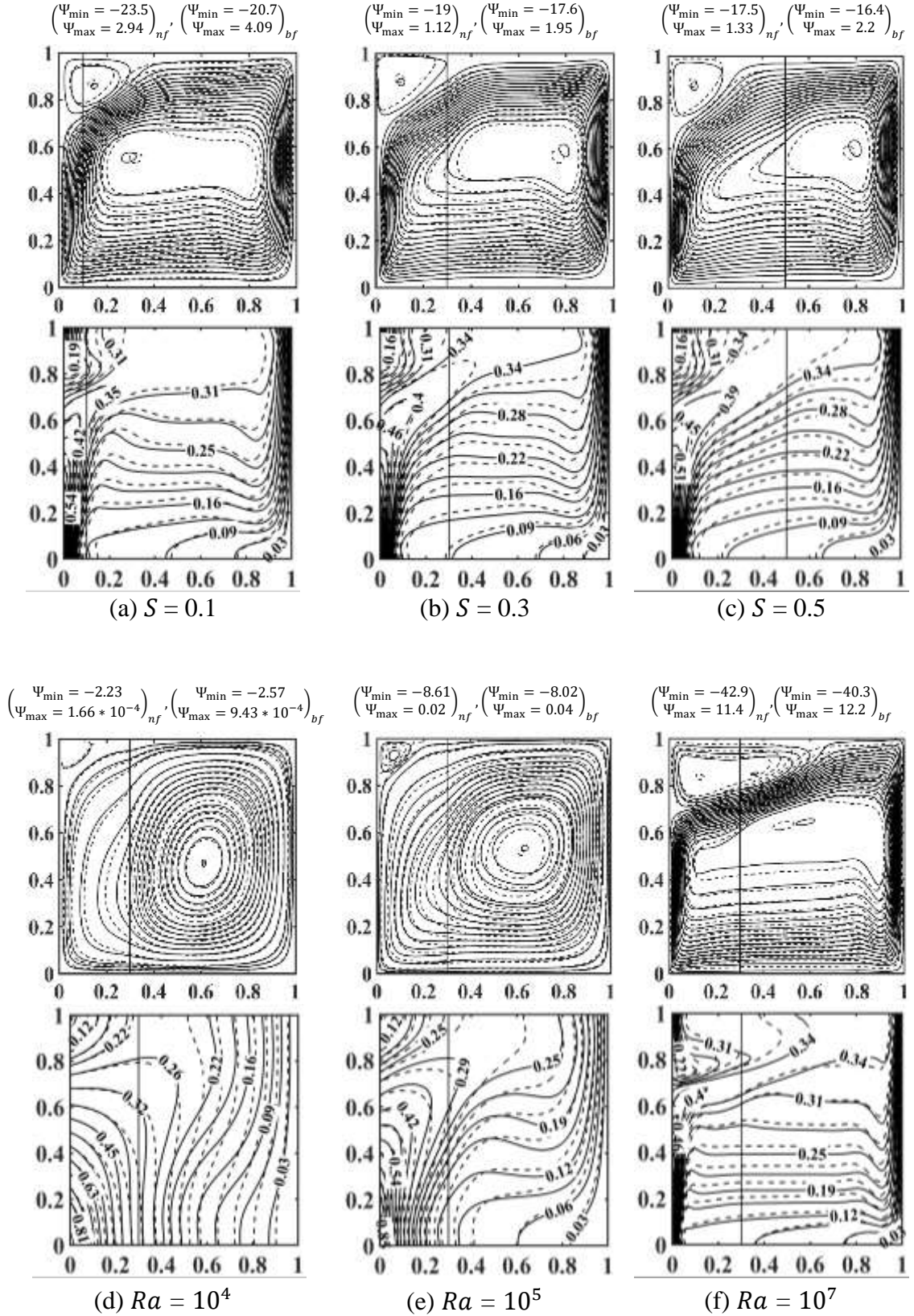


Figure 4.4: Streamlines (upper row) and isotherms (lower row) for case 1 with  $\phi = 0$  (solid lines) and  $\phi = 0.1$  (dashed lines) at different dimensionless parameters, (a-c)  $S$  effect when  $Ra = 10^6$ ,  $Da = 10^{-3}$ , and  $K_r = 1$ , (d-f)  $Ra$  effect when  $Da = 10^{-3}$ ,  $S = 0.3$  and  $K_r = 1$ .

effect on the flow that moves from the nanofluid layer through the porous layer, which results in low flow penetration through the porous layer. The intensity of the secondary circulation is very low compared to the primary circulation, which filled most of the enclosure area. It is interesting to note that, adding a 10% value ratio of nanoparticles to the water leads to a reduction in the circulation strength due to increased viscous forces opposing the buoyancy force at any specified value of  $Ra$ . In contrast, at higher Rayleigh numbers, as shown in Figure 4.4(e) and (f), the intensity of the secondary cell increases, showing greater elongation, pushing the primary cell towards the lower part of the enclosure to a noticeable extent, and with high penetration in the porous layer. The higher values of the Rayleigh number strengthen the natural convection due to an increase in buoyancy inside the enclosure, which leads to a reduction of the temperature of the heat source. The isotherms of Figure 4.4(d)-(f) show an increase in convective heat transfer with increasing Rayleigh number, especially for the nanofluid layer with denser isotherms. In addition, a temperature hot spot at  $\theta \geq 0.31$  occurs in the upper part of the enclosure. This indicates that the diffusion of heat from the left heated source increases due to the strong circulation strength within the main cell.

Figure 4.5(a)-(c) report the variation of the streamlines and isotherms with dimensionless permeability (Darcy number) for  $Ra = 10^6$ ,  $S = 0.3$ , and  $K_r = 1$ . These figures show that the penetration of nanofluid into the porous layer depends on the Darcy number value. At  $Da = 10^{-5}$ , as shown in Figure 4.5(a), the main cell is confined to the region around the nanofluid layer, with low penetration of the fluid through the porous layer. Figure 4.5(b) and (c) shows that increasing  $Da$  to  $10^{-2}$  and  $10^{-1}$ , respectively, results in an increase in the intensity of the main cell accompanied by the appearance of a weak secondary cell at the upper left corner of the enclosure. The main cell centre at high values of  $Da$  moves from the nanofluid layer towards the porous layer close to the left heated wall, whilst it is fully confined to the region of the nanofluid layer for  $Da = 10^{-3}$ , as shown in Figure 4.4(b). It is interesting to note that, the streamlines at the low Darcy number are more affected by the addition of 10% of nanoparticles to the single-phase fluid than at the higher  $Da$  values. This is shown by the  $|\Psi_{min}|$  values, where for  $Da = 10^{-5}$ ,  $10^{-2}$  and  $10^{-1}$ , the percentage variations in  $|\Psi_{min}|$  are 25%, 10.4% and 11%, respectively. The isotherm figures show how the Darcy number can be used as a controlling parameter to translate the convection from the nanofluid layer to the porous

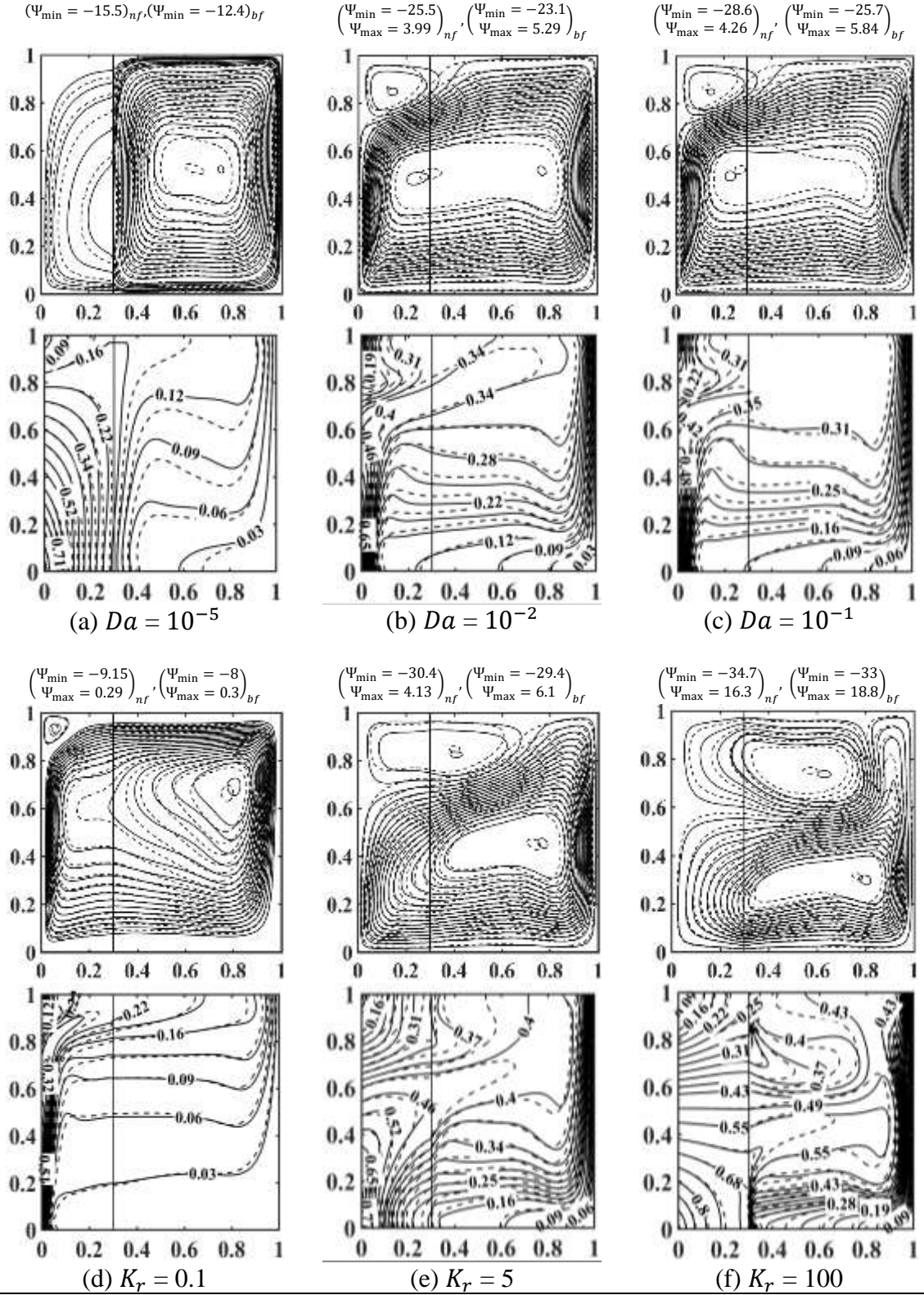


Figure 4.5: Streamlines (upper row) and isotherms (lower row) for case 1 with  $\phi = 0$  (solid lines) and  $\phi = 0.1$  (dashed lines) at different dimensionless parameters, (a-c)  $Da$  effect when  $Ra = 10^6$ ,  $S = 0.3$  and  $K_r = 1$ , and (d-f)  $K_r$  effect when  $Ra = 10^6$ ,  $Da = 10^{-3}$  and  $S = 0.3$ .

layer. The high racking density of the isotherm lines appearing close to the vertical walls at the highest magnitude of  $Da$  is indicative of greater convective heat transfer within the enclosure. This causes the temperature of the heat source to be reduced with an increased permeability of the porous layer matrix.

The effect of thermal conductivity ratio,  $K_r$ , on the streamlines and isotherms for  $Ra = 10^6$ ,  $Da = 10^{-3}$  and  $S = 0.3$  is shown in Figure 4.5(d)-(f). The streamlines show the appearance of two recirculation cells when  $K_r = 0.1$ , as shown in Figure 4.5(d). The centre of the clockwise primary cell is located adjacent to the right cold wall with steeper streamlines on the left-hand heated wall and on the right-hand cooled wall while a small weaker anticlockwise-circulating secondary cell is located at the upper left corner of the enclosure. At  $K_r = 5$  (see Figure 4.5(e)), the extrema stream function values of the main clockwise and the upper left counter-clockwise cells are higher than that at  $K_r = 0.1$ . The primary cell is also compressed by the secondary cell towards the lower right corner of the enclosure. The centres of the primary and of the secondary cells move away from the left-hand heated source wall towards the right-hand cold wall, resulting in a reduced penetration of the nanofluid flow into the porous layer. This pattern increases up to  $K_r = 100$ , resulting in a lower racking density of the streamlines in the region of the left-hand heated wall. This change in the circulation strength is attributed to an increased thermal conductivity ratio (porous/nanofluid). At higher  $K_r$ , the increasing strength and cell size of the upper, anticlockwise-circulating secondary cell causes the hot nanofluid to return the heat towards the upper part of the heat source, which leads to a decrease in the overall heat transfer. However, at lower values of  $K_r$ , a clockwise convection heat transfer dominates the enclosure. The isotherm of Figure 4.5(d)-(f) show that, the convection is transmitted from the nanofluid layer to the porous layer at the lower thermal conductivity ratio of  $K_r = 0.1$ , whilst the isotherm lines are more packed at the left-hand heated wall at higher values of  $K_r$ , signifying conductive heat transfer at this location.

#### **4.3.1.2 Horizontal porous-nanofluid layers (case 2)**

Figure 4.6 shows the streamlines (upper row) and isotherms (lower row) for different effective dimensionless parameters when the nanofluid layer is overlying the porous layer. Figure 4.6(a)-(c) shows the variation of flow and isotherm patterns inside the enclosure with varying porous layer thickness,  $S$ , as  $Ra = 10^6$ ,  $Da = 10^{-3}$ , and  $K_r = 1$ .

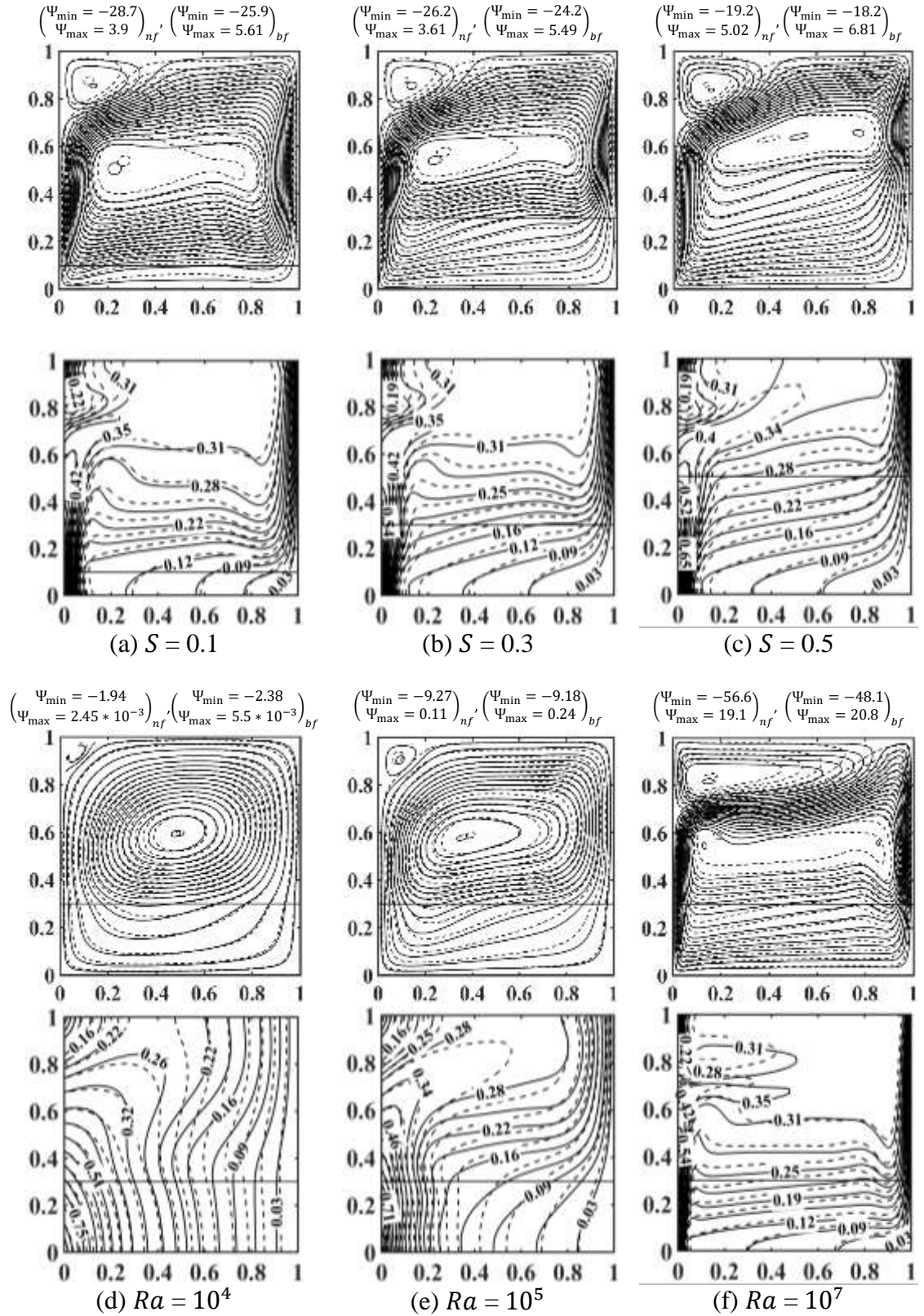


Figure 4.6: Streamlines (upper row) and isotherms (lower row) for case 2 with  $\phi = 0$  (solid lines) and  $\phi = 0.1$  (dashed lines) at different dimensionless parameters, (a-c)  $S$  effect when  $Ra = 10^6$ ,  $Da = 10^{-3}$ , and  $K_r = 1$ , (d-f)  $Ra$  effect when  $Da = 10^{-3}$ ,  $S = 0.3$  and  $K_r = 1$ .

As in the previous case, due to the linear thermal boundary conditions applied to the left-hand sidewall of the enclosure, the nanofluid inside both layers rises along the left-hand heated wall and flows down along the cooled right-hand wall, causing two circulating regions. The primary circulation covers most of the enclosure, rotating in a clockwise direction, while the secondary circulation turns in the anticlockwise direction and is confined to the upper region of the left-hand heated wall. Figure 4.6(a) shows a low penetration of the streamlines into the porous layer as compared with case 1, which shows the effect of the porous slab orientation. It is interesting to note that, the centre of the main cell remains close to the left-hand heated wall while the secondary cell tends to compress the main cell towards the porous layer, which is in contrast with case 1 where the upper circulation tends to push the main cell towards the right-hand cooled wall.  $|\Psi_{min}|$  shows that the intensity of circulations, in this case, is stronger than for case 1 for different thicknesses of the porous layer. However, the addition 10% of nanoparticles to the single-phase fluid by volume leads to a lower increase in the percentage of  $|\Psi_{min}|$  values compared to case 1, except at  $S = 0.3$ , where for  $S = 0.1, 0.3$  and  $0.5$ , the gain in percentages of  $|\Psi_{min}|$  were 10.8%, 8.3% and 5.5%, respectively. Although the increases in percentage were lower in this case, it is expected that the overall higher intensity of the circulation might actually increase the convective heat transfer. The isotherms in the vicinity of the heat source, in this case, is denser than in case 1. The temperature contour with  $\theta \geq 0.31$  is also pushed towards the top left corner of the enclosure with a relatively lower thickness of the thermal boundary (steeper lines) compared to case 1, and this thickness increases with increasing thickness of the porous layer, especially for the nanofluid contour.

Figure 4.6(d)-(f) shows the effect of the Rayleigh number on the streamlines and isotherms for case 2 with  $Da = 10^{-3}$ ,  $S = 0.3$  and  $K_r = 1$ . The streamlines in the upper panel of Figure 4.6(d) depicts the flow inside the enclosure at  $Ra = 10^4$ . It is clear that the porous layer has an effect on the transport flow within the porous layer, with low penetration of the nanofluid. The intensity of the secondary cell is very low as compared with the main cell strength. The intensity of the main circulation is also low, with a horizontal elongation in a semi-circular shape parallel to the interface between the porous and nanofluid layers when compared with case 1 (see Figure 4.4 (d)). A significant change in the flow pattern inside the enclosure occurs by increasing the Rayleigh number to  $Ra$

=  $10^5$  and then to  $Ra = 10^7$ , as shown in Figure 4.6(e) and (f), respectively. The secondary cell circulation at the upper left corner strengthens and extends away from the corner. The primary cell has relatively more intensity than in case 1 (see Figure 4.4(f)). The secondary cell tends to compress the main cell, leading to the generation of two poles whose centres are closed to the cooled right-hand and hot left-hand walls. The isotherms of Figure 4.6(d)-(f) shows that the thickness of the thermal boundary layer is less in case 2 as compared with case 1 due to the augmentation of circulation intensity by the formation of two poles close to the left and right vertical walls.

Figure 4.7(a)-(c) shows the streamlines (upper row) and the isotherms (lower row) at  $Ra = 10^6$ ,  $S = 0.3$  and  $K_r = 1$  for different values of  $Da$ . It can be observed from the streamlines that the nanofluid flow circulation is strongly dependent on the Darcy number. At  $Da = 10^{-5}$ , as shown in Figure 4.7(a), two cells are observed in the enclosure. One is the strong main cell with a clockwise flow circulation, and which is dominated across the majority of the enclosure, while the weak anti-clockwise flow circulation appears at the upper left corner of the enclosure with low penetration into the porous layer. It is interesting to note that, the streamlines at  $Da = 10^{-5}$  for this case have a higher value of  $|\Psi_{min}| = 20.5$  for the nanofluid than  $|\Psi_{min}| = 18.7$  for the single-phase fluid as compared to case 1. The streamlines behave in a different manner than in case 1, as seen in Figure 4.5(a). As  $Da$  increases, the penetration of the nanofluid flow increases. This is accompanied by higher circulation intensities. The addition of 10% Cu nanoparticles by volume to the single-phase fluid result in percentage gains in  $|\Psi_{min}|$  for  $Da = 10^{-5}$ ,  $10^{-2}$  and  $10^{-1}$  of 9.6%, 11.37% and 11.53%, respectively. Although the percentage gain for the case at  $Da = 10^{-5}$  is lower than in case 1, it seems that a higher temperature gradient forms within the thermal boundary layer in the nanofluid layer along the left wall as compared to the vertical left wall in case 1. Another comparison between these cases is that the isotherm  $\theta \geq 0.31$  for  $Da = 10^{-2}$  and  $10^{-1}$  has more spots in the upper part of the enclosure compared to case 1 with greater diffusion of the heat from the heat source, indicating that of the convective heat transfer for case 2 is greater than that for case 1.

Figure 4.7(d)-(f) displays the streamlines (upper row) and isotherms (lower row) with  $Ra = 10^6$ ,  $Da = 10^{-3}$  and  $S = 0.3$  for different thermal conductivity ratios ( $K_r$ ). The streamlines within the enclosure show the typical trends of a primary cell and a secondary

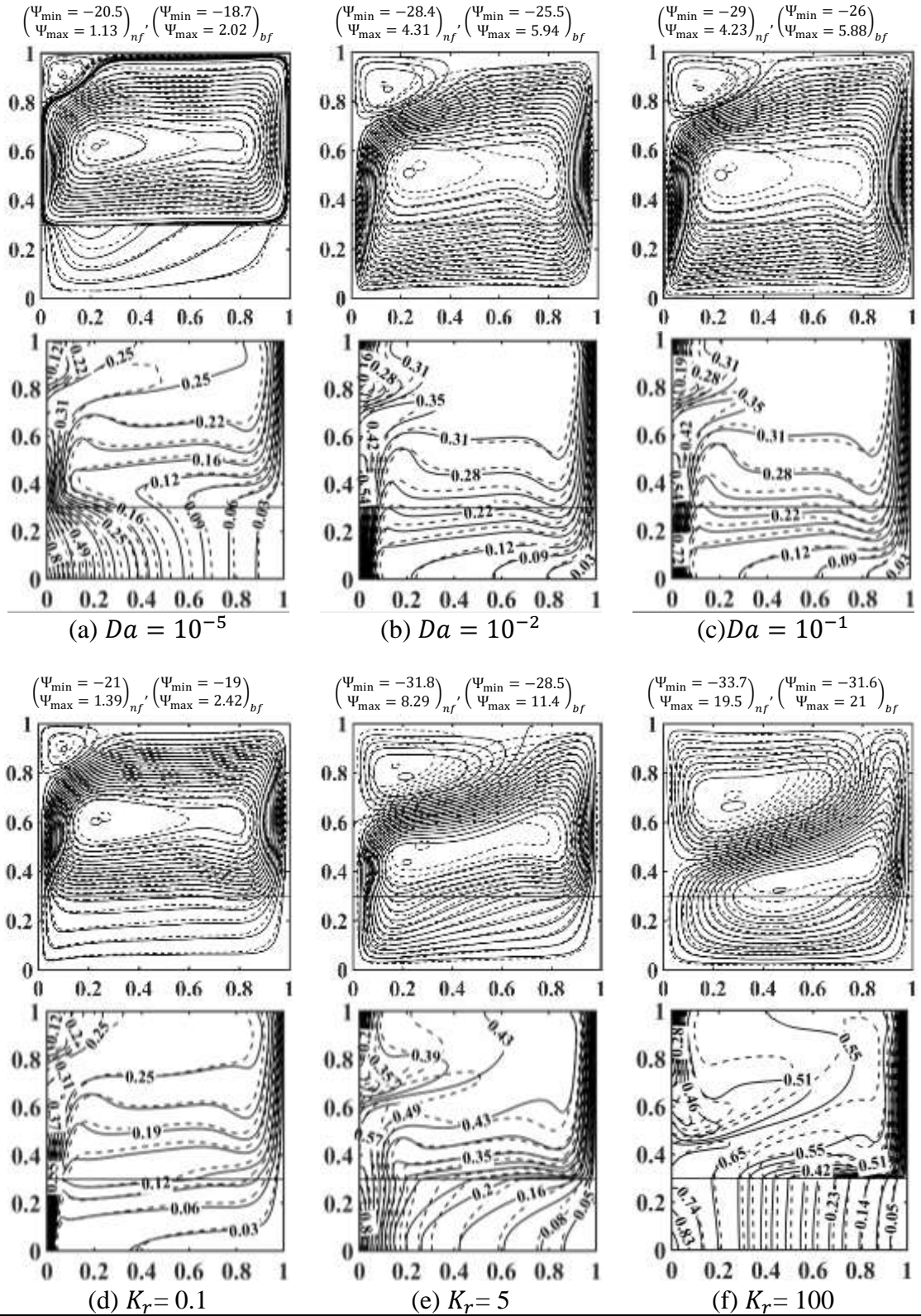


Figure 4.7: Streamlines (upper row) and isotherms (lower row) for case 2 with  $\phi = 0$  (solid lines) and  $\phi = 0.1$  (dashed lines) at different dimensionless parameters, (a-c)  $Da$  effect when  $Ra = 10^6$ ,  $S = 0.3$  and  $K_r = 1$ , and (d-f)  $K_r$  effect when  $Ra = 10^6$ ,  $Da = 10^{-3}$ , and  $S = 0.3$ .

cell inside the enclosure. The location of the main cell centre is close to the left-hand heated sidewall while the secondary circulation is confined to the upper left corner of the enclosure. The intensity of the primary and secondary circulations increases with increasing thermal conductivity ratio. At  $K_r = 0.1$ , the primary cell covered most of the enclosure area with low penetration of the porous layer, as shown in Figure 4.7(d). It is interesting to note that, the stream function strength of the primary cell is significantly greater than that for case 1 at  $K_r = 0.1$ . In addition, the centre of the primary cell is closer to the left-hand heated wall causes denser streamlines along the vertical walls in the nanofluid layer. Figure 4.7(e) shows that the streamlines inside the enclosure for  $K_r = 5$  define a secondary cell of greater intensity and elongation than for  $K_r = 0.1$ , causing the compression of the primary cell towards the porous layer. Another significant point is that, the centres of the nanofluid cells, due to the additional 10% Cu nanoparticles present, move vertically more into the nanofluid layer compared to the centres of the single-phase fluid cells, which leads to the stream function of the nanofluid having greater strength than that of the single-phase fluid. As  $K_r$  increases to  $K_r = 100$ , the flow pattern within the enclosure remains qualitatively constant up to  $K_r = 100$ , though with greater elongation of the secondary cell, which causes the rotation of the flow towards the left-hand heated wall. In Figure 4.7(d)-(f), the horizontal isotherms lines indicate convective heat transfer, while the vertical isotherm lines indicate conductive heat transfer. The isotherm lines are denser and closer to the left and right vertical walls due to the elongation of the cells towards the vertical walls with the reduced thickness of the thermal boundary layer along the vertical walls. At  $K_r = 0.1$  with the isotherm  $\theta \geq 0.25$ , the convective heat transfer is dominant in the enclosure, even at the porous layer, and the heat transport at the top portion of the enclosure is more diffused compared to case 1. As  $K_r$  increases towards 100, the convective heat transfer remains confined to the nanofluid layer, while the conductive heat transfer appears in the porous layer when the thermal boundary layer is relatively thick. The high packing density of the isotherms close to the left and right walls in the nanofluid layer resulted in significant heat diffusion from the heat source when compared to case 1. The increment in  $K_r$  forms two recirculation cells of similar extent in place of one dominant cell. This prevents the flow from residing longer closer to the heat source and to the heat sink. Therefore, the fluid in motion receives and rejects comparatively less heat per full circulation round the cell, resulting

in a lower overall rate of heat transfer. The heat transfer decreases with increasing  $K_r$ , especially in case 1.

### 4.3.2 Velocity distribution

The distributions of the velocity components  $U$ ,  $V$  and of the velocity magnitude  $R$ , are examined at the interface between the porous-nanofluid layers along the  $Y$ -axis and  $X$ -axis for case 1 and case 2, respectively, at  $S = 0.3$ ,  $\phi = 0.1$  and  $K_r = 1$  with  $Ra = 10^4$  and  $10^6$  for different  $Da$  values, as shown in Figure 4.8.

#### 4.3.2.1 Vertical porous-nanofluid layers (Case 1)

Figure 4.8(a) shows the variation of the velocity components for different  $Da$  values at the interface between the porous-nanofluid layers for case 1 as  $S = 0.3$ ,  $\phi = 0.1$  and  $K_r = 1$  when  $Ra = 10^4$  and  $10^6$ . Increasing the Rayleigh number causes a significant augmentation in the velocity components within the enclosure due to the strengthened buoyancy force. The flow exchange through the interface increases and the maximum and minimum velocity components at the interface of the enclosure with  $Da = 10^{-1}$  became greater than those for  $Da = 10^{-5}$ . This is attributed to the increased permeability of the porous layer, which causes a reduction in the resistance offered by the porous layer to the nanofluid flow, resulting in an increase in velocity. Figure 4.8(a)(i) shows the effects of the Darcy and Rayleigh numbers on the horizontal velocity component at the interface for case 1. It is interesting to note that, for the velocity profile at  $Ra = 10^4$ , it appeared that the velocity of the nanofluid flow towards the upper part of the interface is lower than the flow at the bottom of the interface. This is because of the buoyancy force being highest at the bottom left hand-side wall which causes to accelerate the flow at the bottom part of the porous slab. However, this pattern takes the opposite trend with increasing  $Ra$  values because of the increase of the size and strength of the secondary cell at the upper left corner of the enclosure which causes to accelerate the flow at the upper side of the porous slab. The positive and negative values of the horizontal velocity close to the upper and the bottom adiabatic walls, respectively, are attributed to the clockwise flow direction of the primary cell. Figure 4.8(a) (ii) shows the effect of the permeability of the porous layer on the vertical velocity component along the interface for case 1 with different values of  $Ra$ . Parabolic curves of positive values of the vertical velocity are predicted at  $Ra = 10^4$ . Increasing  $Ra$  to  $10^6$  causes a disturbance in this

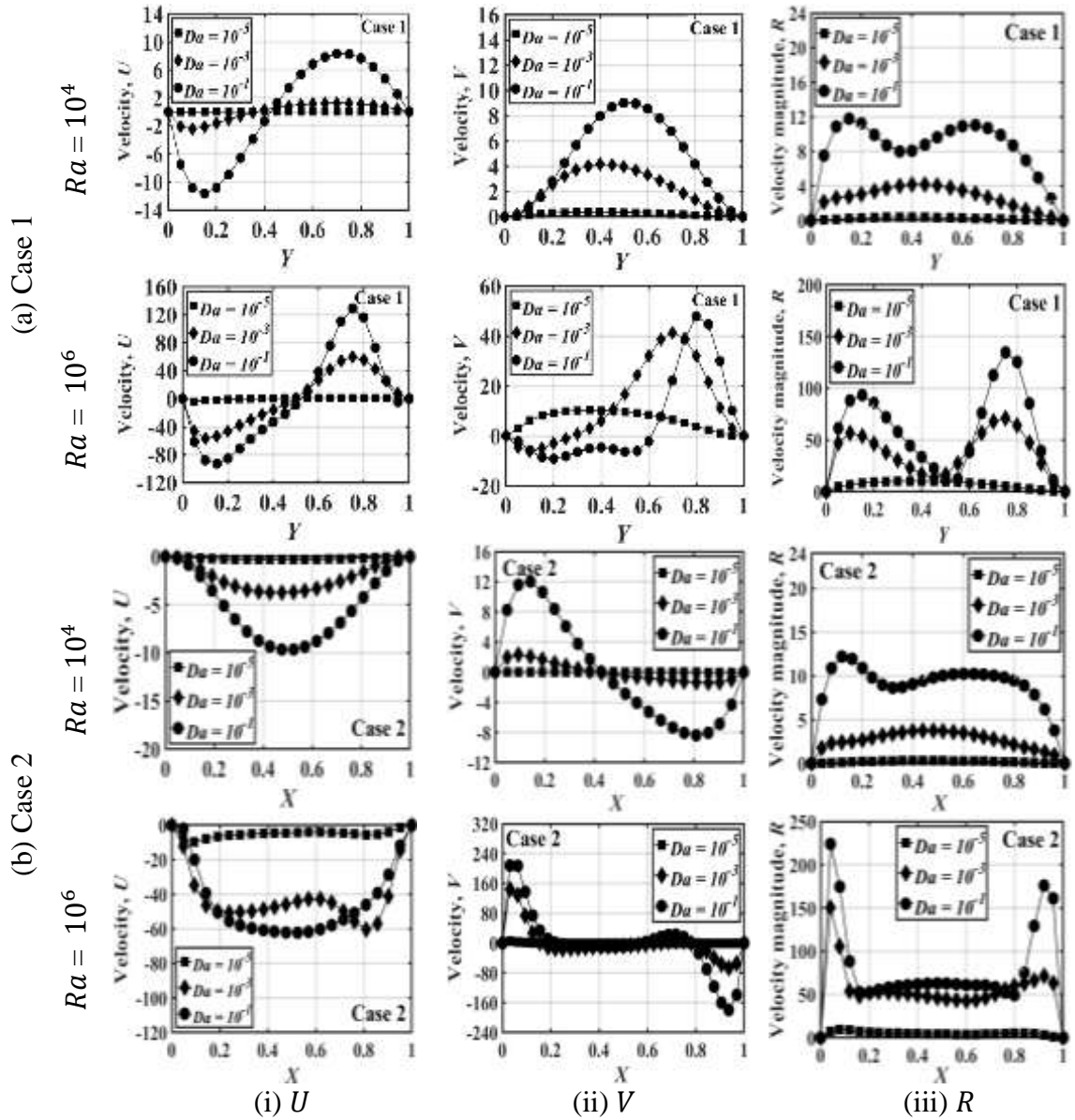


Figure 4.8: Variation of velocity profile components (i)  $U$ , (ii)  $V$ , and (iii)  $R$  at the interface line of (a) case 1 and (b) case 2 for different Darcy numbers as  $S = 0.3$ ,  $\phi = 0.1$  and  $K_r = 1$  at  $Ra = 10^4$  and  $Ra = 10^6$ .

behaviour due to the non-uniform pattern of the streamlines at the interface with higher values of  $Ra$  at approximately  $Y = 0.7$  and  $0.8$  for  $Da = 10^{-3}$  and  $10^{-1}$ , respectively. This is attributed to the higher buoyancy force that is generated at the increased Rayleigh number and due to the higher penetration of the nanofluid through the porous layer at higher Darcy numbers. This leads to the main recirculation cell penetrating strongly into the porous layer. The local distribution of the velocity magnitude for case 1, shown in Figure 4.8(a) (iii), clarifies the effect of the Darcy number on the nanofluid flow inside the enclosure. The velocity magnitude at  $Da = 10^{-5}$  is almost zero compared to the that

at higher value of  $Da$ , which means less hydrodynamic resistance with higher permeability of the porous matrix. At  $Ra = 10^4$  with  $Da = 10^{-1}$ , the velocity magnitude displays two maxima at about  $Y = 0.1$  and  $Y = 0.7$ , while a local minimum occurs at about  $Y = 0.4$ . Increasing  $Ra$  causes the minimum values to approach zero between  $Y = 0.4$  and  $Y = 0.6$ , due to the localization of the cell core at this height inside the enclosure.

#### 4.3.2.2 Horizontal porous-nanofluid layers (Case 2)

Figure 4.8(b) shows the effect of the permeability parameter ( $Da$ ) on the velocity components  $U$ ,  $V$  and the velocity magnitude  $R$  for case 2 as  $S = 0.3$ ,  $\phi = 0.1$  and  $K_r = 1$  when  $Ra = 10^4$  and  $10^6$ . At  $Ra = 10^4$ , as shown in Figure 4.8(b) (i), the curves with negative horizontal velocity values appear at the interface between the porous-nanofluid layers. The symmetric behaviour with negative values results from the main circulation streamlines being undisturbed where the flow turns towards the left wall, with a maximum value at about  $X = 0.5$ . Increasing the Rayleigh number to  $10^6$  leads to an increase in velocity along the interface with considerable disturbance due to the non-uniform paths of the main vortex streamlines in this region.

Figure 4.8(b) (ii) shows the variation of the vertical velocity profile for case 2 for different  $Da$  values along the horizontal interface line at  $Y = 0.3$  for  $\phi = 0.1$  and  $K_r = 1$  when  $Ra = 10^4$  and  $10^6$ . The effect of changing the Darcy number values seems clearer at lower values of  $Ra$ . Increasing  $Da$  causes the vertical velocity component to increase near the vertical walls, where the velocity near the left wall is relatively greater than near the right wall. This is due to the increase of the buoyancy force close to the heated wall. The increase in  $Ra$  value causes a change in the trend of the vertical velocity profile at the interface from an oscillatory to a uniform pattern with near to zero values between  $X = 0.2 - 0.6$ , with large velocities near the vertical walls. This is because of the elongation of the main cell along the interface line. Figure 4.8(b) (iii) illustrates the velocity magnitude of the nanofluid flow for different  $Da$  values along the horizontal interface for case 2 as  $\phi = 0.1$  and  $K_r = 1$  when  $Ra = 10^4$  and  $10^6$ . At  $Ra = 10^4$ , it seems that the pattern seen for the velocity magnitude in this case is similar to the previous case, though with relatively greater strength than for case 1. However, this pattern breaks with increasing  $Ra$  value to  $10^6$ , with a uniform velocity distribution between  $X = 0.2 - 0.8$  with large velocities near the vertical walls of the enclosure. This is due to the dominant and

elongated main circulation pattern along the interface. In general, the velocity magnitude in case 2 is greater than in case 1. This is due to the direction of the porous-nanofluid layers. Therefore, it is expected that the heat removal from the left-hand heated wall for case 2 will be greater than that for case 1.

### 4.3.3 Normalized temperature distribution, $\theta$

In this section, the dimensionless temperature distribution  $\theta$  along the interface at  $X = 0.3$  for (i) case 1 and at  $Y = 0.3$  for (ii) case 2 is examined in terms of the dimensionless parameters (a)  $Ra$ , (b)  $K_r$ , and (c)  $S$ , as shown in Figure 4.9.

#### 4.3.3.1 Vertical porous-nanofluid layers (Case 1)

Figure 4.9(i) (a)-(c) illustrates the dimensionless temperature distribution versus distance along the vertical interface for case 1 at  $X = 0.3$ . In Figure 4.9(i) (a), the temperature distribution shows a higher value at the lower value of  $Ra$  when  $Y = 0$  due to the prevalence locally of conductive heat transfer and a minimum temperature value at the upper part of the interface. This pattern is reversed for high values of  $Ra$  due to the increase in buoyancy, which activities substantial convective heat transfer. The effect of increasing the thermal conductivity ratio (porous to nanofluid) on the temperature distribution along the interface for case 1 is illustrated in Figure 4.9(i) (b). At  $Y = 0$ , the temperature increases with increasing  $K_r$  at the bottom part of the interface between the porous and the nanofluid layers. This is attributed to that, higher values of  $K_r$ , increasing the size and the streamlines strength of the secondary cell and its extension from the porous layer towards the fluid layer. This causes to accelerate and move the core of the primary cell close to the interface line away from the left heated wall with higher streamlines strength compared to the lower values of  $K_r$ , where the core of the primary cell close to the left heated wall as shown in Figure 4.5(d)-(f). The temperature increases monotonically along the interface for low values of  $K_r$  up to  $Y = 1$ , while this behaviour is reversed for high values of  $K_r$ . This is due to the secondary cell effects tends to turn the cold nanofluid from the fluid layer into the porous layer at the upper part of the interface line.

The effect of increasing the porous layer thickness on the temperature profile along the

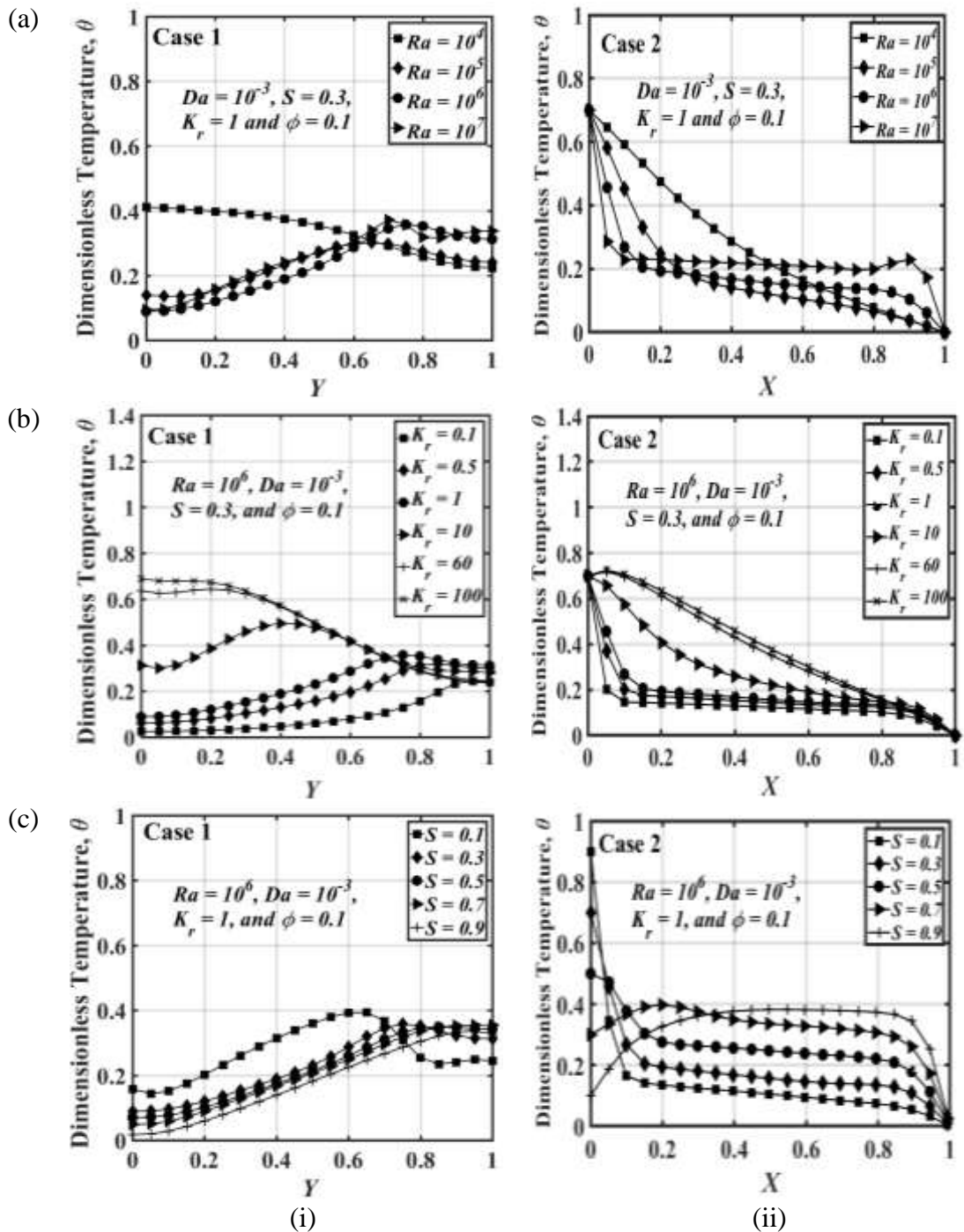


Figure 4.9: Local distribution of dimensionless temperature along the interface line for (i) case 1 and (ii) case 2 with different dimensionless parameters (a)  $Ra$  effect, (b)  $K_r$  effect, and (c)  $S$  effect.

interfaces line for case 1 is illustrated in Figure 4.9(i) (c). The temperature decreases with increasing  $S$  at  $Y = 0 - 0.8$  because of the increasing the interface distance from the heat source. However, at  $Y \geq 0.8$ , the temperature profile behaves in the opposite manner due to the vertical interface being closes to the right-hand cooled wall, where there is a low temperature at the upper part of the enclosure. Increasing the porous layer thickness  $S$  means increasing the flow resistance, which results in reduced heat removal from the left-

hand heated wall. Therefore, at sufficiently large  $S$  and  $Ra$ , the anti-clockwise convective cell transports cold flow from right to left near the top boundary of the interface line.

#### 4.3.3.2 Horizontal porous-nanofluid layers (Case 2)

Figure 4.9(ii) (a-c) illustrates the dimensionless temperature distribution versus distance along the interface for case 2 at  $Y = 0.3$  for various parameter effects. At  $X = 0$ ,  $\theta = 0.7$  for all values of  $Ra$  because the base of the horizontal interface is located on the left-hand heated wall at  $Y = 0.3$ , as shown in Figure 4.9(ii) (a). At  $X \leq 0.1$ , the temperature distribution sharply decreases with increasing  $Ra$ , then  $\theta$  monotonically increases, while the opposite can be seen for  $X > 0.3$ . This indicates that the removal of heat from the heat source increases with increasing Rayleigh number. The variation in the temperature profile along the interface with different values of thermal conductivity ratio for case 2 is illustrated in Figure 4.9(ii) (b). The temperature profile sharply decreases at  $X < 0.2$  with decreasing  $K_r$  values. Low  $K_r$  values result in a decrease in the temperature distribution along the interface due to the dominance of the main circulation along the interface with the convective heat transfer mode through the porous layer. At high values of  $K_r$ , a linear temperature distribution appears along the interface. Figure 4.9(ii) (c) shows the effect of changing  $S$  values on the temperature distribution along the interface between the nanofluid and the porous layers. It is interesting to observe that, the temperature for case 2 is greater than for case 1 at  $X = 0$  for all values of  $S$  due to the linear heating. Increasing  $S$  leads to a rise in the temperature across the interface due to the increase in area of high nanofluid flow due to the porous layer, which leads to a decrease in the stream function strength of the main cell. This also causes an increase in the thermal boundary layer thickness as shown in Figure 4.6(a-c). At  $S \leq 0.5$ , the temperature distribution decreases along the interface due to the distance from the left-hand heated wall. In case 2, the temperature along the interface is a maximum at  $X = 0$  when  $S = 0.1$ , while the opposite behaviour is seen along the interface up to  $X = 1$ . The opposite pattern occurs along the interface in case 1, where  $\theta$  is higher at  $X = 1$  and lowest at  $X = 0$ . The temperature increases with decreasing porous layer thickness along the interface up to  $Y = 0.7$ . This change in the temperature distribution pattern can be attributed to the effect of the porous-nanofluid layers' orientation, which results in different behaviours of the streamlines in the enclosure.

#### 4.3.4 Heat transfer rate: Local Nusselt number

The local Nusselt number is computed by the following relations (Oztop *et al.*, 2012)

$$Nu_{local} = \frac{h.L}{(k)_{bf}} \quad (4.5)$$

The local heat transfer coefficient  $h$  is expressed as

$$h = \frac{(q)_w}{(T_h - T_c)} \quad (4.6)$$

$$(k)_{nf} = -\frac{(q)_w}{\frac{\partial T}{\partial x}} \quad (4.7)$$

By substituting equations (4.6) and equation (4.7) into equation (4.5) and using the dimensionless quantities in equation (B1.10), the local Nusselt number on the hot and cold walls ( $Nu_l$  and  $Nu_r$ ) are written as

$$Nu_{local} = -\frac{(k)_{nf}}{(k)_{bf}} \left( \frac{\partial \theta}{\partial n} \right)_{x=0,1} \quad (4.8)$$

Where  $n$  is the outwards unit normal vector from the boundary wall and for the cold wall  $n = X$ .

The distribution of the local Nusselt number is illustrated in Figure 4.10 under the different effects of selected parameters such as Darcy number (a) and the thermal conductivity ratio (b). The left column represents the local Nusselt number on the left-hand heated wall ( $Nu_l$ ) in Figure 4.10 (i), while the right column represents the local Nusselt number on the right-hand cooled wall ( $Nu_r$ ) in Figure 4.10 (ii). The upper and lower panels represent case 1 and case 2, respectively.

The upper panel plots of Figure 4.10(a) show the local Nusselt number as a function of distance along the left and right walls for case 1 when  $Ra = 10^6$ ,  $\phi = 0.1$ ,  $K_r = 1$  and  $S = 0.3$  for different values of  $Da$ . Figure 4.10(a)(i) shows that the maximum value of the local Nusselt number  $Nu_l$  on the left heated wall (left column) is located at the bottom portion of the left heated wall that is having a maximum temperature of the enclosure due to the linearly heated left sidewall. At  $Y = 0$ , the positive value of the local Nusselt number (heat transport from the wall towards the nanofluid) increases with increasing  $Da$  due to

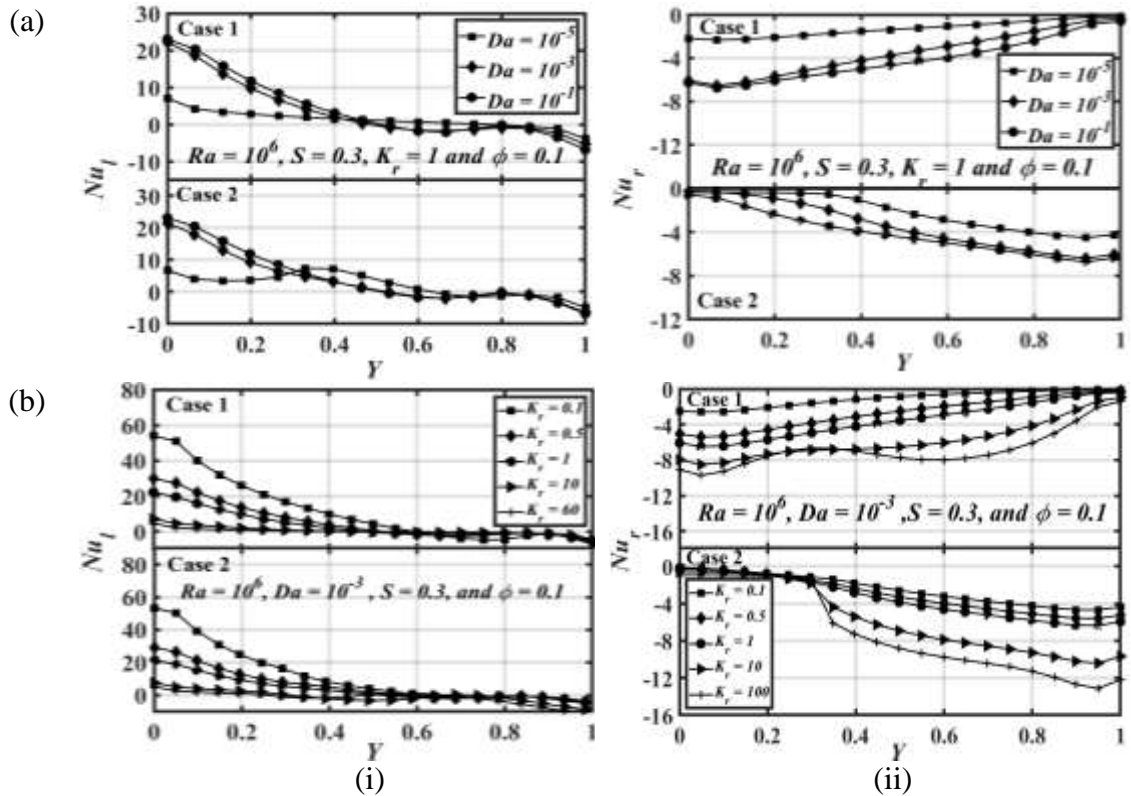


Figure 4.10: Variation of the local Nusselt number along the left hot wall (i) and the right cold wall (ii) with different dimensionless parameters (a)  $Da$  effect and (b)  $K_r$  effect.

an increase in the porous layer's permeability with high streamline strength due to the convective heat transfer mode within the enclosure. At  $Y \geq 0.4$ ,  $Nu_l$  is negative (heat is transported from the nanofluid towards the wall) signifying a reverse heat flux with a minimum  $Nu_l$  at the top portion of the hot left-hand sidewall of the enclosure. The minimum change in  $Nu_l$  is obtained with low Darcy number ( $Da = 10^{-5}$ ) due to the high flow resistance offered by the porous matrix. A comparison of the effects of changing  $Da$  on the local Nusselt number under the same conditions between case 1 and case 2 can be seen in the left-hand column and lower panel plot in Figure 4.10(a) (i), which represents case 2; and it seems a similar trend in  $Nu_l$  is observed as for case 1. However, the maximum value of  $Nu_l$  for  $Da = 10^{-1}$  when  $Y = 0$  in case 2 is relatively greater than the equivalent value for case 1 under the same conditions. This is because the stream function value in case 2 is higher than in case 1. Another significant point that can be determined from this figure is higher values of  $Nu_l$  along the vertical left sidewall at  $Da = 10^{-5}$  over the range  $0 \leq Y \leq 0.5$  which is observed receiving more heat from the heat source in case 2 compared to case 1. Figure 4.10(a) (ii) shows that increasing  $Da$  from  $Da = 10^{-5}$ - $10^{-1}$  causes the right-hand cold sidewall to receive more heat flux from the nanofluid,

which leads to the local Nusselt number taking a more negative value. The maximum heat flux received by the right-hand side wall is at  $Y = 0$  in the case 1 while it is maximum at  $Y = 1$  in case 2. This difference is due to different delivery of the hot nanofluid by the received whole cell to the right-hand side wall. At  $Da = 10^{-5}$ ,  $Nu_r$  appears as a different behaviour as shown in the right column of Figure 4.10(a). In case 2,  $Nu_r$  is almost constant values up to  $Y = 0.3$  due to the dominance of the conductive heat transfer mode at the porous layer.  $Nu_r$  values smoothly increase when  $Y > 0.3$  with maximum values at the top portion of the right-hand cold wall due to the high convective heat transfer inside the enclosure.

Figure 4.10(b) shows the effect of  $K_r$  on the local Nusselt number along the left and right walls of the enclosure for case 1 and 2, as shown respectively in the left (i) and the right (ii) columns of the figure at  $Ra = 10^6$ ,  $Da = 10^{-3}$ ,  $\phi = 0.1$  and  $S = 0.3$ . The upper panel plot of left column of Figure 4.10(b) (i) depicts the effect of  $K_r$  on  $Nu_l$  along the left-hand hot wall. The trend for  $Nu_l$  is similar in behaviour to that of the effects of  $Da$  due to the linearly heated left-hand wall. Increasing  $K_r$  value results in a decrease in the heat transfer rate that results from the dominance of the conductive heat transfer along the left-hand heated wall up to the upper part of the heated wall with a negative value of  $Nu_l$ . The negative value of  $Nu_l$  implies the heat transfer to the left wall that results from the presence of the secondary cell. In case 2,  $Nu_l$  behaves in a similar manner to the variation for case 1 except at the top of the left wall due to the higher density of the isotherm lines for case 2 compared to case 1 (see the lower panels of Figure 4.5(d)-(f) and Figure 4.7(d)-(f)). The upper panel plot of Figure 4.10(b) (ii) in the right column represents the variation of  $Nu_r$  for case 1 along the right-hand cold wall at  $Ra = 10^6$ ,  $Da = 10^{-3}$ ,  $\phi = 0.1$  and  $S = 0.3$  for different  $K_r$ . The largest negative values for  $Nu_r$  are located at the bottom section of the right wall especially at the high value of  $K_r$ . This is due to the moving of the main cell centre location at the lower part of the right-hand side wall.  $Nu_r$  increases at the high values of  $K_r$ , in negative values, while  $Nu_l$  increases in positive values at the low values of  $K_r$ . This is because, at the high value of  $K_r$ , the density of the isotherms is higher along the right-hand cold wall, while the density of isotherms along the left heated side wall is higher at the low value of  $K_r$  as shown in Figure 4.5(d) and Figure 4.5 (f). The oscillatory behaviour of  $Nu_r$  at  $K_r = 100$  may stem from the effect of the plume of nanofluid at  $Y = 0.5$  towards the right wall affecting thermal boundary layer along the

right-hand cold wall (see Figure 4.5(f)). In case 2 (lower panel of the right column of Figure 4.10(b)), under the same conditions and compared with case 1, the maximum values of  $Nu_r$  appear at the top portion of the right-hand side wall, while there is a relatively constant  $Nu_r$  at  $Y < 0.3$  for different  $K_r$  values. This is due to the porous layer effects on the isotherm distribution along the wall which stems from the dominance of the conductive heat transfer (see Figure 4.7(d)-(f)). However, it is interesting to note that,  $Nu_r$  in case 2 has a greater value with a significant increase at the upper of the right wall compared to case 1. This may be attributed to the main cell in case 2 having a greater elongation along the right-hand cold wall and greater penetration into the porous layer than for case 1. In addition, due to the horizontal arrangement of the porous layer under the nanofluid layer, convective heat transfer is still dominant in the nanofluid layer, with greater penetration through the porous layer for different  $K_r$  values compared to case 1. This is due to the greater amount of heat received from the heat source for case 2 than that in case 1.

### 4.3.5 The average Nusselt number, $Nu_{av}$

The average Nusselt number is computed by the following equation

$$Nu_{av} = \int_0^1 Nu_{local} dY \quad (4.9)$$

Figure 4.11 shows the variation of the average Nusselt number  $Nu_{av}$  versus  $Ra$  in (a) case 1 and (b) case 2 for different values of (i)  $S$  and (ii)  $K_r$ . It seems that  $Nu_{av}$  increases with  $Ra$  for both case 1 and case 2, regardless of other parameters. Figure 4.11(a) (i) shows the relationship between  $Nu_{av}$  and  $Ra$  for various  $S$  values in case 1 as  $Da = 10^{-5}$ ,  $\phi = 0.1$  and  $K_r = 1$ . Increasing  $S$  reduces  $Nu_{av}$  for the same  $Ra$ . This is because at higher values of  $S$ , the resistance area of the porous matrix increases, which leads to a reduction of convective heat transport within the porous layer compared to the nanofluid layer. The  $Nu_{av}$  is almost constant at  $Ra \leq 10^4$  due to dominant effect of the conductive heat transfer regardless of the porous layer thickness, implying there is no effect on the global  $Nu_{av}$  for values of  $Ra$  up to  $10^4$  for both case 1 and case 2 as shown in Figure 4.11(b) (i). At a constant value of  $S$ , it is interesting to note that,  $Nu_{av}$  is higher for case 2 than case 1, indicating that the heat transfer rate for case 2 is greater than for case 1. This stems from the fact that the higher intensity of the streamlines and denser isotherms along the

vertical walls with more widely spaced horizontally- running isotherm lines at the upper region of the enclosure, as shown in Figure 4.6(a)-(c) and Figure 4.4(a)-(c), respectively.

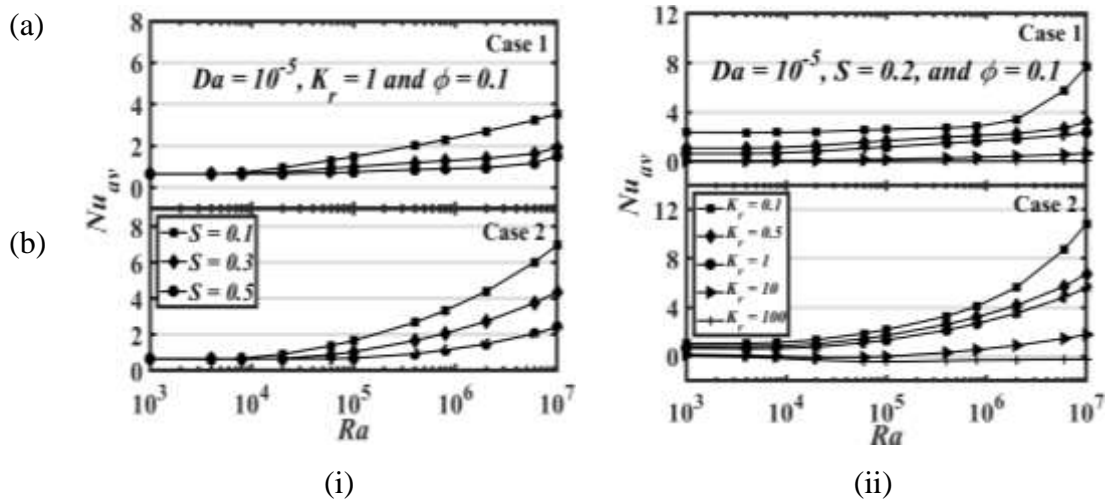


Figure 4.11: Variation of the average Nusselt number versus  $Ra$ , (a)  $S$  effect and (b)  $K_r$  effect. In each plot, the upper panel corresponds to case 1, and the lower panel corresponds to case 2.

Figure 4.11(a) (ii) shows the variation of heat transfer rates versus  $Ra$  along the left-hand heated wall in case 1 as  $Da = 10^{-5}$ ,  $S = 0.2$ , and  $\phi = 0.1$  for different  $K_r$  values. Increasing  $K_r$  increases the convective heat transfer monotonically with  $Ra$ . At  $Ra = 10^7$ , a significant increase in  $Nu_{av}$  for all values of  $K_r$  was found in case 2 compared to case 1 as shown in Figure 4.11(b) (ii), indicating the importance of the porous-nanofluid layer arrangement in the vertical or horizontal direction to heat transfer enhancement inside the enclosure.

Figure 4.12 shows the average Nusselt number versus (i) the Darcy number and (ii) the porous layer thickness for different parameter values for (a) case 1 and (b) case 2. Figure 4.12(i) shows the average Nusselt number versus  $Da$  as  $\phi = 0.1$  and  $K_r = 1$  for  $S = 0.1$ , 0.3 and 0.5. For case 1 shown in Figure 4.12(i) (a), at the highest value of  $Ra$  used in the present study ( $Ra = 10^7$ ), the effect of the porous layer thickness becomes not significant at  $Da > 10^{-3}$ , indicating that the porous layer behaves as a nanofluid layer and that the porous matrix essentially has no effect on the flow circulation.  $Nu_{av}$  decreases suddenly with decreasing  $Da$  values from  $Da = 10^{-3}$  to  $10^{-5}$  due to the decrease in permeability of the porous layer, though this decline is lower at lower  $S$  values. This is because increasing the porous layer thickness increases the flow resistance area produced by the porous layer itself. At values of  $< 10^{-5}$ ,  $Da$  has no effect on heat transfer rate for each

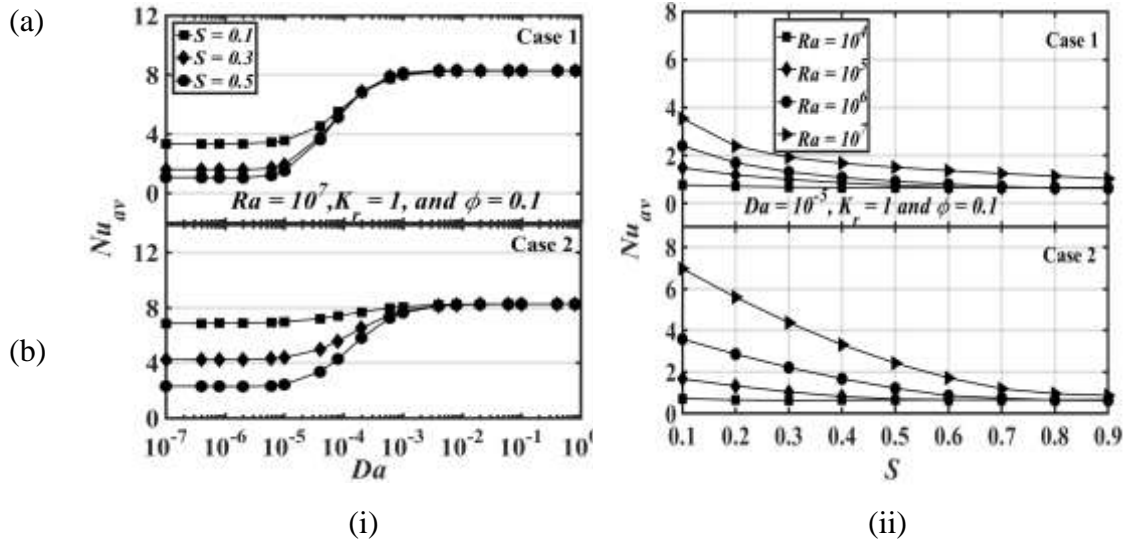


Figure 4.12: Variation of the average Nusselt number with (a)  $Da$  number for different  $S$  and with (b) porous layer thickness  $S$  for different  $Ra$ . In each plot, the upper panel corresponds to case 1, and the lower panel corresponds to case 2.

value of  $S$ . For case 2 shown in Figure 4.12(i) (b), it is interesting to observe that,  $Nu_{av}$  at  $Da = 10^{-3}$  for case 1 is higher than that for case 2 for all values of  $S$ . At  $Da < 10^{-3}$ , there is a differential decrease of  $Nu_{av}$  with more effect of changing  $S$  values compared to case 1 at  $10^{-5} \leq Da \leq 10^{-3}$ . This pattern causes  $Nu_{av}$  to show a lower drop of heat transfer for case 2 than case 1, especially at low Darcy numbers,  $Da < 10^{-3}$ , for each value of  $S$ , indicating the effect of the porous-nanofluid layer direction.

Plots of the average Nusselt number versus  $S$  are used to illustrate the effect of  $S$  on the heat transfer rate at various values of  $Ra$ , as shown in Figure 4.12(ii) in (a) case.1 and (b) case 2. Figure 4.12(ii) (a) illustrates the effect of  $Ra$  for  $Da = 10^{-5}$ ,  $\phi = 0.1$  and  $K_r = 1$  for case 1. A higher value of  $Ra$  results in a higher rate of heat transfer. For a given  $Ra$ , the fluid flow resistance increases with increasing  $S$ , which leads to reducing the convection and results in a lower value of  $Nu_{av}$ . For  $Ra = 10^5$ , the convective heat transfer mode was almost entirely suppressed when  $S \geq 0.6$ , while there is no effect of  $S$  at  $Ra = 10^4$ . In case 2 shown in Figure 4.12(ii) (b), the enhancement in heat transfer rate is more pronounced for case 2 compared to case 1, especially at  $S = 0.1$  for different values of  $Ra$ .

Figure 4.13 illustrates the variation of the average Nusselt number with logarithmic values of (a) the Rayleigh number and (b) the Darcy number for case 1 and case 2 when  $Da = 10^{-3}$ ,  $S = 0.3$ ,  $\phi = 0.1$ , and  $K_r = 0.1$ .  $Nu_{av}$  increases with increasing  $Ra$  in both

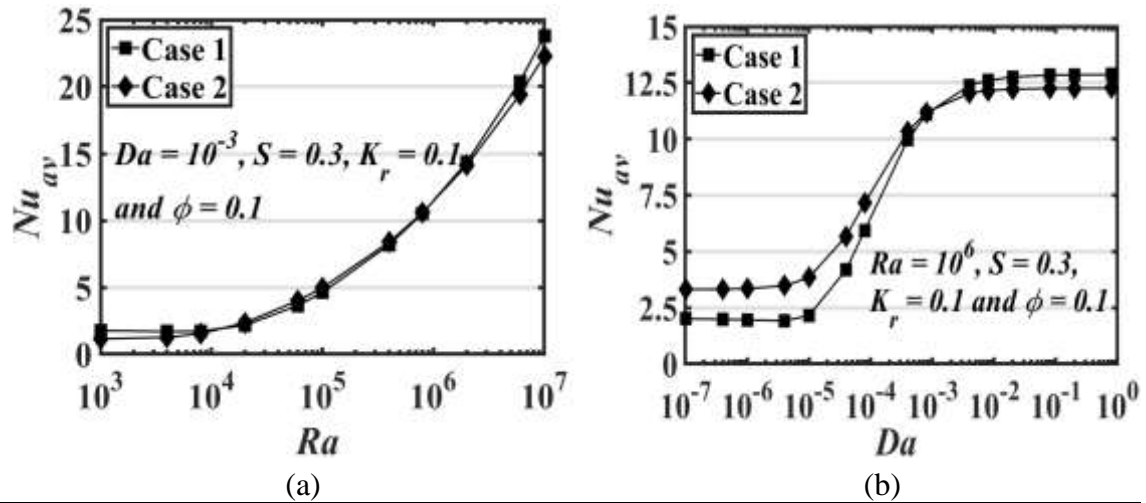


Figure 4.13: Variation of the average Nusselt number with (a)  $Ra$ , and (b)  $Da$ , for case 1 and case 2 with linear heating on the left vertical sidewall.

cases, as shown in Figure 4.13(a). At  $Ra > 10^6$  and  $Ra < 10^4$ ,  $Nu_{av}$  values for case 1 are greater than in case 2, while the opposite behaviour is seen for  $10^4 \leq Ra \leq 10^6$ . Figure 4.13(b) illustrates the variation of the average Nusselt number with  $Da$  as  $Ra = 10^6$ ,  $S = 0.3$ ,  $\phi = 0.1$ , and  $K_r = 1$  for case 1 and case 2. At  $Da > 10^{-3}$ ,  $Nu_{av}$  for case 1 is greater than for case 2, whereas the opposite pattern, with relatively higher changes to the Nusselt number, is shown when  $Da < 10^{-3}$ . In general, at low values of  $Da$ ,  $Nu_{av}$  for case 2 is greater than for case 1, while the opposite is seen at higher values of  $Da$ .

#### 4.4 Conclusions

This study analysed the flow and heat transfer due to natural convection within square enclosures with either a vertical or a horizontal porous slab. The nanofluid is composed of water-based fluid containing Cu nanoparticles. Case 1 corresponds to a vertical slab, while case 2 corresponds to a horizontal slab. In case 1, the porous layer is positioned on the left of the enclosure while it is located at the bottom of the enclosure for case 2. In both cases, a linearly decreasing temperature is applied to the left vertical wall of the enclosure while the right vertical wall is isothermally cooled; the horizontal walls are kept insulated. The results have been obtained in terms of streamlines, isotherms and heat transfer rate. Some of the important conclusions can be summarised as follows:

- Due to the linearly heated left-hand wall and the cold right-hand wall of the enclosure, two regions of flow circulation were observed, made by a main cell rotating in the clockwise direction, covering most of the enclosure area, and by a

secondary cell rotating in the anticlockwise direction in the upper left corner of the enclosure.

- Higher values of  $S$  are predicted to provide lower Nusselt number in case 1 compared to case 2 for different  $Ra$  and  $K_r$  values and at  $Da < 10^{-3}$ .
- Increasing  $Ra$  caused the intensity of the streamlines in case 2 to be stronger than in case 1.
- Lower values of the thermal conductivity ratio,  $K_r$  imply greater heat transfer enhancement than for high thermal conductivity ratios.
- The variation of the rate of heat transfer with  $Ra$  showed that when  $Da = 10^{-3}$ ,  $S = 0.2$ ,  $\phi = 0.1$ , and  $K_r = 0.1$  at  $Ra > 10^6$  and  $Ra < 10^4$ ,  $Nu_{av}$  values for case 1 were greater than for case 2, though the opposite behaviour was observed for  $10^4 \leq Ra \leq 10^6$ , indicative of the importance of the alignment of the porous-nanofluid layers in either the vertical or horizontal direction.
- At the low values of  $K_r$ ,  $Nu_{av}$  was more enhanced for case 2 compared to case 1 at the low values of Darcy number  $Da < 10^{-3}$  whereas the opposite behaviour of  $Nu_{av}$  was observed for high values of  $Da$ . This indicates the importance of the alignment of the porous-nanofluid layers in either the vertical or the horizontal direction.

In general, the effects of the porous slab direction, the Rayleigh number, the Darcy number, the thermal conductivity ratio (porous/ nanofluid), the porous slab thickness, and the nanoparticles volume fraction with the linear thermal boundary condition played an important role in the flow and heat transfer inside the enclosure that filled partly by a porous slab saturated with a nanofluid in a vertical and a horizontal direction. At low values of the thermal conductivity ratio (porous to nanofluid),  $K_r < 1$ , the heat transfer inside the enclosure increased at high values of Darcy number for the vertical direction of the porous slab, while it increased at the low values of the Darcy number for the horizontal direction of the porous slab. The results presented a new trend of the fluid flow and heat transfer inside the enclosure under the effect of the linearly thermal boundary condition on the left sidewall of the enclosure. The porous slab in a vertical or a horizontal direction played a vital role in the heat transfer. It may be interesting for the designer in the modern technology of the industrial engineering applications.

## **Chapter 5: Effects of a Sinusoidally Heated Left Wall on Natural Convection within an Enclosure Filled with Composite Nanofluid-Porous Layers**

### **5.1 Motivation and introduction**

The sinusoidal thermal boundary condition may cause a problem in the thermal management in the system. The governing equations are coupled together linked to the buoyancy force effect. In addition, the alignment of the porous slab in a vertical or horizontal direction with the selected boundary condition may play an important role on the convective heat transfer. Therefore, it is necessary to investigate the effects of the sinusoidal thermal boundary condition and the porous medium alignment to predict the thermal control inside the enclosure. The sinusoidal thermal boundary condition produces a different trend of the flow and heat transfer inside an enclosure partly filled by a porous slab compared to the enclosures that were used in the previous literature. A new simulation results are presented to develop the convective heat transfer inside an enclosure partly filled by a porous slab rather than that of using a porous enclosure under the sinusoidal thermal boundary condition on one side of the enclosure. To the best of the author's knowledge, there was no investigation focused on the natural convection in a square enclosure filled by a vertical or horizontal orientation of the nanofluid-superposed porous layers with sinusoidal heating on the left-hand vertical sidewall. This investigation of the present study may be interested to the designer to predict the convective heat transfer in the next modern industry technology.

Accordingly, this chapter explores by Computational Fluid Dynamics (CFD) the effects of the sinusoidal heating of the left-hand vertical sidewall on the natural convection within a two-dimensional enclosure partially filled by either a vertical or a horizontal porous slab saturated by nanofluid. Two slab orientations are considered, a vertical (case 1) and a horizontal (case 2) configuration. Sinusoidal heating is applied to the left-hand vertical sidewall of the enclosure while a uniform cold temperature is imposed at the right-hand vertical sidewall; the horizontal walls are adiabatic. The range of the heat transfer controlling parameters tested in the present study are: For the Rayleigh number ( $Ra$ ),  $10^3 \leq Ra \leq 10^7$ , the Darcy number ( $Da$ ),  $10^{-7} \leq Da \leq 1$ , the porous layer thickness ( $S$ ),  $0.1 \leq S \leq 0.9$ , the thermal conductivity ratio of the porous medium and

nanofluid ( $K_r$ ),  $0.1 \leq K_r \leq 100$ , the thermal wave number ( $N_{th}$ ),  $1 \leq N_{th} \leq 7$ , the thermal amplitude ( $A_{th}$ ),  $0.2 \leq A_{th} \leq 1$  and the nanoparticle volume fraction ( $\phi$ ),  $\phi = 0.2$ .

## 5.2 A model problem

### 5.2.1 Physical model

The study of the effects of non-uniform heating on the natural convection inside a two-dimensional square enclosure, two cases are defined, as shown schematically in Figure 5.1. Vertical and horizontal alignments of the porous slab were considered for case 1 and case 2, respectively. In case 1, the porous layer is towards the left, and the nanofluid layer is towards the right enclosure. In case 2, the porous layer is under the nanofluid layer. The thicknesses of the porous and nanofluid layers are  $S$  and  $L - S$ , respectively. The differentially heated on the vertical walls causes to develop the fluid flow inside the enclosure due to the horizontal temperature difference. This causes to occur that the density gradient (due to temperature gradient) is horizontal and the gravity vector acts perpendicularly, where the circulation inside the enclosure depends on these vector orientation. The dimensionless governing equations describing the fluid flow and heat transfer inside the nanofluid, and porous layers as shown in Appendix B.1 (equations B1.1-B1.8). The nanofluid consists of water as a base fluid ( $Pr = 6.26$ ) and Cu nanoparticles with  $\phi = 0.2$  with thermal properties are given in Table 3.1.

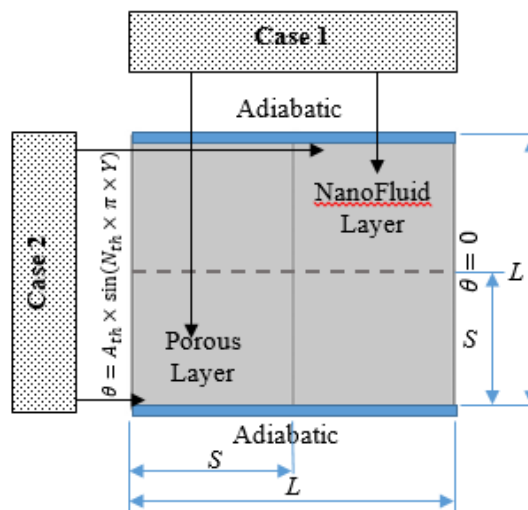


Figure 5.1: Physical domain of vertical (case 1) and horizontal (case 2) directions of the composite nanofluid-porous medium layers.

### 5.2.2 Boundary conditions

The dimensionless governing equations are applied in these cases and the boundary conditions for each case (vertical and horizontal orientation of the porous medium – nanofluid layers) are:

$$\text{At the left hot wall } U = V = 0, \theta = A_{th} \cdot \sin(N_{th} \cdot \pi \cdot Y) \quad (5.1)$$

$$\text{At the right cold wall } U = V = 0, \theta = 0 \quad (5.2)$$

$$\text{At the top and bottom insulated walls } U = V = 0, \frac{\partial \theta}{\partial Y} = 0 \quad (5.3)$$

where

$$X = \frac{x}{L}, Y = \frac{y}{L}, U = \frac{uL}{(\alpha)_{bf}}, V = \frac{vL}{(\alpha)_{bf}}, \theta = \frac{T-T_c}{T_h-T_c} \quad (5.4)$$

These boundary conditions may be occurred in a significant number of engineering applications, such as solar collector systems and the cooling of electronic components (Sivasankaran and Bhuvaneshwari, 2013).

### 5.2.3 Grid independence test

Figure 5.2 shows the meshes of (a) case 1 and (b) case 2. The domain walls and the interface line between the porous and fluid layers were refined to capture the flow state with greater spatial resolution as shown in Figure 5.2(c). The dependence of the prediction on the spatial resolution was tested on 6400, 10,000, 14,400, 16,900, 19,600

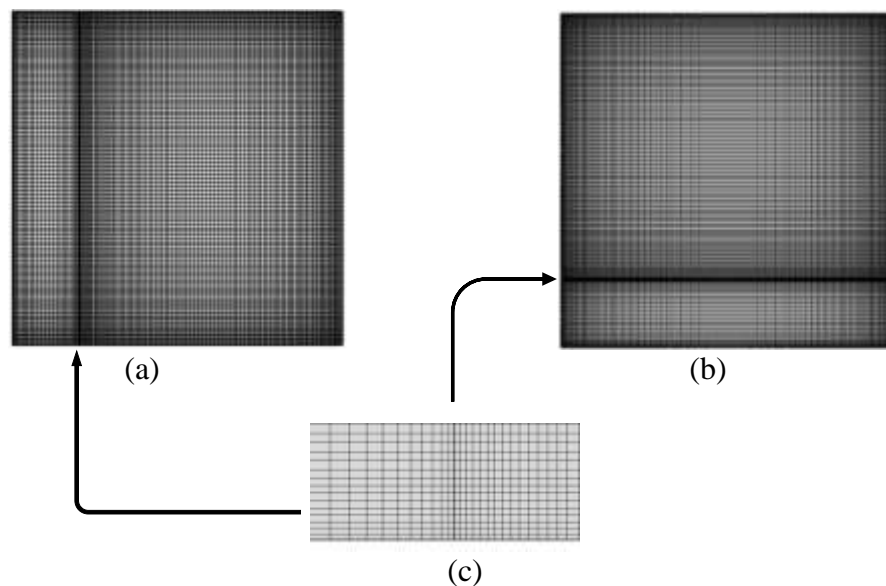


Figure 5.2: Computational mesh of the physical domain for (a) Case 1, (b) Case 2, and (c) Refined mesh.

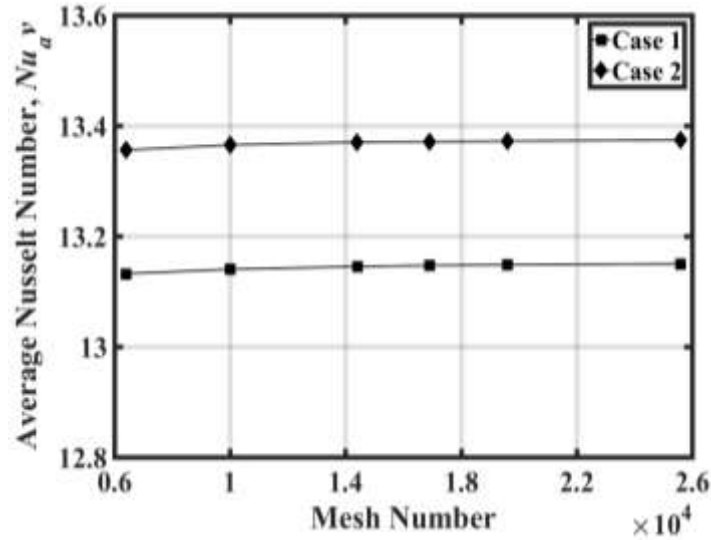


Figure 5.3: Grid testing for the average Nusselt number at different mesh numbers.

and 25,600 grid sizes. The average Nusselt number for cases 1 and 2 at  $Ra = 10^7$ ,  $Da = 10^{-3}$ ,  $K_r = N_{th} = A_{th} = 1$ ,  $\phi = 0.2$  and  $S = 0.2$  on these meshes is shown in Figure 5.3. A grid size of 16,900 was adopted in all cases reported here because this mesh produced an almost identical result for the average Nusselt number as that from the largest two mesh numbers.

## 5.3 Results and discussion

### 5.3.1 Streamlines and isotherms

#### 5.3.1.1 Vertical porous - nanofluid layers (case 1)

The streamlines and isotherms for the vertically porous slabs at different values of  $S$ ,  $Ra$ ,  $Da$ ,  $K_r$ ,  $A_{th}$ , and  $N_{th}$  are presented in Figure 5.4 – 5.7. Water (solid lines) and nanofluid (dashed lines) convective heat transfer was simulated under the sinusoidal temperature distribution on the left sidewall and the isothermal cold temperature on the right sidewall of the enclosure of section 5.2.2. Figure 5.4(a)-(c) shows the predictions for  $S = 0.1, 0.2$  and  $0.5$  at  $Ra = 10^6$ ,  $Da = 10^{-3}$  and  $K_r = A_{th} = N_{th} = 1$ . The streamlines (upper row) show, two regions of circulation inside the enclosure due to the applied boundary conditions. The flow inside the porous layer rises along the left hand heated vertical sidewall due to buoyancy, whilst the flow descends along the right cooled wall in the fluid layer. This generates a strong main vortex with a clockwise flow direction that covers most of the enclosure and a weak secondary cell with an anticlockwise flow direction located in the

upper left-hand corner. At  $S = 0.1$  and  $0.2$ , the main flow circulation cell has two poles with both the base fluid and the nanofluid. These poles are located in the fluid layer. One pole is close to the interface line and the other pole is close to the right cold wall. As  $S$  increased to  $S = 0.5$ , the main cell loses the left pole and only one pole is detected close to the right cold wall. In addition, the clustering of streamlines for both the base fluid and the nanofluid decreases with increasing porous layer thickness. Adding 20% of copper nanoparticles by volume to the base fluid for  $S = 0.1, 0.2$  and  $0.5$  at increases the stream function strength of the primary cell, as shown by changes in  $\Psi_{min}$  of almost 26.5%, 21.25% and 17.45%, respectively. This is attributed to a greater thermal conductivity of the nanofluid compared to the single-phase fluid. The gain reduces with increasing porous layer thickness, due to the flow resistance of the porous layer. The predicted isotherms (lower row of Figure 5.4(a)-(c)), with the single-phase fluid and nanofluid run parallel to the right cold wall, while they turn away from the left-hand heated sidewall at  $0.4 \leq Y \leq 0.6$  due to the non-uniform left wall temperature. The isotherms close along the vertical walls due to the strength of the main circulation cell. The horizontal pattern of the isotherms in the enclosure centre indicates horizontal heat convection within the fluid layer, while the diagonal pattern in the porous layer indicates a buoyancy current dominated heat convection.

Figure 5.4(d)-(f) shows the predicted streamlines and isotherms for the configuration with a vertical porous slab (case 1) at  $Ra = 10^4, 10^5$ , and  $10^7$ ,  $Da = 10^{-3}$ ,  $S = 0.2$  and  $K_r = A_{th} = N_{th} = 1$ . It may be seen from this figure that fluid circulation is strongly dependent on the Rayleigh number. In Figure 5.4(d) at  $Ra = 10^4$ , the centre of the convective cells (with a semi-circular shape) for both the single-phase fluid and nanofluid is almost at the centre of the nanofluid layer, both the same cells size, and having essentially circulation pattern. The circulation strength of the single-phase fluid is stronger than the nanofluid. This is attributed to the low value of the Rayleigh number, where the addition of nanoparticles made the fluid more viscous, resulting in a reduction in the circulation intensity. As the Rayleigh number increases, the strength of the streamlines significantly increases due to the large buoyancy force that causes the main cells to stretch along the enclosure walls. A strengthened primary cell covers the majority of the enclosure area while a comparatively weakness secondary cell is located at the upper left corner of the enclosure. The addition of 20% nanoparticles by volume to the

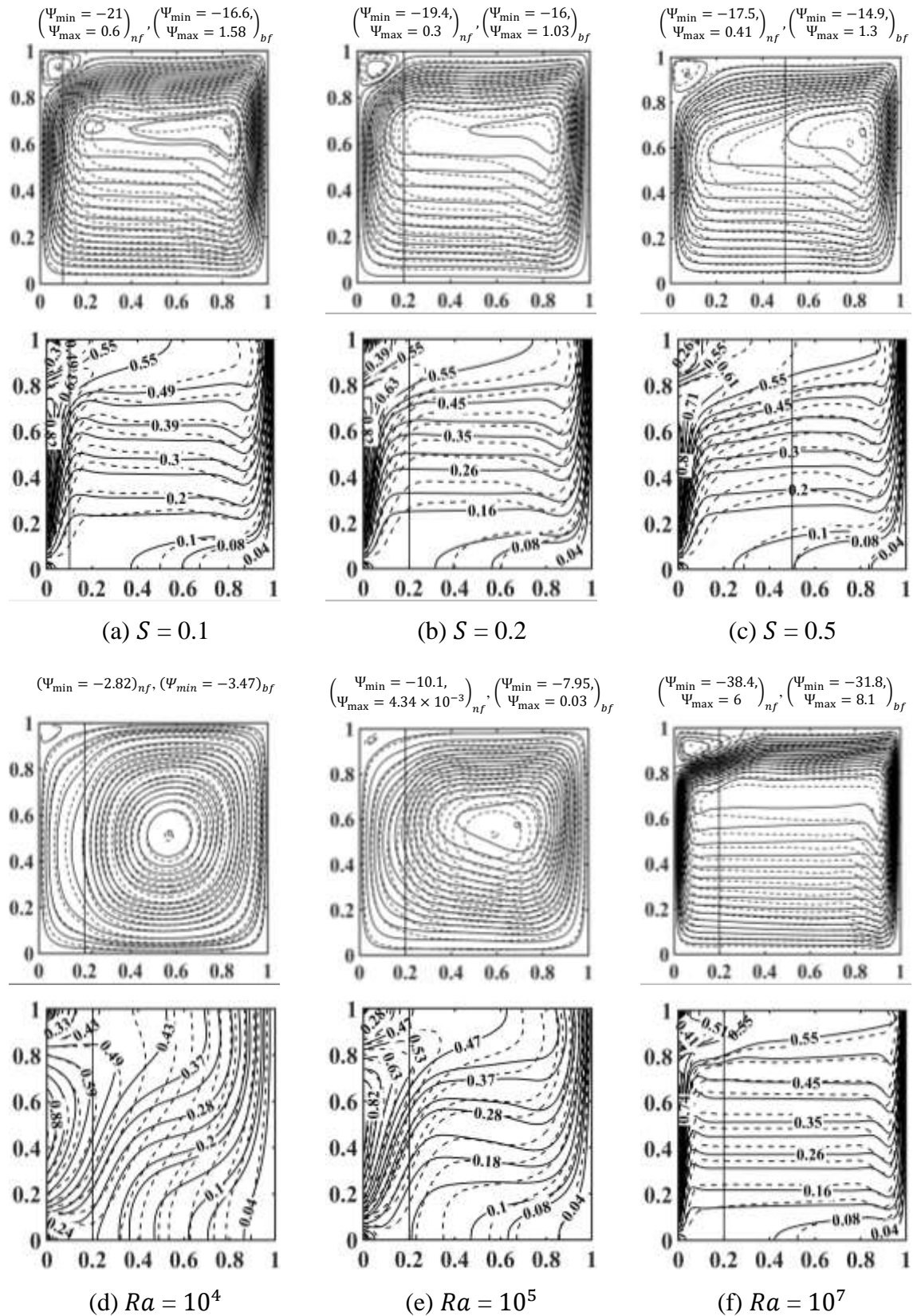


Figure 5.4: Streamlines (upper row) and isotherms (lower row) for case 1 with  $\phi = 0$  (solid lines) and  $\phi = 0.2$  (dashed lines) at different dimensionless parameters, (a-c)  $S$  effect when  $Ra = 10^6$ ,  $Da = 10^{-3}$ , and  $K_r = N_{th} = A_{th} = 1$ , (d-f)  $Ra$  effect when  $Da = 10^{-3}$ ,  $S = 0.2$  and  $K_r = N_{th} = A_{th} = 1$ .

single-phase fluid led to an improvement in the circulation cell strength at  $Ra$   $10^5$  and  $10^7$ , with gains of almost 27% and 20.7%, respectively, in the magnitude of  $\Psi_{min}$ . The difference in the gain with increasing  $Ra$  is due to the lower buoyancy force acting on the single-phase fluid and the nanofluid at  $Ra = 10^5$  as compared with  $Ra = 10^7$ . The increasing intensity of the circulation with increasing Rayleigh number causes the compression of the isotherms close to the vertical walls and the transition from a diagonal orientation of the isotherms at low  $Ra$  to a horizontal orientation of the isotherms at higher  $Ra$ . The horizontal isotherms occurred at the centre zone of the enclosure. The isotherms close to the left wall have greater variation in orientation compared to those near the right wall due to the sinusoidal heating applied at the left wall. The thickness of the thermal boundary layer close to the vertical walls is shown to reduce with increasing  $Ra$ . This gives an indication that the heat transfer by convection strengthens with increasing  $Ra$ .

The effect of the dimensionless permeability parameter (Darcy number) on the streamlines and isotherms for case 1 at  $Ra = 10^6$ ,  $S = 0.2$  and  $K_r = A_{th} = N_{th} = 1$  is illustrated in Figure 5.5(a) and (b) for Darcy numbers  $Da = 10^{-5}$  and  $Da = 10^{-1}$ , respectively. With both the single-phase fluid and the nanofluid, the strength of the stream function increases, as  $Da$  increases. The flow inside the porous layer is driven by the hot portion of the left wall, which heats up the flow along the vertical left sidewall and induces an upwards natural convection stream. There is a comparably lower penetration of the fluid within the porous layer at the low  $Da$  value. The flow then turns downwards along the cooled right sidewall in the nanofluid layer, generating a strong clockwise main vortex covering most of the enclosure area. The fluid at the upper and lower left corners stagnate. There is a change in the main cell centre between the single-phase fluid and the nanofluid as this is lower with the nanofluid. At  $Da = 10^{-3}$ , as shown in Figure 5.4(b), the main vortex extends towards the vertical walls with greater intensity in its stream function. A second pole forms near the left wall. In addition, a weak secondary cell appears at the upper left corner of the enclosure in which the stream function magnitude with the base fluid is greater than that with the nanofluid. Using the nanofluid, the maximum value of the stream function  $\Psi_{min}$  was 24.5 while  $\Psi_{min}$  was 19.2 with pure water. The isotherms show that at the low value of  $Da$ , the clustering of the isotherms along the left hand heated vertical sidewall is lower than that at the right hand cold vertical

sidewall. This is due to the flow resistance in the porous layer from the low  $Da$  value. In addition, the difference in the isotherm lines between the nanofluid and base fluid is more pronounced around the centre zone of the enclosure for the low  $Da$  value compared to the high  $Da$  value. A significant augmentation of the convective heat transfer is predicted for the higher  $Da$  value, which is steeper indicated by isotherms close to the vertical sidewalls and by more horizontal isotherm lines at the enclosure centre.

Figure 5.5(c)-(e) illustrates the influence of the thermal conductivity ratio on the flow and heat transfer within the enclosure for case 1 with non-uniform heating at the left sidewall at  $Ra = 10^6$ ,  $Da = 10^{-3}$ ,  $S = 0.2$  and  $A_{th} = N_{th} = 1$ . At  $K_r = 0.1$ , a large clockwise circulating cell is centred in the fluid layer. This covers the majority of the enclosure area with a comparatively high penetration within the porous layer. A relatively weaker secondary cell, with an anticlockwise flow direction, is confined to the upper left corner of the enclosure. As  $K_r$  is increased, the weak secondary cell extends horizontally and compresses the main cell. This effect is more pronounced with the base fluid than with the nanofluid. This effect reduces the contact area of the main cell with the left heated sidewall. The secondary cell receives heat from the heated fluid and returns it to the upper portion of the heated wall, causing the upper part of the heated wall to act as a heat sink and thus potentially decreasing the rate of heat transfer across the whole wall. Increasing  $K_r$  causes the stream function intensity to increase, as shown by  $\Psi_{min}$ , however the streamlines are less packed on the left heated wall. Therefore, increasing the fluid flow inside the porous enclosure can be controlled by decreasing  $K_r$ . The vertical isotherm pattern on the left wall shows that the convective heat transfer takes place in the porous layer for  $K_r = 0.1$ , while at  $K_r = 5$  and  $100$ , the more concentric streamlines at  $Y = 0$  and  $Y = 1$  at  $X = 0$  indicates conductive heat transfer in the porous layer. The isotherms located near the vertical walls are denser towards the left wall and parallel in the centre zone of the enclosure at  $K_r = 0.1$ . At higher values of  $K_r$ , the isotherms tended to be vertical in the fluid layer with considerable reverse heating towards the upper and lower parts of the left heated wall.

The streamlines (upper row) and isotherms (lower row) for different temperature amplitudes  $A_{th}$  are presented in Figure 5.6(a)-(c). This figure shows the changes in the streamlines over the range  $0.1 \leq A_{th} \leq 1$  for case 1 at  $Ra = 10^6$ ,  $Da = 10^{-3}$ ,  $S = 0.2$

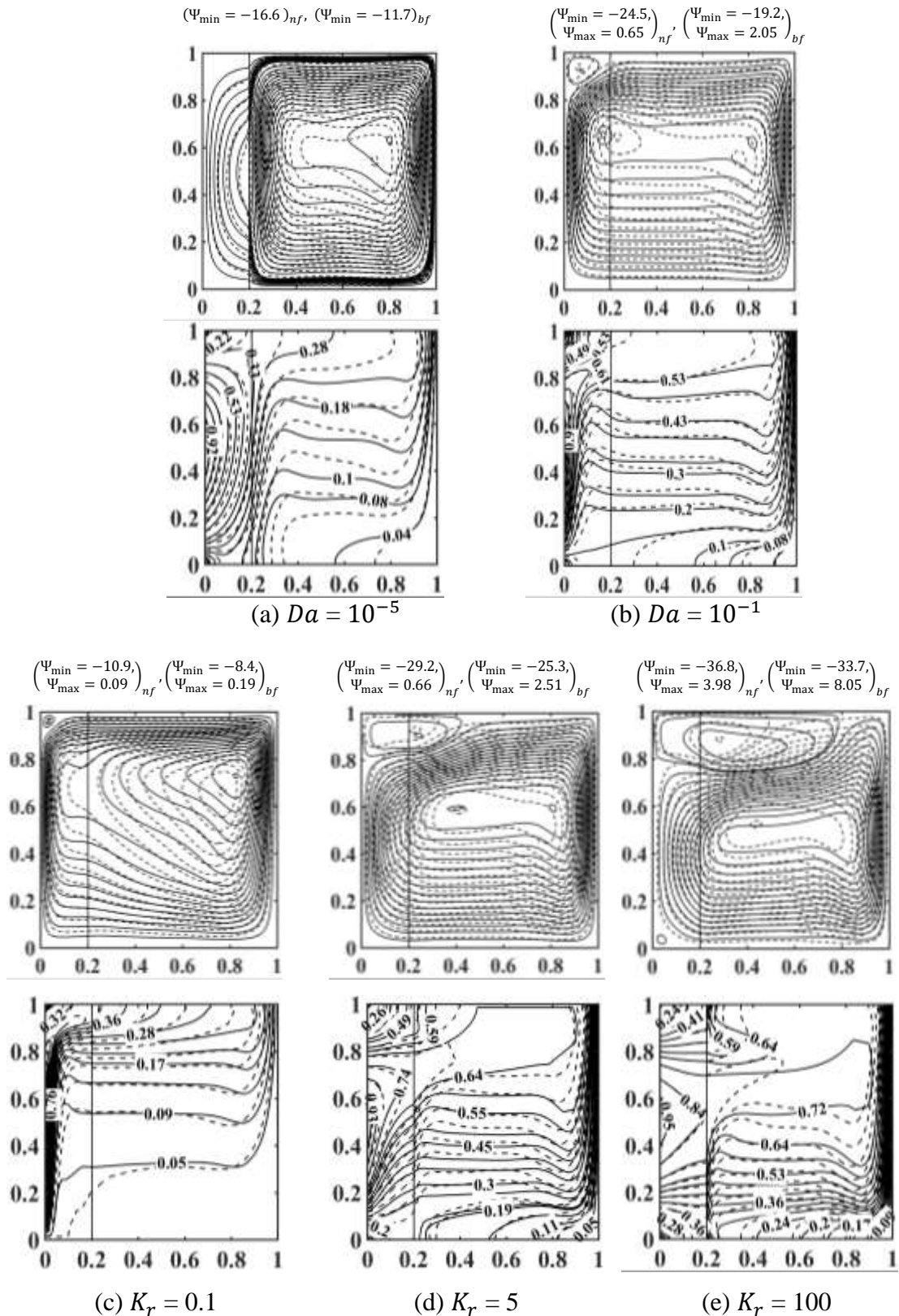


Figure 5.5: Streamlines (upper row) and isotherms (lower row) for case 1 with  $\phi = 0$  (solid lines) and  $\phi = 0.2$  (dashed lines) at different dimensionless parameters, (a-b)  $Da$  effect when  $Ra = 10^6$ ,  $S = 0.2$  and  $K_r = N_{th} = A_{th} = 1$ , and (c-e)  $K_r$  effect when  $Ra = 10^6$ ,  $Da = 10^{-3}$ ,  $S = 0.2$  and  $N_{th} = A_{th} = 1$

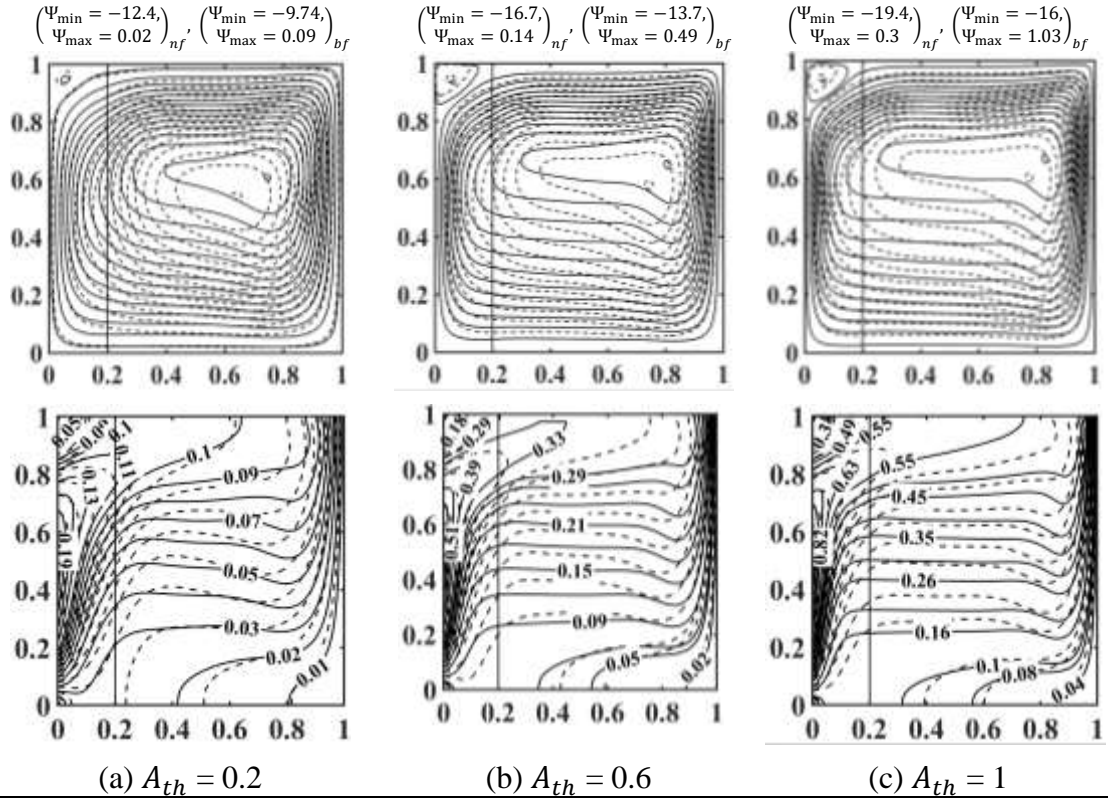


Figure 5.6: Streamlines (upper row) and isotherms (lower row) for case 1 as  $Ra = 10^6$ ,  $Da = 10^{-3}$ ,  $S = 0.2$ ,  $K_r = N_{th} = 1$ ,  $\phi = 0$  (solid lines), and  $\phi = 0.2$  (dashed lines) for different thermal amplitude  $A_{th}$  values.

and  $N_{th} = K_r = 1$ . At  $A_{th} = 0.2$ , the core centre of the nanofluid main cell with the clockwise direction is located in the fluid layer. The more negative  $\Psi_{min}$  predicted with the nanofluid indicates a higher recirculation strength than that of the base fluid due to the higher thermal conductivity of the nanofluid, which increases the buoyancy force which drives natural convection. The heat removal by the main cell from the mid-height portion of the left sidewall is constrained by a secondary circulation cell at the upper left corner of the enclosure towards the left wall. The spacing between isotherms lines near the vertical walls decreased with increasing temperature amplitude  $A_{th}$ , due to the higher heat transport by the main circulation cell. The convective heat transfer for the nanofluid was more pronounced than that for the base fluid at the centre zone of the enclosure, as indicated by the more parallel isotherms with the nanofluid. Increasing the temperature amplitude  $A_{th} = 0.2-1$  increases the heat dissipated from the heat source. This led to an increase in the fluid temperature inside the enclosure.

Figure 5.7(a)-(d) show the streamlines (upper row) and isotherms (lower row) for case 1 for different wave numbers,  $N_{th}$  at  $Ra = 10^6$ ,  $Da = 10^{-3}$ ,  $S = 0.2$  and  $A_{th} = K_r = 1$ .

At  $N_{th} = 2$ , two symmetric cells are formed in the upper and lower halves of the enclosure. The cells are approximately equal strength for both the base fluid and the nanofluid, as shown in Figure 5.7(a). The lower cell worked to remove heat from the wall while the upper cell returned the heat into the left wall. Different locations of the streamlines core centres of the base fluid and nanofluid cells appeared in the nanofluid layer. The core centres of the nanofluid cells are located at around (0.5, 0.3) and (0.5, 0.7) for the lower and upper cells, respectively, while the core centre of the base fluid is located at around (0.7, 0.3) and (0.7, 0.7) for the same cells. The circulation of the nanofluid cells was marginally more intense than that of the base fluid cells, as indicated by the more negative  $\Psi_{min}$ . At  $N_{th} = 3$  and 4, the strength of the circulatory flow of the nanofluid decreases, while it increases for the base fluid. This implies that the non-uniform heating affects the base fluid differently than the nanofluid. At  $N_{th} = 3$ , a non-symmetrical tri-cellular flow structure appears, as shown in Figure 5.7(b). The upper cell stretches into the upper part of the enclosure, while almost symmetrical-looking cells appears in the bottom and middle of the enclosure. In agreement with previous situations regarding the odd and even numbers of the periodicity parameter (Deng and Chang, 2008),  $N_{th}$  produces symmetrical cells for even integer values of  $N_{th}$  and asymmetric cells for odd integer values of  $N_{th}$ . An irregular pattern within the fluid inside the enclosure is generated at  $N_{th} = 7$ . At  $N_{th} = 7$ , Figure 5.7(d) shows a multi-cellular flow along the left heated wall within the porous layer. Elsewhere, two cells of clockwise and anti-clockwise flow directions, respectively, are predicted in the base fluid, while one large clockwise cell is predicted in the nanofluid within the fluid layer. Generally, increasing  $N_{th}$  causes the stream function strength to decrease. The isotherms are shown in the lower row of Figure 5.7(a)-(d). The common behaviour of the isotherms depends on the value of the periodicity parameter, which turn determines the number of circulation cells inside the enclosure. The temperature distribution is broadly symmetric when the periodicity parameter is an even number, while the temperature distribution is asymmetric for odd values of  $N_{th}$ . The temperature distribution on the right vertical sidewall for the even values of  $N_{th}$  is uniform and equal to zero, while the left wall has a symmetric temperature distribution with multiple temperature maxima, due to the non-uniform heating. In contrast, when  $N_{th}$  is odd, an asymmetric distribution of the

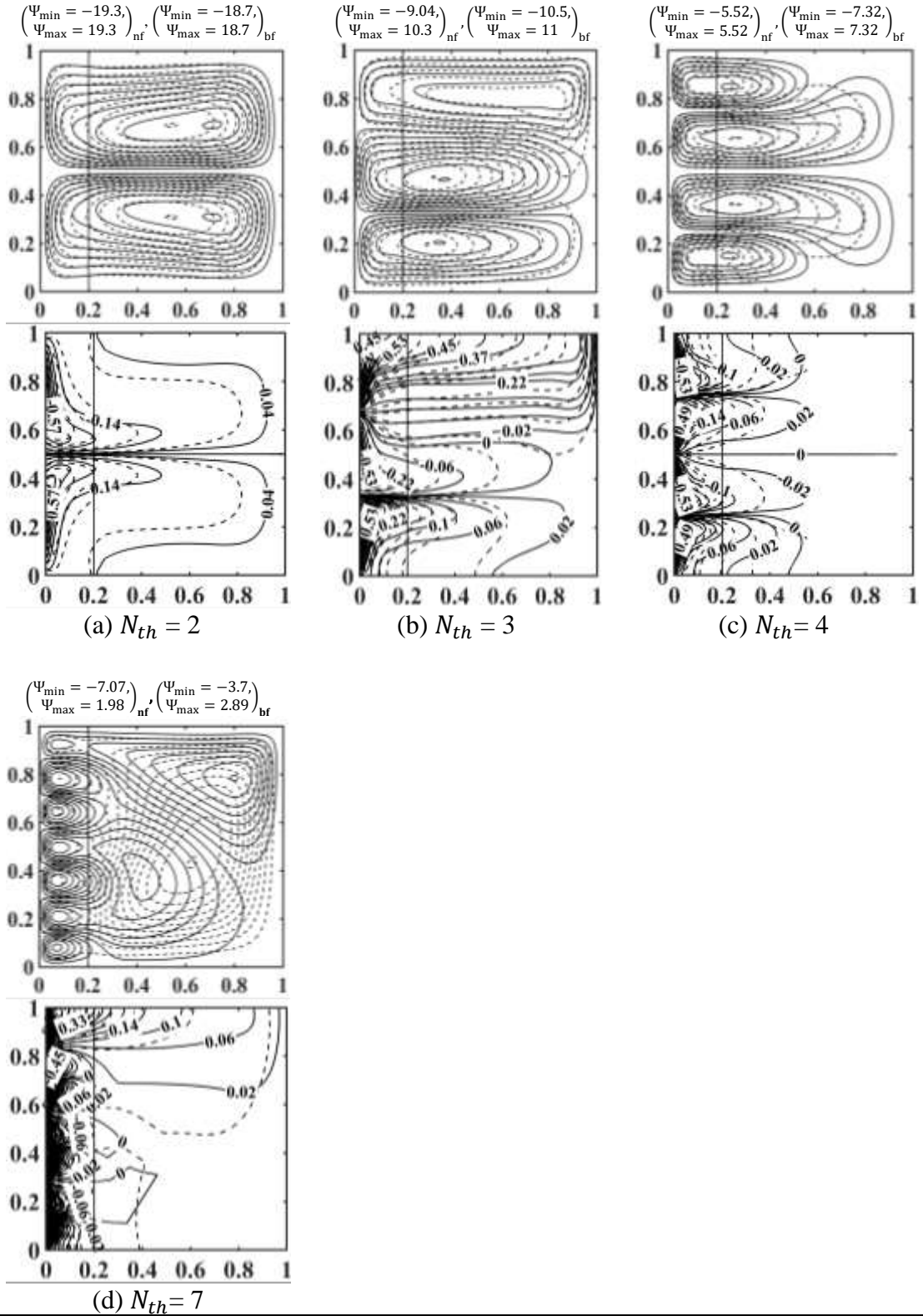


Figure 5.7: Streamlines (upper row) and isotherms (lower row) for case 1 as  $Ra = 10^6$ ,  $Da = 10^{-3}$ ,  $S = 0.2$ ,  $K_r = A_{th} = 1$ ,  $\phi = 0$  (solid lines), and  $\phi = 0.2$  (dashed lines) for different thermal frequency  $N_{th}$  values.

isotherms is predicted towards the left wall, while a cluster of vertically aligned isotherm lines are located around the upper section of the right wall. This cluster weakens between  $N_{th} = 5$  and  $N_{th} = 7$ . Heat is exchanged between the heated and cooled portions of the heated wall at the even values of  $N_{th}$ . The heat received from the hot portion was equal to the heat returned to the cold portion of the active wall of the enclosure. This was because the heat received by the cold fluid from the hot portion of the wall will return via the hot fluid towards the cold portion of the same wall. The asymmetric distribution of isotherms at odd numbers of  $N_{th}$  indicates a positive net heat output to the right wall.

### 5.3.1.2 Horizontal porous - nanofluid layers (case 2)

The streamlines and isotherms for the horizontally aligned nanofluid-porous layers for different combinations of  $S$ ,  $Ra$ ,  $Da$ ,  $K_r$ ,  $A_{th}$  and  $N_{th}$  are presented in Figure 5.8 – 5.11. Figure 5.8(a)-(c) shows streamline (upper row) and isotherm (lower row) contours as  $Ra = 10^6$ ,  $Da = 10^{-3}$  and  $K_r = A_{th} = N_{th} = 1$  for different porous layer thicknesses,  $S$ , when the porous layer is horizontal and underneath the nanofluid layer (case 2). The non-uniform heating on the left sidewall resulted in a clockwise and in an anti-clockwise circulation cell. As shown in Figure 5.8(a) at  $S = 0.1$ , the primary cell, rotating in a clockwise direction, has a high stream function intensity which is driven by the buoyancy of the flow being heated along the left wall, and flowing down along the cooled right sidewall. This results in a large cell with two poles, which are located near each vertical sidewall. This cell covers the majority of the enclosure area with high clustering of the streamlines close to the vertical walls and very low penetration into the porous layer. The secondary cell, rotating in an anticlockwise direction, is located close to the upper left corner of the enclosure. At  $S = 0.2$  and  $S = 0.5$ , the nanofluid cell tends to form a single core centre close to the left heated wall. At  $S = 0.2$ , the strength of the circulation increases as compared to  $S = 0.1$ , and thereafter decreases at  $S = 0.5$ , as indicated by  $\Psi_{min}$ . The intensity of the stream function for case 2 was greater than for case 1 for different porous layer thicknesses. The addition of 20% by volume nanoparticles increased the stream function intensity in the main cell of the nanofluid more compared to that for the single-phase fluid. This was due to the thermal conductivity effect of the nanoparticles, which results in an increase in the buoyancy of the nanofluid.

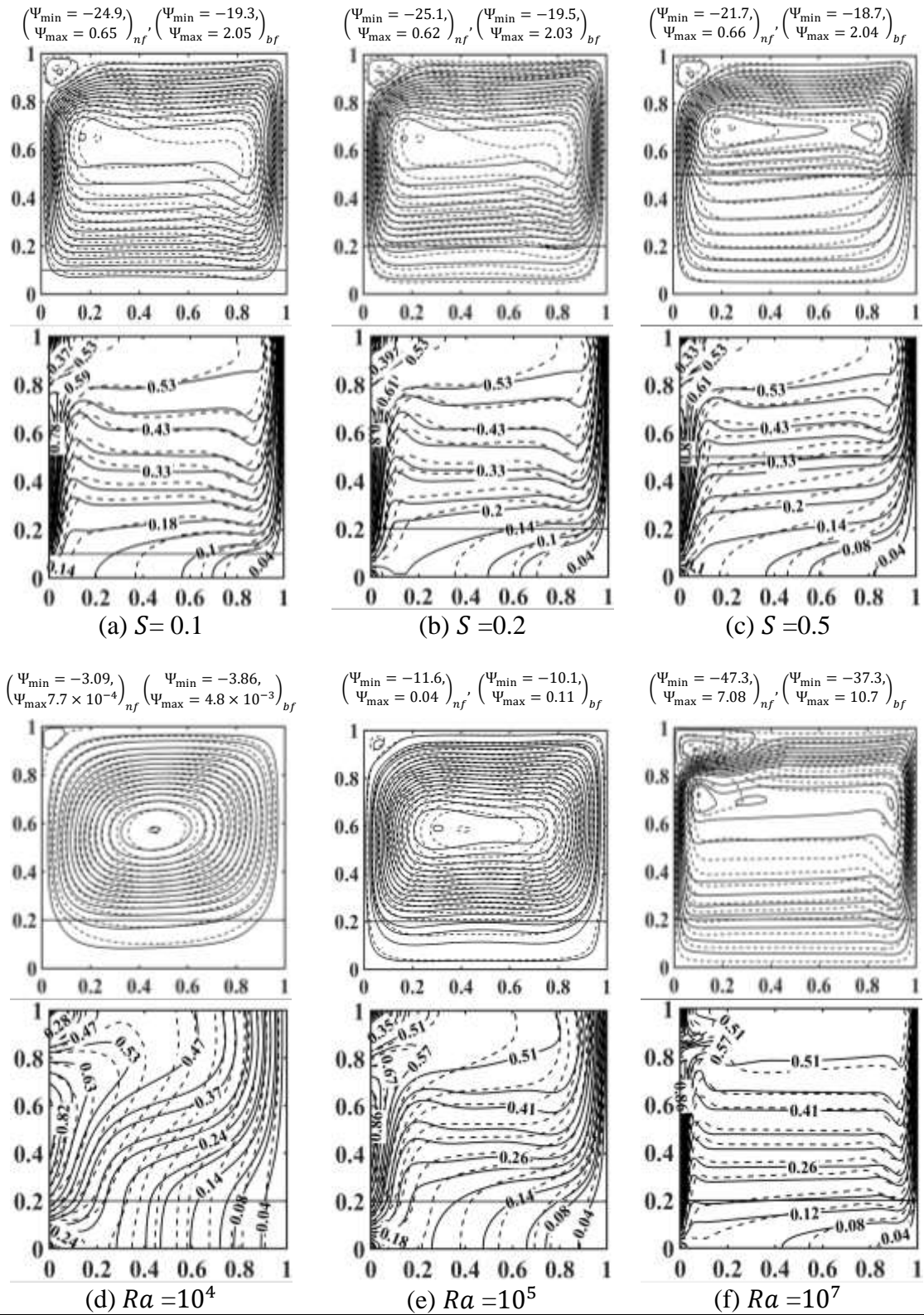


Figure 5.8: Streamlines (upper row) and isotherms (lower row) for case 2 with  $\phi = 0$  (solid lines) and  $\phi = 0.2$  (dashed lines) at different dimensionless parameters, (a-c)  $S$  effect when  $Ra = 10^6$ ,  $Da = 10^{-3}$  and  $K_r = N_{th} = A_{th} = 1$ , (d-f)  $Ra$  effect when  $Da = 10^{-3}$ ,  $S = 0.2$  and  $K_r = N_{th} = A_{th} = 1$ .

The percentage gains due to the addition of nanoparticles are 29%, 28.7% and 16% for  $S$  0.1, 0.2, and 0.5, respectively. The percentage gain due to this addition is greater for case

2 compared to case 1, except at  $S = 0.5$ , where the gain for case 1 is larger. This may be due to the lower contact region of the denser streamlines attached to the heated wall with lower penetration of the flow into the porous layer. The predicted isotherms of the lower row of Figure 5.8(a)-(c) shows more clustered isotherms along the left heated wall for case 2 than for case 1. Convective heat transfer is substantial because the two-pole circulation cells lead to mainly horizontal isotherms within the fluid layer. The difference in the isotherms between the base fluid and the nanofluid is more pronounced at  $S = 0.5$ , where the isotherms of the nanofluid run more diagonally than for the base fluid. It is interesting to note that, changing the porous layer thickness has a greater effect on the isotherms for case 1 than for case 2, as the isotherms in case 1 cluster less tightly with increasing  $S$  inside the vertical porous slab than inside the horizontal porous slab in case 2.

Figure 5.8(d)-(f) shows the effect of increasing the Rayleigh number on the stream function (upper row) and temperature distributions (lower row) for case 2 with  $Da = 10^{-3}$ ,  $S = 0.2$  and  $K_r = A_{th} = N_{th} = 1$ . Figure 5.8(d) shows the streamlines at  $Ra = 10^4$ . A primary cell forms with an elliptical core parallel to the horizontal walls. This cell covers the majority of the enclosure area with a low penetration through the porous layer. A much weaker secondary cell forms at the upper left corner of the enclosure. At  $Ra = 10^5$ , the core of the primary cell elongates horizontally, forming two poles, as shown in Figure 5.8(e), similarly to Figure 5.8(b) when  $Ra = 10^6$ . At the highest Rayleigh number,  $Ra = 10^7$ , the primary cell, with its two poles, stretches horizontally so that the streamlines cluster along the vertical walls in the nanofluid layer. In addition, increasing  $Ra$  increases the strength of the secondary cell, more so for a nanofluid more than for the base fluid. Adding 20% by volume of copper nanoparticles increases the main cell strength of the nanofluid compared to that of the base fluid at the lower Rayleigh number, as indicated by the changes in  $\Psi_{min}$ . Increasing the Rayleigh number caused the intensity of the nanofluid main cell to increase compared to the single-phase fluid. This is indicated by a reduction in  $\Psi_{min}$  of about 14.8%, compared to 26.8% as  $Ra$  increases from  $10^5$  to  $10^7$ , respectively. The percentage gain in  $\Psi_{min}$  for case 2 due to addition of the nanoparticles at  $Ra = 10^5$  is lower than that in case 1. This may be because of the porous-nanofluid layers' direction. As a comparison, the intensity of the circulation cells in case 2 was greater than in case 1. This indicates that the direction of porous-nanofluid layers plays

an important role in heat transfer enhancement. The lower row of Figure 5.8(d)-(f) shows the isotherms for different values of the Rayleigh number. The difference between the base fluid and the nanofluid is more pronounced at the lower value of the Rayleigh number, for which the layer thickness of isotherm lines of the nanofluid near the top right wall is greater than for the base fluid and the isotherm lines are more vertically oriented. This was because the viscous force has a greater effect on the fluid flow than the buoyancy force at the lowest Rayleigh number, which reduces the intensity of the circulation cell of the nanofluid compared to the base fluid. The layer thickness of the isotherm lines over the right wall for case 2 appears to be less than that for case 1, indicating higher convective heat transfer in case 2 compared to case 1. Increasing  $Ra$  produces the heat transfer rate is more enhanced for case 2 than case 1.

The effect of the Darcy number on the streamlines and isotherms for case 2 at  $Ra = 10^6$ ,  $S = 0.2$  and  $K_r = A_{th} = N_{th} = 1$  is shown in Figure 5.9(a) and (b) for Darcy numbers  $Da = 10^{-5}$  and  $Da = 10^{-1}$ , respectively. At both  $Da = 10^{-5}$  and  $10^{-1}$ , the top row of Figure 5.9(a) show that the core centre of the main cell has two poles located close to the vertical walls. At  $Da = 10^{-1}$ , the strength of the main circulation, as indicated by  $\Psi_{min}$ , for both the base fluid and nanofluid was almost identical at  $Da = 10^{-5}$  and  $10^{-1}$ . At both Darcy numbers, the circulation for the base fluid main cell was lower compared to the nanofluid main cell. The coordinates of the core centres were the same at  $Da = 10^{-5}$  and  $10^{-3}$  (as shown in Figure 5.8(b)) and  $10^{-1}$ . It may be noted that the pattern of flow circulation inside the enclosure at  $Da = 10^{-5}$  differs from the circulation flow pattern of case 1. In case 1, the packing density of the streamlines is higher along the right cooled wall. The strength of the main cell recirculation for case 2 is stronger than that in case 1 at  $Da = 10^{-5}$ ,  $10^{-3}$ , and at  $Da = 10^{-1}$ , based on  $\Psi_{min}$ . This difference stems from the different directions of the porous and nanofluid layers, which indicates a greater heat transport for case 2 than for case 1. The isotherms show that the thickness of the thermal layer in case 2 is smaller than case 1, while these were almost identical at higher values of the Darcy number. The convective heat transfer was more pronounced in the nanofluid layer with different Darcy number values. It may be noted that convective heat transfer was more dominant at the left heated wall within the nanofluid layer for all values of Darcy number in case 2 compared to case 1, as indicated by the more vertical isotherms on the left heated wall.

$$\left( \begin{array}{l} \Psi_{\min} = -24.8, \\ \Psi_{\max} = 0.59 \end{array} \right)_{nf}, \left( \begin{array}{l} \Psi_{\min} = -19.3, \\ \Psi_{\max} = 1.91 \end{array} \right)_{bf}$$

$$\left( \begin{array}{l} \Psi_{\min} = -24.8, \\ \Psi_{\max} = 0.68 \end{array} \right)_{nf}, \left( \begin{array}{l} \Psi_{\min} = -19.3, \\ \Psi_{\max} = 2.07 \end{array} \right)_{bf}$$

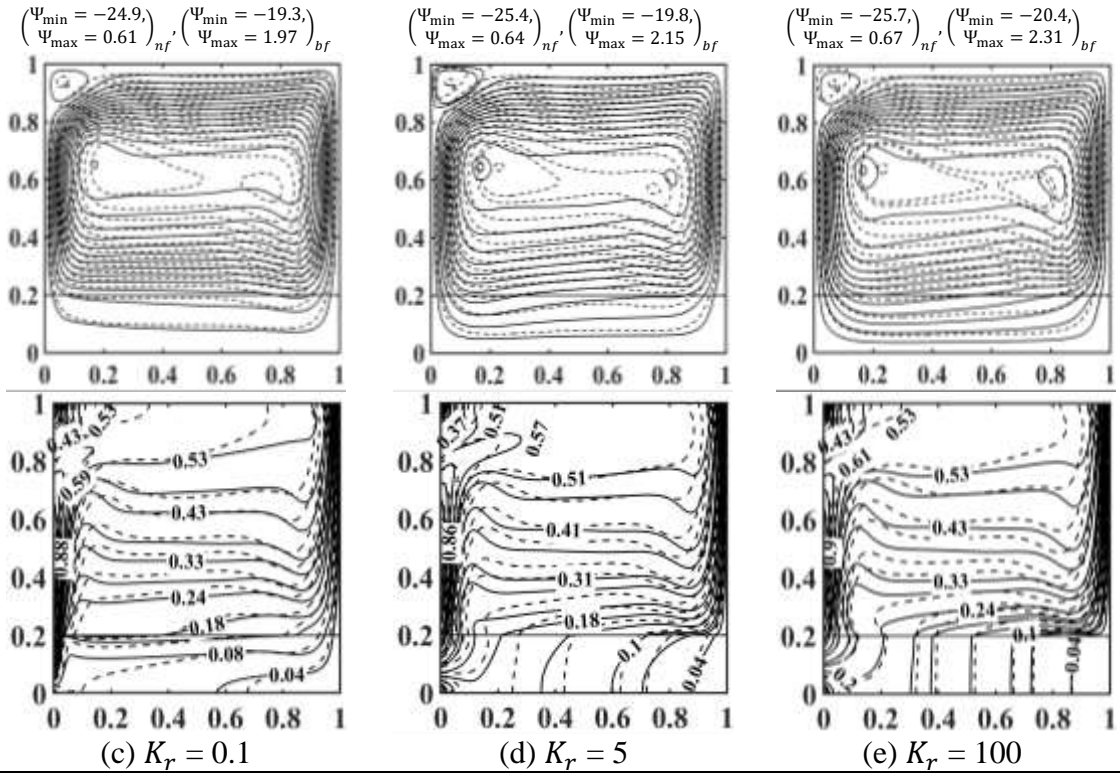
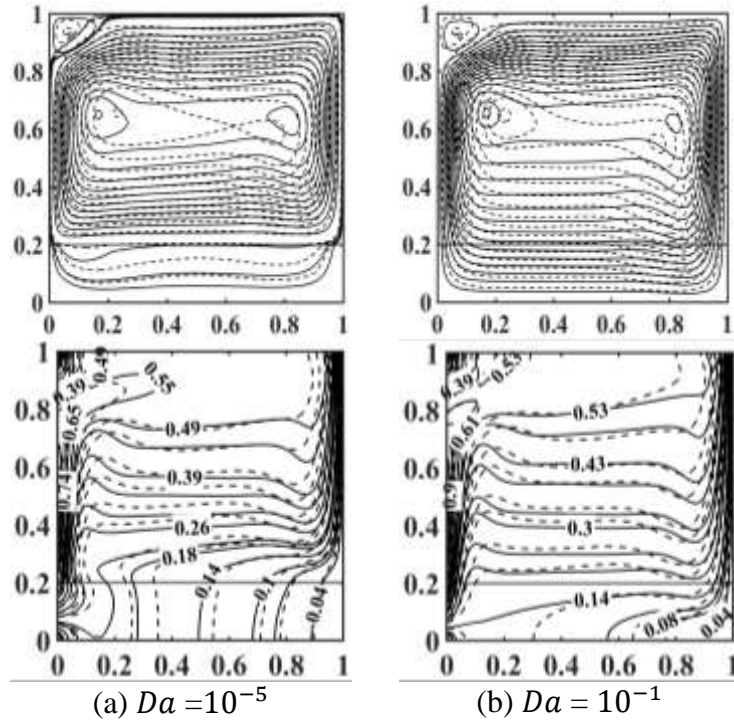


Figure 5.9: Streamlines (upper row) and isotherms (lower row) for case 2 with  $\phi = 0$  (solid lines) and  $\phi = 0.2$  (dashed lines) at different dimensionless parameters, (a-b)  $Da$  effect when  $Ra = 10^6$ ,  $S = 0.2$  and  $K_r = N_{th} = A_{th} = 1$ , and (c-e)  $K_r$  effect when  $Ra = 10^6$ ,  $Da = 10^{-3}$ ,  $S = 0.2$  and  $N_{th} = A_{th} = 1$ .

Figure 5.9(c)-(e) shows the streamlines and isotherms for case 2 at  $Ra = 10^6, Da = 10^{-3}, S = 0.2$  and  $A_{th} = N_{th} = 1$  for  $K_r = 0.1, 5,$  and  $100$ . At all  $K_r$  values, the main cell has two poles for both the base fluid and for the nanofluid. The cell size is almost identical with and without copper nanoparticles. It may be noted that there was no difference in the flow circulation pattern inside the enclosure for all values of  $K_r$  compared to case 1. In case 1, the packing density of the streamlines is higher along the right cooled vertical sidewall with increasing  $K_r$ . The convective heat transfer was dominant at the left heated wall within the nanofluid layer for all values of  $K_r$  for case 2, while in case 1 convective heat transfer was dominant for lower values of  $K_r$  and conductive heat transfer at higher values. At  $K_r = 0.1$ , the stream function for case 2 was of greater strength than case 1, indicated by a lower  $\Psi_{min}$ , although the penetration into the porous layer was greater for case 1. Conversely, increasing  $K_r$  caused a stronger recirculation for case 1 than for case 2, as indicated by  $\Psi_{min}$ .

The effect of the temperature amplitude of the sinusoidal heating on the streamlines (upper row) and isotherms (lower row) in case 2 at  $Ra = 10^6, Da = 10^{-3}, S = 0.2$  and  $K_r = N_{th} = 1$  is shown in Figure 5.10(a)-(c). At  $A_{th} = 0.2$  (see Figure 5.10(a)), the core centre of the nanofluid main cell is located near the left heated wall, while the base fluid main cell has two poles located near each the vertical wall of the enclosure. At  $A_{th} = 0.6$ , the primary cell of the nanofluid has two poles and the streamlines run more diagonally compared to the base fluid main cell. The penetration of the streamlines into the porous layer increases with increasing  $A_{th}$  value, though this effect is clearer for case 1 than case 2. Although case 1 has this feature, the strength of the stream function is higher for case 2 than for case 1, as determined by a lower minimum in  $\Psi_{min}$ . This may be because of the flow resistance that is offered by the porous layer near the heated vertical sidewall, which is greater for case 1 than case 2. The streamlines are steeper towards the left vertical wall for case 2 for all values of  $A_{th}$ , whereas in case 1 the clustering of these lines is more pronounced along the right cooled wall with increasing  $A_{th}$  values. The isotherms of Figure 5.10(a)-(c) (lower row) show that the packing density of the isotherm lines in case 2 near the left wall is lower than in case 1, due to the higher intensity of the stream function in case 2. The difference in the isotherm lines between the nanofluid and base fluid is more pronounced in case 2. Within the porous layer, where there is a

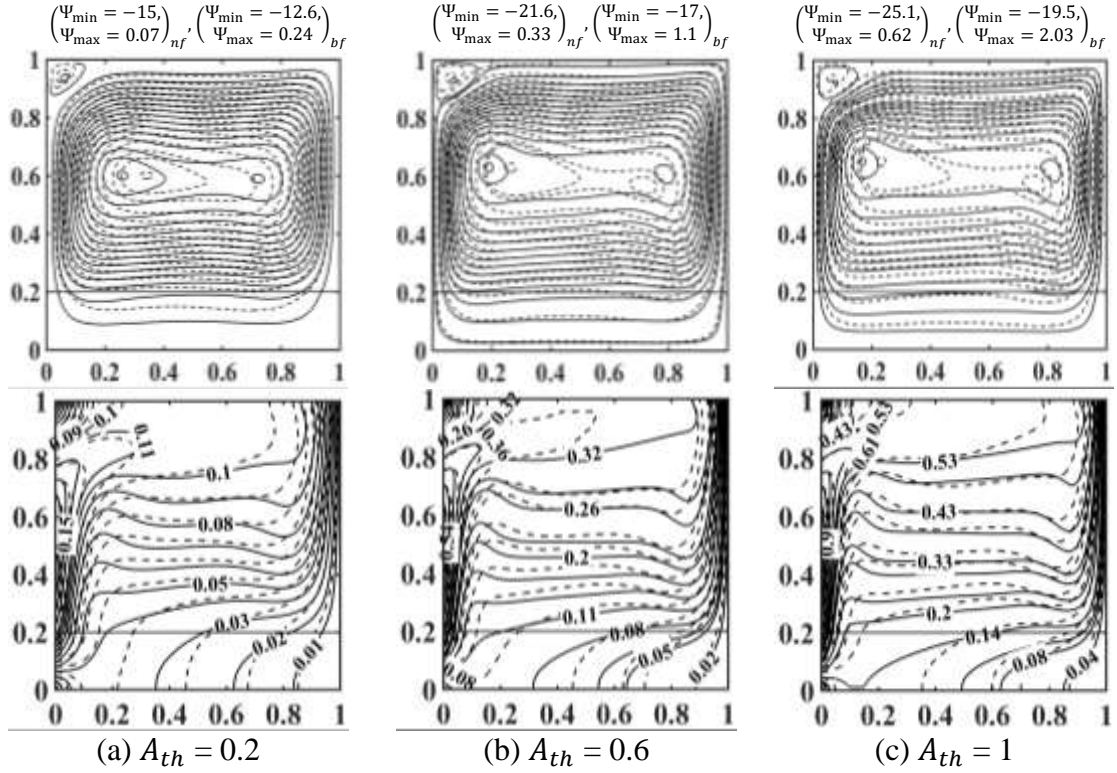


Figure 5.10: Streamlines (upper row) and isotherms (lower row) for case 2 as  $Ra = 10^6$ ,  $Da = 10^{-3}$ ,  $S = 0.2$ ,  $K_r = N_{th} = 1$ ,  $\phi = 0$  (solid lines), and  $\phi = 0.2$  (dashed lines) for different thermal amplitude  $A_{th}$  values.

retardation of the nanofluid's motion in the porous layer due to the addition of nanoparticles, viscous forces may overcome the buoyancy force.

Figure 5.11(a)-(d) illustrates the streamlines (upper row) and the isotherms (lower row) for case 2 with different values of the periodicity parameter  $N_{th}$  at  $Ra = 10^6$ ,  $Da = 10^{-3}$ ,  $S = 0.2$  and  $A_{th} = K_r = 1$ . The strength of the stream function decreases with increasing  $N_{th}$  values, as indicated by higher negative  $\Psi_{min}$  values. The odd and even numbers of the periodicity parameter affect the flow behaviour inside the enclosure. Changing  $N_{th}$  results in symmetric cells for even integers of  $N_{th}$  and asymmetric cells for odd  $N_{th}$  integers. At  $N_{th} = 2$ , two almost symmetric cells form, respectively, in the upper and lower halves of the enclosure, with approximately equal values of the peak circulation, as indicated by  $\Psi_{min}$ , for the base fluid and the nanofluid, as shown in Figure 5.11(a). The peak circulation of the nanofluid cells is marginally more intense than for the base fluid cells. The lower cells rotate in a clockwise direction with  $\Psi_{min} = 19.9$  for the nanofluid and  $\Psi_{min} = 19.2$  for the base fluid, while the upper cells rotate in an anticlockwise direction with  $\Psi_{max} = 25.1$  for the nanofluid and  $\Psi_{max} = 22.5$  for the base

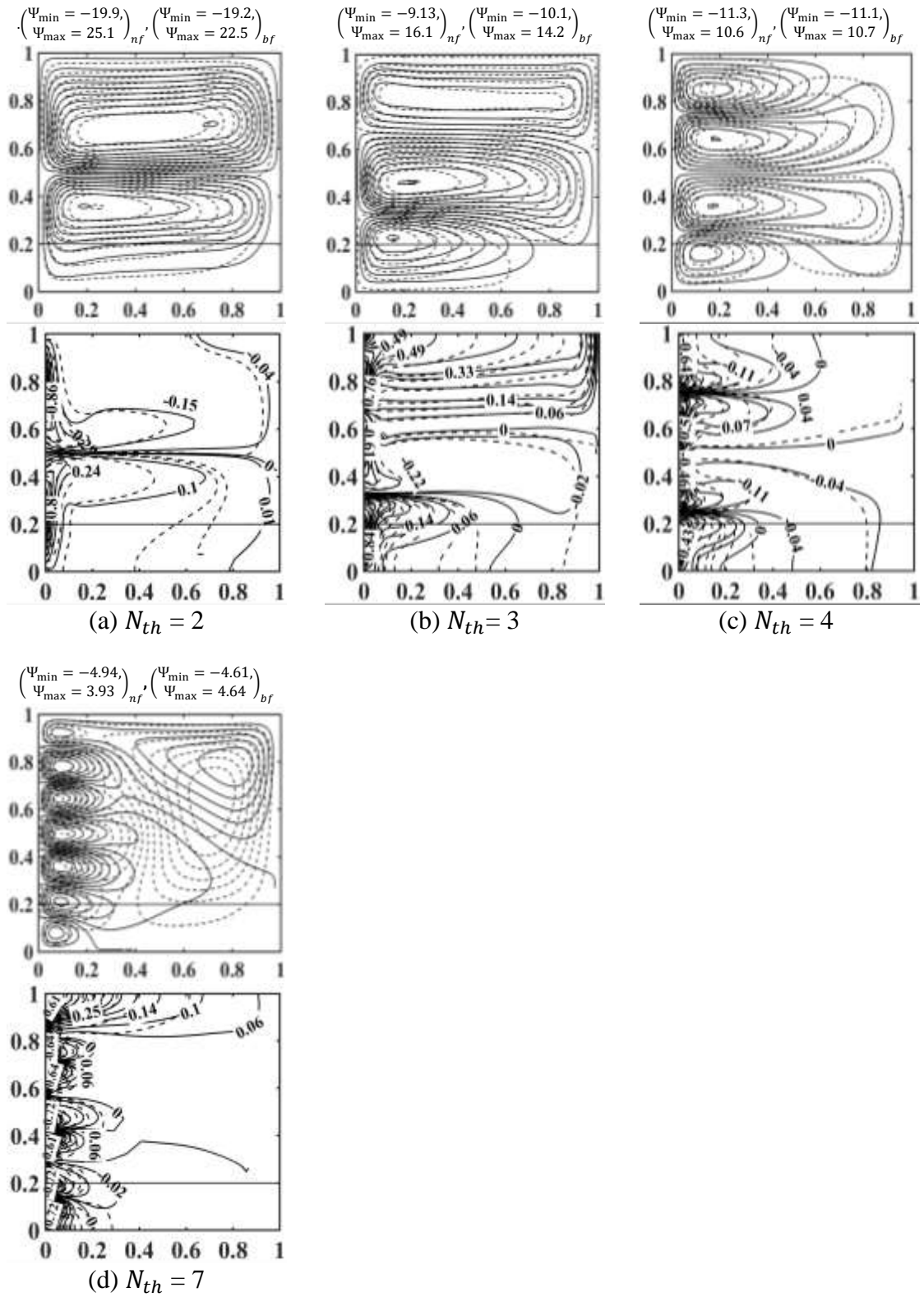


Figure 5.11: Streamlines (upper row) and isotherms (lower row) for case 2 as  $Ra=10^6$ ,  $Da=10^{-3}$ ,  $S=0.2$ ,  $K_r=A_{th}=1$ ,  $\phi=0$  (solid lines), and  $\phi=0.2$  (dashed lines) for different thermal frequency  $N_{th}$  values.

fluid. The upper cells are larger and stronger than the lower cells, because of the flow resistance offered by the porous layer. At  $N_{th} = 3$ , the nanofluid rotates in a clockwise direction in a middle cell between a top and a bottom anti-clockwise cell. This middle cell is less extended than the base fluid cell within the enclosure but has a stronger circulation, as indicated by  $\Psi_{min}$ . The peak anti-clockwise recirculation,  $\Psi_{min}$  in case 2 is higher than for case 1. The isotherms for this test case one shown in the lower row of Figure 5.11(a)-(d). The common behaviour of the isotherms depends on the periodicity parameter and thus in turn on the number of circulation cells inside the enclosure. The temperature distribution is approximately symmetric when the periodicity parameter is an even integer, while it is asymmetric for odd  $N_{th}$ . There is less heat transfer to the right wall when  $N_{th}$  is even. This was because the heat received from the hot portion of the left heated wall is approximately equal to the heat that returns to the cold portion of the left heated wall. Conversely, the asymmetry of the isotherms for odd  $N_{th}$  that may provide heat transfer to the right cold wall for case 2 as for case 1.

### 5.3.2 Velocity magnitude, $R$

The dimensionless velocity magnitude is plotted at the interface between the porous-nanofluid layers along the  $Y$ -axis and  $X$ -axis for (a) case 1 and (b) case 2, respectively, at  $S = 0.2$ ,  $\phi = 0.2$ , and  $K_r = A_{th} = N_{th} = 1$  with  $Ra = 10^4$  and  $Ra = 10^7$  for different  $Da$  values, in Figure 5.12. Figure 5.12(a) shows the effect of increasing  $Ra$  on the velocity magnitude for case 1 at different values of  $Da$ . The effect of increasing the Darcy number is more pronounced at the low Rayleigh number of  $10^4$ , with a maximum value of the velocity magnitude at  $Y = 0.5$ . At the higher  $Ra = 10^7$ , two velocity magnitude maxima occurred at around  $Y = 0.1$  and  $0.9$ , respectively, at high values of  $Da$ , while a velocity minimum occurred between  $Y = 0.6$  and  $0.8$ . This decrease in velocity magnitude is due to the movement of the main cell centre towards this height inside the enclosure.

Figure 5.12(b) shows the variation of the velocity magnitude with  $Ra$  along the horizontal interface for case 2 for three different  $Da$  values. At  $Ra=10^4$ , the profile of the velocity magnitude shows a similar trend at all three Darcy number values as case 1. The velocity magnitude changes at the high number of  $Ra = 10^7$ , specifically, velocity magnitude distribution is approximately uniform between  $X = 0.1$  and  $X = 0.8$ , while

positive higher values of the velocity magnitude appear near the vertical walls of the enclosure. Generally, at the high value of the Rayleigh number, the velocity magnitude for case 2 is higher along the vertical walls than for case 1. Consequently, as it might be expected that, the rate of heat transfer in case 2 is higher than in case 1.

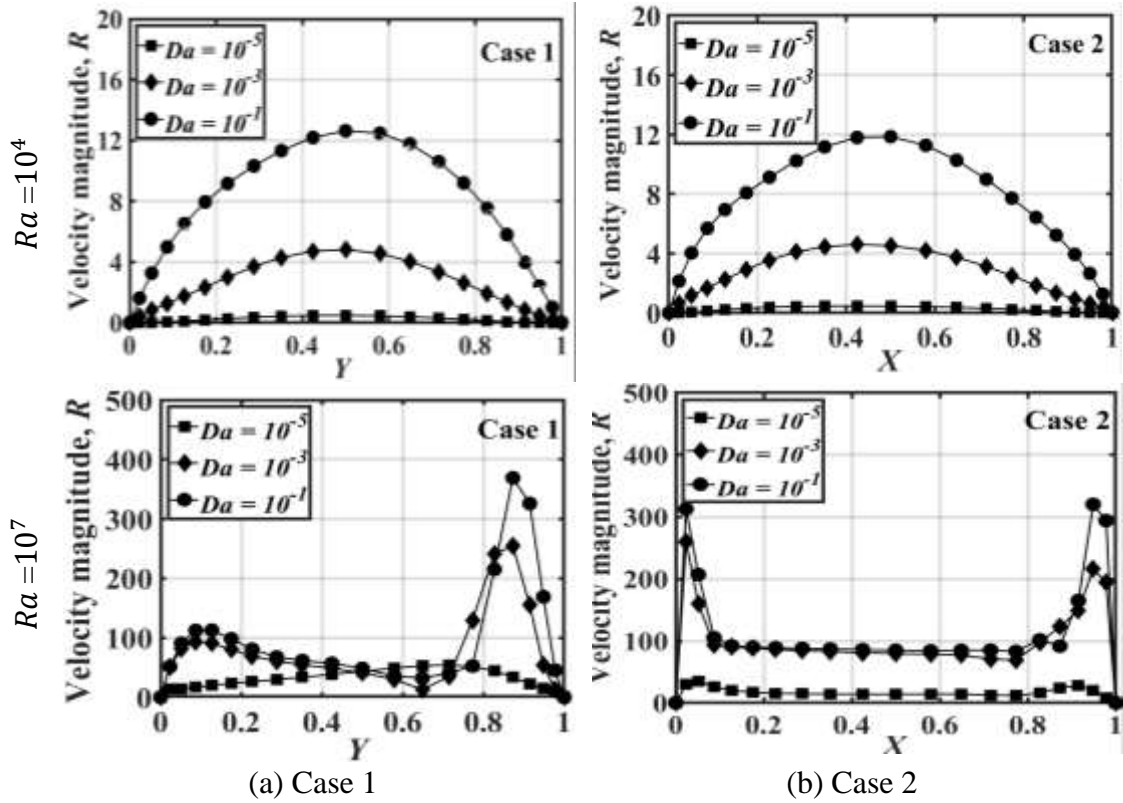


Figure 5.12: Variation of resultant velocity component,  $R$  at the interface line of (a) case 1 and (b) case 2 for different Darcy numbers as  $S = 0.2$ ,  $\phi = 0.2$  and  $K_r = N_{th} = A_{th} = 1$  at  $Ra = 10^4$  and  $Ra = 10^7$ .

### 5.3.3 Normalized temperature distribution, $\theta$

The variation of the normalized temperature distribution along the interface line at  $X = 0.2$  for (i) case 1 and  $Y = 0.2$  for (ii) case 2 when  $Ra = 10^6$ ,  $Da = 10^{-3}$ ,  $S = 0.2$ , and  $\phi = 0.2$  is shown in Figure 5.13, for different values of (a)  $N_{th}$  and (b)  $A_{th}$ . Figure 5.13(i) (a) shows the dimensionless temperature distribution along the vertical interface line at  $X = 0.2$  for case 1 at different wave numbers,  $N_{th}$  at  $K_r = A_{th} = 1$ . The temperature profile is non-monotonic. This is due to the non-uniform temperature imposed on the left heated wall at different  $N_{th}$  values. The maximum temperature along the interface occurs at  $N_{th} = 1$ . This gave an indication that the maximum heat removal from the heat source occurs at  $N_{th} = 1$ . This is evidenced by higher density of the isotherms along most of the left

heated wall produced by the main clockwise circulation shown in Figure 5.4(b). There appears to be no substantial reversal of the heat flux from the nanofluid towards the left heated wall, due to the weak anti-clockwise secondary cell at the upper left corner of the enclosure.

Figure 5.13(i) (b) shows the non-dimensional temperature distribution along the porous - nanofluid interface for case 1 with  $A_{th}$  as  $K_r = N_{th} = 1$ . The variation in temperature distribution increases with increasing  $A_{th}$ . This is due to the extension of the main circulation cell from the fluid layer towards the porous-fluid interface and increasing the streamlines strength for both the main and secondary cells, as shown in Figure 5.6(a)-(c). This causes to increase the clustering of the isotherms along the vertical walls with increasing  $A_{th}$  values. In addition, at all values of  $A_{th}$ , the temperature approximately reached its maximum value at about  $Y = 0.8$ . This is due to the right going heat transport by the main circulation cell at this height along the porous – nanofluid interface, after which the temperature gradually decreases up to  $Y = 1$ .

Figure 5.13(ii) (a) shows the effect of the thermal wave number  $N_{th}$  on the non-dimensional temperature distribution along the interface line at  $Y = 0.2$  for case 2 as  $K_r = A_{th} = 1$ . At  $X = 0$ , the dimensionless temperature at the left heated sidewall, is determined by  $N_{th}$  as an imposed boundary condition. This changes the ensuing temperature distribution at  $X \geq 0$ . In addition, the maximum temperature occurs at  $N_{th} = 3$ . At  $N_{th} = 5$ , the decreasing  $\theta$  trends at  $X > 1$  indicates heat transfer towards the left wall of the enclosure. This effect is greater at  $N_{th} = 7$  than at  $N_{th} = 5$ . This was because, as the thermal wave number  $N_{th}$  increases, the temperature at the left heated wall oscillates more rapidly with  $Y$ , which ultimately causes the decrease of heat transfer towards the right wall. It is interesting to note that at  $N_{th} = 3$  and  $N_{th} = 7$ , the normalized temperature distributions sharply decrease near the left heated wall and approach zero along the interface until  $\theta = 0$  at  $X = 1$ . At  $N_{th} = 1$ , the dimensionless temperature gradually decreases from  $X = 0$  up to  $X = 1$ , starting from a lower wall temperature at  $X = 0$  than for  $N_{th} = 3$ . This is due to  $\theta$  at  $X = 0$  being about 0.6, therefore being more intermediate (lower) than the temperature extrema (+1, -1) at  $N_{th} = 3$  and  $N_{th} = 7$ . The influence of the amplitude parameter on the normalized temperature distribution along

the interface line at  $Y = 0.2$  for case 2 as  $K_r = N_{th} = 1$  is reported in Figure 5.13(ii) (b). This figure shows that the temperature profile rapidly decreased as  $X$  increases from 0 to 0.2 for all values of  $A_{th}$ , and then steadily decreases along the interface line. The temperature along the interface increases with increasing amplitude because of the higher value of the temperature imposed as boundary condition at  $X = 0$ , as  $A_{th}$  increases.

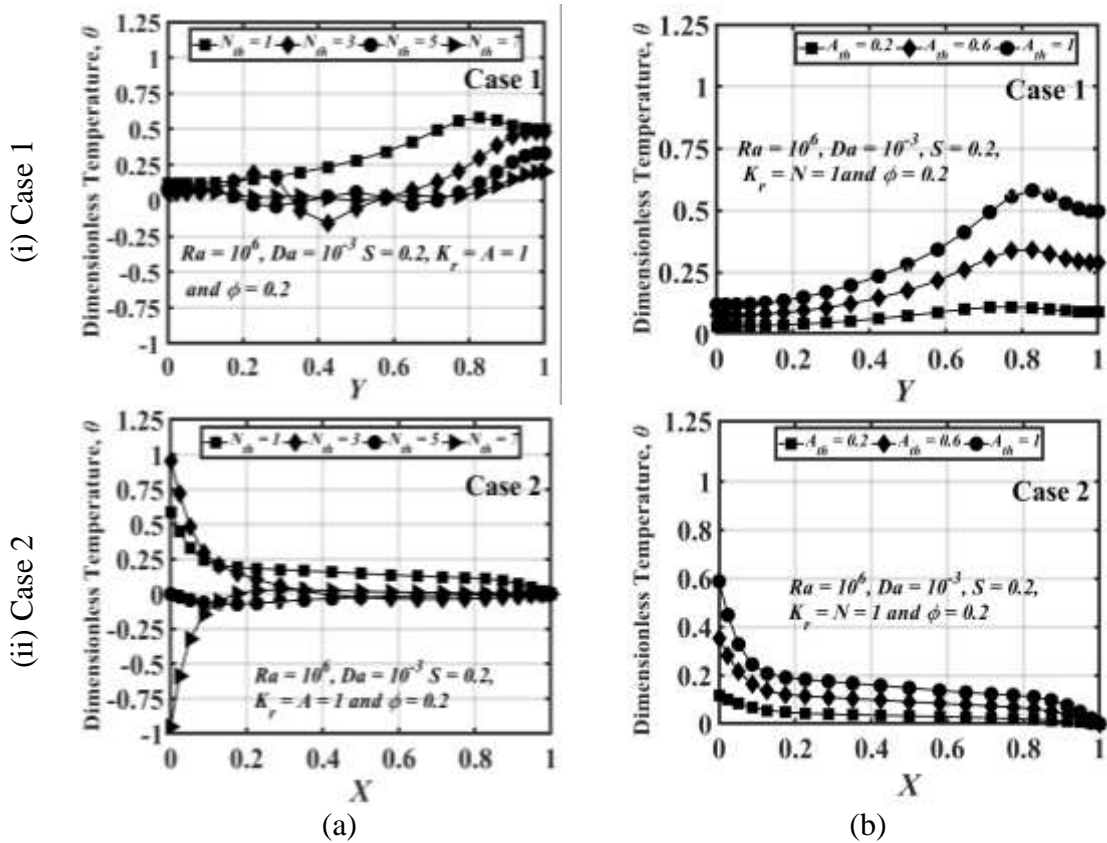


Figure 5.13: Local distribution of the dimensionless temperature along the interface line for (i) case 1 and (ii) case 2 with different dimensionless parameters (a)  $N_{th}$  effect, and (b)  $A_{th}$  effect.

### 5.3.4 Heat transfer rate: Local Nusselt Number

Figure 5.14 shows the predictions of the local Nusselt number on the left ( $Nu_l$ ) and right ( $Nu_r$ ) walls of the enclosure in the left and right columns, respectively, at five increasing values of thermal conductivity ratio,  $K_r$  for (i) case 1 and (ii) case 2 at  $Ra = 10^6$ ,  $Da = 10^{-3}$ ,  $S = 0.2$ ,  $A_{th} = N_{th} = 1$  and  $\phi = 0.2$ . Figure 5.14(a)(i) shows common trend of a single  $Nu_l$  for case 1 due to the maximum temperature imposed at about  $Y = 0.4$  on the left heated sidewall. The local Nusselt number is sensitive to  $K_r$ , and  $Nu_l$  is maximum for the lowest value of  $K_r = 0.1$ . This is due to the high thermal conductivity of the nanofluid enhancing the convective heat transfer inside the porous layer for this thermal

conductivity ratio. The negative distribution in the upper and lower portions of the left heated wall stems from the effect of imposing the left wall boundary conditions  $\theta = 0$  at  $Y = 0$  and  $Y = 1$ , leading to heat transfer towards the left wall at these locations. For case 2 as shown in Figure 5.14(a) (ii), when under the same conditions as case 1, an overall similar trend in the local Nusselt number on the left heated wall can be seen as case 1. However, there is essentially no sensitivity of  $Nu_l$  to variations in  $K_r$  at  $Y > 0.2$ . Increasing  $K_r$  reduces the local Nusselt number along the left heated wall at  $Y < 0.2$ . This was because the effect of increasing  $K_r$  is more pronounced in the porous layer at  $Y < 0.2$  where the heat transport by the nanofluid is more important for the slower moving flow at lower  $K_r$  values. The variation of  $Nu_l$  along with the left wall for case 1 is greater than for case 2. At  $K_r = 0.1$ ,  $Nu_l$  for case 1 is greater than for case 2. This was because the higher conductivity of the nanofluid particles has more important on the retarded fluid through the vertical porous slab next to the heated wall, which reaches a higher temperature in case 1 than in case 2. The high value of  $Nu_l$  in case 2 at the porous layer attributed to increasing of the thermal conductivity of the nanofluid more than the porous slab which causes a packing of the isotherms close to the left wall compared to the other  $K_r$  values as shown in Figure 5.9(c)-(e). At  $K_r \geq 1$ ,  $Nu_l$  for case 2 is higher than for case 1. This is attributed to that in case 2, the dominance of the main circulation cell inside the fluid layer with two poles located near the vertical walls and leads to packing the isotherms along the left vertical wall compared to case 1.

The effect of increasing  $K_r$  on the local Nusselt number along the right wall of the enclosure for (i) case 1 and (ii) case 2 shown in Figure 5.14(b). The local Nusselt number along the right cold wall ( $Nu_r$ ) has negative values for all  $K_r$  values.  $Nu_r$  is more negative over the lower portion of the right cold sidewall in case 1 while it is more negative over the upper portion in case 2. This was due to the differences in the main cell near the right cold sidewall between the two cases. There is no appreciable effect of changing the magnitude of  $K_r$  on the local Nusselt number along the right wall for case 2.

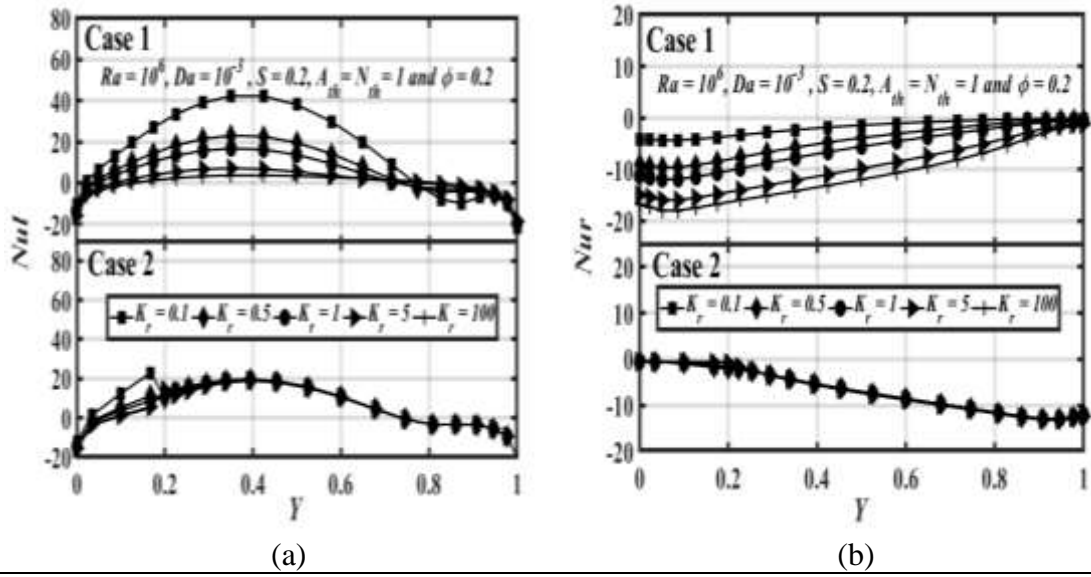


Figure 5.14: Variation of the local Nusselt number along the left hot wall (a) and the right cold wall (b) with different dimensionless thermal conductivity ratio  $K_r$ . In each plot, the upper panel corresponds to case 1, and the lower panel corresponds to case 2.

### 5.3.5 The average Nusselt number, $Nu_{av}$

The average Nusselt number,  $Nu_{av}$  is presented in Figure 5.15 as an aggregate measure of the overall rate of heat transfer. The variation in the average Nusselt number is plotted versus the logarithm of Rayleigh number,  $Ra$ , the logarithm of the Darcy number, and the porous layer thickness for both cases 1 and 2, in Figure 5.15(a)-(c), respectively. In each plot, the upper panel corresponds to case 1 and the lower panel corresponds to case 2. The upper panel of Figure 5.15(a) shows the relationship between  $Nu_{av}$  and  $Ra$  for different values of the thermal amplitude for case 1 at  $Da = 10^{-5}$ ,  $S = 0.2$ ,  $K_r = N_{th} = 1$  and  $\phi = 0.2$ . This figure shows that  $Nu_{av}$  increases as the temperature amplitude increases from 0.2 to 1. The average Nusselt number increases with increasing  $Ra$  for a given temperature amplitude, especially for high values of  $A_{th}$ . For case 2 (the lower panel of Figure 5.15(a)), it is interesting to note that  $Nu_{av}$  for case 2 was higher than for case 1 for all values of  $A_{th}$ , especially at higher values of  $Ra$ . This was because the layer thickness of the isotherm lines in case 2 was smaller than that for case 1 due to the higher intensity of the stream function in case 2.

The upper panel of Figure 5.15(b) shows the variation of  $Nu_{av}$  with the logarithm of  $Da$  for case 1 with different values of periodicity parameter  $N_{th}$  at  $Ra = 10^7$ ,  $K_r = A_{th} = 1$ ,  $S = 0.2$  and  $\phi = 0.2$ . Common to the  $Nu_{av}$  distribution with  $Da$  for all values of  $N_{th}$ ,

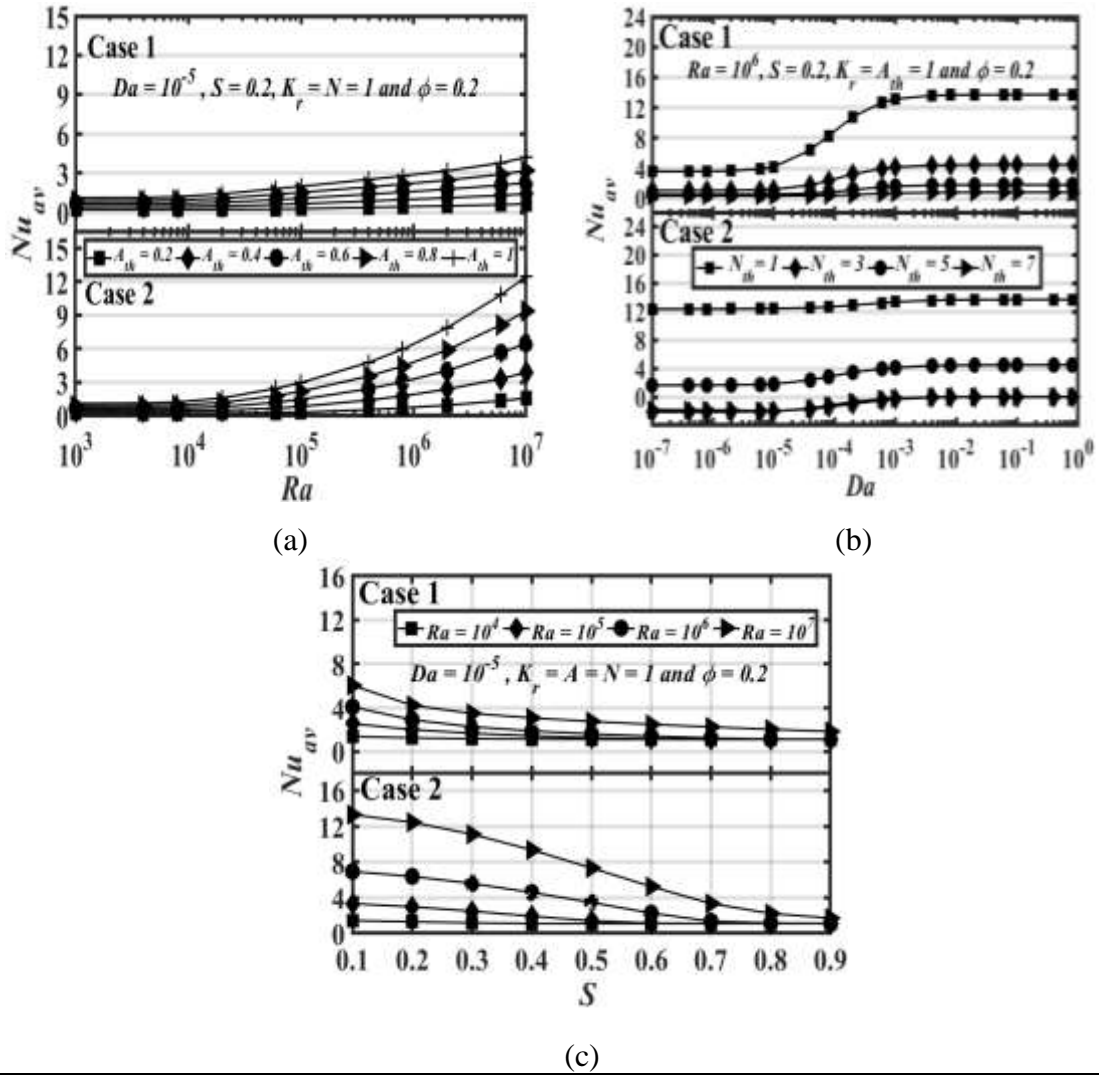


Figure 5.15: Variation of the average Nusselt number with (a)  $Ra$  effect, (b)  $Da$  effect and (c)  $S$  effect. In each plot, the upper panel corresponds to case 1, and the lower panel corresponds to case 2.

$Nu_{av}$  decreases with increasing  $N_{th}$  for all  $Da$  values. A higher  $Nu_{av}$  value is predicted for  $Da \geq 10^{-3}$ , while a low  $Nu_{av}$  is predicted for  $Da \leq 10^{-5}$ , for all  $N_{th}$  values. A rapid decrease of  $Nu_{av}$  with increasing  $N_{th}$  is predicted over the Darcy number for the range  $10^{-5} \leq Da \leq 10^{-3}$ . This is because the porous layer affects the circulation of the main cell. In case 2 (the lower panel of Figure 5.15(b)),  $Nu_{av}$  shows a lower sensitivity with the variation in the Darcy number, especially at  $N_{th} = 1$ . This was because the porous layer only affects the lower portion of the left heated wall ( $S = 0.2$ ) and most of the recirculation cell occupies the nanofluid layer. At  $N_{th} = 1$ ,  $Nu_{av}$  is greater in case 2 compared to that for case 1 at the lower values of  $Da$ .

Figure 5.15(c) shows the effects of the porous layer thickness ratio,  $S$  on  $Nu_{av}$  for different  $Ra$  at  $Da = 10^{-5}$ ,  $K_r = A_{th} = N_{th} = 1$ ,  $S = 0.2$  and  $\phi = 0.2$ . For case 1, this Figure shows that  $Nu_{av}$  increases with  $Ra$  due to the augmentation of the buoyancy forces. For a given  $Ra$ , the heat transfer rate decreases as  $S$  increases due to the flow resistance produced by the porous layer. In addition, there was no significant effect of  $S$  on  $Nu_{av}$  at  $Ra = 10^4$ . It is interesting to note that the maximum  $Nu_{av}$  occurs at  $S = 0.1$  due to the high circulation strength of the main cell. In case 2 (lower panel of Figure 5.15(c)), a significant increase in  $Nu_{av}$  is observed for all Rayleigh numbers compared to case 1, indicating the effect of the nanofluid-porous layers' direction. Specifically, the porous layer has less effect on the streamlines of the main cell in case 2 compared to case 1.

Figure 5.16 shows the variation in  $Nu_{av}$  with the logarithm of  $Ra$  for case 1 (solid line) and case 2 (dashed line) at  $K_r = 1$  and  $K_r = 0.1$  with sinusoidal temperature boundary conditions at the left vertical sidewall, as  $Da = 10^{-3}$ ,  $S = 0.2$ ,  $\phi = 0.2$  and  $A_{th} = N_{th} = 1$ .  $Nu_{av}$  increases with increasing  $Ra$  for all  $K_r$  in both cases. This is due to the greater buoyancy force produced at higher  $Ra$ , especially at  $Ra = 10^7$ .  $Nu_{av}$  at  $K_r = 0.1$  is higher than at  $K_r = 1$ . In addition, at  $K_r = 1$ ,  $Nu_{av}$  in case 2 is slightly higher than for case 1. As  $K_r$  decreases ( $K_r = 0.1$ ),  $Nu_{av}$  for case 1 becomes significantly higher than for case 2,

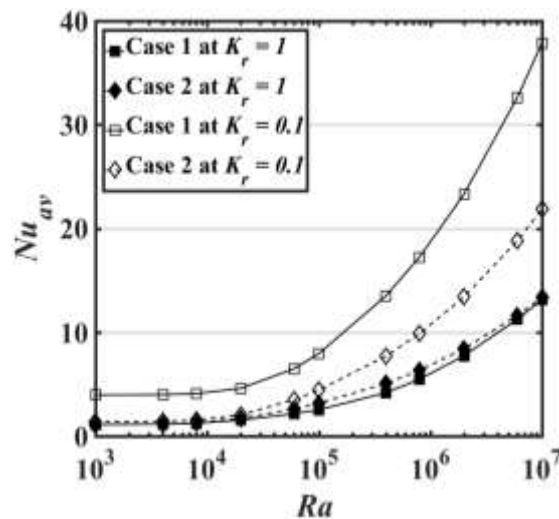


Figure 5.16: Variation of the average Nusselt number with  $K_r = 1$  and  $K_r = 0.1$ , for case 1 (solid lines) and case 2 (dashed lines) with sinusoidal heating on the left vertical sidewall as  $Da = 10^{-3}$ ,  $S = 0.2$ ,  $\phi = 0.2$  and  $N_{th} = A_{th} = 1$ .

where the convection heat transfer at this value of  $K_r$  in case 1 is more dominant than in case 2. This is because that at  $K_r = 0.1$ , the isotherms for case 1 were denser along the left heated wall than that for case 2, as shown in Figure 5.5(c) and Figure 5.9(c), respectively. Generally, the lower value of  $K_r$  produced higher rates of heat transfer in case 1 than in case 2 for different Rayleigh numbers.

## 5.4 Conclusions

Natural convection inside an enclosure filled with composite nanofluid-porous layers with a sinusoidal thermal boundary condition on the left-hand sidewall of the enclosure has been studied. Case 1 and case 2 were considered to illustrate the effects of the vertical and horizontal orientations of the nanofluid-porous layers, respectively. The left wall of the enclosure was sinusoidally heated while the right wall was isothermally cooled. The upper and lower walls of the enclosure were thermally isolated. Cu-water nanofluid was used in a homogenous mixture. The results of this study indicate the following conclusions:

- The intensity of the stream function for case 2 was greater than for case 1 for different porous layer thicknesses. The layer thickness of the isotherm lines for case 2 was less than case 1, indicating higher convective heat transfer in case 2 compared to case 1.
- At the high values of the Rayleigh number and Darcy number, the velocity magnitude for case 2 showed was higher the vertical walls than for case 1. This indicated higher convective heat transfer for case 2 than case 1.
- The penetration of the streamlines into the porous layer increased with increasing  $A_{th}$  value and this was clearer for case 1 than for case 2. Although case 1 has this feature, the strength of the stream function was higher for case 2 than for case 1.
- The temperature distribution along the porous-fluid interface increased with increasing the temperature amplitude  $A_{th}$ , driven by a stronger temperature transport by the main circulation cell at higher  $A_{th}$  values. Furthermore, the rate of heat transfer for case 2 was higher than for case 1 for all values of  $A_{th}$ , especially at higher values of  $Ra$ .

- There was an irregular distribution of the isotherms for odd values of  $N_{th}$ . At low  $Da$  values,  $Nu_{av}$  was higher for case 2 than that for case 1, especially at  $N_{th} = 1$ .
- $Nu_{av}$  increased with increasing  $Ra$  value, especially at  $Ra = 10^7$  for all  $K_r$ . At  $K_r \geq 1$ ,  $Nu_{av}$  for case 2 was higher than for case 1, while at  $K_r = 0.1$ ,  $Nu_{av}$  for case 1 was higher than for case 2. The lower value of  $K_r$  produced a higher  $Nu_{av}$  in case 1 compared to case 2 for different Rayleigh numbers.

In general, the effect of the porous slab direction, the Rayleigh number, the Darcy number, the thermal conductivity ratio (porous/ nanofluid), the temperature amplitude, the temperature wave number, and the nanoparticles volume fraction with the sinusoidal thermal boundary condition played an important role in the trend of the flow and heat transfer inside an enclosure partly filled by a porous slab saturated with a nanofluid in a vertical and a horizontal porous slab. At low values of the thermal conductivity ratio (porous to nanofluid),  $K_r < 1$ , the heat transfer inside the enclosure was higher for all values of Rayleigh number when the porous slab in the vertical direction compared to the horizontal porous slab. The heat transfer was higher for the horizontal porous slab compared to the vertical porous slab with increasing the temperature amplitude of the heated wall and at higher values of the Rayleigh number. A significant increase of the heat transfer at lower values of the Darcy number for the horizontal porous slab compared to the vertical porous slab when the temperature wave number of the heated wall was equal to one. The results predicted a new trend of the flow and heat transfer inside the enclosure under the effect of the sinusoidal thermal boundary condition on the left sidewall of the enclosure. The porous slab in a vertical or a horizontal direction played a vital role in the heat transfer. It may be interesting for the designer in the modern technology of the industrial engineering applications.

# Chapter 6: Natural Convection of a Hybrid Nanofluid in a Square Enclosure Partially Filled with a Porous Medium Using a Thermal Non-Equilibrium Model

## 6.1 Motivation and introduction

The aim of this chapter is to investigate the effects of an isoflux bottom-heating wall on the convective heat transfer inside an enclosure partly filled by a vertical porous slab saturated with a hybrid nanofluid using a local thermal non-equilibrium model LTNE model. A new simulation results is presented to develop the convective heat transfer inside an enclosure partly filled by a porous slab rather than that of using enclosures that were used in the previous literature under an isoflux bottom-heating wall of the enclosure. To the best of author's knowledge, no such an investigation has yet been reported in the literature. Therefore, this study makes an original contribution to this scientific field. This investigation of the present study may be interested to the designer to predict the convective heat transfer in the next modern industry technology.

Accordingly, this chapter deals with the investigation of natural convection inside an enclosure partly filled with a porous medium saturated with a hybrid nanofluid using the LTNE model under the effect of bottom isoflux heating. The bottom wall of the enclosure is partly heated to provide a heat flux, while the other parts of the wall are adiabatic. The top and vertical walls of the enclosure are maintained at constant cold temperatures. Simulations are obtained at the Rayleigh number ( $Ra$ ),  $10^3 \leq Ra \leq 10^7$ , the Darcy number ( $Da$ ),  $10^{-7} \leq Da \leq 1$ , the porous layer thickness ( $S$ ),  $0 \leq S \leq 1$ , the modified conductivity ratio ( $\gamma$ ),  $10^{-1} \leq \gamma \leq 10^4$ , the interphase heat transfer coefficient ( $H$ ),  $10^{-1} \leq H \leq 1000$ , the heat source length ( $B$ ), 0.2, 0.4, 0.6, 0.8 and 1, and the nanoparticle volume fraction ( $\phi$ ),  $0 \leq \phi \leq 0.2$ .

## 6.2 A model problem

### 6.2.1 Physical model

The domain of this study is illustrated in Figure 6.1 as that of a two-dimensional square enclosure partly filled by a porous slab saturated by a nanofluid with side length  $L$ . The bottom wall is partly heated using a heat flux of length  $b$  with a fixed centre location at a distance  $d$  from the vertical wall. The inactive portions of the bottom wall are adiabatic,

while the upper and vertical walls are maintained a constant cooling temperature,  $T_c$ . These boundary conditions cause to generate a temperature difference in the vertical direction. Accordingly, the density and gravity vectors are parallel and opposite to each other and this may play a significant role on the convective heat transfer. The Darcy-Brinkman model is used to model the flow in the porous medium layer. The dimensionless governing equations are applied to represent the flow and heat transfer inside the porous medium and nanofluid layers can be found in Appendix B2 (equations B2.1-B2.9). The hybrid nanofluid consists of Cu – Al<sub>2</sub>O<sub>3</sub>/ water that saturates the vertical porous slab on the left portion of the enclosure, while it filled the rest portion of the enclosure. It is assumed a homogenous mixture, laminar and incompressible. The single-phase fluid and the nanoparticles are in thermal equilibrium. The thermophysical properties of the hybrid nanofluid are given in Table 3.1.

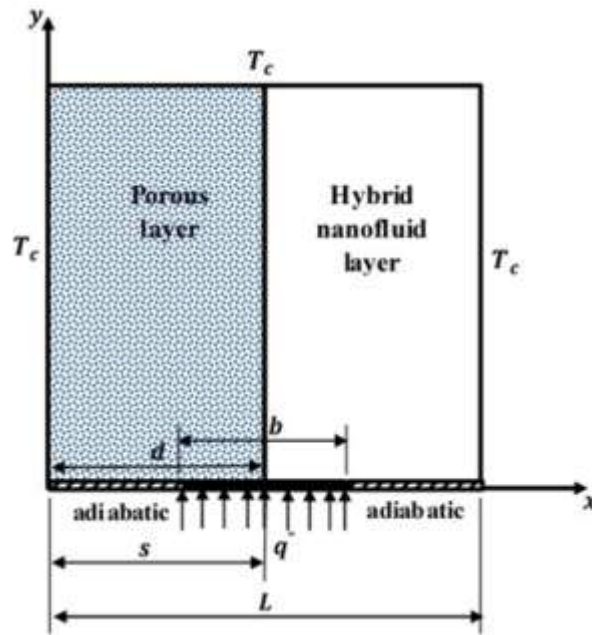


Figure 6.1: Physical domain of composite hybrid nanofluid-porous medium layers.

### 6.2.2 Boundary conditions

The dimensionless governing equations are applied in this case study and the boundary conditions are:

$$U(X, 0) = U(X, 1) = U(0, Y) = U(1, Y) = 0 \quad (6.1)$$

$$V(X, 0) = V(X, 1) = V(0, Y) = V(1, Y) = 0, \quad (6.2)$$

$$\theta(X, 1) = \theta(0, Y) = \theta(1, Y) = 0, \quad (6.3)$$

$$\frac{\partial \theta}{\partial Y}(X, 0) = -\frac{(k)_{bf}}{(k)_{hnf}}, \quad (D - 0.5B) \leq X \leq (D + 0.5B) \quad (6.4)$$

$$\frac{\partial \theta}{\partial Y}(X, 0) = 0, \quad 0 \leq X < (D - 0.5B) \text{ and } (D + 0.5B) < X \leq 1 \quad (6.5)$$

where

$$X = \frac{x}{L}, Y = \frac{y}{L}, U = \frac{uL}{(\alpha)_{bf}}, V = \frac{vL}{(\alpha)_{bf}}, \theta = \frac{T-T_c}{T_h-T_c} \quad (6.6)$$

### 6.2.3 Grid independence test

The physical domain discretisation is realised by using the bilinear quadrilateral element type as shown in Figure 6.2(a). Figure 6.2(b) shows the meshes of the present study close to the domain walls and the interface line between the porous and fluid layers are refined to capture the flow state with greater spatial resolution. The dependence of the predictions on the spatial resolution was tested on  $30 \times 30$ ,  $40 \times 40$ ,  $60 \times 60$ ,  $80 \times 80$ ,  $100 \times 100$ ,  $110 \times 110$ ,  $120 \times 120$ ,  $130 \times 130$ ,  $140 \times 140$  and  $160 \times 160$  to determine the proper grid size of this study. Figure 6.3 shows the average Nusselt numbers is predicted at different grid sizes for an enclosure partly filled by a porous slab saturated with the nanofluid at  $Ra = 10^7$ ,  $Da = 10^{-3}$ ,  $\phi = 0.2$ ,  $B = 0.4$ .  $D = S = 0.5$ ,  $\gamma = 10$  and  $H = 50$ .

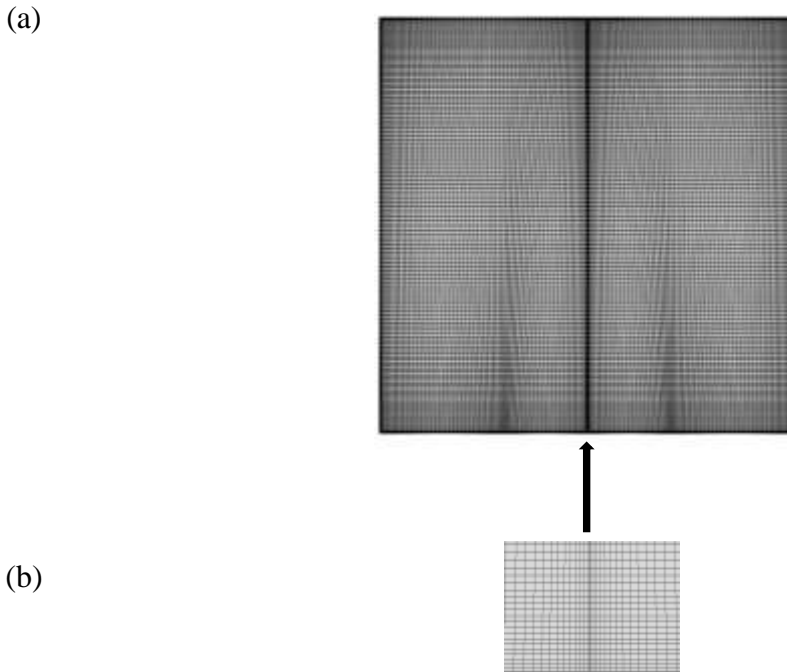


Figure 6.2: Computational mesh of (a) the physical domain and (b) Refined mesh close to the walls and the interface line between the porous and nanofluid layers.

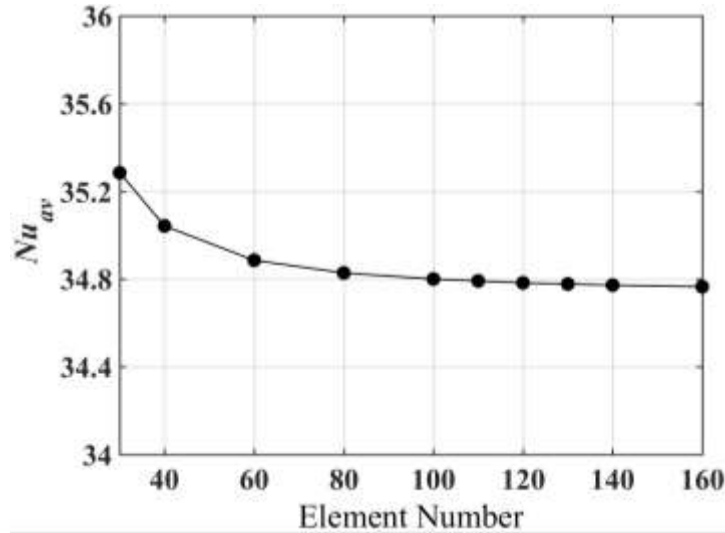


Figure 6.3: Grid testing for the average Nusselt number at different element numbers

A grid size of  $130 \times 130$  was adopted in all cases to assess the accuracy of the numerical procedure because and this mesh produced an almost identical result for the average Nusselt number as that from the largest two mesh numbers.

## 6.3 Results and discussion

### 6.3.1 Streamlines and isotherms

Figure 6.4 shows the effect of Rayleigh number ( $Ra$ ) on (a) the streamlines, (b) the fluid phase isotherms, and (c) the solid phase isotherms at  $Da = 10^{-3}$ ,  $B = 0.4$ ,  $S = D = 0.5$ ,  $\gamma = 10$  and  $H = 1$ . At low values of the Rayleigh number ( $Ra = 10^4$  and  $10^5$ ) as shown in Figure 6.4(a), the fluid near the heat source rises along the porous-fluid interface due to the density variation. The fluid moves towards the upper cold wall at different velocities due to the flow resistance produced by the porous layer. Thereafter, the flow descends along the left and right cooled walls in the porous and fluid layers. This is found to generate a relatively strong main vortex with a clockwise flow direction, which effectively covers the fluid layer, and a weak secondary vortex with an anticlockwise flow direction occupies the porous layer. The pole centres of the vortices are located near the bottom-heated wall. At  $Ra = 10^6$ , the circulation cell of the fluid layer tends to compress the vortex in the porous layer and force it away from the porous-fluid interface, with substantial changes in the circulation strength compared to the lower Rayleigh numbers. Adding 20% of nanoparticles volume fraction results in a decrease in the strength of the flow (see  $\Psi_{min}$  values). This is attributed to that the viscous force effect

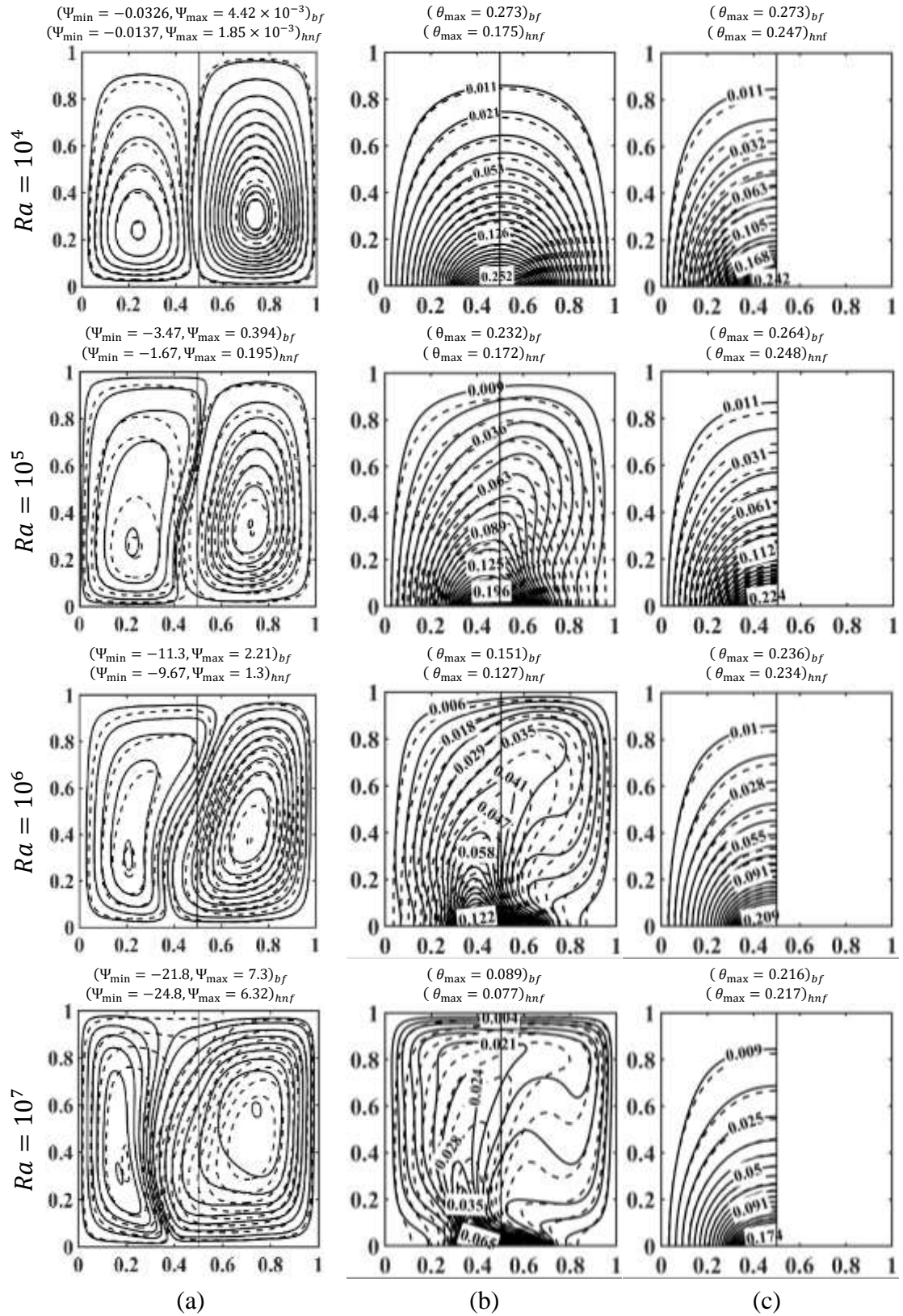


Figure 6.4: Contour maps of (a) the streamlines, (b) the fluid phase isotherms ( $\theta_{max}^f$ ) and (c) the solid phase isotherms ( $\theta_{max}^p$ ) for different Rayleigh numbers, using  $Da = 10^{-3}$ ,  $S = 0.5$ ,  $B = 0.4$ ,  $D = 0.5$ ,  $\gamma = 10$ ,  $H = 1$ ,  $\phi = 0$  (solid lines) and  $\phi = 0.2$  (dashed lines).

is greater than that of the inertial force. At  $Ra = 10^7$ , the circulation cell of the hybrid nanofluid in the porous layer tries to compress the circulation cell in the fluid layer, while for the single-phase fluid, the circulation cell in the fluid layer tries to compress the circulation cell in the porous layer. The streamlines strength of the nanofluid in the porous layer is greater than that of the single-phase fluid compared to other  $Ra$  values, where the inertial force overcame the viscous force. The circulation centre of the hybrid nanofluid in the fluid layer is closer to the bottom heat source than the circulation centre of the single-phase fluid, which results in a greater increase in the streamlines strength of the hybrid nanofluid than that for the single-phase fluid. Figure 6.4(b) shows a uniform distribution of the isotherm lines in the fluid phase is observed with lines parallel to the heat source. At  $Ra = 10^4$ , a symmetrical trend of the isotherms is predicted. This trend is changed with a greater deformation of the isotherm lines with increasing  $Ra$  from  $10^5$  to  $10^7$ . The plume of isotherm lines extends from the porous layer towards the fluid layer with a significant reduction in the thickness of the thermal boundary layer at the heat source line and the vertical cooled walls. This indicates of increasing the heat transfer at higher Rayleigh numbers. The isotherm pattern for the solid phase (porous medium) has a uniform distribution, with an increased isotherm lines density at the heat source with increasing Rayleigh number as shown in Figure 6.4(c). The difference in the temperature distributions between the single-phase fluid and the hybrid nanofluid decreases with increasing Rayleigh number, where the isotherm lines of the single-phase fluid tends to match those of the hybrid nanofluid. It is interesting to note that the presence of the nanoparticles reduces the maximum temperature inside the enclosure, as seen from the  $\theta_{max}$  values for the fluid and solid phases. This is due to the significant increase in the streamline strength and the thermal conductivity effects of the nanofluid.

Figure 6.5 shows the effect of the dimensionless permeability parameter (Darcy number,  $Da$ ) on (a) the streamlines, (b) the fluid phase isotherms, and (c) the solid phase isotherms at  $Ra = 10^6$ ,  $B = 0.4$ ,  $S = D = 0.5$ ,  $\gamma = 10$  and  $H = 1$ . Figure 6.5(a) shows that at  $Da = 10^{-5}$ , two vortices in the single-phase fluid and one in the hybrid nanofluid are predicted in the fluid layers. The primary vortex for both the single-phase fluid and hybrid nanofluid occupies most of the fluid layer and have a clockwise direction of motion. These vortices have a greater strength than the secondary (anticlockwise) vortex for the single-phase fluid that locates in the upper left corner of the fluid layer. There is a very

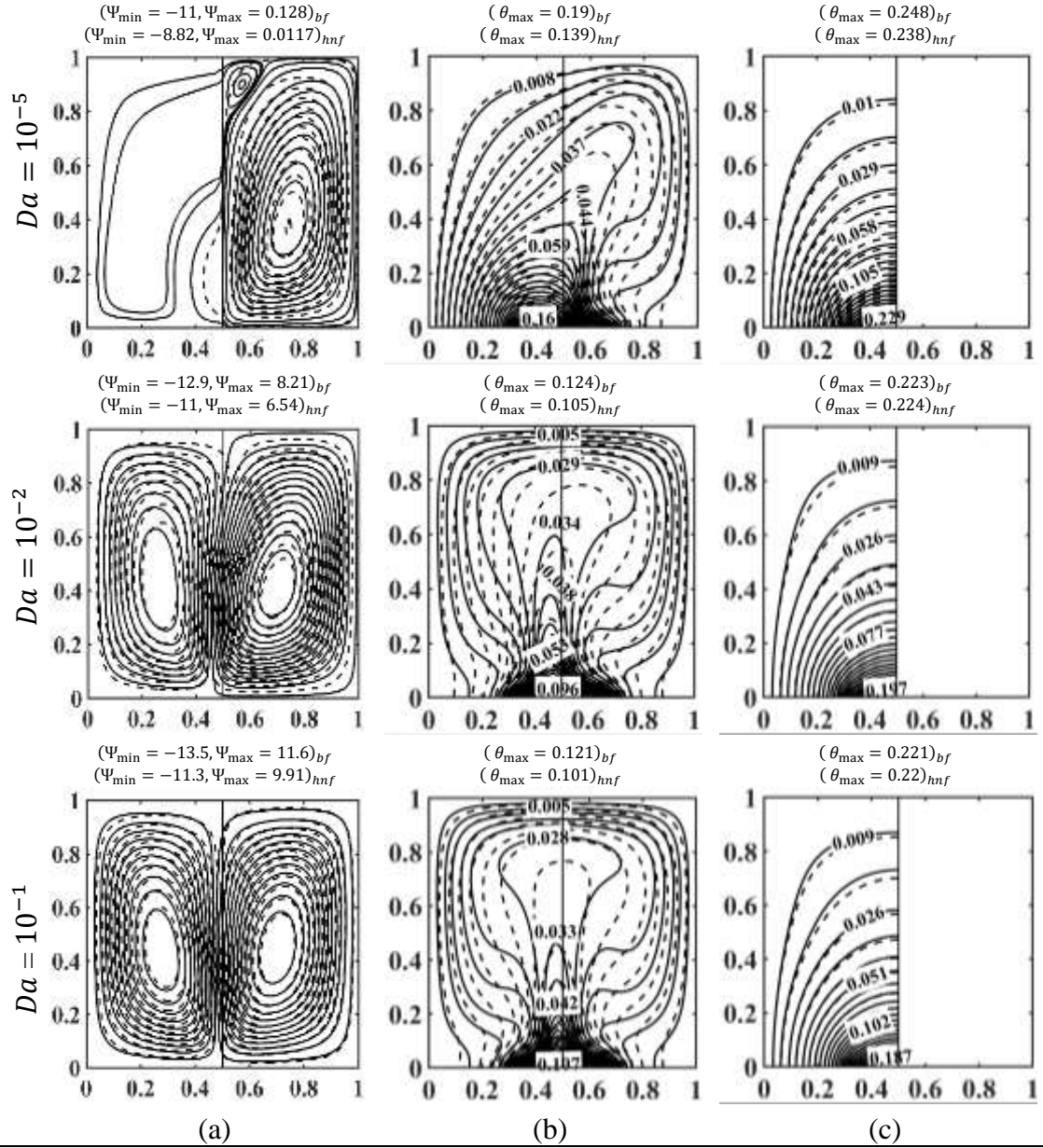


Figure 6.5: Contour maps of (a) the streamlines, (b) the fluid phase isotherms  $(\theta_{\max})_f$ , and (c) the solid phase isotherms  $(\theta_{\max})_p$  for different Darcy numbers, using  $Ra = 10^6$ ,  $S = 0.5$ ,  $B = 0.4$ ,  $D = 0.5$ ,  $\gamma = 10$ ,  $H = 1$ ,  $\phi = 0$  (solid lines) and  $\phi = 0.2$  (dashed lines).

low penetration of the flow at  $Da = 10^{-5}$  for both the single-phase fluid and hybrid nanofluid into the porous layer due to the low permeability of the porous medium. Increasing the Darcy number to  $Da = 10^{-3}$  results in two larger vortices in both the porous and fluid layers compared to  $Da = 10^{-5}$ , as shown in Figure 6.4(a) at  $Ra = 10^6$ . The anti-clockwise circulation cell strength of the fluid has a relatively significant increase in the porous layer as indicated by  $\Psi_{\max}$ , while there is a relatively small increase of the clockwise circulation cell strength of the fluid in the fluid layer as indicated by  $\Psi_{\min}$ . This is due to the lower flow resistance by the porous layer at  $Da = 10^{-3}$ . The thermal

distribution plumes for both the single-phase fluid and hybrid nanofluid in the fluid phase moves from the inclined direction in the fluid layer towards the vertical direction along the interface line, shown in Figure 6.5(b). This leads to a reduction in the thermal boundary layer thickness along the bottom-heated wall with a symmetrical distribution in the isotherm lines. This indicates an enhancing in the convective heat transfer. Figure 6.5(c) shows the isotherms of the solid phase shows a thinner thermal boundary layer as Darcy number increases with an increasing correspondence in the isotherms found in the single-phase fluid and nanofluid cases. The addition of a 20% nanoparticle sample reduces the temperature inside the enclosure, as indicated by a reduction in  $\theta_{max}$  values.

Figure 6.6 shows the effects of the porous layer thickness on (a) the streamlines, (b) the fluid phase isotherms, and (c) the solid phases isotherms at  $Ra = 10^6$ ,  $Da = 10^{-3}$ ,  $B = 0.4$ ,  $D = 0.5$ ,  $\gamma = 10$  and  $H = 1$ . Two symmetrical vortices with elliptical shapes appear inside the enclosure with equal strengths in both the clockwise and anticlockwise flow directions for both the single-phase fluid and the hybrid nanofluid at  $S = 0$ , as shown in Figure 6.6(a). This Figure also shows that at  $S = 0.3$ , asymmetric vortices appear inside the enclosure for both the single-phase fluid and the hybrid nanofluid cases because of the flow resistance of the porous layer. The primary vortex occupies most of the fluid layer and is semi-circular in shape with its centre located almost in the middle of the fluid layer. The secondary vortex centre is located close to the porous-fluid interface at the upper part of the porous layer. A relative increase in the streamline's strengths for this thickness of the porous slab is predicted compared to  $S = 0$ . This is because the main vortex of the fluid layer effectively attached most of the heated source size, which accelerates the flow. Increasing the porous layer thickness to  $S = 1$  leads to a significant reduction in the streamlines strength and produces symmetrical vortices. This is because of the equivalent effects of the porous medium on both vortices, which results in an increase in the temperature inside the enclosure. Figure 6.6(b) shows the isotherms of the fluid phase are symmetrical at  $S = 0$ , where the plume of the isotherm lines is located at the vertical centreline of the enclosure. Greater deformation of the isotherm lines for the fluid phase occurs with increasing  $S$ . At  $S = 1$ , symmetric trend of the isotherm lines occurs with a reduction in the thickness of the thermal boundary layer. This leads to a significant increase in the dimensionless temperature inside the enclosure. The isotherms for the solid phase (porous medium) seem to have a uniform distribution with a lower

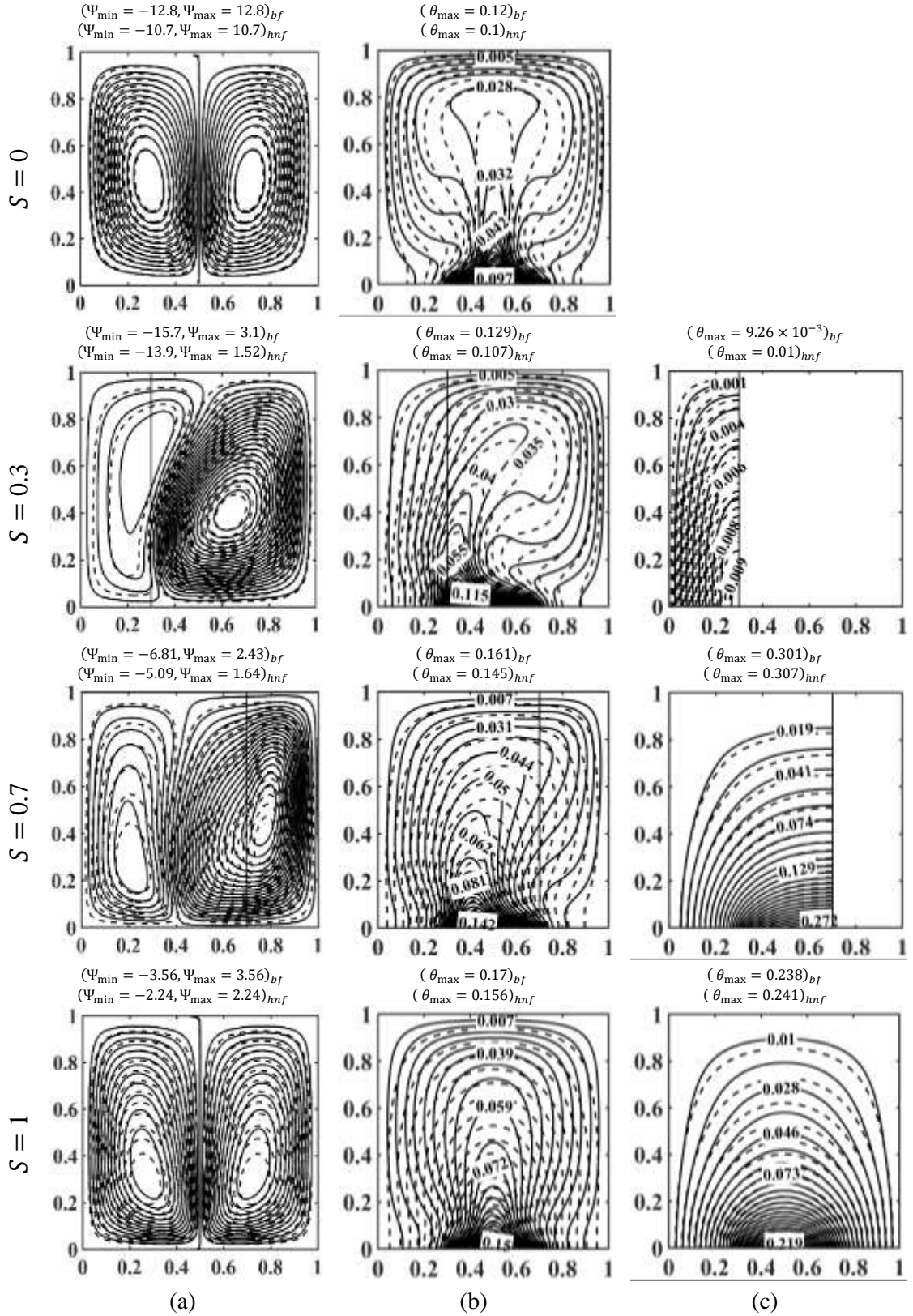


Figure 6.6: Contour maps of (a) the streamlines, (b) the fluid phase isotherms  $(\theta_{max})_f$ , and (c) the solid phase isotherms  $(\theta_{max})_p$  for different porous layer thicknesses, using  $Ra = 10^6$ ,  $Da = 10^{-3}$ ,  $B = 0.4$ ,  $D = 0.5$ ,  $\gamma = 10$ ,  $H = 1$ ,  $\phi = 0$  (solid lines) and  $\phi = 0.2$  (dashed lines).

temperature at  $S = 0.3$ , while the temperature reaches a maximum at  $S = 0.7$ , as shown in Figure 6.6(c). The addition of a 20% sample of nanoparticles to the single-phase fluid results in a reduction in temperature inside the enclosure for the fluid phase. This is because of the increased thermal conductivity of the fluid, which results in greater cooling with the nanofluid than the single-phase fluid. Conversely, this addition increases the temperature of the solid phase due to an increase in the heat received by the porous medium from the heat source compared to the single-phase fluid. This leads to enhancing the heat transfer. When the porous layer is not attached to any part of the heat source, this leads to the temperature of the fluid being greater than the solid phase, while if the porous layer is attached to either a part or the entirety of the heat source this leads to an increased temperature in the solid phase compared to the fluid phase. Generally, the convective heat transfer enhances at  $S = 0.3$  compared to other porous layer thicknesses.

Figure 6.7 shows the effects of increasing the modified conductivity ratio from  $\gamma = 0.1$  to  $\gamma = 1000$  on (a) the streamlines, (b) the fluid phase isotherms, and (c) the solid phase

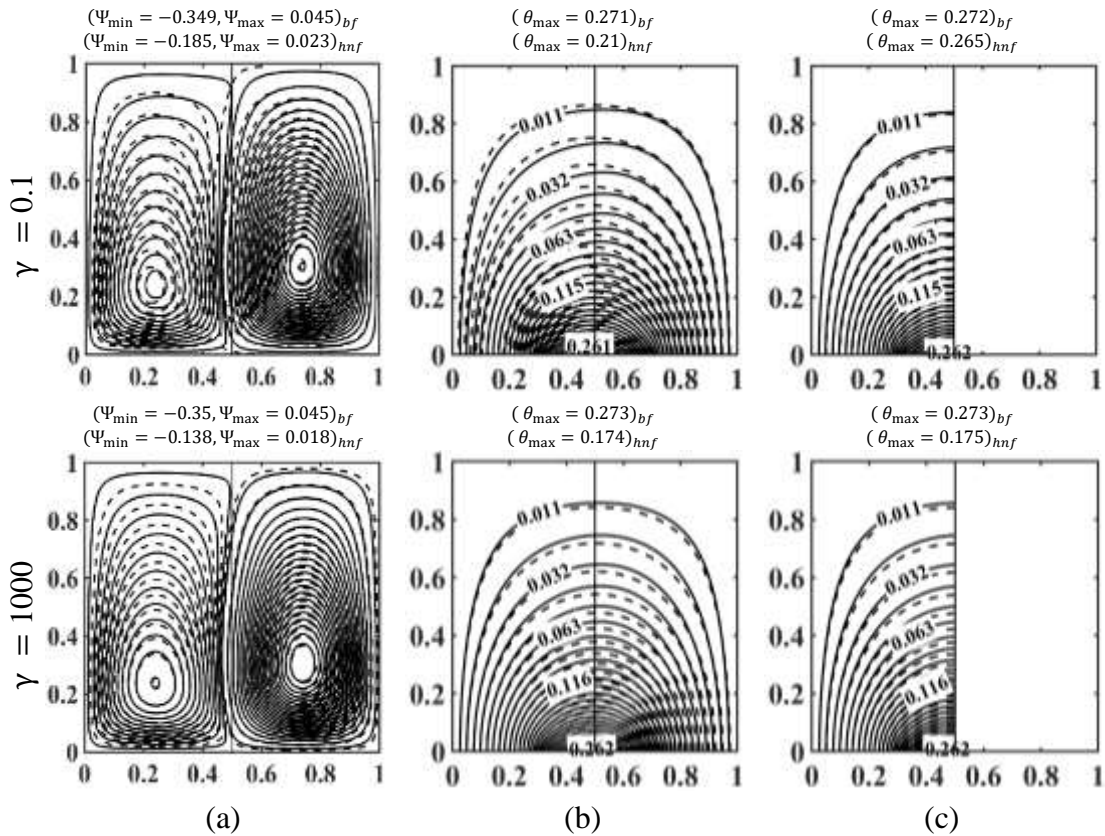


Figure 6.7: Contour maps of (a) the streamlines, (b) the fluid phase isotherms ( $\theta_{max}_f$ ), and (c) the solid phase isotherms ( $\theta_{max}_p$ ) for various modified conductivity ratios, using  $Ra = 10^4$ ,  $Da = 10^{-3}$ ,  $S = 0.5$ ,  $B = 0.4$ ,  $D = 0.5$ ,  $H = 50$ ,  $\phi = 0$  (solid lines) and  $\phi = 0.2$  (dashed lines).

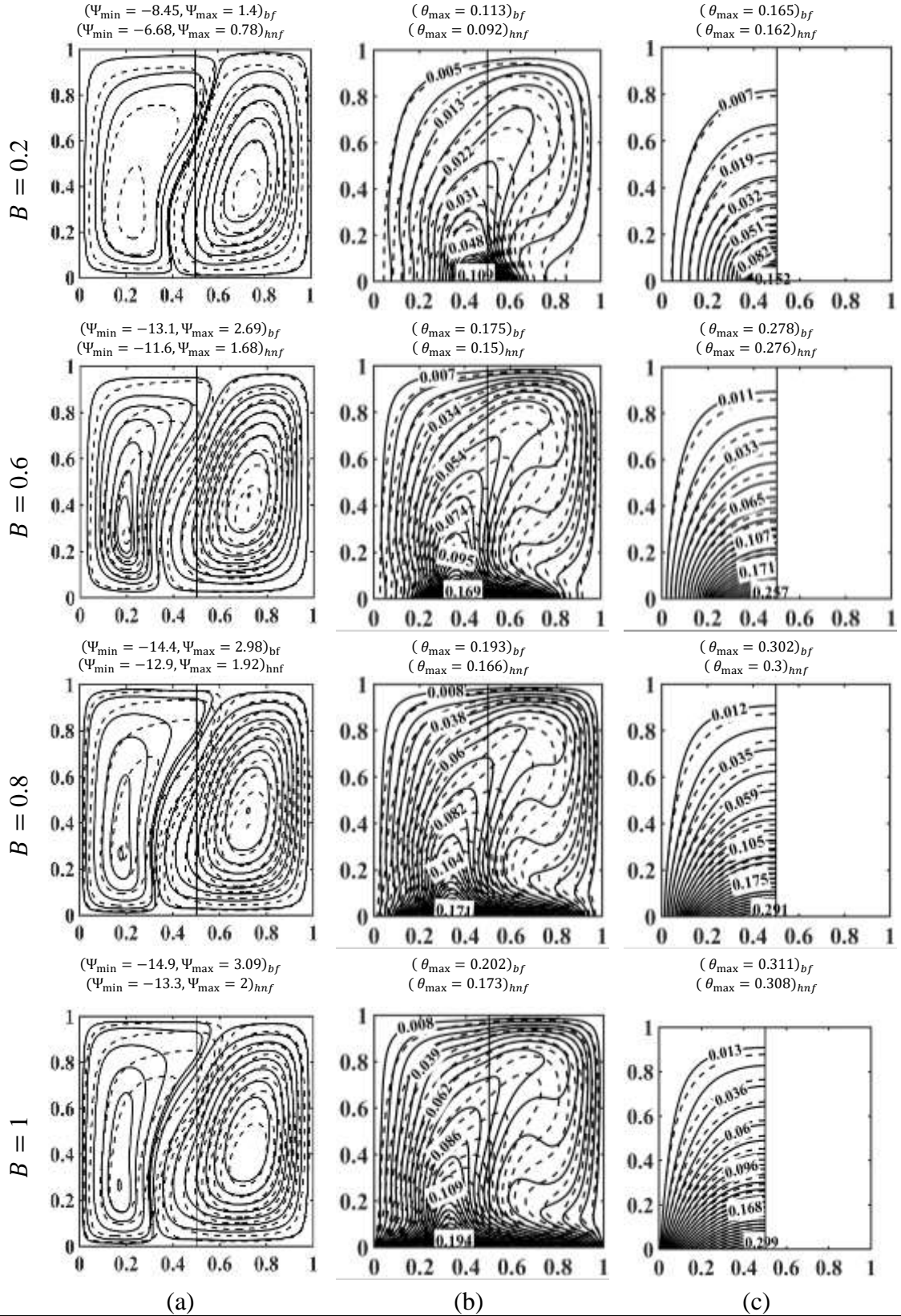


Figure 6.8: Contour maps of (a) the streamlines, (b) the fluid phase isotherms  $(\theta_{max})_f$ , and (c) the solid phase isotherms  $(\theta_{max})_p$  for different bottom-heated wall lengths, using  $Ra = 10^6$ ,  $Da = 10^{-3}$ ,  $S = 0.5$ ,  $D = 0.5$ ,  $\gamma = 10$ ,  $H = 1$ ,  $\phi = 0$  (solid lines) and  $\phi = 0.2$  (dashed lines).

isotherms, at  $Ra = 10^4$ ,  $Da = 10^{-3}$ ,  $B = 0.4$ ,  $S = D = 0.5$  and  $H = 1$ . At  $\gamma = 0.1$ , Figure 6.7(a) shows the flow trend within the enclosure is evident from the two circulatory vortices produced. There is a significant difference of the streamlines trend of the secondary vortices in the porous layer between the hybrid nanofluid and the single-phase fluid, which are of lower intensities compared to the vortices that locate in the fluid layer. Increasing the modified thermal conductivity ratio to 1000 leads to that the streamlines strength of the hybrid nanofluid increase with increasing the thermal conductivity ratio compared to the single-phase fluid, while there are no effects on the streamline's strength in the instance of the single-phase fluid. The hybrid nanofluid vortex moves towards the left cooled wall. This results in a difference in the isotherm lines between the hybrid nanofluid and the single-phase fluid in the porous layer higher than that of the difference in the fluid layer, as shown in Figure 6.7. Figure 6.7(c) shows the isotherm lines within the solid phase. The isotherm lines appear essentially identical for both the single-phase fluid and hybrid nanofluid. A convergence of the temperature distributions occurs in the fluid and solid phases to near identity. This leads to thermal equilibria with similar isotherm patterns and magnitudes in the fluid and porous phases, which is representative of the ideal heat exchange between the fluid and porous phases with greater enhancement of the heat transfer.

Figure 6.8 shows the effects of increasing the length of the heat source,  $B$  on (a) the streamlines, (b) the fluid phase isotherms, and (c) the solid phase isotherms at  $Ra = 10^6$ ,  $Da = 10^{-3}$ ,  $S = D = 0.5$ ,  $\gamma = 10$  and  $H = 1$ . At  $\theta = 0.2$ , two asymmetrical counter-rotating vortices predict inside the enclosure. Increasing  $B$  leads to increase the temperature for the fluid and porous phases as shown in Figure 6.8(b) and (c), respectively. This is due to the large amount of heat generated, which increases the buoyancy force. It is interesting to note that, increasing  $B$  increases the isotherms packing close to the hot and cold walls, especially in the fluid layer.

### **6.3.2 Velocity magnitude, $R$**

To gain a better understanding of the flow and thermal trend in this situation, the dimensionless velocity magnitude with various parameters, such as (a) Rayleigh numbers and (b) modified thermal conductivities along the porous-fluid interface at  $X = 0.5$  is reported in Figure 6.9(a) and Figure 6.9(b), respectively. Figure 6.9(a) shows the non-

dimensional velocity magnitudes for different Rayleigh numbers at  $Da = 10^{-3}$ ,  $B = 0.4$ ,  $S = D = 0.5$ ,  $\gamma = 10$  and  $H = 50$ . Increasing the Rayleigh number increases the non-dimensional velocity magnitude value because of the increased buoyancy force. Oscillation of non-dimensional velocity magnitude pattern occurs inside the cavity, and this oscillation increases with increasing Rayleigh number. This is due to the interaction of the two counter-rotating vortices that occurs in the hybrid nanofluid within the enclosure. Figure 6.9(b) shows the effects of the modified thermal conductivity ratio on the non-dimensional velocity magnitude at  $Ra = 10^6$ ,  $Da = 10^{-3}$ ,  $B = 0.4$ ,  $S = D = 0.5$  and  $H = 50$ . Decreasing the modified thermal conductivity ratio leads to an increase in the velocity magnitude due to the ability of the porous slab to receive heat from the heat source.

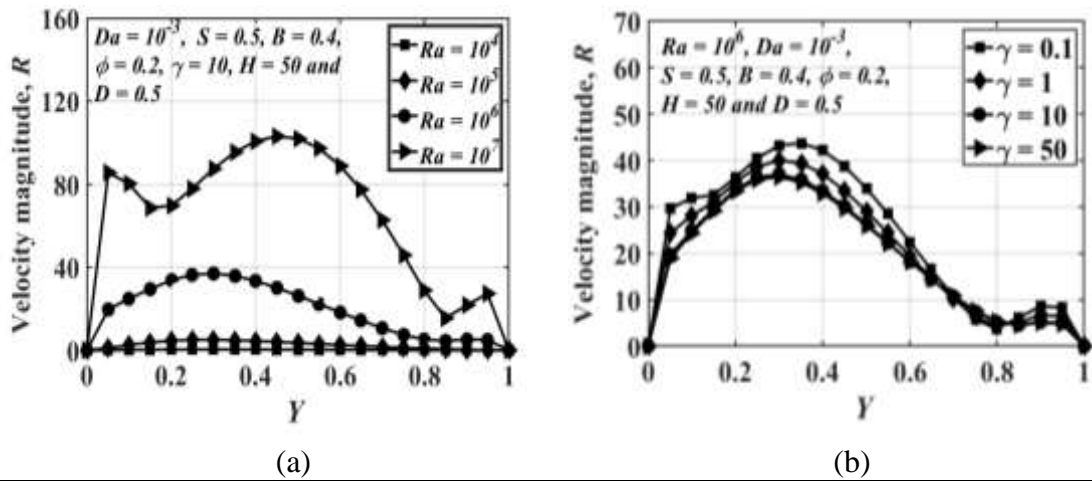


Figure 6.9: Variation of velocity resultant at the interface vertical mid-plane of the domain ( $X = 0.5$ ) for different values of (a) Rayleigh number (b) thermal conductivity ratio.

### 6.3.3 Normalized temperature distribution, $\theta$

Figure 6.10 shows the non-dimensional temperature difference between the solid and hybrid nanofluid phases with different parameters, such as (a) Rayleigh numbers and (b) modified thermal conductivities along the porous-fluid interface at  $X = 0.5$ , as shown in Figure 6.10(a) and Figure 6.10(b), respectively. The maximum non-dimensional temperature difference between the solid and the hybrid nanofluid phases occurs at  $Y = 0$ , while the minimum difference occurs at the upper wall of the enclosure with different Rayleigh numbers, as shown in Figure 6.10(a). The non-dimensional temperature difference decreases with decreasing the Rayleigh number. This means at the lower values of Rayleigh number ( $Ra \leq 10^5$ ), the non-dimensional temperature distribution

of the solid phase (porous medium) is similar to that for the hybrid nanofluid phase. This leads to the thermal equilibrium between the solid and the nanofluid phases, indicating of a high heat transfer between them. Increasing  $Ra$  results in an increase in the temperature difference between the solid and the hybrid nanofluid phases. Increasing the modified thermal conductivity leads to a reduction in the temperature difference between the solid and the nanofluid phases and that ultimately reaches to zero. This indicates of the thermal equilibrium between the solid and the nanofluid phases with a high heat transfer between them, as shown in Figure 6.10(b). Generally, at the high Rayleigh numbers and the low modified thermal conductivity ratios, especially at  $Ra > 10^5$  and  $\gamma < 1$ , the non-dimensional temperature difference between the solid and hybrid nanofluid phases is negative and positive values in the upper and lower parts of the enclosure, respectively.

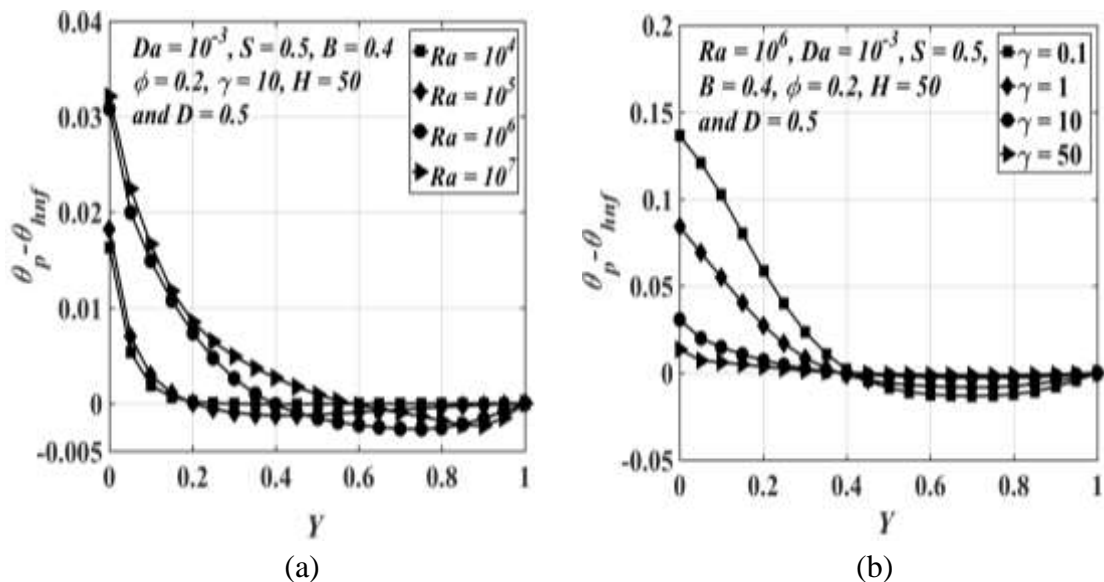


Figure 6.10: Variation of solid-to-fluid temperature difference at the interface vertical mid-plane of the domain ( $X = 0.5$ ) for different values of (a) Rayleigh number (b) thermal conductivity ratio.

Figure 6.11 shows the non-dimensional temperature distribution along the heat source with increasing the thickness of the porous slab for two different Rayleigh numbers, (a)  $Ra = 10^4$  and (b)  $Ra = 10^7$  at  $Da = 10^{-3}$ ,  $B = 0.4$ ,  $D = 0.5$ ,  $\gamma = 10$  and  $H = 50$ . Figure 6.11(a) shows that the temperature distribution seems to be symmetric along the heat source with a maximum value at its centre. Increasing the thickness of the porous slab from 0.0 to 0.3 leads to a reduction in the heat source temperature. However, it is found that increasing the thickness of the porous slab to a higher value than 0.3 increases the non-dimensional temperature of the heat source. This is attributed to the flow resistance

by the porous slab and the reduced strength of the vortices inside the enclosure. This pattern did not appear when increasing the Rayleigh number to  $10^7$ , as shown in Figure 6.11(b), where there is an asymmetric temperature distribution along the heat source when  $0.1 \leq S \leq 0.9$ , while there is a symmetrical distribution when  $S = 0$  and 1 due to the symmetrical vortices' trend within the enclosure. The non-dimensional heat source temperature at  $Ra = 10^4$  is higher than that at  $Ra = 10^7$ .

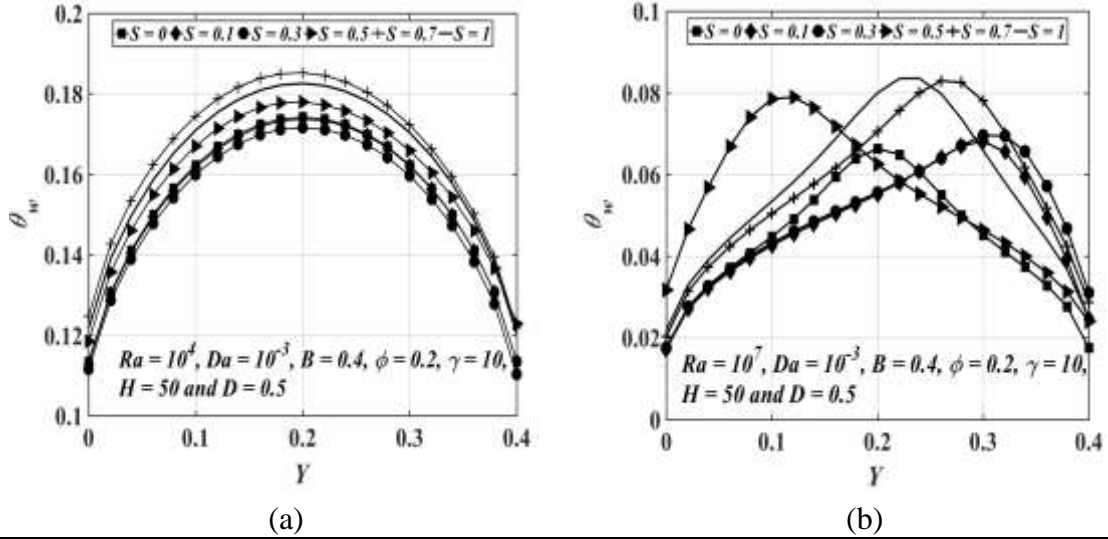


Figure 6.11: Variation of dimensionless temperature along the heat source with different porous layer thickness values when (a)  $Ra = 10^4$  and (b)  $Ra = 10^7$ .

### 6.3.4 Heat transfer rate: Local Nusselt number

The heat conduction is equal to the heat convection and to satisfy the dimensionless heat flux parameter,  $\frac{\partial(T)}{\partial(y)}$  should be equal to  $\frac{(k)_{bf}}{(k)_{hnf}}$  as follows (Aminossadati and Ghasemi, 2009)

$$q'' = \frac{(k)_{hnf}}{(k)_{bf}} \times \frac{\partial(T)}{\partial(y)} = h \times (T_w - T_c) \quad (6.7)$$

$$Nu_{local} = \frac{h.L}{(k)_{bf}} \quad (6.8)$$

The local heat transfer coefficient  $h$  is expressed as

$$Nu_{local} = \frac{h.L}{(k)_{bf}} \quad (6.9)$$

$$(k)_{nf} = \frac{-(q)_w}{\frac{\partial T}{\partial y}} \quad (6.10)$$

$$Nu_{local} = \frac{1}{(T_w - T_c)} \frac{(k)_{nf}}{(k)_{bf}} \cdot \frac{\partial(T)}{\partial(y)} \quad (6.11)$$

The local heat transfer coefficient  $h$  is expressed as

$$h = \frac{1}{(\theta)_w} \quad (6.12)$$

Using the dimensionless quantities in equation (B2.10), The local Nusselt number expressions along the heat source length thus become

$$Nu_{local} = \frac{1}{(\theta)_w} \quad (6.14)$$

Figure 6.12 shows the variation of the local Nusselt number along the heat source with different heat source lengths at  $Ra = 10^6$ ,  $Da = 10^{-3}$ ,  $S = D = 0.5$ ,  $\gamma = 50$  and  $H = 50$ . This figure shows asymmetric profiles for the local Nusselt number along the heat source for all lengths of the heat source,  $B$ . The results trend a different pattern to the previous numerical results for the local Nusselt number presented by Bourantas *et al.* (2014). due to the effects of partially filling to the enclosure by the porous medium in the present study. The new results show that the heat transfer along the heat source is found to take an asymmetric pattern and the highest and lowest local Nusselt numbers are obtained at the ends and at the porous layer near the interface line, respectively. This is attributed to the flow resistance by the porous slab with lower heat transfer rates compared to the fluid layer, where the vortices in the fluid layer have a higher strength of the streamlines compared to the porous layer. Increasing the length of heat source leads to decreasing the local Nusselt number due to the increased heat generation along the heat source.

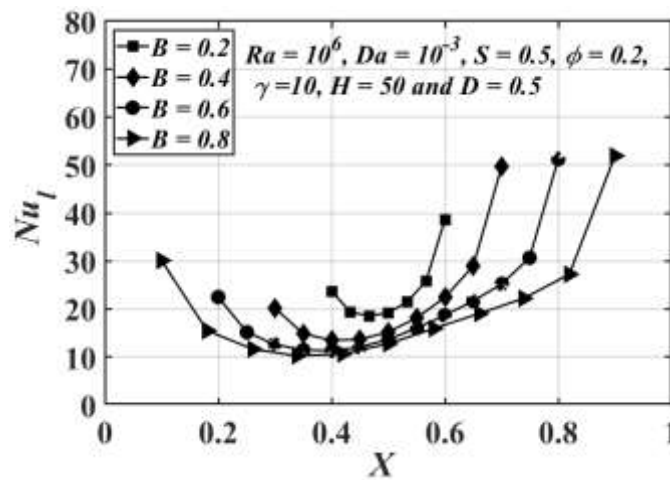


Figure 6.12: Variation of local Nusselt number with different heat source length values.

### 6.3.5 The average Nusselt number, $Nu_{av}$

The average Nusselt number is computed by the following equation

$$Nu_{av} = \frac{1}{B} \int_{D-0.5B}^{D+0.5B} Nu_{local}(X) dX \quad (6.15)$$

It is known that increasing the thickness of the porous medium reduces the heat transfer rate ( $Nu_{av}$ ); however, in this study, with the selected boundary conditions at the lower value of  $Ra$  using different volume fractions, increasing the porous layer thickness to  $S = 0.3$  enhances the heat transfer rate, as shown in Figure 6.13(a). This is attributed to the significant increase in streamline strength of the main vortex inside the fluid layer, which increases the ability of the porous medium to receive the heat from the heat source due to the higher heat exchange between the porous and the hybrid nanofluid. Thus, this leads to a reduction in the temperature of the heat source. This pattern of  $Nu_{av}$  with porous layer thickness disappears at a higher Rayleigh number of  $Ra = 10^7$ , as shown in Figure 6.13(b). Further increases in  $S$  results in a steady decrease in  $Nu_{av}$ . This is because of the reduction in the magnitude of the main vortex stemming from the flow resistance by the increased thickness of the porous slab. The reduction in heat transfer rates due to the increased thickness of the porous layer overcomes by increasing the nanoparticle volume fraction, leading to the improved thermal conductivity of the hybrid nanofluid.

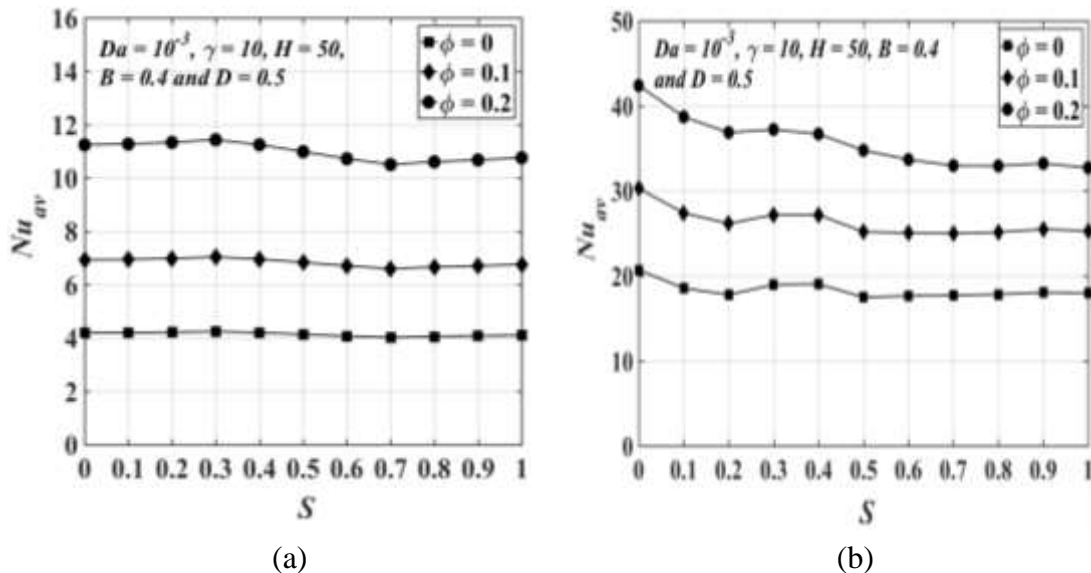


Figure 6.13: Variation of average Nusselt number with porous layer thickness for different values of nanoparticles volume fraction at (a)  $Ra = 10^4$ , and (b)  $Ra = 10^7$ .

Table 6.1 shows the heat gain with increasing nanoparticle volume fraction for different values of  $S$  at  $Ra = 10^4$ . At a constant volume fraction, a relative increase in the heat gain with  $S$  up to  $S = 0.3$  is noted; thereafter, with increasing  $S$  up to  $S = 1$ , the heat gains steadily reduce to a minimum at  $S = 0.7$ . For all values of  $S$ , a significant increase in heat gain occurs with increasing nanoparticle volume fraction ( $\phi$ ) especially at  $S = 0.3$ . At  $S = 0.3$ , the maximum percentage of the heat gain is 39.69%, and is 62.88% when  $\phi$  increases to 0.1 and 0.2, respectively, which shows that the improvement in the heat gain by using the nanofluid is greater than that for the single-phase fluid.

Table 6.1: Heat gain of average Nusselt number with different  $\phi$  and  $S$  values at  $Ra = 10^4$

$\phi \backslash S$	0	0.3	0.7	1
0	4.206	4.243	4.0178	4.1096
$Nu_{av}$ increase %	0	0	0	0
0.1	6.933	7.036	6.597	6.7536
$Nu_{av}$ increase %	39.33	39.69	39.09	39.15
0.2	11.243	11.432	10.503	10.757
$Nu_{av}$ increase %	62.59	62.88	61.74	61.8

Figure 6.14 shows the relationship between  $Nu_{av}$  and Darcy number for different values of  $\gamma$ . Significant increases in the heat transfer rates appears as  $\gamma$  increases from 0.1 to 10, especially at the higher and lower Darcy numbers. The figure shows that the convective heat transfer starts when  $Da \geq 10^{-5}$  and rapidly increases up to  $Da \geq 10^{-1}$ . There is no apparent benefit by reducing  $Da$  to less than  $10^{-5}$ , where there is no enhancement in the

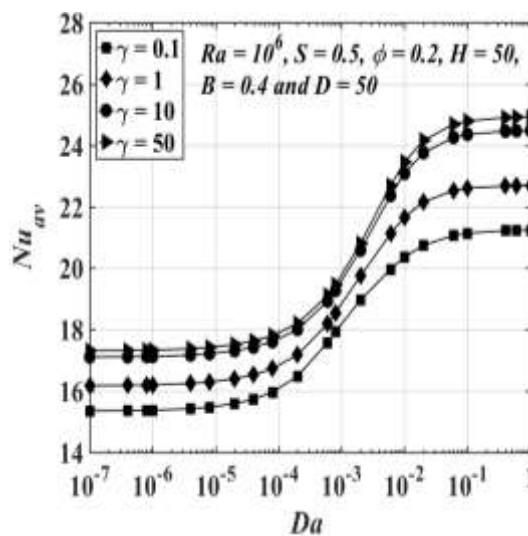


Figure 6.14: Variation of average Nusselt number versus the Darcy number for different thermal conductivity ratio values.

heat transfer rate. However, increasing the value of  $\gamma$  improves the heat transfer rate, which produces a greater enhancement at lower and higher Darcy numbers than in the range  $10^{-4} \leq Da \leq 10^{-2}$ . The enhancement in  $Nu_{av}$  at high  $Da$  is clearer with increasing  $\gamma$ . This is because a larger  $Da$  allows the flow to be freely accelerated within the porous layer compared to the lower  $Da$ .

Figure 6.15 shows the variation of average Nusselt number with Rayleigh number for different isoflux source lengths in both the pure and hybrid nanofluids. At constant  $B$ , the heat transfer rate increases with increasing the Rayleigh number. In the presence of the hybrid nanofluid,  $Nu_{av}$  is greater than that for the single-phase fluid. At  $B = 0.2$  and 1,  $Nu_{av}$  is higher than that at  $B = 0.4$  and 0.8 for both the single-phase fluid and the hybrid nanofluid. The increases in  $Nu_{av}$  at  $B = 0.2$  and  $B = 1$  compared to the other lengths is also predicted in Figure 6.16. A significant reduction in the heat transfer rate occurs when  $B$  increases from 0.2 to 0.8. A steep increase in  $Nu_{av}$  at  $B > 0.8$  for both the hybrid nanofluid and solid phases.  $Nu_{av}$  is inversely proportional to the heat source temperature. Increasing the length of the heat source leads to an increase in the temperature of the fluid and solid phases, as shown in Figure 6.8. However, the maximum  $Nu_{av}$  is at  $B = 0.2$  and  $B = 1$ . This is because that at  $B = 0.2$ , the fluid inside the enclosure could cool the heated source due to its low temperature, despite the lower streamline strength than at  $B = 1$ , and despite the higher temperature of the heat source. This figure also shows that  $Nu_{av}$  for the hybrid nanofluid phase are higher than those of the solid phase. This is indicative of

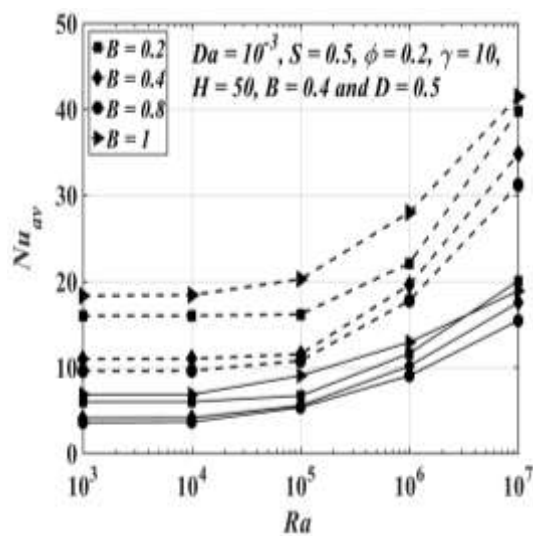


Figure 6.15: Variation of average Nusselt number versus the Rayleigh number for different heat source length values with single-phase fluid (solid line) and Hybrid nanofluid (dashed line).

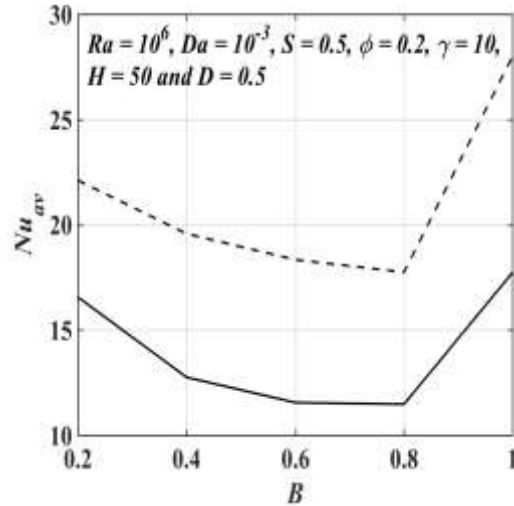


Figure 6.16: Variation of average Nusselt number versus the heat source length with the solid phase of the porous medium (solid line) and Hybrid nanofluid (dashed line).

thermal non-equilibrium between the hybrid nanofluid and solid phases.

In this study, to illustrate the ideal case of heat exchange between the solid and hybrid nanofluid phases, and to satisfy the thermal equilibrium case between them, Figure 6.17 shows the variation of  $Nu_{av}$  with  $H$  for different  $\gamma$ .  $H$  is a measure of the solid/hybrid nanofluid scaled heat transfer coefficient, which shows that the substantial difference in the results for  $Nu_{av}$  between the solid and hybrid nanofluid phases occurs at lower  $H$ . This is indicative of thermal non-equilibrium between the phases. This means that at small  $H$ , the thermal non-equilibrium case is satisfied. At constant  $\gamma$ , as  $H$  increases the thermal equilibrium case occurs and the hybrid nanofluid and solid phases are almost identical, being almost convergent in  $Nu_{av}$ .

The variation in heat transfer rate for the hybrid nanofluid and solid phases with  $\gamma$  is shown in Figure 6.18 for different  $H$  (0.1 - 500). This figure illustrates a large  $\gamma$  results in the equilibrium case between the hybrid nanofluid and the solid phases. This figure also shows that due to the convection process, increasing  $H$  leads to increasing  $Nu_{av}$  in the solid phase due to the decrease in the temperature of the solid, while the heat transfer  $Nu_{av}$  decreases in the hybrid nanofluid phase due to the increased hybrid nanofluid temperature. The  $Nu_{av}$  values are much higher for the hybrid nanofluid than those for the solid phase due to the surface contact between the porous medium material and the bottom heated source.

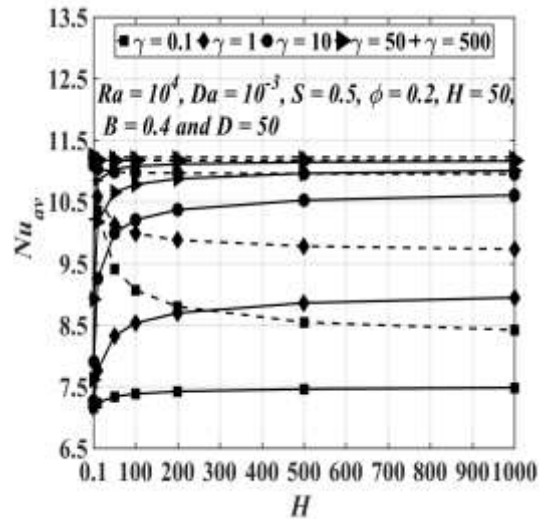


Figure 6.17: Variation of average Nusselt number versus the interface heat transfer coefficient for different thermal conductivity ratio values with the solid phase of the porous medium (solid line) and Hybrid nanofluid (dashed line).

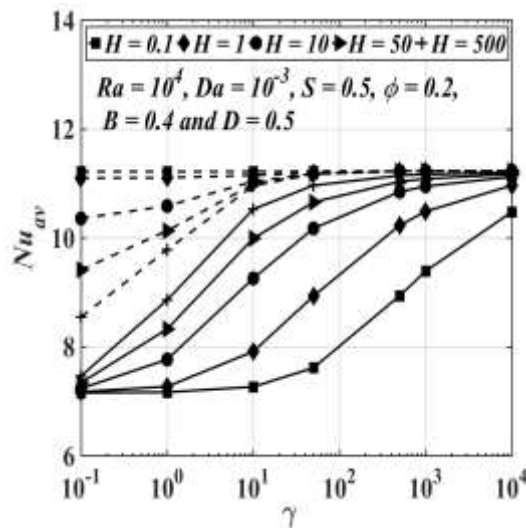


Figure 6.18: Variation of average Nusselt number versus the thermal conductivity ratio values for different interface heat transfer coefficient with the solid phase of the porous medium (solid line) and Hybrid nanofluid (dashed line).

## 6.4 Conclusions

Steady-state natural convection inside an enclosure that has been partly filled with a porous medium saturated with a hybrid nanofluid has been numerically investigated using the thermal non-equilibrium model under the influence of discrete isoflux bottom heating. The nanofluid is composed of water-based fluid containing Cu – Al<sub>2</sub>O<sub>3</sub> nanoparticles. The results obtained in terms of streamlines, isotherms and heat transfer rate. Some of the important conclusions of this study can be summarised as follows:

- Due to the thermal boundary conditions applied, two vortices with asymmetric distributions along the heat source were generated at the porous and the fluid layers; the primary clockwise vortex was located the fluid layer while the secondary anti-clockwise vortex was located in the porous layer. In addition, the stream function strength increased with increasing Rayleigh and Darcy numbers.
- Increasing the Rayleigh number and reducing the modified thermal conductivity ratio led to an increase in the non-dimensional velocity magnitude and temperature difference between the solid and hybrid nanofluid phases (non-equilibrium case), especially when  $Ra > 10^5$  and  $\gamma < 1$ .
- Increasing the length of the heat source reduced the local Nusselt number with an asymmetric distribution along the heat source itself due to the flow resistance from the porous layer compared to the fluid layer.
- Increasing the thickness of the porous medium from 0 to 0.3 increased the strength of the stream function, resulting in greater heat removal from the heat source while a reduced intensity was observed for the stream function with for the increase in the thickness of the porous medium.  $Nu_{av}$  at  $S = 0.3$  and  $Ra = 10^4$  increased with increasing the volume fraction  $\phi = 0, 0.1$  and  $0.2$ , reaching 0, 39.69% and 62.88%, respectively, which was a higher gain than those recorded for  $S = 0$ .
- Increasing the Darcy number,  $Da > 10^{-5}$  enhanced the  $Nu_{av}$  resulting from the higher permeability of the porous medium, while at  $Da \leq 10^{-5}$ , the  $Nu_{av}$  could be improved by increasing the modified thermal conductivity ratio,  $\gamma$ .
- At small values of  $\gamma$ , increasing  $H$  led to an increased  $Nu_{av}$  for the solid phase but a decrease for the hybrid nanofluid phase due to the heat received by the hybrid nanofluid from the solid phase. Increasing  $\gamma$  and  $H$  enhanced the  $Nu_{av}$  and satisfied the thermal equilibrium case.

Generally, the enclosure partly filled by a vertical porous slab saturated with a hybrid nanofluid under the effect of the isoflux heating on the bottom wall of the enclosure produced a significant and different trend of the flow and heat transfer compared to other studies. The use of the nanofluid enhanced the heat transfer more than the single-phase fluid (water). The lower thickness of the porous slab produced a higher heat transfer compared to the porous enclosure. The results may be interesting for the designer in the modern technology of the industrial engineering applications.

# **Chapter 7: Turbulent Natural Convection inside a 3-D Corrugated Sidewall Enclosure Partially Filled with a Porous Medium Saturated by a Hybrid Nanofluid Using $\kappa - \epsilon$ Model**

## **7.1 Motivation and introduction**

Considering investigations in using the thermo-physical and geometrical heat transfer controlling techniques, it can be concluded that these techniques play a vital role in optimising the convective heat transfer inside enclosures. In this study, the suggested enclosure using the combination of the three types of the heat transfer controlling techniques can produce a different heat transfer prediction than using only two types of these techniques as investigated by the previous literature. The corrugated wall produces a significant and different trend of the flow and heat transfer inside an enclosure partly filled by a porous slab compared to the enclosures that were used as flat walls of the enclosure in the previous literature. A new simulation result is presented to develop the convective heat transfer inside an enclosure partly filled by a porous slab rather than that of using a porous enclosure under the effect of the corrugated wall on one side of the enclosure. The present study for the first time explores the turbulent natural convection within an enclosure partially filled with a porous slab saturated with a hybrid nanofluid under the effect of a right corrugated sidewall of the enclosure. This investigation of the present study may be interesting to the designer to predict the convective heat transfer in the next modern industry technology.

Accordingly, in this chapter, this configuration is modelled for the ranges of the Rayleigh number ( $Ra$ ),  $10^8 \leq Ra \leq 10^{11}$ , the Darcy number ( $Da$ ),  $10^{-5} \leq Da \leq 1$ , the porous layer thickness ( $S$ ),  $0 \leq S \leq 1$ , the corrugated wall frequency ( $N_{cr}$ ),  $1 \leq N_{cr} \leq 4$ , the corrugated wall amplitude ( $A_{cr}$ ),  $0.05 \leq A_{cr} \leq 0.2$ , the thermal conductivity ratio  $K_r = 1$ , and the nanoparticle volume fraction ( $\phi$ ),  $0 \leq \phi \leq 0.2$ .

## **7.2 A model problem**

### **7.2.1 Physical model**

The problem considered is shown schematically in Figure 7.1. The three-dimensional enclosure that has a corrugated right wall and the rest of the walls are flat. The enclosure is partly filled with a porous medium saturated with an incompressible hybrid nanofluid.

The enclosure is heated with a constant temperature,  $T_h$  at the left flat surface and cooled from the opposing corrugated vertical side-wall uniform temperature,  $T_c$ . The other walls are adiabatic. The differentially heated on the vertical walls causes to develop the fluid flow inside the enclosure due to the horizontal temperature difference. This produces a density gradient (due to temperature gradient) in a horizontal direction and the gravity vector acts perpendicularly inside the enclosure, where the circulation inside the enclosure depends on these vector orientation. The thickness of the porous medium and that of the hybrid nanofluid layers are  $S$  and  $L - S$ , respectively. The right surface of the enclosure was assumed as a sinusoidal wavy wall with the following relation:

$$X = \int_0^1 A_{cr} \times \sin(N_{cr} \times \pi \times Y) dY dZ \quad (7.1)$$

Three-dimensional Reynolds-Averaged Navier-Stokes (RANS) governing equations can be found in Appendix C. The hybrid nanofluid, composed of Cu – Al<sub>2</sub>O<sub>3</sub>/ water, saturates the porous layer on the left and fill the fluid layer on the right. The flow is assumed a homogenous mixture, steady, turbulent, and incompressible. The single-phase fluid and the nanoparticles are modelled as in thermal equilibrium. The thermo-physical properties of the hybrid nanofluid are given in Table 3.1.

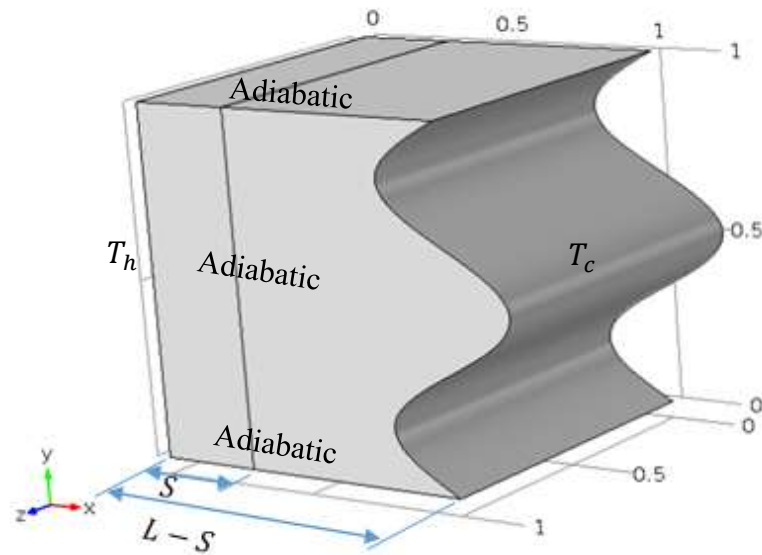


Figure 7.1: Three-Dimensional physical domain of the corrugated enclosure.

### 7.2.2 Boundary conditions

The dimensionless flow and heat governing equations in Appendix C are applied in this case study and the boundary conditions are:

$$\text{At the left hot plane wall } U = V = W = 0, \theta = 1 \quad (7.2)$$

$$\text{At the right cold plane wall } U = V = W = 0, \theta = 0 \quad (7.3)$$

$$\text{Other plane walls } U = V = W = 0 \text{ and } \frac{d\theta}{dn} = 0 \text{ (adiabatic)} \quad (7.4)$$

where  $n$  is the wall normal unit vectors and

$$X = \frac{x}{L}, Y = \frac{y}{L}, Z = \frac{z}{L}, U = \frac{uL}{(\alpha)_{bf}}, V = \frac{vL}{(\alpha)_{bf}}, W = \frac{wL}{(\alpha)_{bf}} \text{ and } \theta = \frac{T-T_c}{T_h-T_c} \quad (7.5)$$

### 7.2.3 Grid independent test

Figure 7.2 illustrates the grid of the three-dimensional domain using unstructured tetrahedral cells where the mesh nearby the walls and the interface plane between the porous and fluid layers is refined using the wall function characteristic to capture the variables. The grid refinement of the domain is performed for the three-dimensional enclosure partly filled with a porous medium saturated with a Cu – AL<sub>2</sub>O<sub>3</sub> hybrid nanofluid with the following parameter values:  $Ra = 10^{11}$ ,  $Da = 10^{-3}$ ,  $S = 0.3$ ,  $N_{cr} = 3$ ,  $A_{cr} = 0.1$ ,  $K_r = 1$  and  $\phi = 0.1$ . The grid independence test for three-dimensional computational

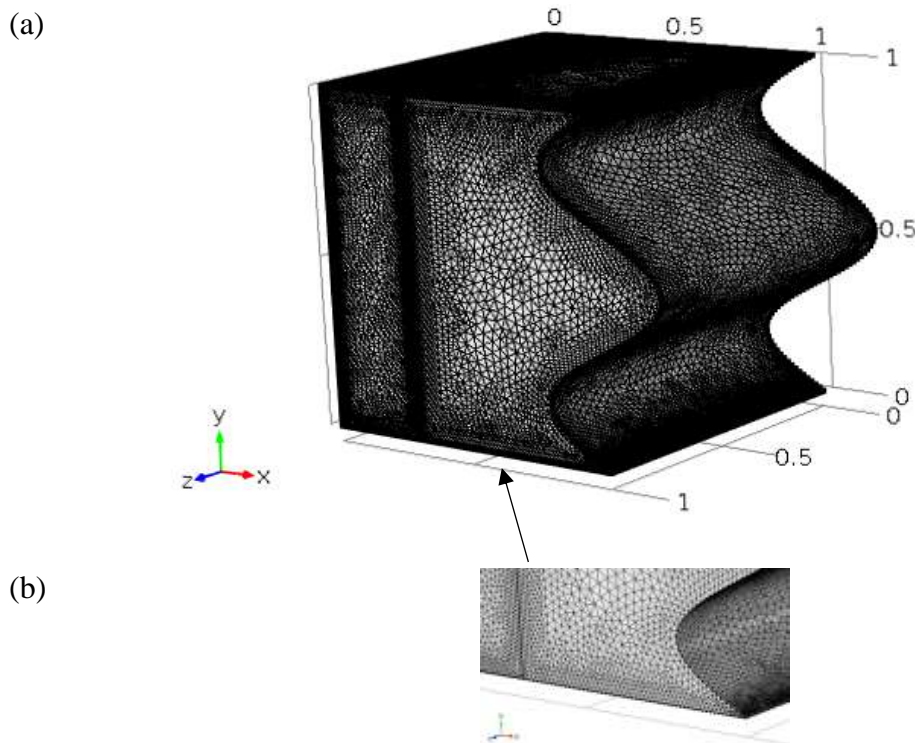


Figure 7.2: Non-dimensional computational mesh of (a) the physical domain and (b) refined mesh close to the walls.

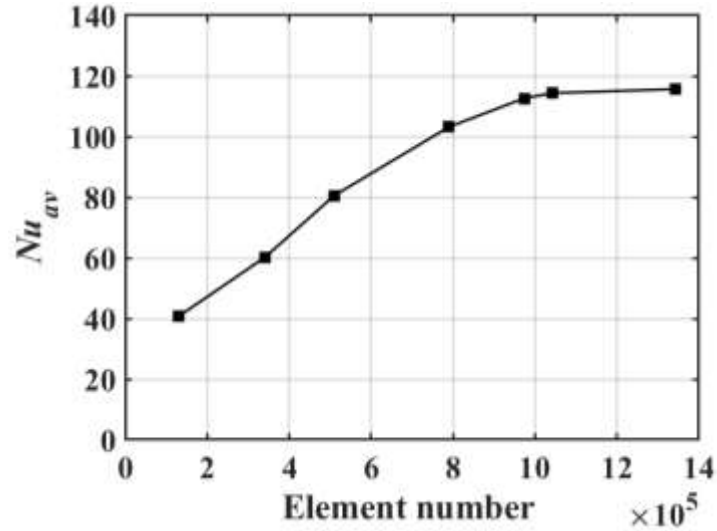


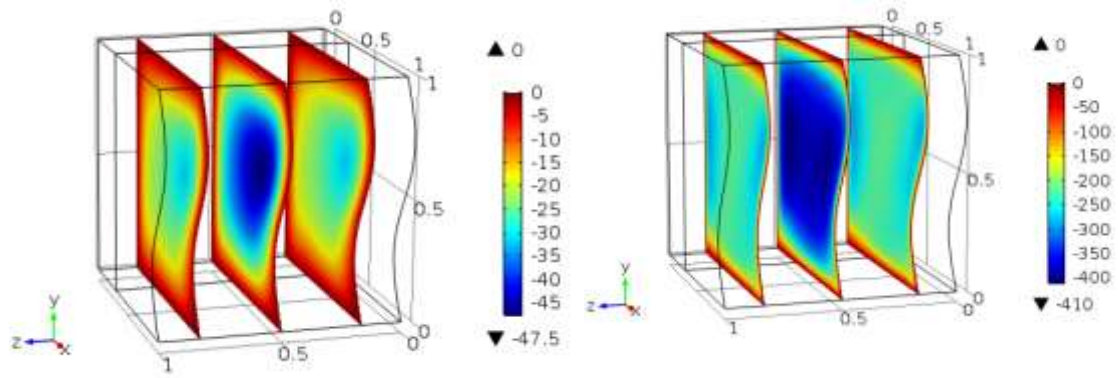
Figure 7.3: Mesh dependence of the average Nusselt number for different mesh sizes.

domain with the grid size of 130107, 341232, 510402, 790076, 973432, 1042,655, 1341723 versus the average Nusselt number is performed to satisfy the suitable mesh number in the present study as shown in Figure 7.3. A grid size of 973432 shows satisfactory mesh convergence for the average Nusselt number. This value is used for the remainder of this chapter.

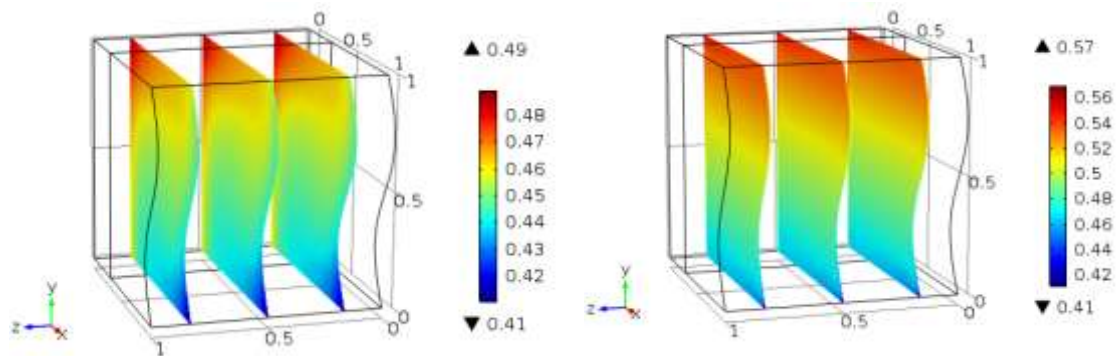
## 7.3 Results and discussion

### 7.3.1 Streamlines and isotherms

Figure 7.4 shows the slice of stream function and temperature distribution inside the three-dimensional enclosure when the Rayleigh number increases from  $10^8$  to  $10^{11}$ . At  $Ra = 10^8$ , the fluid near the left vertical sidewall inside the porous layer rises towards the upper cold wall due to the density variation. Thereafter, the flow descends along the right cooled corrugated wall in the fluid layer. This is found to generate vortices with a clockwise flow direction, which effectively covers the fluid and porous layers at  $XY$  plane along the  $Z$ -axis. It is interesting to note that the pole centre of the vortex is located near the corrugated wall with higher strength at  $Z = 0.5$  compared to other vortices along the  $Z$ -axis. Increasing the Rayleigh number to  $10^{11}$  leads to generating two vortices, one of them locates at the porous layer while another confines at the fluid layer with higher intensity of the streamlines compared to the low value of Rayleigh number. The predicted temperature distribution shows the fluid temperature increases with increasing the



Stream function



Temperature distribution

(a)  $Ra = 10^8$

(b)  $Ra = 10^{11}$

Figure 7.4: Iso-colour levels of the stream function,  $\Psi$  and of temperature normalized in the  $XY$ -planes along  $Z$ -axis as  $Da = 10^{-3}$ ,  $N_{cr} = 2$ ,  $A_{cr} = 0.1$ ,  $S = 0.3$ ,  $\phi = 0.1$  and  $K_r = 1$  at (a)  $Ra = 10^8$  and (b)  $Ra = 10^{11}$ .

Rayleigh number with a high diffusion inside the enclosure due to increasing the buoyancy force.

Figure 7.5 and Figure 7.6 show the prediction of the streamlines and the isotherms for different values of Rayleigh number ( $Ra$ ) and Darcy number ( $Da$ ). In Figure 7.5, the strength of the convective flow has a direct relationship with the maximum value of the stream function. Increasing the Rayleigh number leads to increasing the maximum value of the stream function, hence the convective flow strength increases with the Rayleigh number. At  $Ra = 10^8$  and  $Da = 10^{-5}$ , the core centre of the vortex locates and confines at the fluid layer close to the porous-fluid interface. A low stratification of the streamlines of the vortex appears within the porous layer due to the flow resistance by the porous slab due to the low value of the Darcy number.

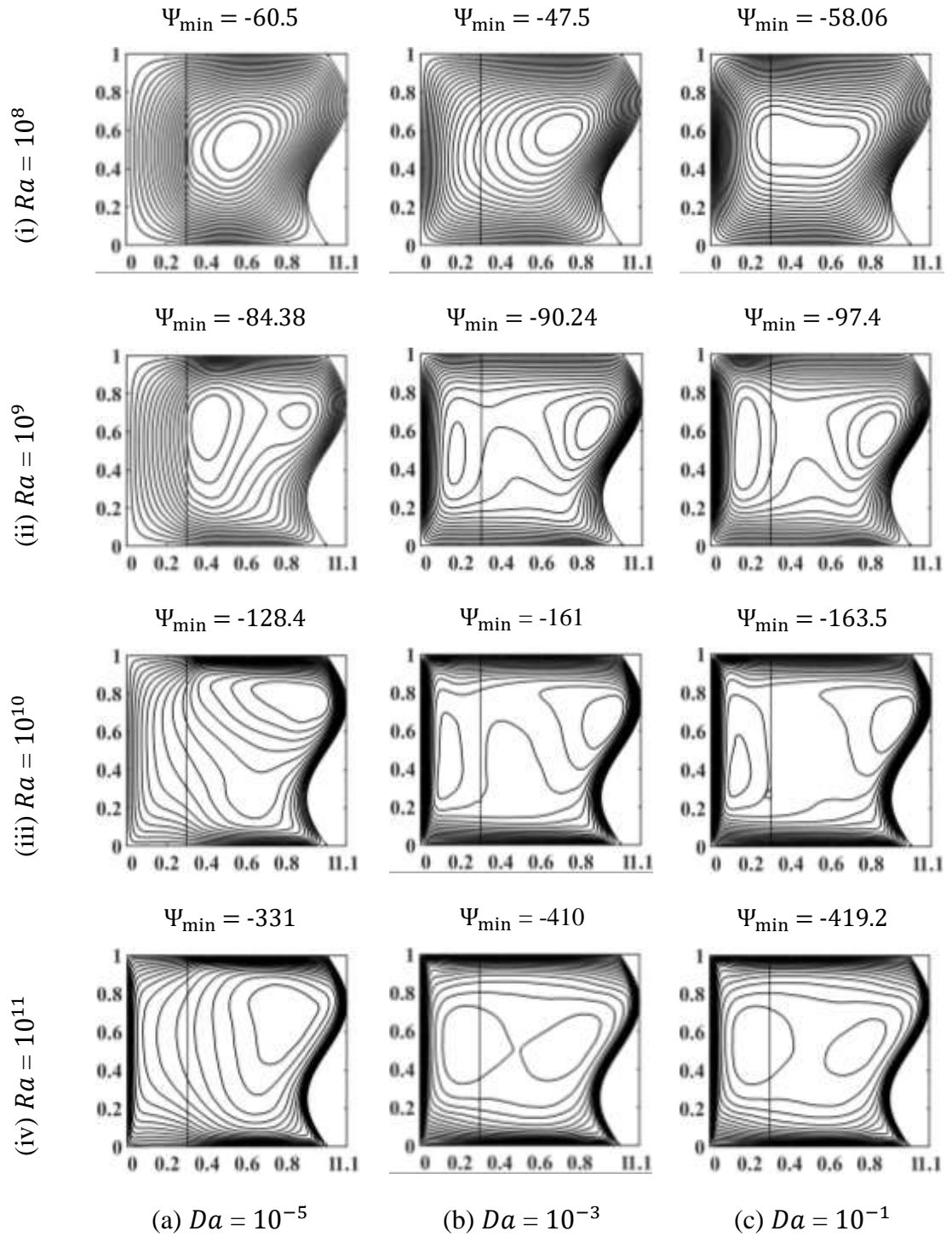


Figure 7.5: Streamlines at different values of Rayleigh numbers in the  $XY$ - plane and  $Z = 0.5$  as  $N_{cr} = 2$ ,  $A_{cr} = 0.1$ ,  $S = 0.3$ ,  $\phi = 0.1$  and  $K_r = 1$  at (a)  $Da = 10^{-5}$ , (b)  $Da = 10^{-3}$  and (c)  $Da = 10^{-1}$ .

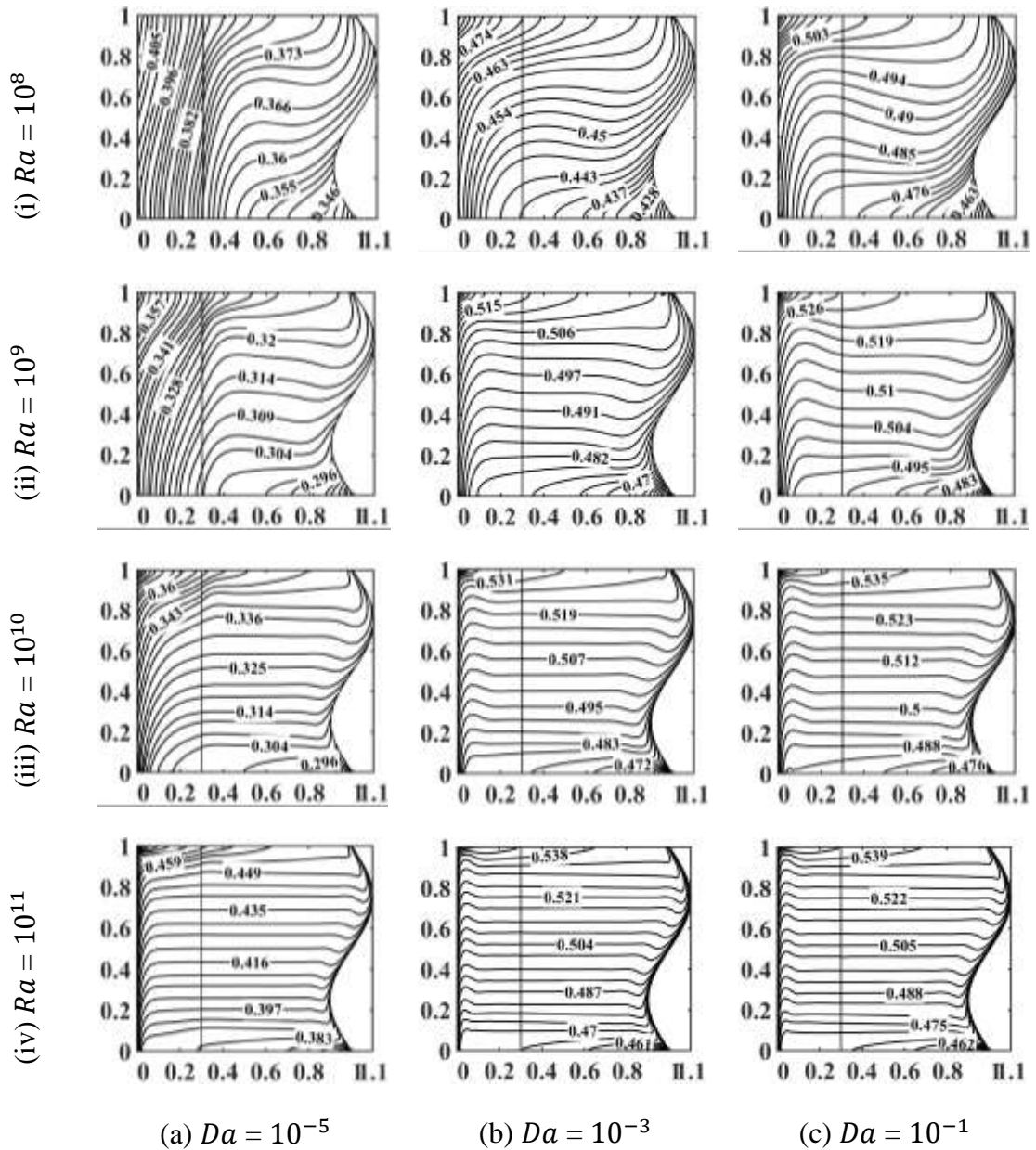


Figure 7.6: Isotherms at different values of Rayleigh numbers in the  $XY$ - plane and  $Z = 0.5$  as  $N_{cr} = 2$ ,  $A_{cr} = 0.1$ ,  $S = 0.3$ ,  $\phi = 0.1$  and  $K_r = 1$  at (a)  $Da = 10^{-5}$ , (b)  $Da = 10^{-3}$  and (c)  $Da = 10^{-1}$ .

At  $Da = 10^{-3}$ , the centre of the vortex moves towards the right corrugated cooled wall with a high penetration of the flow that increases the density of the streamlines within the porous layer. The maximum strength of the streamlines is lower value compared to  $Da = 10^{-5}$ , while increasing the Darcy number to  $10^{-1}$  leads to stretching the vortex towards the porous layer and increasing the penetration and the strength of the streamlines. Higher  $Ra$  and increasing  $Da$  from  $10^{-5}$  to  $10^{-1}$  generates two clockwise circulations close to the left and right vertical walls with more penetration, strength and density of the streamlines

compared to  $Ra = 10^8$ . This act leads to form the stratification of temperature with a lower packing density of the isotherms close to the vertical walls especially at the higher  $Ra$  and the  $Da$  numbers that indicates to the convective heat transfer as shown in Figure 7.6. This is due to the dominance of the convective heat transfer mode compared to the lower values of  $Ra$  and  $Da$  numbers that satisfies the conductive heat transfer mode.

The effect of the wave number and the amplitude of the corrugated wall on the streamlines and isotherms shown in Figure 7.7 and Figure 7.8. Figure 7.7 shows that increasing  $A_{cr}$  leads to increasing the streamlines strength for all values of  $N_{cr}$ . This is due to extending the vortex at the fluid layer towards the porous-fluid interface and closer to the vortex at the porous layer. However, increasing the wave number of the corrugated wall from  $N_{cr} = 1$  to  $N_{cr} = 2$ , the streamlines strength abates for all values of corrugated amplitude. This is due to the cell centre in the fluid layer moving away from the porous-fluid interface that decelerates the flow inside the enclosure. Increasing  $N_{cr}$  from  $N_{cr} = 2$  to  $N_{cr} = 3$  leads to increasing the streamlines strength. The vortex moves in the fluid layer towards the porous-fluid interface. It is important to observe that, increasing  $A_{cr}$  significantly separates the streamlines from the bottom part of the corrugated wall, especially at  $N_{cr} = 3$ . In addition, these separated streamlines contribute to accelerate the vortex inside the porous layer. The maximum temperature distribution of the fluid occurs at  $A_{cr} = 0.05$ , especially at  $N_{cr} = 2$  as shown in Figure 7.8. This is due to the cell centre in the fluid layer moving towards the corrugated wall. Increasing the corrugated wall amplitude from  $A_{cr} = 0.05$  to  $A_{cr} = 2$  reduces the fluid temperature due to the cell centre in the fluid layer moving towards the porous-fluid interface, especially at  $N_{cr} = 3$ . This is due to the augmentation of the streamline's strength and the convection flow at these values of the parameters. It is interesting to note that, at  $A_{cr} = 0.2$ , higher fluid temperature occurs at  $N_{cr} = 1$ . This is due to the lower effect of the separated streamlines at the bottom part of the corrugated wall inside the fluid layer compared to the other wave number values of the corrugated wall.

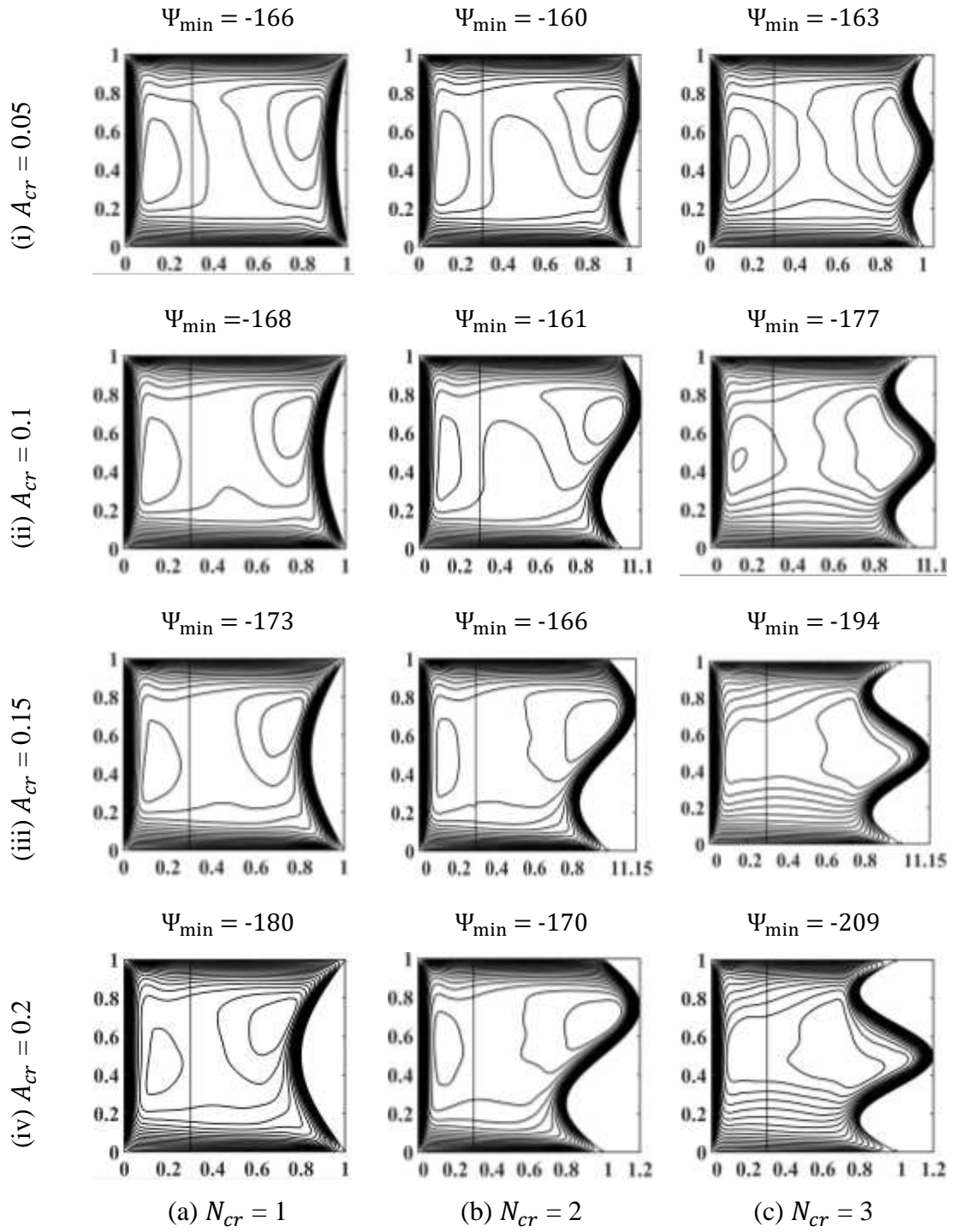


Figure 7.7: Streamlines at different corrugated wall amplitudes in the  $XY$ - plane and  $Z = 0.5$  as  $Ra = 10^{10}$ ,  $Da = 10^{-3}$ ,  $S = 0.3$ ,  $\phi = 0.1$  and  $K_r = 1$  at (a)  $N_{cr} = 1$ , (b)  $N_{cr} = 2$  and (c)  $N_{cr} = 3$ .

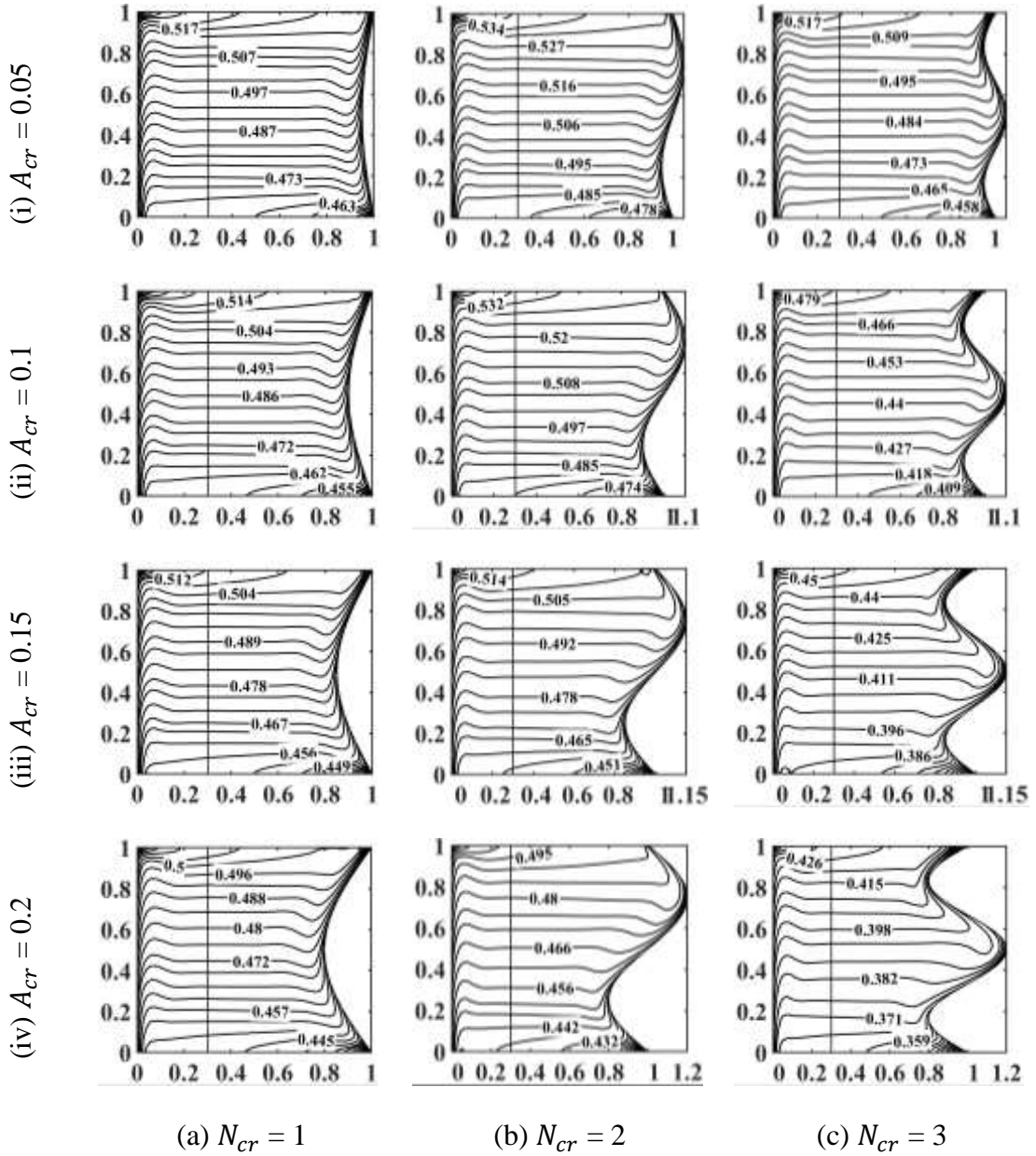


Figure 7.8: Isotherms at different corrugated wall amplitudes in the  $XY$ - plane and  $Z = 0.5$  as  $Ra = 10^{10}$ ,  $Da = 10^{-3}$ ,  $S = 0.3$ ,  $\phi = 0.1$  and  $K_f = 1$  at (a)  $N_{cr} = 1$ , (b)  $N_{cr} = 2$  and (c)  $N_{cr} = 3$ .

### 7.3.2 Average normalized turbulent kinetic energy, $K$

The effect of increasing the amplitude and the wave number of the corrugated wall on the average normalized turbulent kinetic energy in the  $YZ$ -plane and  $X = 0.3$  (interface plane) at (a)  $Ra = 10^8$ , and (b)  $Ra = 10^{10}$  shown in Figure 7.9. At  $Ra = 10^8$  and low values of  $A_{cr}$ , the average kinetic energy reduces with increasing  $N_{cr}$  as indicated in (Figure 7.9 (a)). Conversely, this trend satisfies as  $A_{cr}$  increases. As  $Ra = 10^{10}$ ,  $K$  gradually increases with increasing  $A_{cr}$  for all values of  $N_{cr}$ , especially, at  $A_{cr} = 0.2$  and  $N_{cr} = 3$ . This is due

to increasing the buoyancy force inside the enclosure as  $Ra$  increases. A minimum value of the streamline's strength is recorded at  $N_{cr} = 2$  compared to  $N_{cr} = 1$  and 3 for all values of  $A_{cr}$  shown in Figure 7.7. This is due to the cell centre in the fluid layer moving towards the corrugated wall away from the porous-fluid interface and from the vortex that is confined in the porous layer.

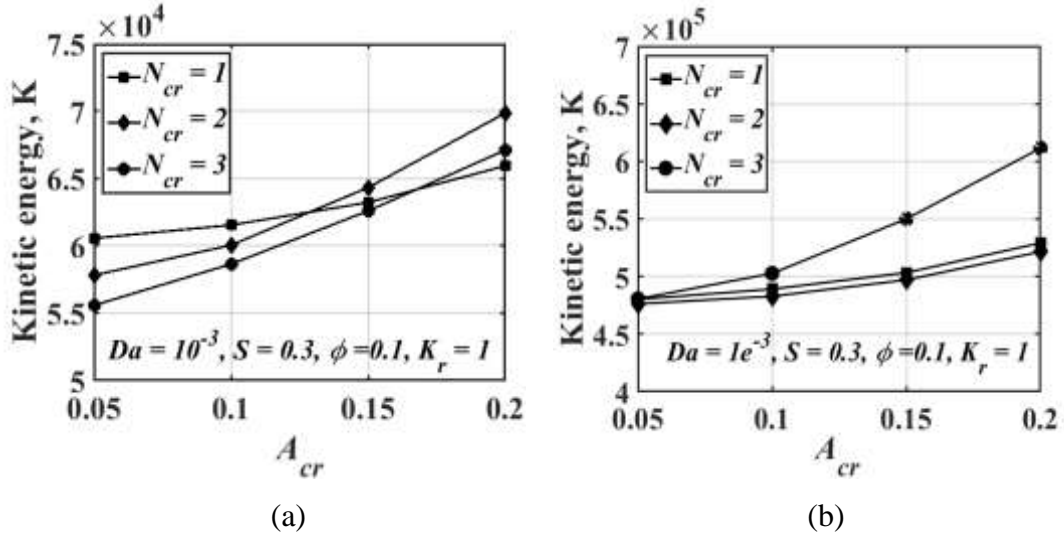


Figure 7.9: Variation of average turbulent kinetic energy versus the corrugated wall amplitude for different wave number of the corrugated wall on the  $X = 0.3$  (interface plane) at (a)  $Ra = 10^8$ , and (b)  $Ra = 10^{10}$ .

### 7.3.3 Average normalized temperature distribution, $\theta$

Figure 7.10 shows the dimensionless average fluid temperature distribution versus the corrugated wall amplitude for different wave number corrugated wall in the  $YZ$ -plane and  $X = 0.3$  (interface plane) at (a)  $Ra = 10^8$ , and (b)  $Ra = 10^{10}$ . At  $Ra = 10^8$  as shown Figure 7.10 (a), the average temperature of the fluid gradually reduces with increasing  $A_{cr}$  and  $N_{cr}$  values, especially, at  $A_{cr} = 0.2$ . At  $Ra = 10^{10}$  as shown in Figure 7.10 (b), the average temperature increases due to increasing the buoyancy force. A significant increase in the average fluid temperature is recorded at  $N_{cr} = 2$  compared to  $N_{cr} = 1$  and 3 for low values of  $A_{cr}$ , while at  $A_{cr} = 0.2$ , increasing  $N_{cr}$  leads to a significant reducing in the average temperature of the fluid. This is attributed to that, increasing  $A_{cr}$  leads to moving the vortex inside the fluid layer towards the porous-fluid interface and the vortex inside the porous layer, especially at  $N_{cr} = 1$  and 3. Generally, at low values of  $Ra$ , a significant decrease in the average fluid temperature is predicted, especially, at  $A_{cr} = 0.2$  compared to the  $Ra = 10^{10}$ .

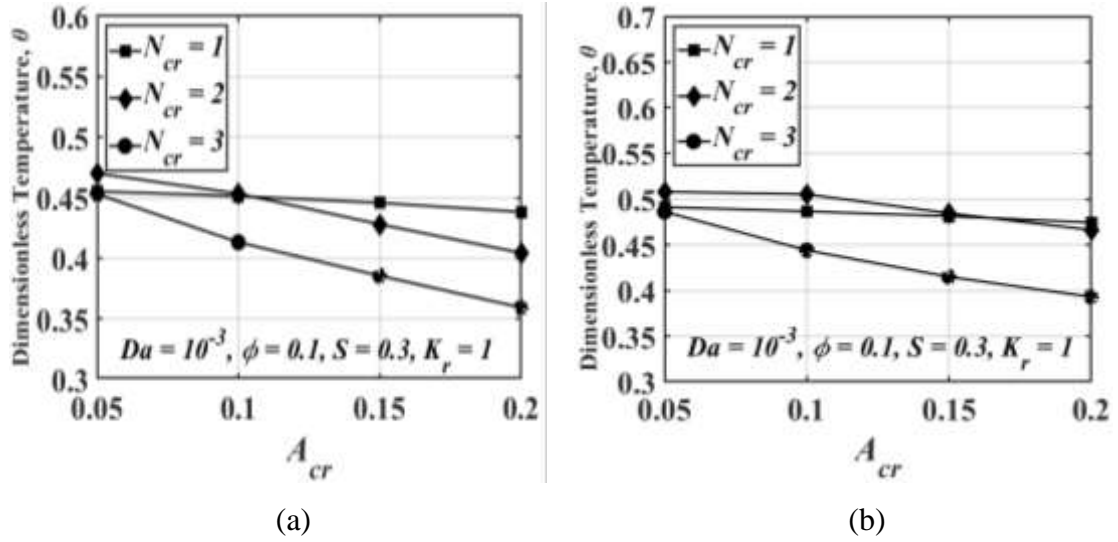


Figure 7.10: Variation of average dimensionless temperature versus the corrugated wall amplitude for different wave number corrugated wall on the  $X = 0.3$  (interface plane) at (a)  $Ra = 10^8$ , and (b)  $Ra = 10^{10}$ .

### 7.3.4 The average Nusselt number, $Nu_{av}$

The local and average Nusselt number can be calculated using the equations (4.5), (4.6) and (4.7) with the effective thermal conductivity shown in the following relation, where, the effective thermal conductivity which is equal to the summation of the laminar and turbulent thermal conductivity of the hybrid nanofluid (Mebrouk *et al.*, 2016).

$$k_{eff} = k_{Laminar} + k_{Turbulent} \quad (7.6)$$

$$k_{Turbulent} = k_{flux,turbulent} + k_{dis,turbulent} = \frac{(\mu_{turbulent})_{hnf} \times (Cp)_{hnf}}{Pr_{turbulent}} \quad (7.7)$$

$$k_{flux,turbulent} \text{ is the turbulent heat flux.} \quad (7.8)$$

$k_{dis,turbulent}$  is the turbulent thermal dispersion.

$$Nu_{local} = -K_{eff} \left( \frac{\partial \theta}{\partial X} \right)_{X=0} \quad (7.9)$$

$$Nu_{av} = \frac{1}{Surface\ area} \iint_0^1 Nu_{local} dYdZ \quad (7.10)$$

Figure 7.11 shows the variation of the average Nusselt number,  $Nu_{av}$  versus the Rayleigh number,  $Ra$  for different nanoparticles volume fraction ( $\phi$ ) at (a)  $Da = 10^{-5}$  and (b)  $Da = 10^{-3}$ . Figure 7.11 (a) shows that  $Nu_{av}$  gradually increases with increasing the value of  $Ra$ . Increasing the nanoparticles volume fraction enhances the  $Nu_{av}$  more than the single-phase fluid. This enhancement is more pronounced at the high  $Ra$ . It is interesting

to observe that; the  $Nu_{av}$  enhances by increasing  $\phi$  despite the low value of  $Da$ . At  $Da = 10^{-3}$  (Figure 7.11 (b)), the  $Nu_{av}$  improves due to increasing the permeability of the porous layer, especially at high values of  $Ra$ .

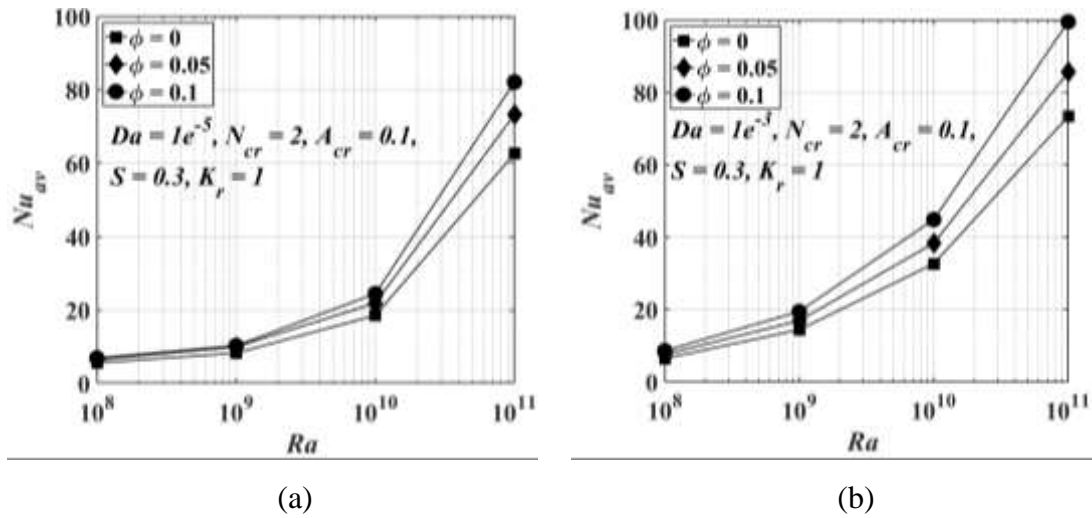


Figure 7.11: Variation of the average Nusselt number versus the Rayleigh number for different values of the nanoparticles volume fraction at (a)  $Da = 10^{-5}$ , and (b)  $Da = 10^{-3}$ .

The variation of the average Nusselt number versus the Darcy number for different wave number corrugated wall of the enclosure at (a)  $Ra = 10^8$  and (b)  $Ra = 10^{11}$  shown in Figure 7.12. Figure 7.12 (a) shows at  $Ra = 10^8$ , increasing  $N_{cr}$  leads to increasing the  $Nu_{av}$  due to the increase in the surface area that subjected to the convection especially at the high values of Darcy number. It is interesting to note that, at  $a \leq 10^{-4}$ , the  $Nu_{av}$  is almost constant and when  $Da > 10^{-4}$ , it increases gradually up to  $Da = 10^{-2}$  and

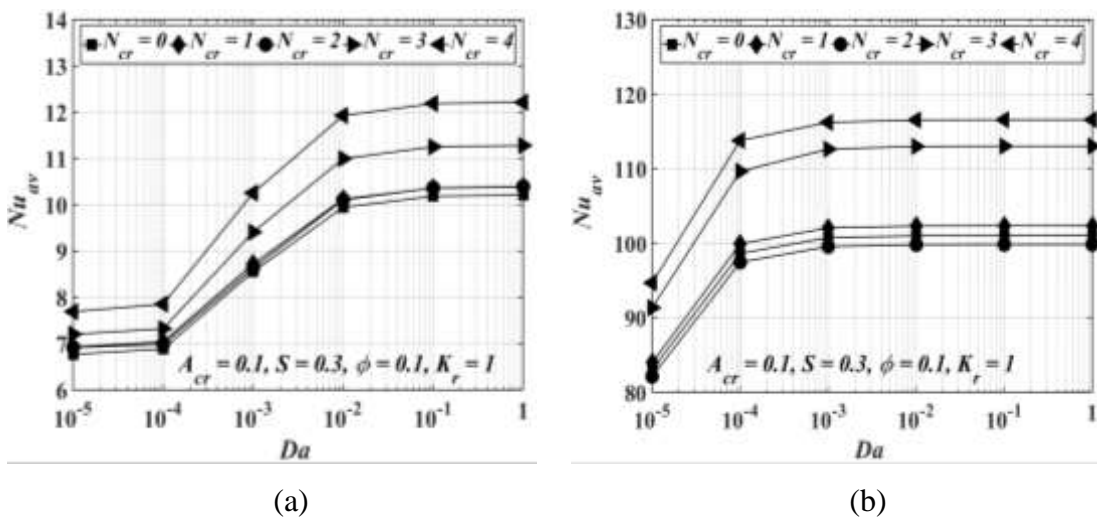


Figure 7.12: Variation of the average Nusselt number versus the Darcy number for different values of the wave number of the corrugated wall at (a)  $Ra = 10^8$  and (b)  $Ra = 10^{11}$ .

thereafter,  $Nu_{av}$  steadily increases at  $Da = 1$ . A significant increase in the  $Nu_{av}$  occurs at  $Ra = 10^{11}$  due to the increase in the buoyancy force. The heat transfer rate at  $Ra = 10^{11}$  and  $Da = 10^{-4}$  is higher than that at  $Da = 10^{-5}$  compared to the  $Ra = 10^8$  shown in Figure 7.12 (b). It is interesting to observe that, a significant difference in the values of  $Nu_{av}$  between the  $Ra = 10^8$  and the  $Ra = 10^{11}$  when  $N_{cr}$  increases from 2 to 3 and 4. This is due to increasing the surface area that subjected to the flow convection.

Figure 7.13 shows the variation of  $Nu_{av}$  versus the Darcy number for different corrugated wall amplitude of the enclosure at (a)  $Ra = 10^8$  and (b)  $Ra = 10^{11}$ . The trend of the  $Nu_{av}$  with increasing  $A_{cr}$  and  $Da$  is similar trend to that in Figure 7.12. Increasing  $A_{cr}$  enhances  $Nu_{av}$ . This is due to moving the vortex at the fluid layer towards the porous-fluid interface as well as increasing the surface area that subjected to the flow convection. In addition, increasing  $Ra$  from  $10^8$  to  $10^{11}$  leads to a significant increase in the  $Nu_{av}$ .

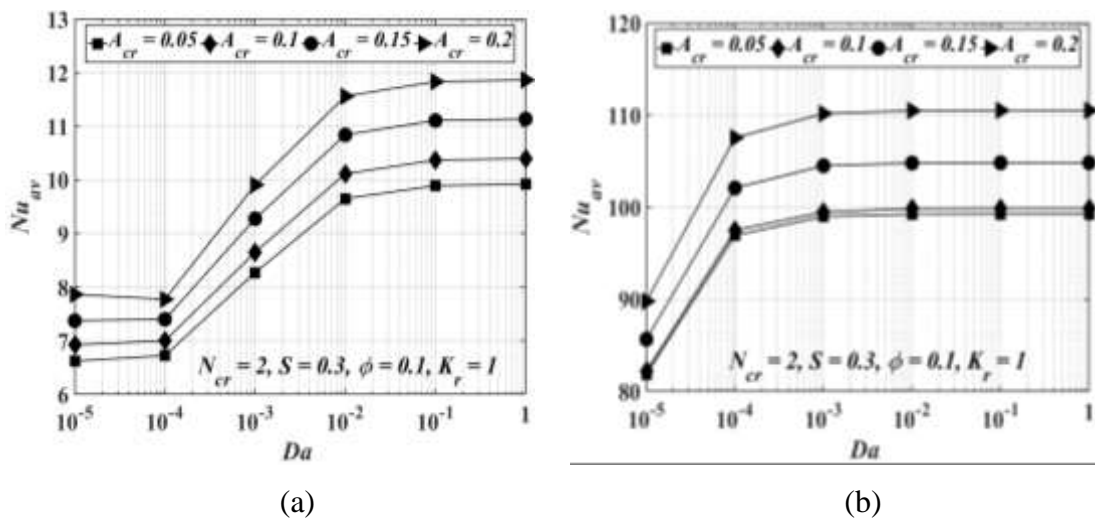


Figure 7.13: Variation of the average Nusselt number versus the Darcy number for different values of the corrugated wall amplitude at (a)  $Ra = 10^8$  and (b)  $Ra = 10^{11}$ .

The variation of  $Nu_{av}$  versus the corrugated wall amplitude for different values of the wave number corrugated wall at (a)  $Ra = 10^8$  and (b)  $Ra = 10^{10}$  shown in Figure 7.14. The common behaviour of the  $Nu_{av}$  with  $A_{cr}$  shows a significant increase in the heat transfer with increasing the corrugated wall amplitude for all  $N_{cr}$  values. Figure 7.14 (a) shows at  $Ra = 10^8$  and  $A_{cr} = 0.05$ , a maximum  $Nu_{av}$  occurs at  $N_{cr} = 1$ , while a minimum  $Nu_{av}$  satisfies at  $N_{cr} = 2$ . Increasing  $A_{cr}$  leads to a steady increase in the  $Nu_{av}$  for  $N_{cr} = 1$ , while a sharp increase in the  $Nu_{av}$  occurs at  $N_{cr} = 2$  and  $N_{cr} = 3$ . At  $A_{cr} = 0.2$ , increasing the wave number corrugated wall leads to a significant improvement in the

$Nu_{av}$ . At  $Ra = 10^{10}$  (Figure 7.14 (b)),  $Nu_{av}$  enhances due to increasing the buoyancy force inside the enclosure. At the lower values of  $A_{cr}$ , the maximum  $Nu_{av}$  occurs at  $N_{cr} = 3$ , while the minimum  $Nu_{av}$  occurs at  $N_{cr} = 2$ . This is due to moving the centre of the vortex inside the fluid layer at  $N_{cr} = 2$  away from the porous-fluid interface towards the right corrugated wall. At  $A_{cr} = 0.2$ ,  $Nu_{av}$  enhances with increasing the wave number of the corrugated wall, especially at  $N_{cr} = 3$ .

In general, increasing  $N_{cr}$  and  $A_{cr}$  contributes to cool the working fluid inside the enclosure and thus, enhances the convective heat transfer.

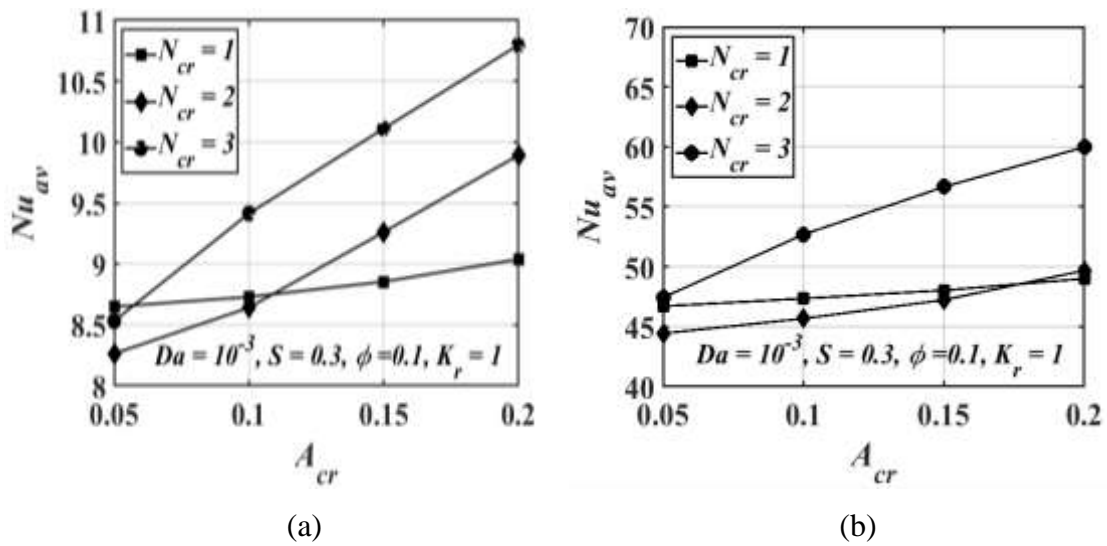


Figure 7.14: Variation of the average Nusselt number versus the corrugated wall amplitude for different values of the wave number of the corrugated wall at (a)  $Ra = 10^8$  and (b)  $Ra = 10^{10}$ .

The variation of the  $Nu_{av}$  versus the porous layer thickness ( $S$ ) for different values of the nanoparticles volume fraction shown in Figure 7.15. Using the hybrid nanofluid, increasing the nanoparticles volume fraction improves the  $Nu_{av}$  compared to the single-phase fluid. Adding these nanoparticles leads to enhancing the thermal conductivity of the single-phase fluid. Increasing the porous layer thickness from  $S = 0$  to  $S = 0.3$  enhances  $Nu_{av}$ . This is attributed to the significant increase in streamlines strength of the main vortex inside the porous and fluid layers (not shown here) up to this value of  $S$  and thereafter, higher porous thickness reduces the streamlines strength due to increasing the flow resistance by the porous layer.

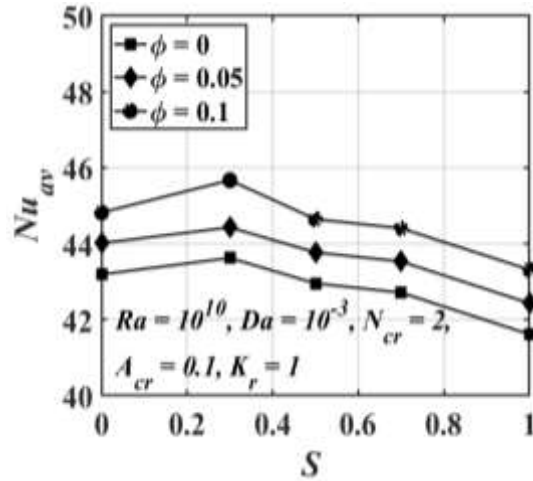


Figure 7.15: Variation of the average Nusselt number versus the porous layer thickness for different values of the nanoparticles volume fraction.

## 7.4 Conclusions

Reynolds averaged turbulent natural convection inside a three-dimensional enclosure with a right-hand side corrugated wall partly filled with a porous slab saturated with a hybrid nanofluid has been numerically investigated. The enclosure is uniformly heated with a constant temperature,  $T_h$  at the left flat surface and cooled from the opposing corrugated vertical side wall at constant temperature,  $T_c$ . The other walls are thermally insulated. The porous layer is located on the left close to the heat source while the fluid layer is located on the right close to the right corrugated wall. The nanofluid was composed of water-based fluid containing Cu – Al<sub>2</sub>O<sub>3</sub> nanoparticles. The results obtained in terms of streamlines, isotherms and average Nusselt number. The results of this study indicate the following conclusions:

- At high values of  $Ra$  and  $Da$ , one circulation cell was generated inside the enclosure. The circulation increased with increasing  $Ra$  and  $Da$  and the circulation is greater at  $Z = 0.5$  on the  $XY$ - plane.
- Increasing  $A_{cr}$  led to a higher circulation, as determined from  $\Psi_{min.}$ , for all values of  $N_{cr}$ . Increasing  $N_{cr}$  from 1 to 2, reduced the circulation for all values of  $A_{cr}$ , while it increased when  $N_{cr}$  increased from 2 to 3.
- Increasing  $A_{cr}$  from 0.05 to 0.2 reduced the fluid temperature in the enclosure due to the cell centre in the fluid layer moving towards the porous-fluid interface, especially when  $N_{cr} = 3$ .

- At  $Ra = 10^8$ , and low values of  $A_{cr}$ , as  $N_{cr}$  values increase, the average kinetic energy reduces. Conversely, K increases with  $N_{cr}$ , at  $A_{cr} = 0.2$  and  $Ra = 10^8$ . At the higher Rayleigh number of  $10^{10}$ , K gradually increases with increasing  $A_{cr}$  for all values of  $N_{cr}$ , especially, for  $A_{cr} = 0.2$  and  $N_{cr} = 3$ .
- A small increase in the average fluid temperature on the porous-fluid interface plane was recorded at  $N_{cr} = 2$  compared to  $N_{cr} = 1$  and 3 for  $A_{cr} = 0.05$ , while increasing  $A_{cr}$  to 0.2 caused to a significant reduction in the average temperature of the fluid. Generally, increasing  $N_{cr}$ ,  $A_{cr}$  resulted in cooler working fluid inside the enclosure and thus, enhancing the heat transfer performance.
- The lower thickness of the porous layer improved the average Nusselt number. In addition, the average Nusselt number is enhanced by using the hybrid nanofluid compared to the base fluid.

Generally, the results predicted a new trend of the flow and heat transfer using the vertical porous slab saturated with a hybrid nanofluid inside the enclosure compared to other studies. It may be interesting for the designer in the modern technology of the industrial engineering applications.

## Chapter 8: Conclusions and Recommendations

### 8.1 Conclusions

In this thesis, steady-state laminar and turbulent convection flows inside enclosures partly filled with a porous medium saturated with a nanofluid with various thermal boundary conditions have been studied. The CFD simulations used the Galerkin finite element method to solve the governing equations implemented with the SIMPLE algorithm in COMSOL Multiphasic 5.1a and 5.3a. The Darcy-Brinkmann model was adopted to model the porous layer. Two main enclosure geometries are used with various thermal boundary conditions. First geometry shape is a two-dimensional enclosure with flat walls for the laminar flow investigation. Second geometry shape is a three-dimensional enclosure with a wavy right surface while the rest surfaces are flat for the turbulent flow investigation. A single-phase fluid and two types of nanofluids have been studied in this project. From the present studies, the following conclusions are drawn:

#### 8.1.1 Natural Convection within an Enclosure Filled with Composite Nanofluid-Porous Layers with a Linearly Heated Left Wall

The selected boundary conditions generate two vortices inside the enclosure. A stronger clockwise vortex covered most of the enclosure area and a second weaker anticlockwise vortex confined in the upper left corner of the enclosure. The nanofluid produced a higher average Nusselt number compared to the base fluid. The use of an enclosure partly filled by a porous slab provided a higher average Nusselt number than that for an enclosure filled by a porous slab. Increasing  $Ra$  caused the intensity of the streamlines in case 2 to be stronger than that in case 1. Lower values of  $K_r$  are predicted to provide higher Nusselt numbers. At the low values of thermal conductivity ratio  $K_r < 1$ , and  $Da < 10^{-3}$ , the average Nusselt number was higher for case 2 compared to case 1 while a higher Darcy number gave the converse. Higher values of  $S$  are predicted to provide lower Nusselt number in case 1 compared to case 2 for different  $Ra$  and  $K_r$  values and at  $Da < 10^{-3}$ . The linear thermal boundary condition and the alignment of the porous slab in a vertical or a horizontal direction played an important role in the trend of the convective heat transfer inside an enclosure partly filled by a porous slab saturated with a nanofluid.

### **8.1.2 Effects of a Sinusoidally Heated Left Wall on Natural Convection within an Enclosure Filled with Composite Nanofluid-Porous Layers**

The results show that the thinner porous layers strongly enhanced the average Nusselt number. The average Nusselt number increased with increasing  $Ra$  and  $A_{th}$ , while it decreased with increasing odd values of  $N_{th}$ . The use of an enclosure partly filled by a porous slab provided a higher average Nusselt number than that for an enclosure filled by a porous slab. At the low values of the Darcy number, the average Nusselt number was increased in case 2 compared to case 1 when  $K_r \geq 1$  for different values of  $A_{th}$ ,  $N_{th}$ , and  $Ra$ . The low values of  $K_r$  produced higher average Nusselt number predictions in case 1 compared to case 2 for different values of the Rayleigh numbers. The sinusoidal thermal boundary condition and the alignment of the porous slab in a vertical or a horizontal direction played an important role in the trend of the convective heat transfer inside an enclosure partly filled by a porous slab saturated with a nanofluid.

### **8.1.3 Natural Convection of a Hybrid Nanofluid in a Square Enclosure Partially Filled with a Porous Medium Using a Thermal Non-Equilibrium Model**

Two vortices with asymmetric distributions along the heat source were generated at the porous and the fluid layers; the primary clockwise vortex was located the fluid layer while the secondary anti-clockwise vortex was located in the porous layer. In addition, the stream function strength increased with increasing Rayleigh and Darcy numbers. It has been concluded that the average Nusselt number using a hybrid nanofluid ( $Cu - Al_2O_3$ /water) was higher than that with the single-phase fluid. Further, at  $Ra \leq 10^5$  the average Nusselt number maintained its maximum value when  $S$  reached the critical value ( $S = 0.3$ ). Therefore, the use of an enclosure partly filled by a porous slab provided a higher average Nusselt number than that for an enclosure filled by a porous slab. The values of  $S$ ,  $Da$ , and  $B$  were found to have a significant effect on the heat removal from the heat source. At small values of  $\gamma$ , increasing  $H$  led to an increased  $Nu_{av}$  for the solid phase but a decrease for the hybrid nanofluid phase due to the heat received by the hybrid nanofluid from the solid phase. Increasing the values of  $\gamma$  and  $H$  can strongly enhance the average Nusselt number.

### **8.1.4 Turbulent Natural Convection inside a 3-D Corrugated Sidewall Enclosure Partially Filled with a Porous Medium Saturated by a Hybrid Nanofluid Using $\kappa - \epsilon$ Model**

At high values of  $Ra$  and  $Da$ , the selected boundary conditions generated two vortices inside the enclosure. One of vortices' core centre was located at the porous layer and another vortex's core centre was located at the fluid layer. The high value of circulation was highest on the  $Z = 0.5$  plane. The lowest circulation was at  $N_{cr} = 2$  for all  $A_{cr}$  values, while the circulation strength increased with increasing  $A_{cr}$  for all  $N_{cr}$  values. Increasing  $N_{cr}$  and  $A_{cr}$  values caused to cool the fluid temperature inside the enclosure due to increasing the cooled surface area except when  $N_{cr} = 2$ . The hybrid nanofluid was produced more enhancement of Nusselt number compared to the base fluid. The use of an enclosure partly filled by a porous slab provided a higher average Nusselt number than that for an enclosure filled by a porous slab.

## **8.2 Recommended future work**

Natural convection inside enclosures is one of the most highly investigated subjects because of its wide applications, as mentioned earlier in the literature review. Accordingly, the literature review observed that numerous researchers have been continually investigating and developing on the idea of using the heat transfer controlling techniques. Based on this project, the following recommendation could be made for a future study:

- An experimental study can be contracted to validate the results of the present study.
- A comparison of various types of nanoparticles used in the nanofluid as an extension for the selected geometries in the present study could be made.
- The study of non-uniform thermal boundary condition on the laminar natural convection inside a two-dimensional corrugated enclosure partly filled by a porous medium saturated with a hybrid nanofluid
- The effects of non-uniform thermal boundary condition on the unsteady laminar natural convection inside a three-dimensional corrugated enclosure partly filled with a porous medium using a local thermal non-equilibrium model can be investigated.

- The study of local thermal non-equilibrium model for laminar or turbulent natural convection inside other shapes of enclosure partly filled with a porous medium saturated with a nanofluid using other ranges of physical and geometrical parameters could be conducted.
- A numerical study of a three-dimensional unsteady turbulent natural convection inside an enclosure partly filled with a porous medium saturated with a nanofluid with non-uniform thermal boundary conditions and other ranges of physical and geometrical parameters could also be undertaken.

## References

- AAIZA, G., KHAN, I. & SHAFIE, S. 2015. Energy Transfer in Mixed Convection MHD Flow of Nanofluid Containing Different Shapes of Nanoparticles in a Channel Filled with Saturated Porous Medium. *Nanoscale research letters*, 10, 1-14.
- ABRAMOV, A. & SMIRNOV, E. M. 2006. Numerical simulation of turbulent convection of air in a square cavity heated on the side. *High temperature*, 44, 91-98.
- ABU-NADA, E. & OZTOP, H. F. 2011. Numerical analysis of Al<sub>2</sub>O<sub>3</sub>/water nanofluids natural convection in a wavy walled cavity. *Numerical Heat Transfer, Part A: Applications*, 59, 403-419.
- AFRAND, M. 2017. Experimental study on thermal conductivity of ethylene glycol containing hybrid nano-additives and development of a new correlation. *Applied Thermal Engineering*, 110, 1111-1119.
- AFRAND, M., NADOOSHAN, A. A., HASSANI, M., YARMAND, H. & DAHARI, M. 2016. Predicting the viscosity of multi-walled carbon nanotubes/water nanofluid by developing an optimal artificial neural network based on experimental data. *International Communications in Heat and Mass Transfer*, 77, 49-53.
- AKBARI, O. A., SAFAEI, M. R., GOODARZI, M., AKBAR, N. S., ZARRINGHALAM, M., SHABANI, G. A. S. & DAHARI, M. 2016. A modified two-phase mixture model of nanofluid flow and heat transfer in a 3-D curved microtube. *Advanced Powder Technology*, 27, 2175-2185.
- AL-AMIRI, A., KHANAFER, K., BULL, J. & POP, I. 2007. Effect of sinusoidal wavy bottom surface on mixed convection heat transfer in a lid-driven cavity. *International Journal of Heat and Mass Transfer*, 50, 1771-1780.
- AL-NIMR, M. & KHADRAWI, A. 2003. Transient free convection fluid flow in domains partially filled with porous media. *Transport in porous media*, 51, 157-172.
- ALSABERY, A., CHAMKHA, A., HASHIM, I. & SIDDHESHWAR, P. 2017a. Effects of Nonuniform Heating and Wall Conduction on Natural Convection in a Square Porous Cavity Using LTNE Model. *Journal of Heat Transfer*, 139, 122008.
- ALSABERY, A., CHAMKHA, A., HUSSAIN, S., SALEH, H. & HASHIM, I. 2015. Heatline visualization of natural convection in a trapezoidal cavity partly filled with nanofluid porous layer and partly with non-Newtonian fluid layer. *Advanced Powder Technology*, 26, 1230-1244.
- ALSABERY, A., CHAMKHA, A., SALEH, H. & HASHIM, I. 2017b. Natural convection flow of a nanofluid in an inclined square enclosure partially filled with a porous medium. *Scientific Reports*, 7, 2357.

- ALSABERY, A., ISMAEL, M., CHAMKHA, A. & HASHIM, I. 2018. Numerical Investigation of Mixed Convection and Entropy Generation in a Wavy-Walled Cavity Filled with Nanofluid and Involving a Rotating Cylinder. *Entropy*, 20, 664.
- ALSABERY, A., SALEH, H., HASHIM, I. & SIDDHESHWAR, P. 2016. Transient natural convection heat transfer in nanoliquid-saturated porous oblique cavity using thermal non-equilibrium model. *International Journal of Mechanical Sciences*, 114, 233-245.
- ALTAÇ, Z. & UĞURLUBILEK, N. 2016. Assessment of turbulence models in natural convection from two-and three-dimensional rectangular enclosures. *International Journal of Thermal Sciences*, 107, 237-246.
- AMECTHERMASOL. 2017. *MPC Application Introduction* [Online]. Available: <https://amecthermasol.co.uk/datasheets/MPC303050WT.pdf> [Accessed 13/03/2019].
- AMINOSSADATI, S. & GHASEMI, B. 2009. Natural convection cooling of a localised heat source at the bottom of a nanofluid-filled enclosure. *European Journal of Mechanics-B/Fluids*, 28, 630-640.
- AOUNALLAH, M., ADDAD, Y., BENHAMADOUCHE, S., IMINE, O., ADJLOUT, L. & LAURENCE, D. 2007. Numerical investigation of turbulent natural convection in an inclined square cavity with a hot wavy wall. *International Journal of Heat and Mass Transfer*, 50, 1683-1693.
- ARPINO, F., MASSAROTTI, N. & MAURO, A. 2011. Efficient three-dimensional FEM based algorithm for the solution of convection in partly porous domains. *International Journal of Heat and Mass Transfer*, 54, 4495-4506.
- ASSATO, M. & DE LEMOS, M. J. 2009. Turbulent flow in wavy channels simulated with nonlinear models and a new implicit formulation. *Numerical Heat Transfer, Part A: Applications*, 56, 301-324.
- BADRUDDIN, I. A., ZAINAL, Z., NARAYANA, P. A. & SEETHARAMU, K. 2007. Numerical analysis of convection conduction and radiation using a non-equilibrium model in a square porous cavity. *International journal of thermal sciences*, 46, 20-29.
- BAGCHI, A. & KULACKI, F. 2011. Natural convection in fluid–superposed porous layers heated locally from below. *International Journal of Heat and Mass Transfer*, 54, 3672-3682.
- BAGCHI, A. & KULACKI, F. A. Natural Convection in Horizontal Fluid-Superposed Porous Layers Heated Locally From Below. ASME 2010 International Mechanical Engineering Congress and Exposition, 2010. American Society of Mechanical Engineers, 1571-1579.
- BAGCHI, A. & KULACKI, F. A. 2014. *Natural Convection in Superposed Fluid-Porous Layers*, Springer.

- BALLA, C. S. & NAIKOTI, K. 2015. Soret and Dufour effects on free convective heat and solute transfer in fluid saturated inclined porous cavity. *Engineering Science and Technology, an International Journal*, 18, 543-554.
- BARAKOS, G., MITSOULIS, E. & ASSIMACOPOULOS, D. 1994. Natural convection flow in a square cavity revisited: laminar and turbulent models with wall functions. *International Journal for Numerical Methods in Fluids*, 18, 695-719.
- BASAK, T. & CHAMKHA, A. J. 2012. Heatline analysis on natural convection for nanofluids confined within square cavities with various thermal boundary conditions. *International Journal of Heat and Mass Transfer*, 55, 5526-5543.
- BASAK, T., PRADEEP, P. K., ROY, S. & POP, I. 2011. Finite element based heatline approach to study mixed convection in a porous square cavity with various wall thermal boundary conditions. *International Journal of Heat and Mass Transfer*, 54, 1706-1727.
- BASAK, T., ROY, S., MATTA, A. & POP, I. 2010. Analysis of heatlines for natural convection within porous trapezoidal enclosures: effect of uniform and non-uniform heating of bottom wall. *International Journal of Heat and Mass Transfer*, 53, 5947-5961.
- BASAK, T., ROY, S., SINGH, A. & BALAKRISHNAN, A. 2009. Natural convection flows in porous trapezoidal enclosures with various inclination angles. *International Journal of Heat and Mass Transfer*, 52, 4612-4623.
- BASAK, T., ROY, S. & TAKHAR, H. S. 2007. Effects of nonuniformly heated wall (s) on a natural-convection flow in a square cavity filled with a porous medium. *Numerical Heat Transfer, Part A: Applications*, 51, 959-978.
- BASHIRNEZHAD, K., RASHIDI, M. M., YANG, Z., BAZRI, S. & YAN, W.-M. 2015. A comprehensive review of last experimental studies on thermal conductivity of nanofluids. *Journal of Thermal Analysis and Calorimetry*, 122, 863-884.
- BAYTAS, A. 2003. Thermal non-equilibrium natural convection in a square enclosure filled with a heat-generating solid phase, non-Darcy porous medium. *International journal of energy research*, 27, 975-988.
- BAYTAS, A. C. & POP, I. 2002. Free convection in a square porous cavity using a thermal nonequilibrium model. *International Journal of Thermal Sciences*, 41, 861-870.
- BEAVERS, G. S. & JOSEPH, D. D. 1967. Boundary conditions at a naturally permeable wall. *Journal of fluid mechanics*, 30, 197-207.
- BECKERMANN, C., RAMADHYANI, S. & VISKANTA, R. 1987. Natural convection flow and heat transfer between a fluid layer and a porous layer inside a rectangular enclosure. *Journal of heat transfer*, 109, 363-370.

- BENNACER, R., BEJI, H. & MOHAMAD, A. 2003. Double diffusive convection in a vertical enclosure inserted with two saturated porous layers confining a fluid layer. *International Journal of Thermal Sciences*, 42, 141-151.
- BOURANTAS, G., SKOURAS, E., LOUKOPOULOS, V. & BURGANOS, V. 2014. Heat transfer and natural convection of nanofluids in porous media. *European Journal of Mechanics-B/Fluids*, 43, 45-56.
- BRAGA, E. J. & DE LEMOS, M. J. 2004. Turbulent natural convection in a porous square cavity computed with a macroscopic  $\kappa$ - $\epsilon$  model. *International Journal of Heat and Mass Transfer*, 47, 5639-5650.
- BRAGA, E. J. & DE LEMOS, M. J. 2009. Laminar and turbulent free convection in a composite enclosure. *International Journal of Heat and Mass Transfer*, 52, 588-596.
- BURGERSCENTRUM, J. 2015. Finite element methods for the incompressible Navier-Stokes equations.
- CARVALHO, P. H. & DE LEMOS, M. J. 2013. Turbulent free convection in a porous square cavity using the thermal equilibrium model. *International Communications in Heat and Mass Transfer*, 49, 10-16.
- CARVALHO, P. H. & DE LEMOS, M. J. 2014. Turbulent free convection in a porous cavity using the two-temperature model and the high Reynolds closure. *International Journal of Heat and Mass Transfer*, 79, 105-115.
- CHAMKHA, A. J. & ISMAEL, M. A. 2014. Natural convection in differentially heated partially porous layered cavities filled with a nanofluid. *Numerical Heat Transfer, Part A: Applications*, 65, 1089-1113.
- CHAMKHA, A. J., SAZEGAR, S., JAMESAHAR, E. & GHALAMBAZ, M. 2019. Thermal non-equilibrium heat transfer modeling of hybrid nanofluids in a structure composed of the layers of solid and porous media and free nanofluids. *Energies*, 12, 541.
- CHAND, R. & RANA, G. 2012. On the onset of thermal convection in rotating nanofluid layer saturating a Darcy–Brinkman porous medium. *International Journal of Heat and Mass Transfer*, 55, 5417-5424.
- CHEN, X., YU, P., SUI, Y., WINOTO, S. & LOW, H. 2009. Natural convection in a cavity filled with porous layers on the top and bottom walls. *Transport in porous media*, 78, 259-276.
- CHENG, P. 1978. Heat transfer in geothermal systems. *Advances in heat transfer*, 14, 1-105.
- CHOL, S. 1995. Enhancing thermal conductivity of fluids with nanoparticles. *ASME-Publications-Fed*, 231, 99-106.

- CORCIONE, M. 2010. Heat transfer features of buoyancy-driven nanofluids inside rectangular enclosures differentially heated at the sidewalls. *International Journal of Thermal Sciences*, 49, 1536-1546.
- CORCIONE, M., CIANFRINI, M. & QUINTINO, A. 2015. Enhanced natural convection heat transfer of nanofluids in enclosures with two adjacent walls heated and the two opposite walls cooled. *International Journal of Heat and Mass Transfer*, 88, 902-913.
- DASTMALCHI, M., SHEIKHZADEH, G. & ARANI, A. A. 2015. Double-diffusive natural convective in a porous square enclosure filled with nanofluid. *International Journal of Thermal Sciences*, 95, 88-98.
- DE LEMOS, M. J. 2012. *Turbulence in porous media: modeling and applications*, Elsevier.
- DE LEMOS, M. J. & BRAGA, E. J. 2003. Modeling of turbulent natural convection in porous media. *International communications in heat and mass transfer*, 30, 615-624.
- DE LEMOS, M. J. & PEDRAS, M. H. 2001. Recent mathematical models for turbulent flow in saturated rigid porous media. *Journal of Fluids Engineering*, 123, 935-940.
- DE MEDEIROS, J. M., MARCONDES, F. & GURGEL, J. M. 1999. Natural convection in a porous cavity using the generalized model with uniform porosity.
- DENG, Q.-H. & CHANG, J.-J. 2008. Natural convection in a rectangular enclosure with sinusoidal temperature distributions on both side walls. *Numerical Heat Transfer, Part A: Applications*, 54, 507-524.
- DIXIT, H. & BABU, V. 2006. Simulation of high Rayleigh number natural convection in a square cavity using the lattice Boltzmann method. *International journal of heat and mass transfer*, 49, 727-739.
- DIXON, J. 2013. *Mixed convection in horizontal fluid-superposed porous layers*. University of Minnesota.
- DOGONCHI, A., CHAMKHA, A. J. & GANJI, D. 2018. A numerical investigation of magneto-hydrodynamic natural convection of Cu–water nanofluid in a wavy cavity using CVFEM. *Journal of Thermal Analysis and Calorimetry*, 1-13.
- DOL, H. & HANJALIĆ, K. 2001. Computational study of turbulent natural convection in a side-heated near-cubic enclosure at a high Rayleigh number. *International Journal of Heat and Mass Transfer*, 44, 2323-2344.
- DU, Z.-G. & BILGEN, E. 1990. Natural convection in vertical cavities with partially filled heat-generating porous media. *Numerical heat transfer*, 18, 371-386.
- ELSHEHABEY, H. M. & AHMED, S. E. 2015. MHD mixed convection in a lid-driven cavity filled by a nanofluid with sinusoidal temperature distribution on the both

- vertical walls using Buongiorno's nanofluid model. *International Journal of Heat and Mass Transfer*, 88, 181-202.
- ELSHARBINY, S. M., RAITHBY, G. & HOLLANDS, K. 1982. Heat transfer by natural convection across vertical and inclined air layers. *Journal of Heat Transfer*, 104, 96-102.
- FAGHIRI, A. H. 2014. *Unsteady natural convection within a differentially heated porous enclosure*. Eastern Mediterranean University (EMU)-Doğu Akdeniz Üniversitesi (DAÜ).
- FARD, A., GHASEMI, B. & KOHYANI, M. 2012. Heat generation effects on natural convection in porous cavity with different walls temperature. *Frontiers in Heat and Mass Transfer (FHMT)*, 3.
- FAROUK, B. & GUCERI, S. 1982. Laminar and turbulent natural convection in the annulus between horizontal concentric cylinders. *Journal of Heat Transfer*, 104, 631-636.
- FLETCHER, C. A. Computational techniques for fluid dynamics. Volume 1-Fundamental and general techniques. Volume 2-Specific techniques for different flow categories. Berlin and New York, Springer-Verlag, 1988, p. Vol. 1, 418 p.; vol. 2, 493 p., 1988.
- FRAIKIN, M.-P., PORTIER, J. J. & FRAIKIN, C. J. 1982. APPLICATION OF A  $k-\epsilon$  TURBULENCE MODEL TO AN ENCLOSED BUOYANCY DRIVEN RECIRCULATING FLOW. *Chemical Engineering Communications*, 13, 289-314.
- FUSEGI, T., HYUN, J. M. & KUWAHARA, K. 1991. Three-dimensional simulations of natural convection in a sidewall-heated cube. *International journal for numerical methods in fluids*, 13, 857-867.
- GAROOSI, F., SAFAEI, M. R., DAHARI, M. & HOOMAN, K. 2015. Eulerian-Lagrangian analysis of solid particle distribution in an internally heated and cooled air-filled cavity. *Applied Mathematics and Computation*, 250, 28-46.
- GOBIN, D., GOYEAU, B. & NECULAE, A. 2005. Convective heat and solute transfer in partially porous cavities. *International Journal of Heat and Mass Transfer*, 48, 1898-1908.
- GOODARZI, M., SAFAEI, M., VAFAI, K., AHMADI, G., DAHARI, M., KAZI, S. & JOMHARI, N. 2014. Investigation of nanofluid mixed convection in a shallow cavity using a two-phase mixture model. *International Journal of Thermal Sciences*, 75, 204-220.
- GORLA, R. R. S., CHAMKHA, A. J. & RASHAD, A. M. 2011. Mixed convective boundary layer flow over a vertical wedge embedded in a porous medium saturated with a nanofluid: natural convection dominated regime. *Nanoscale research letters*, 6, 1-9.

- GORLA, R. S. R., SIDDIQA, S., MANSOUR, M., RASHAD, A. & SALAH, T. 2017. Heat Source/Sink Effects on a Hybrid Nanofluid-Filled Porous Cavity. *Journal of Thermophysics and Heat Transfer*.
- GOYEAU, B. & GOBIN, D. 1999. Heat transfer by thermosolutal natural convection in a vertical composite fluid-porous cavity. *International communications in heat and mass transfer*, 26, 1115-1126.
- GROŞAN, T., REVNIC, C., POP, I. & INGHAM, D. 2015. Free convection heat transfer in a square cavity filled with a porous medium saturated by a nanofluid. *International Journal of Heat and Mass Transfer*, 87, 36-41.
- HASAN, M. N., SAHA, S. C. & GU, Y. 2012. Unsteady natural convection within a differentially heated enclosure of sinusoidal corrugated side walls. *International Journal of Heat and Mass Transfer*, 55, 5696-5708.
- HASHEMI AMREI, S. & DEHKORDI, A. M. 2014. Modeling and CFD Simulation of a Mixed-Convection Flow of Regular Fluids and Nanofluids in Vertical Porous and Regular Channels. *Heat Transfer—Asian Research*, 43, 243-269.
- HASSAN, A. A. & ISMAEL, M. A. 2015. Mixed Convection in Superposed Nanofluid and Porous Layers Inside Lid-Driven Square Cavity. *Int. J. of Thermal & Environmental Engineering*, 10, 93-104.
- HENKES, R., VAN DER VLUGT, F. & HOOGENDOORN, C. 1991. Natural-convection flow in a square cavity calculated with low-Reynolds-number turbulence models. *International Journal of Heat and Mass Transfer*, 34, 377-388.
- HIROYUKI, O., AKIRA, M., MASARU, O., CHURCHILL, S. W. & LIOR, N. 1985. Numerical calculations of laminar and turbulent natural convection in water in rectangular channels heated and cooled isothermally on the opposing vertical walls. *International journal of heat and mass transfer*, 28, 125-138.
- HUSSAIN, S. H. 2016. Analysis of heatlines and entropy generation during double-diffusive MHD natural convection within a tilted sinusoidal corrugated porous enclosure. *Engineering Science and Technology, an International Journal*, 19, 926-945.
- HUSSAIN, S. H., HUSSEIN, A. K. & MAHDI, M. M. 2011. Natural convection in a square inclined enclosure with vee-corrugated sidewalls subjected to constant flux heating from below. *Nonlinear Analysis*, 16, 152-169.
- HUSSAIN, S. H. & RAHOMEY, M. S. 2018. Comparison of Natural Convection around a Circular Cylinder with Different Geometries of Cylinders inside a Square Enclosure Filled with Ag-Nanofluid Superposed Porous-Nanofluid Layers.
- HUSSAIN, S. H., SABAH, R. & HASSAN ALI, F. 2013. Numerical study of natural convection heat transfer of air flow inside a corrugated enclosure in the presence

of an inclined heated plate. *Progress in Computational Fluid Dynamics, an International Journal*, 13, 34-43.

- HUSSEIN, A. K. & HUSSAIN, S. H. 2016. Heatline visualization of natural convection heat transfer in an inclined wavy cavities filled with nanofluids and subjected to a discrete isoflux heating from its left sidewall. *Alexandria Engineering Journal*.
- INCE, N. & LAUNDER, B. 1989. On the computation of buoyancy-driven turbulent flows in rectangular enclosures. *International Journal of Heat and Fluid Flow*, 10, 110-117.
- ISMAEEL, M. E. 2011. Heat Transfer in a Square Porous Cavity With Partial Heating and Cooling for Opposite Vertical Walls. *Al-Rafadain Engineering Journal*, 19.
- ISMAEL, M. A. & CHAMKHA, A. J. 2015. Conjugate natural convection in a differentially heated composite enclosure filled with a nanofluid. *Journal of Porous Media*, 18.
- IZADI, M., HOGHOUGHI, G., MOHEBBI, R. & SHEREMET, M. 2018. Nanoparticle migration and natural convection heat transfer of Cu-water nanofluid inside a porous undulant-wall enclosure using LTNE and two-phase model. *Journal of Molecular Liquids*, 261, 357-372.
- KAKAÇ, S. & PRAMUANJAROENKIJ, A. 2009. Review of convective heat transfer enhancement with nanofluids. *International Journal of Heat and Mass Transfer*, 52, 3187-3196.
- KARIMI, A. & AFRAND, M. 2018. Numerical study on thermal performance of an air-cooled heat exchanger: Effects of hybrid nanofluid, pipe arrangement and cross section. *Energy Conversion and Management*, 164, 615-628.
- KEFAYATI, G. R. 2013. Lattice Boltzmann simulation of MHD natural convection in a nanofluid-filled cavity with sinusoidal temperature distribution. *Powder technology*, 243, 171-183.
- KHANAFER, K., AL-AZMI, B., MARAFIE, A. & POP, I. 2009. Non-Darcian effects on natural convection heat transfer in a wavy porous enclosure. *International Journal of Heat and Mass Transfer*, 52, 1887-1896.
- KHASHAN, S., AL-AMIRI, A. & POP, I. 2006. Numerical simulation of natural convection heat transfer in a porous cavity heated from below using a non-Darcian and thermal non-equilibrium model. *International Journal of Heat and Mass Transfer*, 49, 1039-1049.
- KIM, M. C., LEE, S. B., KIM, S. & CHUNG, B. J. 2003. Thermal instability of viscoelastic fluids in porous media. *International journal of heat and mass transfer*, 46, 5065-5072.

- KOCUTAR, P., ŠKERGET, L. & RAVNIK, J. 2015. Hybrid LES/URANS simulation of turbulent natural convection by BEM. *Engineering Analysis with Boundary Elements*, 61, 16-26.
- KUMAR, V. 2011. Coupling of free flow and flow in porous media—a dimensional analysis. *Forschungsbericht, Institut für Wasserbau, Lehrstuhl für Hydromechanik und Hydrosystemmodellierung, Universität Stuttgart*.
- KUZNETSOV, G. V. & SHEREMET, M. A. 2010. Numerical simulation of turbulent natural convection in a rectangular enclosure having finite thickness walls. *International Journal of Heat and Mass Transfer*, 53, 163-177.
- MAHDI, R. A., MOHAMMED, H. & MUNISAMY, K. 2013. Improvement of convection heat transfer by using porous media and nanofluid: Review. *International Journal of Science and Research*, 2, 34-47.
- MAHMOUDI, A., MEJRI, I., ABBASSI, M. A. & OMRI, A. 2014. Lattice Boltzmann simulation of MHD natural convection in a nanofluid-filled cavity with linear temperature distribution. *Powder Technology*, 256, 257-271.
- MARKATOS, N. C. & PERICLEOUS, K. 1984. Laminar and turbulent natural convection in an enclosed cavity. *International Journal of Heat and Mass Transfer*, 27, 755-772.
- MEBROUK, R., KADJA, M., LACHI, M. & FOHANNO, S. 2016. Numerical study of natural turbulent convection of nanofluids in a tall cavity heated from below. *Thermal Science*, 89-89.
- MHARZI, M., DAGUENET, M. & DAOUDI, S. 2000. Thermosolutal natural convection in a vertically layered fluid-porous medium heated from the side. *Energy conversion and management*, 41, 1065-1090.
- MIROSHNICHENKO, I., SHEREMET, M. A. & MOHAMAD, A. 2016. Numerical simulation of a conjugate turbulent natural convection combined with surface thermal radiation in an enclosure with a heat source. *International Journal of Thermal Sciences*, 109, 172-181.
- MIROSHNICHENKO, I. V. & SHEREMET, M. A. 2018. Turbulent natural convection combined with thermal surface radiation inside an inclined cavity having local heater. *International Journal of Thermal Sciences*, 124, 122-130.
- MOHEBBI, R., MEHRYAN, S., IZADI, M. & MAHIAN, O. 2019. Natural convection of hybrid nanofluids inside a partitioned porous cavity for application in solar power plants. *Journal of Thermal Analysis and Calorimetry*, 1-15.
- MUSHATE, K. S. 2011. CFD prediction of natural convection in a wavy cavity filled with porous medium. *Global Journal of Research Engineering*, 11, 29-42.

- MUTHTAMILSELVAN, M. 2011. Analysis of Heat and Mass Transfer in a Porous Cavity Containing Water near Its Density Maximum. *Applied Mathematics*, 2, 927.
- NASRIN, R. & ALIM, M. 2013. Performance of nanofluids on heat transfer in a wavy solar collector. *International Journal of Engineering, Science and Technology*, 5, 58-77.
- NASRIN, R. & PARVIN, S. 2012. Investigation of buoyancy-driven flow and heat transfer in a trapezoidal cavity filled with water–Cu nanofluid. *International Communications in Heat and Mass Transfer*, 39, 270-274.
- NGUYEN, M. T., ALY, A. M. & LEE, S.-W. 2015. Natural convection in a non-darcy porous cavity filled with cu–water nanofluid using the characteristic-based split procedure in finite-element method. *Numerical Heat Transfer, Part A: Applications*, 67, 224-247.
- NIELD, D. A. & BEJAN, A. 2006. *Convection in porous media*, Springer Science & Business Media.
- OZOE, H., MOURI, A., HIRAMITSU, M., CHURCHILL, S. & LIOR, N. 1986. Numerical calculation of three-dimensional turbulent natural convection in a cubical enclosure using a two-equation model for turbulence. *Journal of heat transfer*, 108, 806-813.
- OZTOP, H. F., MOBEDI, M., ABU-NADA, E. & POP, I. 2012. A heatline analysis of natural convection in a square inclined enclosure filled with a CuO nanofluid under non-uniform wall heating condition. *International Journal of Heat and Mass Transfer*, 55, 5076-5086.
- PATANKAR, S. 1980. *Numerical heat transfer and fluid flow*, CRC press.
- PORDANJANI, A. H., JAHANBAKHSHI, A., NADOOSHAN, A. A. & AFRAND, M. 2018. Effect of two isothermal obstacles on the natural convection of nanofluid in the presence of magnetic field inside an enclosure with sinusoidal wall temperature distribution. *International Journal of Heat and Mass Transfer*, 121, 565-578.
- POULIKAKOS, D., BEJAN, A., SELIMOS, B. & BLAKE, K. 1986. High Rayleigh number convection in a fluid overlaying a porous bed. *International Journal of Heat and Fluid Flow*, 7, 109-116.
- PROMTHAISONG, P., JEDSADARATANACHAI, W. & EIAMSA-ARD, S. 2016. 3D Numerical study on the flow topology and heat transfer characteristics of turbulent forced convection in spirally corrugated tube. *Numerical Heat Transfer, Part A: Applications*, 69, 607-629.
- PUTRA, N., ROETZEL, W. & DAS, S. K. 2003. Natural convection of nano-fluids. *Heat and Mass Transfer*, 39, 775-784.

- RAO, S. S. & SRIVASTAVA, A. 2016. Interferometric study of natural convection in a differentially-heated cavity with Al<sub>2</sub>O<sub>3</sub>-water based dilute nanofluids. *International Journal of Heat and Mass Transfer*, 92, 1128-1142.
- ROLAND, W. L., NITHIARASU, P. & SEETHARAMU, K. 2004. Fundamentals of the finite element method for heat and fluid flow. John Wiley & Sons Ltd, Southern Gate, Chichester, West Sussex PO19.
- ROSLAN, R., SALEH, H. & HASHIM, I. 2012. Effect of rotating cylinder on heat transfer in a square enclosure filled with nanofluids. *International Journal of Heat and Mass Transfer*, 55, 7247-7256.
- SABEUR-BENDEHINA, A., IMINE, O. & ADJLOUT, L. 2011. Laminar free convection in undulated cavity with non-uniform boundary conditions. *Comptes Rendus Mécanique*, 339, 42-57.
- SABOUR, M. & GHALAMBAZ, M. 2016. Natural convection in a triangular cavity filled with a nanofluid-saturated porous medium using three heat equation model. *Canadian Journal of Physics*, 94, 604-615.
- SAFAEI, M. R., JAHANBIN, A., KIANIFAR, A., GHAREHKHANI, S., KHERBEET, A. S., GOODARZI, M. & DAHARI, M. 2016. Mathematical modeling for nanofluids simulation: a review of the latest works. *Modeling and Simulation in Engineering Sciences*. InTech.
- SAJJADI, H., ABBASSI, M. B. & KEFAYATI, G. R. 2013. Lattice Boltzmann simulation of turbulent natural convection in a square cavity using Cu/water nanofluid. *Journal of Mechanical Science and Technology*, 27, 2341-2349.
- SALAT, J., XIN, S., JOUBERT, P., SERGENT, A., PENOT, F. & LE QUERE, P. 2004. Experimental and numerical investigation of turbulent natural convection in a large air-filled cavity. *International Journal of Heat and Fluid Flow*, 25, 824-832.
- SALEH, H., ROSLAN, R. & HASHIM, I. 2011. Natural convection heat transfer in a nanofluid-filled trapezoidal enclosure. *International Journal of Heat and Mass Transfer*, 54, 194-201.
- SARKAR, J., GHOSH, P. & ADIL, A. 2015. A review on hybrid nanofluids: recent research, development and applications. *Renewable and Sustainable Energy Reviews*, 43, 164-177.
- SATHE, S., LIN, W.-Q. & TONG, T. 1988. Natural convection in enclosures containing an insulation with a permeable fluid-porous interface. *International journal of heat and fluid flow*, 9, 389-395.
- SATHIYAMOORTHY, M., BASAK, T., ROY, S. & POP, I. 2007a. Steady natural convection flow in a square cavity filled with a porous medium for linearly heated side wall (s). *International Journal of Heat and Mass Transfer*, 50, 1892-1901.

- SATHIYAMOORTHY, M., BASAK, T., ROY, S. & POP, I. 2007b. Steady natural convection flows in a square cavity with linearly heated side wall (s). *International Journal of Heat and Mass Transfer*, 50, 766-775.
- SELIMEFENDIGIL, F., ÖZTOP, H. F. & CHAMKHA, A. J. 2016. MHD mixed convection and entropy generation of nanofluid filled lid driven cavity under the influence of inclined magnetic fields imposed to its upper and lower diagonal triangular domains. *Journal of Magnetism and Magnetic Materials*.
- SHARIF, M. & LIU, W. 2003. Numerical Study of Turbulent Natural Convection in a Side-Heated Square Cavity at Various Angles of Inclination. *Numerical Heat Transfer: Part A: Applications*, 43, 693-716.
- SHARMA, A. K., VELUSAMY, K., BALAJI, C. & VENKATESHAN, S. 2007. Conjugate turbulent natural convection with surface radiation in air filled rectangular enclosures. *International Journal of Heat and Mass Transfer*, 50, 625-639.
- SHEREMET, M. A. & POP, I. 2014. Conjugate natural convection in a square porous cavity filled by a nanofluid using Buongiorno's mathematical model. *International Journal of Heat and Mass Transfer*, 79, 137-145.
- SHEREMET, M. A. & POP, I. 2018. Effect of local heater size and position on natural convection in a tilted nanofluid porous cavity using LTNE and Buongiorno's models. *Journal of Molecular Liquids*.
- SHEREMET, M. A., POP, I. & NAZAR, R. 2015a. Natural convection in a square cavity filled with a porous medium saturated with a nanofluid using the thermal nonequilibrium model with a Tiwari and Das nanofluid model. *International Journal of Mechanical Sciences*, 100, 312-321.
- SHEREMET, M. A., POP, I. & RAHMAN, M. 2015b. Three-dimensional natural convection in a porous enclosure filled with a nanofluid using Buongiorno's mathematical model. *International Journal of Heat and Mass Transfer*, 82, 396-405.
- SHEREMET, M. A., POP, I. & SHENOY, A. 2015c. Unsteady free convection in a porous open wavy cavity filled with a nanofluid using Buongiorno's mathematical model. *International Communications in Heat and Mass Transfer*, 67, 66-72.
- SHIRVAN, K. M., ELLAHI, R., MAMOURIAN, M. & MOGHIMAN, M. 2017. Effects of wavy surface characteristics on natural convection heat transfer in a cosine corrugated square cavity filled with nanofluid. *International Journal of Heat and Mass Transfer*, 107, 1110-1118.
- SINGH, A., PAUL, T. & THORPE, G. 1999. Natural convection due to heat and mass transfer in a composite system. *Heat and mass transfer*, 35, 39-48.

- SINGH, S. & BHARGAVA, R. 2014. Numerical study of natural convection within a wavy enclosure using meshfree approach: Effect of corner heating. *The Scientific World Journal*, 2014.
- SIVASANKARAN, S. & BHUVANESWARI, M. 2013. Natural convection in a porous cavity with sinusoidal heating on both sidewalls. *Numerical Heat Transfer, Part A: Applications*, 63, 14-30.
- SIVASANKARAN, S., MALLESWARAN, A., LEE, J. & SUNDAR, P. 2011. Hydro-magnetic combined convection in a lid-driven cavity with sinusoidal boundary conditions on both sidewalls. *International Journal of Heat and Mass Transfer*, 54, 512-525.
- SOJOUDI, A., SAHA, S. C., KHEZERLOO, M. & GU, Y. 2014. Unsteady natural convection within a porous enclosure of sinusoidal corrugated side walls. *Transport in Porous Media*, 104, 537-552.
- SONG, M. & VISKANTA, R. 1994. Natural convection flow and heat transfer within a rectangular enclosure containing a vertical porous layer. *International journal of heat and mass transfer*, 37, 2425-2438.
- TAKABI, B. & SALEHI, S. 2014. Augmentation of the heat transfer performance of a sinusoidal corrugated enclosure by employing hybrid nanofluid. *Advances in Mechanical Engineering*, 6, 147059.
- TATSUO, N., TORU, T., MITSUHIRO, S., YUJI, K. & HIROYUKI, O. 1986. Numerical analysis of natural convection in a rectangular enclosure horizontally divided into fluid and porous regions. *International journal of heat and mass transfer*, 29, 889-898.
- TIWARI, A., SINGH, A., CHANDRAN, P. & SACHETI, N. 2012. Natural convection in a cavity with a sloping upper surface filled with an anisotropic porous material. *Acta Mechanica*, 223, 95-108.
- TONG, T. & SUBRAMANIAN, E. 1986. Natural convection in rectangular enclosures partially filled with a porous medium. *International journal of heat and fluid flow*, 7, 3-10.
- VASSEUR, P., WANG, C. & SEN, M. 1989. Thermal instability and natural convection in a fluid layer over a porous substrate. *Wärme-und Stoffübertragung*, 24, 337-347.
- WALKER, K. L. & HOMSY, G. M. 1978. Convection in a porous cavity. *J. Fluid Mech*, 87, 449-474.
- WU, F., WANG, G. & ZHOU, W. 2016. Buoyancy induced convection in a porous cavity with sinusoidally and partially thermally active sidewalls under local thermal non-equilibrium condition. *International Communications in Heat and Mass Transfer*, 75, 100-114.

- WU, F., ZHOU, W. & MA, X. 2015. Natural convection in a porous rectangular enclosure with sinusoidal temperature distributions on both side walls using a thermal non-equilibrium model. *International Journal of Heat and Mass Transfer*, 85, 756-771.
- WU, Z. & MIRBOD, P. 2018. Experimental analysis of the flow near the boundary of random porous media. *Physics of Fluids*, 30, 047103.
- XXXX. Available: <http://store.logicneed.com/product/16073> [Accessed].
- YANG, Y.-T., TANG, H.-W., ZENG, B.-Y. & WU, C.-H. 2015. Numerical simulation and optimization of turbulent nanofluids in a three-dimensional rectangular rib-grooved channel. *International Communications in Heat and Mass Transfer*, 66, 71-79.
- ZHANG, Z., CHEN, W., ZHU, Z. & LI, Y. 2014. Numerical exploration of turbulent air natural-convection in a differentially heated square cavity at  $Ra = 5.33 \times 10^9$ . *Heat and Mass Transfer*, 50, 1737-1749.

## Appendices

### Appendix A: Equations discretization and shape function

#### A1: Non-linear discretization equations

##### A1.1 Equations discretization of the nanofluid layer

The weighted form of the nanofluid governing equations at nodes of internal domain  $\Omega$  becomes

##### Momentum equation

###### In the X-direction

$$\begin{aligned}
 Res_{sn}^{(1)} = & \sum_{sn=1}^{SN} ((U)_{nf})_{sn} \cdot \int_{\Omega} \left[ \left( \sum_{sn=1}^{SN} ((U)_{nf})_{sn} \cdot (F)_{sn} \right) \frac{\partial (F)_{sn}}{\partial X} + \right. \\
 & \left( \sum_{sn=1}^{SN} ((V)_{nf})_{sn} \cdot (F)_{sn} \right) \frac{\partial (F)_{sn}}{\partial Y} + \\
 & \left. \left( \sum_{sn=1}^{SN} ((W)_{nf})_{sn} \cdot (F)_{sn} \right) \frac{\partial (F)_{sn}}{\partial Z} \right] (\Phi)_{sn} \cdot dX dY dZ + \\
 & \frac{(\rho)_{bf}}{(\rho)_{nf}} \sum_{sn=1}^{SN} \int_{\Omega} (P)_{sn} \cdot \frac{\partial (F)_{sn}}{\partial X} \cdot (\Phi)_{sn} \cdot dX + \\
 & \frac{(\rho)_{bf}}{(\rho)_{nf} \cdot (1-\phi)^{2.5}} \cdot Pr \cdot \sum_{sn=1}^{SN} ((U)_{nf})_{sn} \cdot \int_{\Omega} \left[ \frac{\partial \Phi_{sn}}{\partial X} \frac{\partial F_{sn}}{\partial X} + \frac{\partial \Phi_{sn}}{\partial Y} \frac{\partial F_{sn}}{\partial Y} + \right. \\
 & \left. \frac{\partial \Phi_{sn}}{\partial Z} \frac{\partial F_{sn}}{\partial Z} \right] \cdot dX dY dZ = 0
 \end{aligned} \tag{A1.1}$$

###### In the Y-direction

$$\begin{aligned}
 Res_{sn}^{(2)} = & \sum_{sn=1}^{SN} ((V)_{nf})_{sn} \int_{\Omega} \left[ \left( \sum_{sn=1}^{SN} ((U)_{nf})_{sn} (F)_{sn} \right) \frac{\partial (F)_{sn}}{\partial X} + \right. \\
 & \left( \sum_{sn=1}^{SN} ((V)_{nf})_{sn} (F)_{sn} \right) \frac{\partial (F)_{sn}}{\partial Y} + \\
 & \left. \left( \sum_{sn=1}^{SN} ((W)_{nf})_{sn} (F)_{sn} \right) \frac{\partial (F)_{sn}}{\partial Z} \right] (\Phi)_{sn} \cdot dX dY dZ + \\
 & \frac{\rho_{bf}}{\rho_{nf}} \sum_{sn=1}^{SN} \int_{\Omega} (P)_{sn} \frac{\partial (F)_{sn}}{\partial Y} (\Phi)_{sn} dY +
 \end{aligned}$$

$$\frac{(\rho)_{bf}}{(\rho)_{nf} \cdot (1-\phi)^{2.5}} \cdot Pr \cdot \sum_{sn=1}^{SN} ((V)_{nf})_{sn} \cdot \int_{\Omega} \left[ \frac{\partial \Phi_{sn}}{\partial X} \frac{\partial F_{sn}}{\partial X} + \frac{\partial \Phi_{sn}}{\partial Y} \frac{\partial F_{sn}}{\partial Y} + \frac{\partial \Phi_{sn}}{\partial Z} \frac{\partial F_{sn}}{\partial Z} \right] \cdot dX dY dZ = 0 \quad (A1.2)$$

**In the Z-direction**

$$\begin{aligned} Res_{sn}^{(3)} = & \sum_{sn=1}^{SN} (W_{nf})_{sn} \int_{\Omega} \left[ \left( \sum_{sn=1}^{SN} (U_{nf})_{sn} F_{sn} \right) \frac{\partial F_{sn}}{\partial X} + \right. \\ & \left. \left( \sum_{sn=1}^{SN} (V_{nf})_{sn} F_{sn} \right) \frac{\partial F_{sn}}{\partial Y} + \left( \sum_{sn=1}^{SN} (W_{nf})_{sn} F_{sn} \right) \frac{\partial F_{sn}}{\partial Z} \right] \Phi_{sn} \cdot dX dY dZ + \\ & \frac{\rho_{bf}}{\rho_{nf}} \sum_{sn=1}^{SN} \int_{\Omega} P_{sn} \frac{\partial F_{sn}}{\partial Z} \Phi_{sn} \cdot dZ + \\ & \frac{(\rho)_{bf}}{(\rho)_{nf} \cdot (1-\phi)^{2.5}} \cdot Pr \cdot \sum_{sn=1}^{SN} ((W)_{nf})_{sn} \cdot \int_{\Omega} \left[ \frac{\partial \Phi_{sn}}{\partial X} \frac{\partial F_{sn}}{\partial X} + \frac{\partial \Phi_{sn}}{\partial Y} \frac{\partial F_{sn}}{\partial Y} + \right. \\ & \left. \frac{\partial \Phi_{sn}}{\partial Z} \frac{\partial F_{sn}}{\partial Z} \right] \cdot dX dY dZ = 0 \end{aligned} \quad (A1.3)$$

**Energy equation**

$$\begin{aligned} Res_{sn}^{(4)} = & \sum_{sn=1}^{SN} (\theta_{nf})_{sn} \int_{\Omega} \left[ \left( \sum_{sn=1}^{SN} (U_{nf})_{sn} F_{sn} \right) \frac{\partial F_{sn}}{\partial X} + \right. \\ & \left. \left( \sum_{sn=1}^{SN} (V_{nf})_{sn} F_{sn} \right) \frac{\partial F_{sn}}{\partial Y} + \left( \sum_{sn=1}^{SN} (W_{nf})_{sn} F_{sn} \right) \frac{\partial F_{sn}}{\partial Z} \right] \Phi_{sn} \cdot dX dY dZ + \\ & \frac{\alpha_{nf}}{\alpha_{bf}} \sum_{sn=1}^{SN} (\theta_{nf})_{sn} \int_{\Omega} \left( \frac{\partial \Phi_{sn}}{\partial X} \frac{\partial F_{sn}}{\partial X} + \frac{\partial \Phi_{sn}}{\partial Y} \frac{\partial F_{sn}}{\partial Y} + \frac{\partial \Phi_{sn}}{\partial Z} \frac{\partial F_{sn}}{\partial Z} \right) dX dY dZ = 0 \end{aligned} \quad (A1.4)$$

## A.1.2 Equations discretization of the porous medium layer

**Momentum equations**

**In the X-direction**

$$\begin{aligned} Res_{sn}^{(5)} = & \sum_{sn=1}^{SN} (U_{nf})_{sn} \int_{\Omega} \left[ \left( \sum_{sn=1}^{SN} (U_{nf})_{sn} F_{sn} \right) \frac{\partial F_{sn}}{\partial X} + \left( \sum_{sn=1}^{SN} (V_{nf})_{sn} F_{sn} \right) \frac{\partial F_{sn}}{\partial Y} + \right. \\ & \left. \left( \sum_{sn=1}^{SN} (W_{nf})_{sn} F_{sn} \right) \frac{\partial F_{sn}}{\partial Z} \right] \Phi_{sn} \cdot dX dY dZ + \frac{\rho_{bf}}{\rho_{nf}} \sum_{sn=1}^{SN} \int_{\Omega} P_{sn} \frac{\partial F_{sn}}{\partial X} \Phi_{sn} \cdot dX + \\ & \frac{(\rho)_{bf}}{(\rho)_{nf} \cdot (1-\phi)^{2.5}} Pr \sum_{sn=1}^{SN} ((U)_{nf})_{sn} \cdot \int_{\Omega} \left[ \frac{\partial \Phi_{sn}}{\partial X} \frac{\partial F_{sn}}{\partial X} + \frac{\partial \Phi_{sn}}{\partial Y} \frac{\partial F_{sn}}{\partial Y} + \frac{\partial \Phi_{sn}}{\partial Z} \frac{\partial F_{sn}}{\partial Z} \right] \cdot dX dY dZ = \\ & + \frac{\vartheta_{nf} Pr}{\vartheta_{bf} Da} \int_{\Omega} \left( \sum_{sn=1}^{SN} (U_{nf})_{sn} F_{sn} \right) \Phi_{sn} \cdot dX dY dZ = 0. \end{aligned} \quad (A1.5)$$

### In the Y-direction

$$\begin{aligned}
Res_{sn}^{(6)} = & \sum_{sn=1}^{SN} (V_{nf})_{sn} \int_{\Omega} \left[ \left( \sum_{sn=1}^{SN} (U_{nf})_{sn} F_{sn} \right) \frac{\partial F_{sn}}{\partial X} + \right. \\
& \left. \left( \sum_{sn=1}^{SN} (V_{nf})_{sn} F_{sn} \right) \frac{\partial F_{sn}}{\partial Y} + \left( \sum_{sn=1}^{SN} (W_{nf})_{sn} F_{sn} \right) \frac{\partial F_{sn}}{\partial Z} \right] \Phi_{sn} \cdot dX dY dZ + \\
& \frac{\rho_{bf}}{\rho_{nf}} \sum_{sn=1}^{SN} \int_{\Omega} P_{sn} \frac{\partial F_{sn}}{\partial X} \Phi_{sn} \cdot dX + \\
& \frac{(\rho)_{bf}}{(\rho)_{nf} \cdot (1-\phi)^{2.5}} \cdot Pr \sum_{sn=1}^{SN} ((V)_{nf})_{sn} \cdot \int_{\Omega} \left[ \frac{\partial \Phi_{sn}}{\partial X} \frac{\partial F_{sn}}{\partial X} + \frac{\partial \Phi_{sn}}{\partial Y} \frac{\partial F_{sn}}{\partial Y} + \right. \\
& \left. \frac{\partial \Phi_{sn}}{\partial Z} \frac{\partial F_{sn}}{\partial Z} \right] \cdot dX dY dZ + \frac{\vartheta_{nf} Pr}{\vartheta_{bf} Da} \int_{\Omega} \left( \sum_{sn=1}^{SN} (V_{nf})_{sn} F_{sn} \right) \Phi_{sn} \cdot dX dY dZ + \\
& \frac{(\rho\beta)_{nf}}{\rho_{nf} \beta_{bf}} Ra \cdot Pr \int_{\Omega} \left( \sum_{sn=1}^{SN} (\theta_p)_{sn} F_{sn} \right) \Phi_{sn} \cdot dX dY dZ = 0
\end{aligned} \tag{A1.6}$$

### In the Z-direction

$$\begin{aligned}
Res_{sn}^{(7)} = & \sum_{sn=1}^{SN} (W_{nf})_{sn} \int_{\Omega} \left[ \left( \sum_{sn=1}^{SN} (U_{nf})_{sn} F_{sn} \right) \frac{\partial F_{sn}}{\partial X} + \right. \\
& \left. \left( \sum_{sn=1}^{SN} (V_{nf})_{sn} F_{sn} \right) \frac{\partial F_{sn}}{\partial Y} + \left( \sum_{sn=1}^{SN} (W_{nf})_{sn} F_{sn} \right) \frac{\partial F_{sn}}{\partial Z} \right] \Phi_{sn} \cdot dX dY dZ + \\
& \frac{\rho_{bf}}{\rho_{nf}} \sum_{sn=1}^{SN} \int_{\Omega} P_{sn} \frac{\partial F_{sn}}{\partial X} \Phi_{sn} dX + \\
& \frac{(\rho)_{bf}}{(\rho)_{nf} \cdot (1-\phi)^{2.5}} \cdot Pr \sum_{sn=1}^{SN} ((W)_{nf})_{sn} \cdot \int_{\Omega} \left[ \frac{\partial \Phi_{sn}}{\partial X} \frac{\partial F_{sn}}{\partial X} + \frac{\partial \Phi_{sn}}{\partial Y} \frac{\partial F_{sn}}{\partial Y} + \right. \\
& \left. \frac{\partial \Phi_{sn}}{\partial Z} \frac{\partial F_{sn}}{\partial Z} \right] \cdot dX dY dZ + \frac{\vartheta_{nf} Pr}{\vartheta_{bf} Da} \int_{\Omega} \left( \sum_{sn=1}^{SN} (W_{nf})_{sn} F_{sn} \right) \Phi_{sn} \cdot dX dY dZ = 0
\end{aligned} \tag{A1.7}$$

### Energy equation

$$\begin{aligned}
Res_{sn}^{(8)} = & \sum_{sn=1}^{SN} (\theta_p)_{sn} \int_{\Omega} \left[ \left( \sum_{sn=1}^{SN} (U_{nf})_{sn} F_{sn} \right) \frac{\partial F_{sn}}{\partial X} + \right. \\
& \left. \left( \sum_{sn=1}^{SN} (V_{nf})_{sn} F_{sn} \right) \frac{\partial F_{sn}}{\partial Y} + \left( \sum_{sn=1}^{SN} (W_{nf})_{sn} F_{sn} \right) \frac{\partial F_{sn}}{\partial Z} \right] \Phi_{sn} \cdot dX dY dZ + \\
& \frac{\alpha_{nf}}{\alpha_{bf}} \cdot dX dY dZ = 0
\end{aligned} \tag{A1.8}$$

## A2: Shape function:

A two-dimensional square element for four nodes has been supposed to describe how to find the unknown variables by using the shape function as shown in Figure A2.1. The linear unknown variables are represented by fourth order polynomials function

$$\Phi(X, Y) = c_1 + c_2X + c_3Y + c_4XY \quad (\text{A2.1})$$

The gradient varies of the unknown variables may be written as

$$\frac{\partial \Phi}{\partial X} = c_2 + c_4Y \quad (\text{A2.2})$$

$$\frac{\partial \Phi}{\partial Y} = c_3 + c_4X \quad (\text{A2.3})$$

where  $\Phi$  is the unknown variable at any location  $(X, Y)$  and the parameters  $c_1, c_2, c_3$  and  $c_4$  are constant. Since there are four arbitrary constants in the linear representation, it requires only four nodes to determine the values of  $c_1, c_2, c_3$  and  $c_4$ . In the simplest form of the element, a rectangular element is shown in Figure A2.1. Solving these equations will obtain the values of  $c_1, c_2, c_3$  and  $c_4$  by substituting the values of the unknown variables  $\Phi_1, \Phi_2, \Phi_3$  and  $\Phi_4$  into equation (A2.1) for the nodes  $(X_1, Y_1), \dots, (X_4, Y_4)$ , and replacing these relationships into equation (A2.1) and collating the coefficients of  $\Phi_1, \Phi_2, \Phi_3$  and  $\Phi_4$ , to get:

$$\Phi(X, Y) = \sum_{sn=1}^{SN} \Phi_{sn} F_{sn}(X, Y) \quad (\text{A2.4})$$

$$\Phi(X, Y) = F_1(X_1, Y_1)\Phi_1(X_1, Y_1) + F_2(X_2, Y_2)\Phi_2(X_2, Y_2) + F_3(X_3, Y_3)\Phi_3(X_3, Y_3) + F_4(X_4, Y_4)\Phi_4(X_4, Y_4) \quad (\text{A2.5})$$

$$\text{or } \Phi = [F_1 \ F_2 \ F_3 \ F_4] \begin{Bmatrix} \Phi_1 \\ \Phi_2 \\ \Phi_3 \\ \Phi_4 \end{Bmatrix} \quad (\text{A2.6})$$

In the final matrix form

$$\Phi = [F][\Phi] \quad (\text{A2.7})$$

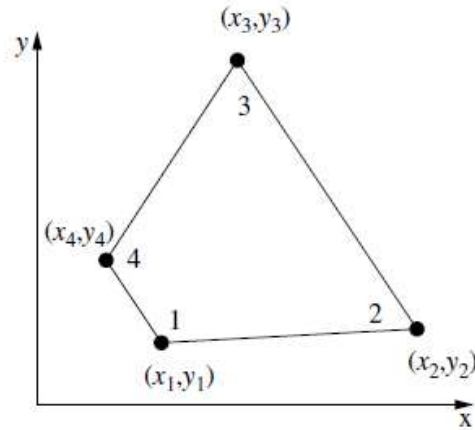


Figure A2.1: A simple rectangular element (Roland *et al.*, 2004)

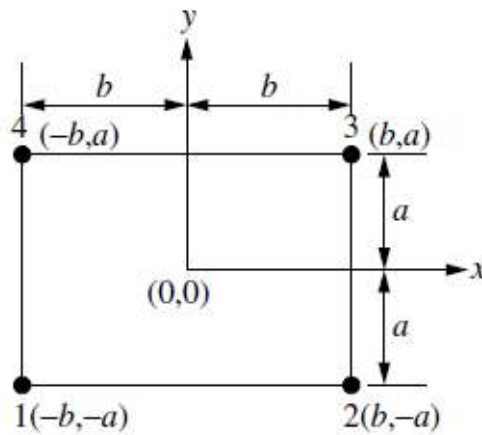


Figure A2.2: A simple rectangular element (Roland *et al.*, 2004)

The summation of the shape functions within domain is equal to unity

$$\sum_{sn=1}^4 F_{sn} = 1 \quad (\text{A2.8})$$

Lagrangian polynomial interpolation function is used to determine the shape function which is the ratio of two products

$$F_{ap}^e(X) = \prod_{op=1}^{sn} \frac{X - X_{op}}{X_{ap} - X_{op}} \quad (\text{A2.9})$$

Where  $e$  is the element contains  $sn$  nodes,  $ap \neq op$ .  $ap$  is the applied point and  $op$  is the other selected point close to the applied point.  $X = \frac{x}{L}$  and  $Y = \frac{y}{L}$ .

These shape functions can be expressed in terms of length ratios  $\frac{X}{b} = \xi$  and  $\frac{Y}{a} = \eta$  where,  $-1 \leq \xi \leq 1$  and  $-1 \leq \eta \leq 1$  are the non-dimensional coordinate of an element shown in Figure A2.3 for the simple rectangular element Figure A2.2.

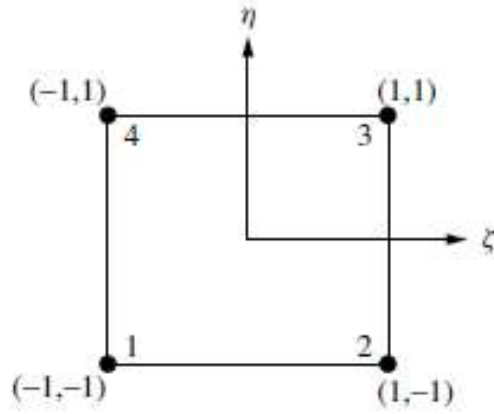


Figure A2.3: Non-dimensional coordinates of a rectangular (Roland *et al.*, 2004)

The linear Lagrangian multipliers are given for the four nodal shape functions as follows:

$$F_1 = \frac{(X-b)(Y-a)}{(-b-b)(-a-a)} = \frac{1}{4ab} (b-X)(a-Y) = \frac{1}{4} (1-\xi)(1-\eta)$$

$$F_2 = \frac{(X-(-b))(Y-a)}{(-b-(-b))(-a-a)} = \frac{1}{4ab} (b+X)(a-Y) = \frac{1}{4} (1+\xi)(1-\eta)$$

$$F_3 = \frac{(X-(-b))(Y-(-a))}{(b-(-b))(a-(-a))} = \frac{1}{4ab} (b+X)(a+Y) = \frac{1}{4} (1+\xi)(1+\eta)$$

$$F_4 = \frac{(X-b)(Y-(-a))}{(-b-b)(a-(-a))} = \frac{1}{4ab} (b-X)(a+Y) = \frac{1}{4} (1-\xi)(1+\eta) \quad (\text{A2.10})$$

The general form of the shape functions can be written as

$$F_{sn} = (1 + \xi \xi_{sn})(1 + \eta \eta_{sn}) \quad (\text{A2.11})$$

Where  $(\xi_{sn}, \eta_{sn})$  represent the coordinate of the node 'sn'.

The variation of the unknown variables and shape functions of the typical rectangular element is

$$\frac{d\Phi}{dX} = \frac{dF_1}{dX}\Phi_1 + \frac{dF_2}{dX}\Phi_2 + \frac{dF_3}{dX}\Phi_3 + \frac{dF_4}{dX}\Phi_4 = \frac{1}{4ab} [-(a-Y)\Phi_1 + (a-Y)\Phi_2 + (a+Y)\Phi_3 - (a+Y)\Phi_4] \quad (\text{A2.12})$$

Similarly,

$$\frac{d\Phi}{dY} = \frac{dF_1}{dY}\Phi_1 + \frac{dF_2}{dY}\Phi_2 + \frac{dF_3}{dY}\Phi_3 + \frac{dF_4}{dY}\Phi_4 = \frac{1}{4ab} [-(b-X)\Phi_1 - (b+X)\Phi_2 + (b+X)\Phi_3 + (b-X)\Phi_4] \quad (\text{A2.13})$$

In matrix form

$$D = \begin{Bmatrix} \frac{d\Phi}{dX} \\ \frac{d\Phi}{dY} \end{Bmatrix} = \frac{1}{4b} \begin{bmatrix} -(a-Y) & (a-Y) & (a+Y) & -(a+Y) \\ -(b-X) & -(b+X) & (b+X) & (b-X) \end{bmatrix} \begin{Bmatrix} \Phi_1 \\ \Phi_2 \\ \Phi_3 \\ \Phi_4 \end{Bmatrix} \quad (\text{A2.14})$$

$$D = [B]\{\Phi\} \quad (\text{A2.15})$$

The  $[B]$  matrix is given as

$$[B] = \frac{1}{4} \begin{bmatrix} -(1-\eta) & (1-\eta) & (1+\eta) & -(1+\eta) \\ -(1-\xi) & -(1+\xi) & (1+\xi) & (1-\xi) \end{bmatrix} \quad (\text{A2.16})$$

## Appendix B: Laminar flow governing equations

### B1: Two-dimensional laminar flow governing dimensionless equations using a local thermal equilibrium model (LTE)

The dimensionless governing equations for the nanofluid layer are (Hussain and Rahomey, 2018):

#### Continuity equation

$$\frac{\partial(U)_{nf}}{\partial X} + \frac{\partial(V)_{nf}}{\partial Y} = 0 \quad (\text{B1.1})$$

#### Momentum equations

##### In the X-direction

$$(U)_{nf} \frac{\partial(U)_{nf}}{\partial X} + (V)_{nf} \frac{\partial(U)_{nf}}{\partial Y} = -\frac{\partial P}{\partial X} + \frac{(\rho)_{bf}}{(\rho)_{nf} \times (1-\phi)^{2.5}} \times Pr \times \left( \frac{\partial^2(U)_{nf}}{\partial X^2} + \frac{\partial^2(U)_{nf}}{\partial Y^2} \right) \quad (\text{B1.2})$$

##### In the Y-direction

$$(U)_{nf} \frac{\partial(V)_{nf}}{\partial X} + (V)_{nf} \frac{\partial(V)_{nf}}{\partial Y} = -\frac{\partial P}{\partial Y} + \frac{(\rho)_{bf}}{(\rho)_{nf} \times (1-\phi)^{2.5}} \times Pr \times \left( \frac{\partial^2(V)_{nf}}{\partial X^2} + \frac{\partial^2(V)_{nf}}{\partial Y^2} \right) + \frac{(\rho\beta)_{nf}}{(\rho)_{nf} \times (\beta)_{bf}} \times Pr \cdot Ra \cdot (\theta)_{nf} \quad (\text{B1.3})$$

#### Energy Equation

$$(U)_{nf} \frac{\partial(\theta)_{nf}}{\partial X} + (V)_{nf} \frac{\partial(\theta)_{nf}}{\partial Y} = \left( \frac{(\alpha)_{nf}}{(\alpha)_{bf}} \right) \times \left[ \left( \frac{\partial^2(\theta)_{nf}}{\partial X^2} + \frac{\partial^2(\theta)_{nf}}{\partial Y^2} \right) \right] \quad (\text{B1.4})$$

On the other hand, the dimensionless governing equations for the porous layer are:

#### Quantity Equation

$$\frac{\partial(U)_{nf}}{\partial X} + \frac{\partial(V)_{nf}}{\partial Y} = 0 \quad (\text{B1.5})$$

#### Momentum equations

##### In the X-direction

$$(U)_{nf} \frac{\partial(U)_{nf}}{\partial X} + V \frac{\partial(U)_{nf}}{\partial Y} = -\frac{\partial P}{\partial X} + \frac{(\rho)_{bf}}{(\rho)_{nf} \times (1-\phi)^{2.5}} \cdot Pr \left( \frac{\partial^2(U)_{nf}}{\partial X^2} + \frac{\partial^2(U)_{nf}}{\partial Y^2} \right) - \frac{(\rho)_{bf}}{(\rho)_{nf} \times (1-\phi)^{2.5}} \cdot \frac{Pr}{Da} \cdot (U)_{nf} \quad (B1.6)$$

**In the Y-direction**

$$(U)_{nf} \frac{\partial(V)_{nf}}{\partial X} + (V)_{nf} \frac{\partial(V)_{nf}}{\partial Y} = -\frac{\partial P}{\partial Y} + \frac{(\rho)_{bf}}{(\rho)_{nf} \times (1-\phi)^{2.5}} \times Pr \left( \frac{\partial^2(V)_{nf}}{\partial X^2} + \frac{\partial^2(V)_{nf}}{\partial Y^2} \right) + \frac{(\rho \times \beta)_{nf}}{(\rho)_{nf} \times (\beta)_{bf}} \times Pr \cdot Ra \cdot (\theta)_{nf} - \frac{(\rho)_{bf}}{(\rho)_{nf} \times (1-\phi)^{2.5}} \times \frac{Pr}{Da} (V)_{nf} \quad (B1.7)$$

**Energy equation**

$$(U)_{nf} \frac{\partial(\theta)_p}{\partial X} + (V)_{nf} \frac{\partial(\theta)_p}{\partial Y} = \left( \frac{(\alpha)_{nf}}{(\alpha)_{bf}} \right) * \left[ \left( \frac{\partial^2(\theta)_p}{\partial X^2} + \frac{\partial^2(\theta)_p}{\partial Y^2} \right) \right] \quad (B1.8)$$

The temperature of the nanofluid and porous medium are assumed equal and thermally equilibrium. The stream function intensity and the direction of the streamlines can be simulated using the following equation, where the positive sign of  $\Psi$  refers to an anticlockwise flow direction, and a negative sign indicates a clockwise flow direction.

$$\frac{\partial^2 \Psi}{\partial X^2} + \frac{\partial^2 \Psi}{\partial Y^2} = \frac{\partial U}{\partial Y} - \frac{\partial V}{\partial X} \quad (B1.9)$$

The dimensionless dependent and independent variables and parameters are as follows:

$$X = \frac{x}{L}, Y = \frac{y}{L}, U = \frac{uL}{(\alpha)_{bf}}, V = \frac{vL}{(\alpha)_{bf}}, P = \frac{PL}{(\rho)_{bf} \times (\alpha)_{bf}^2}, \Psi = \frac{\Psi}{(\alpha)_{bf}}, (\theta)_{nf} = \frac{T_{nf} - T_c}{T_h - T_c}, (\theta)_p = \frac{T_p - T_c}{T_h - T_c}, Ra = \frac{(\beta)_{bf} \times g \times \Delta T \times L^3}{(\vartheta)_{bf} \times (\alpha)_{bf}}, Pr = \frac{(\vartheta)_{bf}}{(\alpha)_{bf}}, \text{ and } Da = \frac{\lambda}{L^2} \quad (B1.10)$$

### Thermo-physical properties of the nanofluid

$$(\rho)_{nf} = (1 - \phi)(\rho)_{bf} + \phi(\rho)_{np} \quad (B1.11)$$

$$(\mu)_{nf} = \frac{(\mu)_{bf}}{(1-\phi)^{2.5}} \quad (B1.12)$$

$$(\rho C_p)_{nf} = (1 - \phi)(\rho C_p)_{bf} + \phi(\rho C_p)_{np} \quad (B1.13)$$

$$(\beta)_{nf} = (1 - \phi)(\rho\beta)_{nf} + \phi(\rho\beta)_{np} \quad (B1.14)$$

$$(\rho\beta)_{nf} = (1 - \phi)\rho_{bf} + \phi\rho_{np} \quad (B1.15)$$

$$(k)_{nf} = \frac{((k)_{np} + 2(k)_{bf}) - 2\phi((k)_{bf} - (k)_{np})}{((k)_{np} + 2(k)_{bf}) + \phi((k)_{bf} - (k)_{np})} (k)_{bf} \quad (B1.16)$$

$$(K)_{eff} = (K)_r * \frac{(k)_{nf}}{(k)_{bf}} \quad (B1.17)$$

where  $(K)_r$  is the porous/nanofluid thermal conductivity ratio,  $(K)_{eff}$  is the effective thermal conductivity, and

$$(\alpha)_{nf} = \frac{(k)_{nf}}{(\rho C_p)_{nf}} \quad (B1.18)$$

$$(\alpha)_{eff} = \frac{(k)_{eff}}{(\rho C_p)_{nf}} \quad (B1.19)$$

## B2: Two-dimensional laminar flow governing dimensionless equations using a local thermal non-equilibrium model (LTNE)

### Hybrid nanofluid layer

#### Continuity equation

$$\frac{\partial(U)_{hnf}}{\partial X} + \frac{\partial(V)_{hnf}}{\partial Y} = 0 \quad (B2.1)$$

#### Momentum equation

##### In the X-direction

$$(U)_{hnf} \frac{\partial(U)_{hnf}}{\partial X} + (V)_{hnf} \frac{\partial(U)_{hnf}}{\partial Y} = -\frac{\partial P}{\partial X} + \frac{(\rho)_{bf}}{(\rho)_{hnf} \times (1-\phi)^{2.5}} \times Pr \times \left( \frac{\partial^2(U)_{hnf}}{\partial X^2} + \frac{\partial^2(U)_{hnf}}{\partial Y^2} \right) \quad (B2.2)$$

**In the Y-direction**

$$(U)_{hnf} \frac{\partial(V)_{hnf}}{\partial X} + (V)_{hnf} \frac{\partial(V)_{hnf}}{\partial Y} = -\frac{\partial P}{\partial Y} + \frac{(\rho)_{bf}}{(\rho)_{hnf} \times (1-\phi)^{2.5}} \times Pr \times \left( \frac{\partial^2(V)_{hnf}}{\partial X^2} + \frac{\partial^2(V)_{hnf}}{\partial Y^2} \right) + \frac{(\rho\beta)_{hnf}}{(\rho)_{hnf} \times (\beta)_{bf}} \times Pr.Ra. (\theta)_{hnf} \quad (B2.3)$$

**Energy equation**

$$(U)_{hnf} \frac{\partial(\theta)_{hnf}}{\partial X} + (V)_{hnf} \frac{\partial(\theta)_{hnf}}{\partial Y} = \left( \frac{(\alpha)_{hnf}}{(\alpha)_{bf}} \right) \times \left[ \left( \frac{\partial^2 \theta_{hnf}}{\partial X^2} + \frac{\partial^2 \theta_{hnf}}{\partial Y^2} \right) + H * ((\theta)_p - (\theta)_{hnf}) \right] \quad (B2.4)$$

**Porous medium layer**

**Continuity equation**

$$\frac{\partial(U)_{hnf}}{\partial X} + \frac{\partial(V)_{hnf}}{\partial Y} = 0 \quad (B2.5)$$

**Momentum equations**

**In the X-direction**

$$(U)_{hnf} \frac{\partial(U)_{hnf}}{\partial X} + (V)_{hnf} \frac{\partial(U)_{hnf}}{\partial Y} = -\frac{\partial P}{\partial X} + \frac{(\rho)_{bf}}{(\rho)_{hnf} \times (1-\phi)^{2.5}} \times Pr \left( \frac{\partial^2(U)_{hnf}}{\partial X^2} + \frac{\partial^2(U)_{hnf}}{\partial Y^2} \right) - \frac{(\rho)_{bf}}{(\rho)_{hnf} \times (1-\phi)^{2.5}} \times \frac{Pr}{Da} \times (U)_{hnf} \quad (B2.6)$$

**In the Y-direction**

$$(U)_{hnf} \frac{\partial(V)_{hnf}}{\partial X} + (V)_{hnf} \frac{\partial(V)_{hnf}}{\partial Y} = -\frac{\partial P}{\partial Y} + \frac{(\rho)_{bf}}{(\rho)_{hnf} \times (1-\phi)^{2.5}} \times Pr \left( \frac{\partial^2(V)_{hnf}}{\partial X^2} + \frac{\partial^2(V)_{hnf}}{\partial Y^2} \right) + \frac{(\rho \times \beta)_{hnf}}{(\rho)_{hnf} \times (\beta)_{bf}} \times Pr.Ra. (\theta)_{hnf} - \frac{(\rho)_{bf}}{(\rho)_{hnf} \times (1-\phi)^{2.5}} \times \frac{Pr}{Da} (V)_{hnf} \quad (B2.7)$$

**Energy equation**

$$(U)_{hnf} \frac{\partial(\theta)_{hnf}}{\partial X} + (V)_{hnf} \frac{\partial(\theta)_{hnf}}{\partial Y} = \left( \frac{(\alpha)_{hnf}}{(\alpha)_{bf}} \right) * \left[ \left( \frac{\partial^2(\theta)_{hnf}}{\partial X^2} + \frac{\partial^2(\theta)_{hnf}}{\partial Y^2} \right) + H * ((\theta)_{hnf} - (\theta)_p) \right] \quad (B2.8)$$

$$\frac{\partial(\theta)_p}{\partial X} + \frac{\partial(\theta)_p}{\partial Y} = \gamma * H * [(\theta)_p - (\theta)_{hnf}] \quad (B2.9)$$

These governing equations are performed based on the dimensionless transform parameters as follows

$$\begin{aligned}
 X &= \frac{x}{L}, Y = \frac{y}{L}, U = \frac{u \times L}{(\alpha)_{bf}}, V = \frac{v \times L}{(\alpha)_{bf}}, P = \frac{P \times L}{(\rho)_{hnf}(\alpha)_{bf}^2}, \Psi = \frac{\Psi}{(\alpha)_{bf}}, \Delta T = \frac{q'' \times L}{(k)_{bf}}, \\
 (\theta)_{hnf} &= \frac{(T)_{hnf} - (T)_c}{(T)_w - (T)_c}, (\theta)_p = \frac{(T)_p - (T)_c}{(T)_w - (T)_c}, Ra = \frac{(\beta)_{bf} \times g \times \Delta T \times L^3}{(\vartheta)_{bf} \times (\alpha)_{bf}}, Pr = \frac{(\vartheta)_{bf}}{(\alpha)_{bf}}, Da = \\
 \frac{K}{L^2}, \gamma &= \frac{(k)_{hnf}}{(k)_p}, H = \frac{h \times L^2}{(k)_{hnf}}
 \end{aligned} \tag{B2.10}$$

The stream function intensity and the direction of the streamlines can be simulated using the following equation, where the positive sign of  $\Psi$  refers to an anticlockwise flow direction, and a negative sign indicates a clockwise flow direction.

$$\frac{\partial^2 \Psi}{\partial X^2} + \frac{\partial^2 \Psi}{\partial Y^2} = \frac{\partial U}{\partial Y} - \frac{\partial V}{\partial X} \tag{B2.11}$$

### Thermo-physical properties of the hybrid nanofluid

The physical property equations for the Cu – Al<sub>2</sub>O<sub>3</sub>/water hybrid nanofluid are simulated with a nanoparticle volume fraction,  $\phi$ , depending on the physical properties of the nanofluid equations presented in the reference (Gorla *et al.*, 2017).

$$(\rho)_{hnf} = [(\phi)_{Cu} \times (\rho)_{Cu} + (\phi)_{Al_2O_3} \times (\rho)_{Al_2O_3}] + (1 - \phi) \times (\rho)_{bf} \tag{B2.12}$$

$$(\mu)_{hnf} = \frac{(\mu)_{bf}}{[1 - ((\phi)_{Cu} + (\phi)_{Al_2O_3})]^{2.5}} \tag{B2.13}$$

$$(\rho \times Cp)_{hnf} = [(\phi)_{Cu} \times (\rho \times Cp)_{Cu} + (\phi)_{Al_2O_3} \times (\rho \times Cp)_{Al_2O_3}] + (1 - \phi) \times (\rho \times Cp)_{bf} \tag{B2.14}$$

$$(\rho \times \beta)_{hnf} = [(\phi)_{Cu} \times (\rho \times \beta)_{Cu} + (\phi)_{Al_2O_3} \times (\rho \times \beta)_{Al_2O_3}] + (1 - \phi) \times (\rho \times \beta)_{bf} \tag{B2.15}$$

$$\begin{aligned}
 (k)_{hnf} &= \left\{ \left[ \frac{[(\phi)_{Cu} \times (k)_{Cu} + (\phi)_{Al_2O_3} \times (k)_{Al_2O_3}]}{\phi} + 2 \times (k)_{bf} + 2 \times [(\phi)_{Cu} \times \right. \right. \\
 &\left. \left. (k)_{Cu} + (\phi)_{Al_2O_3} \times (k)_{Al_2O_3}] - 2 \times \phi \times (k)_{bf} \right] \times \right.
 \end{aligned}$$

$$\left[ \frac{[(\phi)_{Cu} \times (k)_{Cu} + (\phi)_{Al_2O_3} \times (k)_{Al_2O_3}]}{\phi} + 2 \times (k)_{bf} - [(\phi)_{Cu} \times (k)_{Cu} + (\phi)_{Al_2O_3} \times (k)_{Al_2O_3}] + (\phi) \times (k)_{bf} \right]^{-1} \times (k)_{bf}. \quad (B2.16)$$

$$(\alpha)_{hnf} = \frac{(k)_{hnf}}{(\rho \times Cp)_{hnf}} \quad (B2.17)$$

## Appendix C: Three-dimensional turbulent flow governing equations

### Nanofluid layer

#### Continuity equation

$$\frac{\partial(U)_{hnf}}{\partial X} + \frac{\partial(V)_{hnf}}{\partial Y} + \frac{\partial(W)_{hnf}}{\partial Z} = 0 \quad (C.1)$$

#### Momentum equations

##### In the X-direction

$$\begin{aligned} (U)_{hnf} \times \frac{\partial(U)_{hnf}}{\partial X} + (V)_{nf} \times \frac{\partial(U)_{hnf}}{\partial Y} + (W)_{nf} \times \frac{\partial(U)_{hnf}}{\partial Z} = -\frac{\partial}{\partial X} \left( P + \frac{2}{3} \times Pr^2 \times \right. \\ \left. K \right) + Pr \times (I + (\mu)_{td}) \times \left[ 2 \times \frac{\partial}{\partial X} \times \left( \frac{\partial(U)_{hnf}}{\partial X} \right) + \frac{\partial}{\partial Y} \times \left( \left( \frac{\partial(U)_{hnf}}{\partial Y} + \frac{\partial(V)_{hnf}}{\partial X} \right) \right) + \right. \\ \left. \frac{\partial}{\partial Z} \left( \frac{\partial(U)_{hnf}}{\partial Z} + \frac{\partial(W)_{hnf}}{\partial X} \right) \right] \end{aligned} \quad (C.2)$$

##### In the Y-direction

$$\begin{aligned} (U)_{hnf} \times \frac{\partial(V)_{hnf}}{\partial X} + (V)_{nf} \times \frac{\partial(V)_{hnf}}{\partial Y} + (W)_{nf} \times \frac{\partial(V)_{hnf}}{\partial Z} = -\frac{\partial}{\partial Y} \left( P + \frac{2}{3} \times Pr^2 \times \right. \\ \left. K \right) + Pr \times (I + (\mu)_{td}) \times \left[ \frac{\partial}{\partial X} \times \left( \frac{\partial(U)_{hnf}}{\partial Y} + \frac{\partial(V)_{hnf}}{\partial X} \right) + 2 \times \frac{\partial}{\partial Y} \times \left( \frac{\partial(V)_{hnf}}{\partial Y} \right) + \right. \\ \left. \frac{\partial}{\partial Z} \left( \frac{\partial(V)_{hnf}}{\partial Z} + \frac{\partial(W)_{hnf}}{\partial Y} \right) \right] + \frac{(\rho\beta)_{hnf}}{\rho_{hnf} \times \beta_{bf}} \times Pr \times Ra \times (\theta)_{hnf} \end{aligned} \quad (C.3)$$

##### In the Z-direction

$$\begin{aligned} (U)_{hnf} \times \frac{\partial(W)_{hnf}}{\partial X} + (V)_{hnf} \times \frac{\partial(W)_{hnf}}{\partial Y} + (W)_{hnf} \times \frac{\partial(W)_{hnf}}{\partial Z} = -\frac{\partial}{\partial Z} \left( P + \frac{2}{3} \times \right. \\ \left. Pr^2 \times K \right) + Pr \times (I + (\mu)_{td}) \times \left[ \frac{\partial}{\partial X} \times \left( \frac{\partial(W)_{hnf}}{\partial X} + \frac{\partial(U)_{hnf}}{\partial Z} \right) + \frac{\partial}{\partial Y} \left( \frac{\partial(W)_{hnf}}{\partial Y} + \right. \right. \\ \left. \left. \frac{\partial(V)_{hnf}}{\partial Z} \right) + 2 \times \frac{\partial}{\partial Z} \times \left( \frac{\partial(W)_{hnf}}{\partial Z} \right) \right] \end{aligned} \quad (C.4)$$

## Porous layer

### Continuity equation

$$\frac{\partial(U)_{hnf}}{\partial X} + \frac{\partial(V)_{hnf}}{\partial Y} + \frac{\partial(W)_{hnf}}{\partial Z} = 0 \quad (C.5)$$

### Momentum equations

#### In the X-direction

$$\begin{aligned} (U)_{hnf} \times \frac{\partial(U)_{hnf}}{\partial X} + V \times \frac{\partial(U)_{hnf}}{\partial Y} + W \times \frac{\partial(U)_{hnf}}{\partial Z} = -\frac{\partial}{\partial X} \left( P + \frac{2}{3} \times Pr^2 \times K \right) + \\ Pr \times (I + (\mu)_{td}) \times \left[ 2 \times \frac{\partial}{\partial X} \times \left( \frac{\partial(U)_{hnf}}{\partial X} \right) + \frac{\partial}{\partial Y} \times \left( \left( \frac{\partial(U)_{hnf}}{\partial Y} + \frac{\partial(V)_{hnf}}{\partial X} \right) \right) + \right. \\ \left. \frac{\partial}{\partial Z} \left( \frac{\partial(U)_{hnf}}{\partial Z} + \frac{\partial(W)_{hnf}}{\partial X} \right) \right] - I \times \frac{Pr}{Da} \times (U)_{hnf} \end{aligned} \quad (C.6)$$

#### In the Y-direction

$$\begin{aligned} (U)_{hnf} \times \frac{\partial(V)_{hnf}}{\partial X} + (V)_{hnf} \times \frac{\partial(V)_{hnf}}{\partial Y} + (W)_{hnf} \times \frac{\partial(V)_{hnf}}{\partial Z} = -\frac{\partial}{\partial Y} \left( P + \frac{2}{3} \times Pr^2 \times K \right) + \\ Pr \times (I + (\mu)_{td}) \times \left[ \frac{\partial}{\partial X} \times \left( \frac{\partial(U)_{hnf}}{\partial Y} + \frac{\partial(V)_{hnf}}{\partial X} \right) + 2 \times \frac{\partial}{\partial Y} \times \left( \frac{\partial(V)_{hnf}}{\partial Y} \right) + \right. \\ \left. \frac{\partial}{\partial Z} \left( \frac{\partial(V)_{hnf}}{\partial Z} + \frac{\partial(W)_{hnf}}{\partial Y} \right) \right] + \frac{(\rho\beta)_{hnf}}{\rho_{hnf} \times \beta_{bf}} \times Pr \times Ra \times \theta_{hnf} - I \times \frac{Pr}{Da} \times (V)_{hnf} \end{aligned} \quad (C.7)$$

#### In the Z-direction

$$\begin{aligned} (U)_{hnf} \times \frac{\partial(W)_{hnf}}{\partial X} + (V)_{hnf} \times \frac{\partial(W)_{hnf}}{\partial Y} + (W)_{hnf} \times \frac{\partial(W)_{hnf}}{\partial Z} = -\frac{\partial}{\partial Z} \left( P + \frac{2}{3} \times Pr^2 \times K \right) + \\ Pr \times (I + (\mu)_{td}) \times \left[ \frac{\partial}{\partial X} \times \left( \frac{\partial(W)_{hnf}}{\partial X} + \frac{\partial(U)_{hnf}}{\partial Z} \right) + \frac{\partial}{\partial Y} \left( \frac{\partial(W)_{hnf}}{\partial Y} + \right. \right. \\ \left. \left. \frac{\partial(V)_{hnf}}{\partial Z} \right) + 2 \times \frac{\partial}{\partial Z} \times \left( \frac{\partial(W)_{hnf}}{\partial Z} \right) \right] - I \times \frac{Pr}{Da} \times (W)_{hnf} \end{aligned} \quad (C.8)$$

where,

$$I = \frac{1}{\frac{(1-\phi)^{2.5}}{(\rho)_{hnf}} \frac{(\rho)_{bf}}{(\rho)_{bf}}} \quad (C.9)$$

$$(\mu)_{td} = (\rho)_{bf} \times C_\mu \times \left( \frac{K^2}{E} \right) \quad (C.10)$$

### Energy equation

$$(U)_{hnf} \times \frac{\partial(\theta)_{hnf}}{\partial X} + (V)_{hnf} \times \frac{\partial(\theta)_{hnf}}{\partial Y} + (W)_{hnf} \times \frac{\partial(\theta)_{hnf}}{\partial Z} = (k_{eff}) \times \left[ \frac{\partial^2(\theta)_{hnf}}{\partial X^2} \times \frac{\partial^2(\theta)_{hnf}}{\partial Y^2} \times \frac{\partial^2(\theta)_{hnf}}{\partial Z^2} \right] \quad (C.11)$$

$$(U)_{nf} \times \frac{\partial\theta}{\partial X} + (V)_{nf} \times \frac{\partial\theta}{\partial Y} + (W)_{nf} \times \frac{\partial\theta}{\partial Z} = \left( I + (\mu)_{td} \times \frac{Pr}{Pr_t} \right) \times \left[ \frac{\partial^2\theta}{\partial X^2} \times \frac{\partial^2\theta}{\partial Y^2} \times \frac{\partial^2\theta}{\partial Z^2} \right] \quad (C.12)$$

### Turbulent kinetic energy:

$$(U)_{hnf} \times \frac{\partial K}{\partial X} + (V)_{hnf} \times \frac{\partial K}{\partial Y} + (W)_{hnf} \times \frac{\partial K}{\partial Z} = Pr \times \left( I + \frac{(\mu)_{td}}{Pr_t} \right) \times \left[ \frac{\partial^2 K}{\partial X^2} \times \frac{\partial^2 K}{\partial Y^2} \times \frac{\partial^2 K}{\partial Z^2} \right] + \frac{(\mu)_{td}}{Pr} \times \left\{ 2 \times \left[ \left( \frac{\partial(U)_{hnf}}{\partial X} \right)^2 + \left( \frac{\partial(V)_{hnf}}{\partial Y} \right)^2 + \left( \frac{\partial(W)_{hnf}}{\partial Z} \right)^2 \right] + \left[ \left( \frac{\partial(U)_{hnf}}{\partial Y} + \frac{\partial(V)_{hnf}}{\partial X} \right)^2 + \left( \frac{\partial(V)_{hnf}}{\partial Z} + \frac{\partial(W)_{hnf}}{\partial Y} \right)^2 + \left( \frac{\partial(W)_{hnf}}{\partial X} + \frac{\partial(U)_{hnf}}{\partial Z} \right)^2 \right] \right\} - Pr \times E \quad (C.13)$$

### Dissipation rate of turbulence kinetic energy:

$$(U)_{hnf} \times \frac{\partial E}{\partial X} + (V)_{hnf} \times \frac{\partial E}{\partial Y} + (W)_{hnf} \times \frac{\partial E}{\partial Z} = Pr \times \left( I + \frac{(\mu)_{td}}{Pr_t} \right) \times \left[ \frac{\partial^2 E}{\partial X^2} \times \frac{\partial^2 E}{\partial Y^2} \times \frac{\partial^2 E}{\partial Z^2} \right] - C_2 \times \frac{Pr}{\frac{(\rho)_{hnf}}{(\rho)_{bf}}} \times \frac{E^2}{k} - C_3 \times \left( \frac{(\mu)_{td}}{Pr} \right) \times \left( \frac{(\beta)_{hnf}}{(\beta)_{bf}} \right) + C_1 \times \left( \frac{(\mu)_{td}}{Pr} \right) \times \left\{ 2 \times \left[ \left( \frac{\partial(U)_{hnf}}{\partial X} \right)^2 + \left( \frac{\partial(V)_{hnf}}{\partial Y} \right)^2 + \left( \frac{\partial(W)_{hnf}}{\partial Z} \right)^2 \right] + \left[ \left( \frac{\partial(U)_{hnf}}{\partial Y} + \frac{\partial(V)_{hnf}}{\partial X} \right)^2 + \left( \frac{\partial(V)_{hnf}}{\partial Z} + \frac{\partial(W)_{hnf}}{\partial Y} \right)^2 + \left( \frac{\partial(W)_{hnf}}{\partial X} + \frac{\partial(U)_{hnf}}{\partial Z} \right)^2 \right] \right\} \quad (C.14)$$

where the coefficients of the  $\kappa$ - $\varepsilon$  model have the following standard values (Braga and de Lemos, 2004):

$$C_\mu = 0.09, C_1 = 1.44, C_2 = 1.92, C_3 = 0.7, \sigma_k = 1, \sigma_\varepsilon = 1.3, \text{ and } Pr_T = 1 \quad (C.15)$$

The stream function intensity and the direction of the streamlines can be simulated using the following equation, where the positive sign of  $\Psi$  refers to an anticlockwise flow direction, and a negative sign indicates a clockwise flow direction.

$$U = \frac{\partial\Psi_Z}{\partial Y} - \frac{\partial\Psi_Y}{\partial Z}, V = \frac{\partial\Psi_X}{\partial Z} - \frac{\partial\Psi_Z}{\partial X}, \text{ and } W = \frac{\partial\Psi_Y}{\partial X} - \frac{\partial\Psi_X}{\partial Y} \quad (C.16)$$

The dimensionless parameters of the dependent and independent variables as follows:

$$\begin{aligned}
 X &= \frac{x}{L}, Y = \frac{y}{L}, U = \frac{uL}{\alpha_{bf}}, V = \frac{vL}{\alpha_{bf}}, P = \frac{PL}{(\rho)_{bf} \cdot (\alpha)_{bf}^2}, \Psi = \frac{\Psi}{(\alpha)_{bf}}, \theta_{nf} = \frac{T_{nf}-T_c}{T_h-T_c}, \theta_p = \\
 &= \frac{T_p-T_c}{T_h-T_c}, Ra = \frac{\beta_{bf} \cdot g \cdot \Delta T \cdot L^3}{\vartheta_{bf} \cdot \alpha_{bf}}, Pr = \frac{\vartheta_{bf}}{\alpha_{bf}}, Da = \frac{\lambda}{L^2} \cdot \mu_{nfd} = \frac{\mu_{nf}}{\mu_{bf}}, \mu_{td} = \frac{\mu_{tnf}}{\mu_{bf}}, K = \frac{\kappa}{\left(\frac{(\alpha_{bf})^2}{L^2}\right)}, \\
 \text{and } E &= \frac{\epsilon}{\left(\frac{(\alpha_{bf})^3}{L^4}\right)}. \tag{C.17}
 \end{aligned}$$

## Appendix D: List of publications

One journal paper has been published from the content of Chapter 4. The outcomes of Chapter 6 have been published in one journal paper.

### Journal papers:

---

Journal paper 1	B.M. Al-Srayyih, S. Gao, S.H. Hussain, Effects of linearly heated left wall on natural convection within a superposed cavity filled with composite nanofluid-porous layers, <i>Advanced Powder Technology</i> , 30(1) (2019) 55-72.
Journal paper 2	B.M. Al-Srayyih, S. Gao, S.H. Hussain, Natural convection flow of a hybrid nanofluid in a square enclosure partially filled with a porous medium using a thermal non-equilibrium model, <i>Physics of Fluids</i> , 31(4) (2019) 043609.

---